# High-Temperature Metamorphic Reactions from the Macro-Scale to the Micro-Scale

by

Sabastien Dyer

A thesis
presented to the University of Waterloo
in fulfillment of the
thesis requirement for the degree of
Doctor of Philosophy
in
Earth Sciences

Waterloo, Ontario, Canada, 2025

© Sabastien Dyer 2025

**Examining Committee Membership**

The following served on the Examining Committee for this thesis. The decision of the Examining Committee is by majority vote.

| | |
|---|---|
| External Examiner: | Dr. Xu Chu<br>Associate Professor |
| Supervisor(s): | Chris Yakymchuk<br>Associate Professor |
| Internal Member: | Shoufa Lin<br>Professor |
| | Shaun Frape<br>Professor |
| Internal-External Member: | Yuri Leonenko<br>Professor |

## Author's Declaration

This thesis consists of material all of which I authored or co-authored: see Statement of Contributions included in the thesis. This is a true copy of the thesis, including any required final revisions, as accepted by my examiners.

I understand that my thesis may be made electronically available to the public.

## Statement of Contributions

Chapters 1 and 5 are solely authored by Sabastien Dyer with input from thesis supervisor Chris Yakymchuk. Chapters 2–4 are prepared as manuscripts that have been submitted or will be submitted to academic journals for publication. For these chapters, writing, data interpretation, and figure preparation were done primarily by Sabastien Dyer. The contributions of co-authors are summarized below.

Chapter 2 was submitted and accepted for publication by the journal *Contributions to Mineralogy and Petrology* (Dyer et al., 2025). Samples were collected by Sabastien Dyer, Carson Kinney, and Chris Yakymchuk. Electron probe microanalysis was completed at the University of Toronto by Sabastien Dyer with assistance from Yanan Liu. Laser ablation inductively coupled plasma mass spectrometry was done primarily by Sabastien Dyer with assistance from Ivan Edgeworth and Brian Kendall (co-authors). Thermodynamic modelling, petrography, and figure preparation were done primarily by Sabastien Dyer with input from Chris Yakymchuk (supervisor). The manuscript was primarily written by Sabastien Dyer with guidance from Chris Yakymchuk (supervisor) and edits from Ivan Edgeworth and Brian Kendall. Further revisions have been added to this paper following comments from an anonymous reviewer, Jesse Reimink and journal editor Othmar Müntener during the peer-review process for *Contributions to Mineralogy and Petrology*.

Citation: Dyer, S. C., Edgeworth, I., Kendall, B., and Yakymchuk, C. (2025). Late-orogenic retrograde zircon growth. *Contributions to Mineralogy and Petrology*, 180(5):31

Chapter 3 was prepared for submission to the journal *Lithos*. Samples were collected by Sabastien Dyer, Carson Kinney, and Chris Yakymchuk. Additional samples were provided by R. Jamieson collected as part of a thesis by T. Slagstad. Electron probe microanalysis was completed at the University of Toronto by Sabastien Dyer with assistance from Yanan Liu. Laser ablation inductively coupled mass spectrometry was done primarily by Sabastien Dyer with assistance from Ivan Edgeworth and Brian Kendall (co-authors). Petrography, and figure preparation were done primarily by Sabastien Dyer with input from Chris Yakymchuk (supervisor). The manuscript was primarily written by Sabastien Dyer with guidance from Chris Yakymchuk (supervisor) and contributions and input provided by Fred Gaidies (co-author).

Chapter 4 was prepared for submission to the journal *Journal of Metamorphic Geology*. Samples were collected by Sabastien Dyer, Carson Kinney, and Chris Yakymchuk. Electron probe microanalysis was completed at the University of Toronto by Sabastien Dyer with assistance from Yanan Liu. Laser ablation inductively coupled mass spectrometry was done primarily by Sabastien Dyer with assistance from Ivan Edgeworth and Brian Kendall

(co-authors). Thermodynamic modelling, petrography, and figure preparation were done primarily by Sabastien Dyer with input from Chris Yakymchuk (supervisor). The manuscript was primarily written by Sabastien Dyer with guidance from Chris Yakymchuk (supervisor).

## Abstract

Metamorphic reactions are the basis of metamorphic petrology and the lens through which we interpret metamorphic rocks and processes. They serve both as tectonic indicators, revealing the pressure–temperature history of a rock, and as tectonic drivers, responsible for the production of fluids and melts that are critical to many geological processes in the crust. At high temperatures, two types of reactions that have emphasized importance are melting reactions that have implications for large-scale crustal reworking and reactions that grow accessory minerals that we use to date petrological processes.

Zircon is the most common geochronometer, but its behaviour at high temperatures is poorly understood. Zircon-forming reactions were investigated in granulite-facies metagranitoids in the Grenville province to better understand how zircon grows during metamorphism at high temperatures. Zircon growth occurred during retrogression as a result of melt crystallization and titanomagnetite breakdown. With this information, the dates of metamorphic zircon that were measured were interpreted as cooling dates, and provided additional context that suggests that the major orogenic phase of Grenville Orogen may have begun tens of millions of years earlier than previously thought.

Zircon was also used as a proxy to investigate the kinetics of trace elements in intergranular melt during melt crystallization in a migmatite. Key trace elements including Hf, U, Th, Y, and heavy rare earth elements were analyzed in multiple metamorphic zircon rims to compare relative concentration of zircon that grew coevally in the same thin section. The significant differences observed in concentration of these elements across zircon grains suggests rates of diffusion of these key trace elements are slower than zircon growth in migmatites. Zircon growth probably occurred as a result of size-dependent interface-controlled growth, implying that Zr diffusion was relatively fast in the melt.

On the macro-scale, evidence of regionally extensive $H_2O$-fluxed melting reactions have been observed in multiple distinct tectonic environments across the globe, yet there is no generic tectonic model that explains regional-scale $H_2O$-fluxed melting in the crust. Regional scale $H_2O$-fluxed melting was studied in the Muskoka domain of the Grenville province. In the Muskoka domain, $H_2O$-fluxed melting dominated throughout the region and until now, the source and mechanism of the $H_2O$ transport into the Muskoka domain has been unclear. Multiple examples of pegmatites with amphibole and leucosome-rich reaction selvages were found throughout the domain that show how $H_2O$ may have been transported into and through the Muskoka domain. Using a two-stage melting model, it was shown that melt generated at depth through hydrate-breakdown melting contains enough $H_2O$ to readily melt the rocks in the Muskoka domain through diffusive $H_2O$-fluxed melting, with no fluid exsolution required.

Metamorphic reactions are used to understand regional tectonics, but there are significant gaps in our understanding of these reactions on both the micro-scale and the macro-scale. The geochronological tools that are used to unravel metamorphism are based on micro-scale processes that are still poorly understood. Simultaneously, our understanding of macro-scale tectonic processes involving $H_2O$ transport in the crust, which influence our interpretation of metamorphic rocks, is limited with $H_2O$-fluxed melting. This thesis addresses our limits of understanding and shows how understanding metamorphic reactions allows us to better understand regional tectonics.

**Acknowledgements**

There are so many people who have supported me through this journey and I wish I could personally thank them all, and while there is technically no word limit on this section I do still want to be brief. My supervisor Chris Yakymchuk provided so much support, guidance, and kindness throughout my whole degree. Even through the pandemic, parental leave, and a sabbatical, he was always there to help when I needed it. I also want to thank my committee members Shoufa Lin and Shaun Frape for their advice and input throughout my time at Waterloo. I also want to acknowledge the financial support of the Ontario Graduate Scholarship and NSERC.

There are many people that have come and gone during my time in this program who have become good friends and whose support has helped me overcome some of my greatest challenges. Carson Kinney, my PhD compatriot who has been there since the first day out in the field and almost every day in our shared office progressing and suffering side by side as we faced down this immense task. Jillian Kendrick who always offered wisdom and witty remarks and who I could always count on to jump up in excitement when I had a cool thin section to show her. Sophie Gagnon, Zach Adam, Iris Li, Qiháng Wú, Ludovico Scorsoilini, Gabriel dos Santos, Tong Hong, Ivan Edgeworth, and Philip Wright and all the other friends I have made along the way have provided many fun nights out or afternoons at the pub and many needed distractions during the workday. I am grateful for all of you that helped contribute to a wonderful and supportive environment at the University of Waterloo.

My family has been a constant support throughout my schooling, and I am sure they are all very relieved that it is coming to an end. They have always been there to offer love, support, and advice no matter the situation and I will be forever grateful for having a family that cares so much about me. My mom, Alison Brown; my dad, Nick Dyer; and my brother, Sam Dyer, have all helped me reach this point and I know that I am making them proud with completing this thesis.

Finally, and most importantly, I want to acknowledge my partner Sarah Moldaver. It is difficult to describe how much support Sarah has given me throughout the past five years. Despite the many years of long-distance, and the many challenges that she has faced herself as a graduate student, she has always given me so much love and encouragement and support. She has helped me succeed and grow in the many years we have been together, and I know that will continue to be true in the years to come.

## Dedication

This is dedicated to everyone that is trapped in a hole.

# Table of Contents

**Examining Committee** ii

**Author's Declaration** iii

**Statement of Contributions** iv

**Abstract** vi

**Acknowledgements** viii

**Dedication** ix

**List of Figures** xv

**List of Tables** xvii

**1 Introduction** 1

1.1 Reactions driving tectonic processes . . . . . 1

1.2 Partial melting . . . . . 2

1.3 Understanding tectonism from reactions . . . . . 3

1.4 Accessory minerals . . . . . 3

1.5 Grenville Province and regional geology . . . . . 5

1.5.1 The Grenville Province and Central Gneiss Belt . . . . . 5

1.5.2 The Muskoka domain . . . 6
1.6 Thesis format and objectives . . . 8

**2 Late-orogenic retrograde zircon growth** **10**
2.1 Summary . . . 10
2.2 Introduction . . . 11
2.3 Geological Setting . . . 12
2.3.1 Grenville Province . . . 12
2.3.2 Muskoka domain . . . 12
2.3.3 Sample descriptions . . . 14
2.4 Methods . . . 15
2.4.1 Whole-rock geochemistry . . . 15
2.4.2 Zircon imaging . . . 15
2.4.3 Mineral compositions . . . 16
2.4.4 Zircon geochronology . . . 16
2.4.5 Phase equilibrium modelling . . . 17
2.4.6 Mineral–melt Zr partition modelling . . . 18
2.5 Results . . . 18
2.5.1 Whole rock chemical compositions . . . 18
2.5.2 Mineral assemblages and microstructures . . . 18
2.5.3 Major mineral compositions . . . 23
2.5.4 Concentration of Zr in major and accessory minerals . . . 23
2.5.5 U-Pb zircon geochronology . . . 23
2.5.6 Equilibrium phase relations . . . 24
2.5.7 Zr reservoirs during melting . . . 24
2.6 Discussion . . . 25
2.6.1 Model limitations . . . 25
2.6.2 Metamorphic zircon . . . 26

2.6.3 P–T–t constraints on Grenvillian metamorphism . . . . . 30
2.7 Conclusions . . . . . 34
**References** . . . . . 35

**3 Sluggish mobility of trace elements in suprasolidus metamorphic systems: implications for zircon petrochronology** **55**
3.1 Summary . . . . . 55
3.2 Introduction . . . . . 56
3.3 Regional context and petrography . . . . . 58
3.4 Analytical methods . . . . . 60
3.4.1 SEM and cathodoluminescence imaging . . . . . 60
3.4.2 Electron Probe Microanalysis . . . . . 62
3.5 Results . . . . . 62
3.5.1 Zircon textures . . . . . 62
3.5.2 U and Th zoning . . . . . 63
3.5.3 Y and Yb zoning . . . . . 64
3.5.4 Hf zoning . . . . . 65
3.6 Discussion . . . . . 65
3.6.1 Zircon growth mechanisms . . . . . 65
3.6.2 Trace element mobility . . . . . 66
3.6.3 Analytical smoothing of profiles . . . . . 66
3.6.4 Diffusion limited trace elements in zircon . . . . . 69
3.6.5 Implications . . . . . 70
3.7 Conclusions . . . . . 72
**References** . . . . . 74

**4 Regionally extensive $H_2O$-fluxed melting in the Grenville Province 86**
4.1 Summary . . . 86
4.2 Introduction . . . 87
4.3 Geological setting . . . 88
4.3.1 Grenville Province . . . 88
4.3.2 Muskoka domain . . . 89
4.3.3 Migmatites . . . 90
4.3.4 Pegmatites . . . 91
4.4 Methods . . . 92
4.4.1 Whole-rock geochemistry . . . 92
4.4.2 Amphibole compositions . . . 93
4.4.3 Zircon U–Pb geochronology . . . 93
4.4.4 Phase equilibrium modelling . . . 94
4.4.5 $H_2O$-fluxed melting models . . . 94
4.5 Results . . . 96
4.5.1 Petrography . . . 96
4.5.2 Whole rock geochemistry . . . 98
4.5.3 Amphibole compositions . . . 98
4.5.4 Pegmatite U–Pb zircon geochronology . . . 100
4.5.5 T–X diagrams . . . 101
4.5.6 $H_2O$-fluxed melting models . . . 102
4.6 Discussion . . . 103
4.6.1 Model limitations . . . 103
4.6.2 Evidence for $H_2O$-fluxed melting . . . 104
4.6.3 Sources of $H_2O$ . . . 107
4.6.4 $H_2O$-fluxed melting models . . . 108
4.6.5 Comparison with migmatites . . . 109
4.6.6 Tectonic implications . . . 111
4.7 Conclusion . . . 112
**References** . . . 114

**5 Conclusions** **135**

5.1 Summary of research . . . . . 135

5.2 Future work and recommendations . . . . . 136

5.2.1 Trace element mobility . . . . . 137

5.2.2 $H_2O$-present melting . . . . . 137

**References** **139**

**APPENDICES** **162**

**A Supplementary Material for Chapter 2** **163**

**B Supplementary Material for Chapter 3** **166**

**C Supplementary Material for Chapter 4** **171**

# List of Figures


1.1 Map of the Grenville Province and Central Gneiss Belt . . . . . 9

2.1 Map of the Grenville Province and Central Gneiss Belt . . . . . 44
2.2 Outcrop photos . . . . . 45
2.3 Thin section photomicrographs . . . . . 46
2.4 Cathodoluminescence images of zircon . . . . . 47
2.5 Zr concentrations of major minerals . . . . . 48
2.6 Zircon ages . . . . . 49
2.7 Pseudosections . . . . . 50
2.8 Model of spinel and ilmenite proportions and composition . . . . . 51
2.9 Model of Zr content of key phases . . . . . 52
2.10 Zircon reaction sketch . . . . . 53
2.11 P–T path . . . . . 54

3.1 Location of zircon in thin section . . . . . 81
3.2 Cathodoluminescence images of zircon . . . . . 82
3.3 Zircon grain size plot . . . . . 83
3.4 Zircon trace element profiles . . . . . 84
3.5 Overlay of zircon trace element profile . . . . . 85

4.1 Map of the Grenville Province and Central Gneiss Belt . . . . . 122
4.2 Migmatites in the Muskoka domain . . . . . 123

4.3 Pegmatites in the Muskoka domain . . . . . 124
4.4 Photomicrographs of reaction selvages and hosts . . . . . 125
4.5 Molar Na + Ca, Fe* + Mg + Ti, K ternary diagram . . . . . 126
4.6 Molar An-Ab-Or ternary diagram . . . . . 127
4.7 Calcium amphibole classification plot . . . . . 128
4.8 Chondrite-normalized REE plots for amphibole . . . . . 129
4.9 Pegmatite concordia plots . . . . . 130
4.10 T–X pseudosections . . . . . 131
4.11 Schematic sketch of $H_2O$-fluxed melting process . . . . . 132
4.12 Results of $H_2O$-fluxed melting model . . . . . 133
4.13 Schematic cross-section of tectonic model for the Muskoka domain . . . . . 134

A.1 Concordia diagrams of the secondary standards . . . . . 165

B.1 U–Pb date profiles of zircon . . . . . 167
B.2 EPMA lines on zircon . . . . . 168
B.3 Y and Yb profiles of zircon . . . . . 169
B.4 U profile rescaling example . . . . . 170

C.1 Concordia diagram of the secondary standards . . . . . 173

# List of Tables

2.1 Bulk rock composition in weight % . . . . . 43

# Chapter 1

# Introduction

## 1.1 Reactions driving tectonic processes

The fundamental processes that drive metamorphism are chemical reactions. These may be reactions between minerals or fluids or melts within the crust. Such reactions result in wholesale changes of a rock's mineral assemblage. It is this change in mineral assemblage that help define metamorphism (Spear, 1995; Powell and Holland, 2008). The changes that occur in crustal rocks as a result of these chemical reactions are also significant contributors to the forces that drive tectonism on earth. For instance, the metamorphism of oceanic crust into dense eclogites contributes to the negative buoyancy of the down-going slab, which pulls the slab downward during subduction (e.g. Duesterhoeft et al., 2014).

At high temperatures, metamorphic reactions transform crustal rocks into granulite-facies assemblages, which make up the bulk of the lower continental crust (Ellis, 1987; Harley, 1989; Bohlen and Mezger, 1989; Rudnick and Fountain, 1995). Perhaps the most important metamorphic reactions that are recorded in a majority of granulite-facies rocks is partial melting. Partial melting in the crust plays a significant role in a large swathe of tectonic processes, including crustal differentiation (e.g. Hacker et al., 2011; Johnson et al., 2012), arc magmatism (e.g. Clemens et al., 2021; Collins et al., 2020), and the formation and stabilization of the continental crust (e.g. Moyen and Stevens, 2006; Moyen, 2011). Due to its significant impact on the tectonic processes and structure of the crust, understanding partial melting reactions has been an important topic of ongoing study in high-temperature rocks.

## 1.2 Partial melting

Partial melting in the crust can be an extremely important process in regional tectonics and processes including crustal differentiation. Because silicate melt is less dense than the surrounding residue, it is commonly lost from the source and this ultimately contributes to a chemically stratified continental crust. This melt loss can result in significant changes to the composition and mineral assemblage of a rock and therefore its physical properties (Diener and Fagereng, 2014; Jackson et al., 2004; White and Powell, 2002; Vanardois et al., 2024). High volumes of melt can also weaken the rock and—when this occurs on a regional scale—can result in the collapse and extension of an orogen and influencing global tectonics in the process (e.g. Rey et al., 2009; King et al., 2011; Whitney et al., 2013; Moyen, 2011).

There are two types of partial melting reactions: hydrate-breakdown melting and fluid-fluxed melting (Brown, 2007, 2013; Weinberg and Hasalová, 2015). Hydrate-breakdown melting occurs as a result of high-temperature breakdown reactions of hydrous minerals with melt as a product. These are considered to be the most common and regionally significant melting reactions as they only require sufficient input of heat to occur. Fluid-fluxed melting reactions in contrast occur as a result of the addition of hydrous fluids and have been historically considered to be less prominent, localized processes where fluid transport occurs and is added to sufficiently hot rocks to induce a melting reaction (Brown, 2013; Weinberg and Hasalová, 2015; Pichavant et al., 2024; Zhu et al., 2025).

The study of partially-melted rocks, or migmatites, largely occurs at the rock outcrop. This is where a geologist can best see the evidence of melting reactions in leucosomes and peritectic minerals grown from incongruent melting reactions (Sawyer, 2008). The outcrop is where the amount of melt generated can best be assessed by looking at the amount of leucosome and the textural relationship that leucosome has with the rock that it is hosted in (e.g. White et al., 2005; Guernina and Sawyer, 2003). These observations inform our understanding of the regional tectonics and structure of the crust, and whether we interpret these melting reactions as hydrate-breakdown melting or fluid-fluxed melting will significantly influence tectonic processes and our understanding of orogenesis.

The assumption that fluid-fluxed melting is relatively unimportant to regional processes has resulted in a majority of research into partial melting to focus on hydrate-breakdown melting. This is despite dozens of studies in regions across the globe that suggest that fluid-fluxed melting does in fact have regional significance in a wide variety of tectonic environments (Weinberg and Hasalová, 2015; Volante et al., 2025; Xia et al., 2025; Errázuriz-Henao et al., 2024; Lei et al., 2024; Qi et al., 2023; Vanardois et al., 2024). This under-emphasis of fluid-fluxed melting may be due to the physical constraints on fluid transport in

the crust that make it challenging to propose a regional model for fluid-fluxed melting that can be liberally applied under the diverse tectonic conditions where $H_2O$-fluxed melting can be found. Models of $H_2O$-fluxed melting via the diffusive addition of $H_2O$ from hydrous silicate melts (Tafur and Diener, 2020) present a less restrictive mechanism of $H_2O$-transport compared to free fluid models, but this has remained an under-explored model for $H_2O$-fluxed melting and there has been no investigation into how such a model could influence regional tectonics.

## 1.3 Understanding tectonism from reactions

While metamorphic reactions can drive tectonic processes, the inverse is true as well. Metamorphic reactions are indirectly driven by tectonic processes as a result of changing temperatures and pressures, and our understanding of these metamorphic reactions allow us to infer tectonic processes based on the mineral assemblages and textures left behind in the rock record (Powell and Holland, 2008). This relationship between tectonism and metamorphism is the primary motivation for a majority of research into metamorphic petrology. Well-understood metamorphic reactions allow us to chart a pressure–temperature (P–T) history of a rock that can then be related to the greater tectonic history of the region (Spear, 1995). One additional and crucial piece of information required to do this is timing. Linking metamorphism to an absolute date requires the dating of key minerals formed by metamorphic reactions like garnet (e.g. Tual et al., 2025; Simpson et al., 2023), or indirectly linking important geochronometers like zircon to metamorphic reactions (Rubatto, 2002; Taylor et al., 2017; Rubatto and Hermann, 2007). This act of linking the age of a mineral—particularly an accessory mineral—to a petrological process is called "petrochronology" and has been the focus of many metamorphic studies for the past two decades (e.g. Kohn et al., 2015; Taylor et al., 2017; Kelsey and Powell, 2011; Spear, 2010; Kirkland et al., 2018, 2020; Cisneros de León et al., 2022; Cioffi et al., 2019).

## 1.4 Accessory minerals

In metamorphic rocks, accessory minerals such as zircon, monazite, and allanite have been the focus of petrochronological studies as these minerals incorporate significant amounts of U or Th that make them effective geochronometers (Volante et al., 2024), but their low abundance and significant incorporation of trace elements makes them challenging to determine their formation reactions and link those to specific P–T conditions. Since trace

elements such as Zr or rare earth elements (REE) are important structural constituents in these minerals, modelling these minerals and understanding their conditions of formation requires effective activity composition models for Zr and REE in any phase that contains appreciable amounts of these trace elements. There has been some progress in developing such models (Kohn et al., 2015; Kelsey and Powell, 2011; Spear, 2010), but these models still require assumptions of equilibrium. While the assumption of equilibrium throughout a $\sim 100$ cm$^3$ sample has often been shown to be effective for modelling minerals composed of major elements (Palin et al., 2016; Lanari and Duesterhoeft, 2019; Powell et al., 2005), this has not been well established for minerals whose essential structural constituents are trace elements, such as Zr in zircon. Central to this is our limited understanding of rates of grain-boundary diffusion of trace elements in metamorphic rocks, which can be too slow to allow equilibration in a $\sim 100$ cm$^3$ sample even in suprasolidus rocks (Acosta-Vigil et al., 2012; McLeod et al., 2012).

Due to the lack of solid solution models that incorporate trace elements and poor understanding of trace element diffusion in metamorphic rocks which both limit our ability to quantitatively predict accessory minerals, we often rely on other methods to assess the relative timing of their growth. Trace elements in these minerals are commonly used as a simple way to evaluate what other minerals were present at the time of growth (e.g. Taylor et al., 2017; Hermann and Rubatto, 2003). These trace element indicators are popular for inferring igneous, metamorphic, and sedimentary processes despite the aforementioned limitations on our understanding of trace element diffusion in metamorphic rocks because it requires only measurement of trace elements of the accessory mineral, which is most commonly done as mineral separates without petrological context. While analytical techniques for trace element measurements of minerals are well established and common, the least ambiguous observation for understanding mineral reactions are textures. By interpreting textures of these accessory minerals and linking them to the growth or breakdown of P–T sensitive major minerals that can be effectively modelled, their ages can be connected to the P–T conditions where those major minerals occur, unlocking our ability to piece together tectonic histories.

Zircon being perhaps the most significant geochronometer in its well-established reliability for geochronology, is an important mineral to understand the reactions and kinetics that result in its growth during metamorphism. New zircon growth during metamorphism requires a source of Zr. There have been several sources of Zr proposed for the growth of metamorphic zircon including: garnet (Fraser et al., 1997; Degeling et al., 2001; Tomkins et al., 2005), amphibole (Fraser et al., 1997; Kohn et al., 2015), ilmenite (Bingen, 2001; Morisset and Scoates, 2008; Beckman et al., 2017), rutile (Ewing et al., 2013; Kohn et al., 2015; Pape et al., 2016), baddeleyite (Beckman et al., 2017; Cisneros de León et al., 2022),

and melt (Kelsey et al., 2008; Kohn et al., 2015; Yakymchuk, 2023). Despite these numerous possible reactants for zircon growth reactions, there still remains much uncertainty around the specific reactions that occur and even whether they occur during prograde or retrograde metamorphism. The particular distinction between prograde and retrograde zircon growth is particularly relevant to our interpretation of metamorphic zircon ages and the tectonic relevance of those ages. The kinetics of zircon growth are also not well established with very few studies investigating the rate-limiting mechanisms of zircon growth (Miyazaki et al., 2018, 2019) and there remain no empirical studies into the effects of trace element diffusion rates on metamorphic zircon composition.

## 1.5 Grenville Province and regional geology

### 1.5.1 The Grenville Province and Central Gneiss Belt

The Grenville Province is the exposed root of the Grenville orogeny that was assembled in the Mesoproterozoic between ca. 1.1 and 1.0 Ga (Fig. 1.1 A). This was during an alleged period of quiescence in global tectonics (Tang et al., 2021) wherein the Grenville orogeny developed during the formation of the supercontinent Rodinia (Rivers et al., 2012). As it is contiguously exposed from Lake Huron in Ontario to the eastern coast of Labrador, the Grenville Province offers unique insight into Proterozoic geology. In addition, it is composed of multiple tectonic belts and terranes that variably record multiple tectonometamorphic events throughout the Proterozoic. While the Grenville orogeny is often compared to the Himalayan orogeny (Indares, 2020; Hynes and Rivers, 2010), there are distinct differences in its assembly and form that provide insight into global tectonics during the Proterozoic (e.g. Jamieson et al., 2010; Brudner et al., 2022), a period of earth's history that is tectonically distinct from the Archean and the Phanerozoic and can provide insight into the global transition from ancient tectonic processes to the tectonic processes observed on Earth today (Brown et al., 2020). As recent challenges (Gervais et al., 2023) to the accepted model of the Grenville have shown, the tectonic conditions that led to the formation of the Grenville Province are still unclear and further work is required into the region to determine its place in earth's global tectonic history.

The Central Gneiss Belt is one of the aforementioned tectonic belts that makes up a majority of the Grenville Province in Ontario dominates the Ontario, extending from the Composite Arc Boundary thrust zone in the southeast to the Grenville Front Tectonic Zone in the northwest (Fig. 1.1 B). The allochthon boundary thrust divides the Central Gneiss Belt into the parautochthonous belt and the allochthonous belt. The Central Gneiss Belt is

divided by the allochthon boundary thrust into the parautochthonous belt and allochthonous belt. The dominant metamorphic signature in the Central Gneiss Belt is Grenvillian (*sensu stricto*) in age (ca. 1.1–1.0 Ga), with the allochthonous belt metamorphosed only during the Ottawan phase (ca. 1090–1020 Ma) and the parautochthonous belt overprinted by the Rigolet phase (ca. 1005–980 Ma) (Rivers, 2008; Rivers et al., 2012).

The allochthonous belt is composed primarily of variably metamorphosed igneous rocks including: a $\geq$ 1460 Ma calc-alkaline suite containing meta-tonalite, meta-granodiorite and meta-gabbro; a 1460–1430 Ma anorthosite-mangerite-charnockite-granite suite containing meta-monzonite, meta-monzodiorite, meta-gabbro, and meta-anorthosite; 1170–1150 Ma coronitic metagabbros; syn-deformational syenite pegmatite dikes (1100–1050 Ma); and post-deformational ($\sim$1000 Ma) granite pegmatite dykes that crosscut both the calc-alkaline suite and the anorthosite-mangerite-charnockite-granite suite (Ketchum and Davidson, 2000; Slagstad, 2003; Rivers and Schwerdtner, 2015; Culshaw et al., 2016). The allochthonous belt is further subdivided into a granulite-facies Allochthonous Polycyclic Belt that contains evidence for pre-Grenvillian metamorphism (>1.1 Ga) and the amphibolite-facies Allochthonous Monocyclic Belt that contains no discernible evidence of pre-Genvillian metamorphism (Ketchum and Davidson, 2000). Both the Allochthonous Polycyclic Belt and Allochthonous Monocyclic Belt are composed of multiple domains that are separated by shear zones. These domains are interpreted to represent thrust sheets that developed during orogenesis (Culshaw et al., 1997; Jamieson et al., 2010). This thesis is focused on the formation of the Muskoka domain and related Opeongo domain in the Allochthonous Monocyclic Belt and metamorphic processes that occurred within these domains.

### 1.5.2 The Muskoka domain

The Muskoka domain is a $\sim$7 km thick package of amphibolite-facies orthogneiss structurally below the Composite Arc Boundary thrust zone (Fig. 1.1 B) and structurally above the Algonquin, Rosseau, and Go-Home domains (Rivers, 2008; Jamieson and Beaumont, 2011; Dickin et al., 2017; Rivers and Schwerdtner, 2015). The Muskoka domain includes the Moon River and Seguin subdomains in the west and extends east where there is an uncertain transition into the related Opeongo domain, which is composed of similar rock types (Culshaw et al., 2016). The Opeongo and Muskoka domains have also been grouped together by Nd model ages and complimentary zircon Hf isotopes into a single allochthon called the Muskoka allochthon that extends into western Quebec with a full orogen-parallel length of $\sim$ 300 km (Dickin et al., 2017; Dickin and Strong, 2019; Slagstad et al., 2025).

The Muskoka domain is dominated by stromatic migmatites in which the mesosome, leucosome, and melanosome occur as continuous and parallel layers of variable thickness

(Slagstad et al., 2005, 2004). These migmatites typically have granodioritic mesosome and frequently contain amphibole porphyroblasts within the leucosome. Metamorphism of these rocks is estimated to have reached a peak pressure of 9–12 kbar (uncertain temperature Anovitz and Essene, 1990; Timmerman et al., 2002) and a peak temperature of 750–850 °C (uncertain pressure Timmerman et al., 2002). The exact timing of peak metamorphism remains uncertain, however multiple cooling ages have been measured: U–Pb dates of zircon in leucosome in the calc-alkaline rocks can be interpreted to record melt crystallization at ca. 1070–1060 Ma (Fig. 1.1 B; Slagstad et al., 2004; Timmerman et al., 2002). The large volume of leucosome observed in these rocks and occurrence of amphibole porphyroblasts in the leucosome that may have formed as the product of a peritectic melting reaction suggests that melting in the Muskoka domain must have required the addition of $H_2O$ in order to produce these features at the estimated peak temperatures (Slagstad et al., 2005). No clear source for $H_2O$ has been found for this regionally extensive $H_2O$-fluxed melting, but it has been suggested that $H_2O$ infiltrated from the surface during extension and orogenic collapse (Rivers and Schwerdtner, 2015). However, the tectonometamorphic history of the Muskoka domain is still unclear and it is challenging to understand where $H_2O$ could come from and how it infiltrated the Muskoka domain without a clearer understanding of the history and formation of the Muskoka domain itself.

There have been two tectonic models proposed for the Muskoka domain that explain its structural placement in the Grenville stack and the strong extensional deformation observed throughout the domain. One model suggests that the Muskoka domain developed during convergence in which ductile flow and extension occurred in the domain as it was thrusted over the underlying units (Jamieson et al., 2007). In this model, melting and deformation occurred during continent–continent convergence and crustal thickening. The alternate model proposes that deformation and partial melting of the Muskoka domain dominantly occurred during orogenic collapse where the Muskoka domain acted as a detachment zone between the Central Gneiss Belt and the Composite Arc Belt (Rivers and Schwerdtner, 2015). These two models are not necessarily mutually exclusive, but there is sparse metamorphic evidence available to support or refute either model.

The Muskoka domain provides a convenient geological laboratory to address broader questions about metamorphic reactions at high temperatures. Being composed primarily of meta-granitoids, the Muskoka domain contains some uniquely Zr-rich rocks that provide an excellent opportunity to interrogate zircon forming reactions. While there has been work done in the past modelling meta-granitoids (e.g. Bader et al., 2014; Duan et al., 2023; Chen et al., 2008), there has not been any connection made between these models and zircon-forming reactions within these rock types. The protracted residence time at high temperatures (Slagstad et al., 2004) also makes this region a good laboratory to investigate

the kinetics behind these zircon-forming reactions. On the macro-scale, the extensive $H_2O$-fluxed melting over a large contiguous region make the Muskoka domain the ideal location to investigate $H_2O$-fluxed melting reactions and melting processes in the middle to lower crust.

## 1.6 Thesis format and objectives

This thesis is composed of five chapters. Chapter 1 is an introductory chapter, chapters 2–4 are prepared as articles for publication in scientific journals, and chapter 5 is a concluding chapter. Two chapters (Chapters 2 & 3) are investigations into the reactions and kinetics around metamorphic zircon growth in rocks that reached the granulite facies. Chapter 2 provides the first ever reported empirical evidence of retrograde metamorphic zircon growth as a result of titanomagnetite breakdown and provides additional insight into the tectonics of the Muskoka domain in the Grenville province where this study was conducted. Chapter 3 provides empirical evidence of slow diffusion in suprasolidus migmatites and the first study that shows how this influences zircon growth and composition. Chapter 4 is an investigation into regional-scale diffusive $H_2O$-fluxed melting and is the first study to proposes a tectonic model for how this may have occurred. Each chapter has an associated reference list and appendix with supplementary data.

The central goal of this thesis is to investigate the reactions that occur at high temperatures in metamorphic rocks which are both driven by tectonics and help drive tectonic processes. The research within this thesis utilizes field and petrographic evidence in combination with analytical techniques to measure mineral composition and dates as well as established and novel forward modelling of phase equilibria and melting. The integrated approach that has been employed emphasizes that good petrographic and field observations are essential for effective petrochronological and metamorphic studies where direct observations of the processes under investigation can not be made. Chapter 2 takes a strong focus on textures and U–Pb measurements of zircon observed *in situ* within thin sections to assess zircon-forming reactions in granulite-facies rocks. Chapter 3 focuses even more specifically on the trace element composition of metamorphic zircon as a proxy for melt composition to assess the mobility of trace elements within suprasolidus rocks. Chapter 4 takes a regional focus, utilizing field observations to inform a model on $H_2O$-fluxed melting and regional tectonic model.

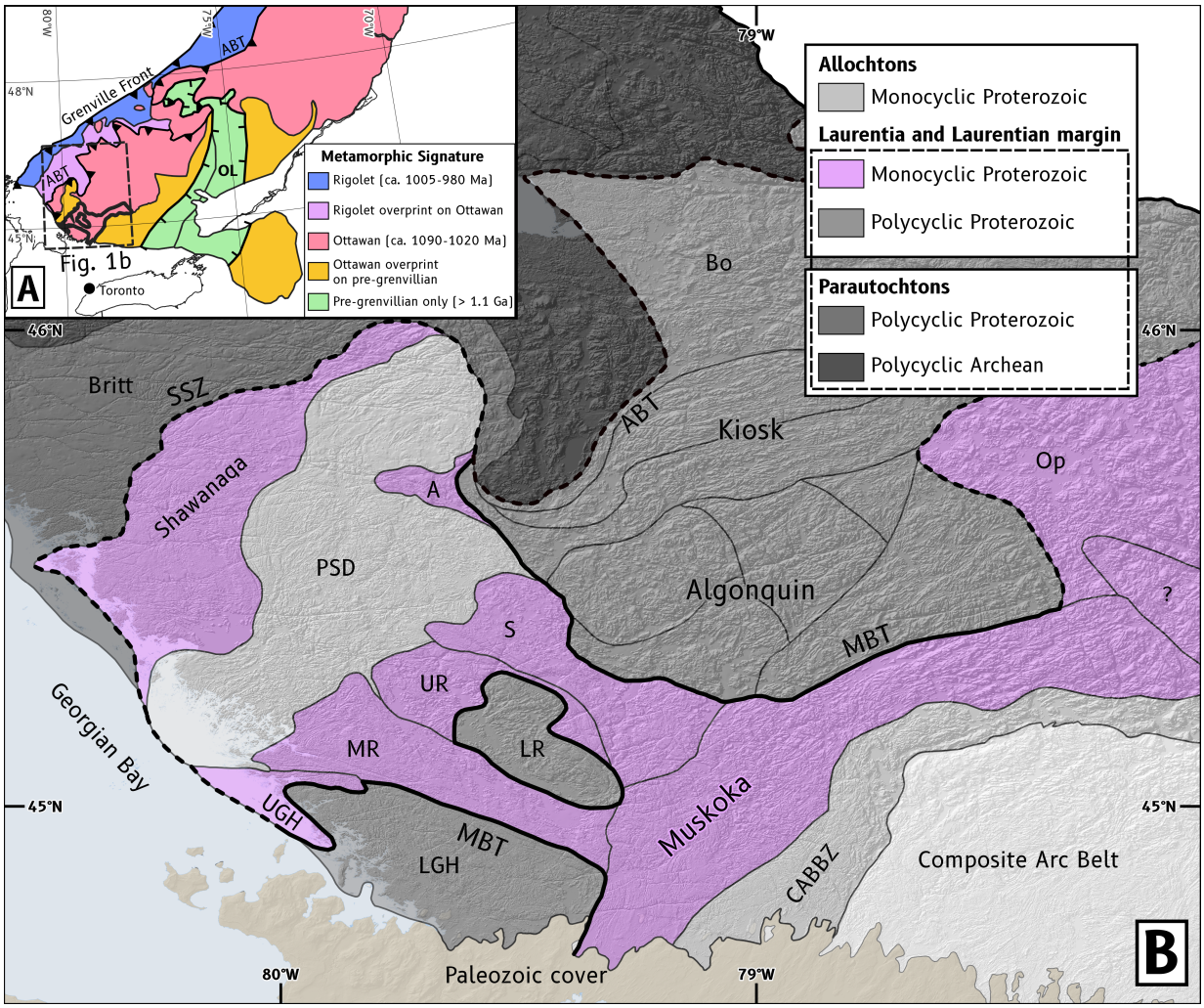


**Figure 1.1: (A)**: Overview map of the Grenville Province showing metamorphic affinity of different regions in the Grenville (Modified after Rivers (2008)). Abbreviations: OL = Orogenic Lid; ABT = Allochthon Boundary Thrust. **(B)**: Map of the Central Gneiss Belt in Ontario with the Muskoka domain highlighted (Modified after Culshaw et al. (2016)). The Muskoka domain is the natural laboratory that was used to address broader questions about high-temperature metamorphic reactions including zircon-forming reactions and kinetics and $H_2O$-fluxed melting reactions. Abbreviations: MBT = Monocyclic Boundary Thrust; SSZ = Shawanaga shear zone; CABBZ = Composite Arc Belt Boundary Zone; UGH, LGH, UR, LR, A, Op = upper-, lower Go Homme, upper-, lower Rosseau, Ahmic, Opeongo domains; MR, S = Moon River, Seguin subdomains; PSD = Parry Sound domain; Bo = Bonfield domain.

# Chapter 2

# Late-orogenic retrograde zircon growth

## 2.1 Summary

Metamorphic zircon is commonly assumed to record growth during prograde or peak metamorphic conditions. However, numerical models of zircon predict growth during cooling. Linking the relative timing of zircon growth to a metamorphic evolution requires determining the potential zircon forming reactions during protracted metamorphic cycles. Meta-granitoids from the Grenville Province in Ontario contain a high proportion of igneous zircon with metamorphic rims that provide a rare opportunity to study zircon forming reactions *in situ*; acquiring U-Pb dates while maintaining their petrographic context and textural setting in thin section. Textures and trace element composition of major minerals indicate that metamorphic zircon grew as a result of melt crystallization and breakdown of titanomagnetite. Phase equilibrium modelling shows that these reactions occurred during retrograde metamorphism. Measured U–Pb dates of these retrograde metamorphic zircons are between ca. 1100 and 1070 Ma. This contradicts previous interpretations of regional geology that suggest prograde and peak metamorphism occurred between 1080 and 1050 Ma. These results highlight the need to carefully analyze the metamorphic textures of zircon to provide the necessary context to assess the zircon-forming reaction and its link to the pressure–temperature history of the rock. Without this context, pressure-temperature-time paths determined with zircon dates should be treated with caution and could be incorrectly linked to disparate stages of orogenic cycles.

## 2.2 Introduction

How does zircon grow during metamorphism? Determining zircon forming reactions in metamorphic systems is challenging and has only been addressed in a few studies (Hoskin and Schaltegger, 2003; Rubatto, 2017; Volante et al., 2024). The results of these studies suggest that zircon-forming reactions vary, depending on the Zr-bearing minerals present within the rock and the composition and nature of metamorphic fluids and anatectic melt. The growth of zircon in metamorphic systems has been proposed to result from the liberation of Zr during the breakdown of: garnet (Fraser et al., 1997; Degeling et al., 2001; Tomkins et al., 2005), amphibole (Fraser et al., 1997; Kohn et al., 2015), ilmenite (Bingen, 2001; Morisset and Scoates, 2008; Beckman et al., 2017), rutile (Ewing et al., 2013; Kohn et al., 2015; Pape et al., 2016), baddeleyite (Beckman et al., 2017; Cisneros de León et al., 2022), as well as crystallization from anatectic melt (Kelsey et al., 2008; Kohn et al., 2015; Yakymchuk, 2023).

Many metamorphic studies that utilize zircon to determine P–T–t paths interpret zircon ages as representative of prograde or peak metamorphism (e.g. Schneider et al., 2013; Marsh and Culshaw, 2014; Culshaw et al., 2016). This is sometimes supported by *in situ* textural relationships (e.g. Cesare et al., 2009), but most studies analyze zircon separates with little consideration for their textural context. Zircon growth models have contradicted this interpretation of metamorphic zircon and instead suggest retrograde zircon growth occurs more frequently (Kelsey et al., 2008; Kelsey and Powell, 2011; Yakymchuk and Brown, 2014; Kohn et al., 2015). This is because the phases with relatively high concentrations of Zr are more likely to break down — or crystallize in the case of melt — with decreasing pressures or temperatures. The Zr-bearing phases that have been modelled are rutile (Kohn et al., 2015), garnet (Kelsey and Powell, 2011), and melt (Kelsey and Powell, 2011; Yakymchuk and Brown, 2014; Yakymchuk, 2023), but, in general, Ti-rich minerals incorporate high concentrations of Zr (Bea et al., 2006). These models are all dependent on phase equilibrium modelling and coupled to either zircon saturation models (e.g. Yakymchuk and Brown, 2014) or solution models that incorporate Zr (e.g. Kelsey and Powell, 2011) and mass balance (e.g. Kohn et al., 2015). Although numerical models are effective tools for understanding metamorphic processes, petrographic evidence of retrograde zircon-forming reactions has been documented (e.g. Tomkins et al., 2005), though only rarely. Here we present empirical evidence that tests the predictions of these numerical models.

We examine zircon-forming reactions that include the breakdown of titanomagnetite during cooling after peak metamorphism from high-grade granitoids in the southwestern Grenville Province of Canada. The investigated samples contain an unusually large proportion of coarse-grained zircon that are amenable to *in situ* geochronology. We demonstrate

that the timing of cooling — and concomitant zircon growth — is inconsistent with some regional tectonic models of the southwestern Grenville Province. Our results suggest that this part of the Grenville Province already began cooling during a time period that is generally considered the metamorphic peak (ca. 1080–1050 Ma Rivers, 2008), indicating that orogenesis may have commenced earlier than previously thought. This highlights the importance of understanding the P–T conditions of zircon growth when using zircon to interpret the orogenic evolution of a region.

## 2.3 Geological Setting

### 2.3.1 Grenville Province

The Grenville Province is a regionally extensive orogenic belt that is contiguously exposed in Canada from central Ontario to the coast of Labrador (e.g. Rivers, 2012). It consists of several distinct terranes exhibiting multiple stages of tectonism. The two pre-Grenvillian phases are the Elzevirian (1245–1225 Ma) and the Shawinigan (1190–1140 Ma) orogenies (Rivers, 2008). These pre-Grenvillian phases are interpreted to record the assembly of the Composite Arc Belt (CAB) and the Frontenac-Adirondack Belt respectively (Rivers et al., 2012). The two phases of the Grenville orogeny (*sensu stricto*) are the Ottawan (1090–1020 Ma) and the Rigolet (1005–980 Ma) (Rivers, 2008). Earlier stages of metamorphism are best preserved in the southeast portion of the Grenville in the CAB and Frontenac-Adirondack Belt (Fig. 2.1 A). To the northwest of the CAB is the Central Gneiss Belt, which can be divided into the Allochthonous Belt and the Parautochthonous Belt and are separated by the allochthon boundary thrust (ABT) (Rivers, 2008; Ketchum and Davidson, 2000). The Allochthonous Belt is on the southern side of the ABT and is dominated by Ottawan metamorphism. The Parautochthonous Belt is on the northern side of the ABT and extends to the northern edge of the Grenville province and is dominated by Rigolet metamorphism. These belts are further subdivided into multiple domains and terranes; we focus on the Muskoka domain and related Opeongo domain in the Allochthonous Belt (Fig. 2.1 B).

### 2.3.2 Muskoka domain

The Muskoka domain is a package of amphibolite-facies orthogneiss with up to 70 km of orogen-perpendicular intermittent exposure in Ontario with a ∼120 km orogen-parallel extent from Georgian Bay in the west to Algonquin Park in the east (Fig. 2.1 B) (Slagstad,

2003; Slagstad et al., 2004, 2005; Rivers and Schwerdtner, 2015). In eastern Ontario, the Muskoka domain transitions into the potentially related Opeongo domain (Culshaw et al., 2016, 2023). The Opeongo domain contains similar lithologies as the Muskoka domain and there is structural and geochemical evidence to suggest it is contiguous with the Muskoka domain (McMullen, 1999; Dickin et al., 2017; Culshaw et al., 2016). The thickness of the Muskoka domain is ∼5 km at its westernmost exposure where it is situated structurally above the Algonquin, Rosseau, and Go-Home domains and below the Composite Arc Belt boundary zone (Rivers, 2008; Jamieson and Beaumont, 2011; Dickin et al., 2017). The Muskoka and Opeongo domains are considered allochthonous and are composed of a $\geq$ 1460 Ma calc-alkaline suite containing meta-tonalite, meta-granodiorite and meta-gabbro; a 1460–1430 Ma anorthosite-mangerite-charnockite-granite suite containing meta-monzonite, meta-monzodiorite, meta-gabbro, and meta-anorthosite; 1170–1150 Ma coronitic metagabbros; syn-deformational syenite pegmatite dikes (1100–1050 Ma); and post-deformational (∼1000 Ma) granite pegmatite dykes that crosscut both the calc-alkaline suite and the anorthosite-mangerite-charnockite-granite suite (Ketchum and Davidson, 2000; Slagstad, 2003; Rivers and Schwerdtner, 2015; Culshaw et al., 2016). The calc-alkaline suite dominates the domain, primarily occurring as stromatic and patchy migmatites with amphibole and biotite-rich melanosome and alkali feldspar and quartz-rich leucosome (Slagstad et al., 2005).

The Muskoka domain has similar lithologies to the underlying allochthonous Algonquin, Rosseau, and Go-Home domains, but they differ in two key aspects. The first is that the underlying domains show evidence of having been metamorphosed at >1100 Ma, prior to the main Ottawan phase of the Grenville orogeny. These poly-metamorphic rocks are referred to as "polycyclic," along with the underlying parautochthonous units (Ketchum and Davidson, 2000). The second differentiating factor is that the underlying domains dominantly exhibit anhydrous mineral assemblages consistent with granulite-facies metamorphism (e.g. paucity of biotite and amphibole; abundance of garnet, orthopyroxene, and clinopyroxene), whereas the Muskoka domain is dominated by hydrous mineral assemblages with many amphibole and biotite-rich gneisses with isolated occurrences of anhydrous mineral assemblages — typically in large and weakly deformed granitoid bodies — similar to those present in underlying domains (Timmerman et al., 2002). In addition, the Muskoka domain shows evidence of widespread fluid-fluxed melting whereas the underlying domains were dominated by hydrate-breakdown melting (Slagstad et al., 2005).

Peak metamorphism was proposed to have occurred between 1080–1060 Ma based on U-Pb dates of zircon from migmatite leucosome and granulite veins (Timmerman et al., 2002). Estimates of peak pressure have been constrained to 9–12 kbar (Anovitz and Essene, 1990; Timmerman et al., 2002) and peak temperature estimates range from 750 to 850 °C (Timmerman et al., 2002). These P–T estimates place the Muskoka domain in the upper-

amphibolite to lower-granulite facies, which aligns with the observed mineral assemblages in the region, with rocks containing abundant biotite and amphibole alongside isolated occurrences of anhydrous mineral assemblages.

There are two distinct tectonic models proposed for the evolution of the Muskoka domain in the context of Grenvillian orogenesis. Jamieson and Beaumont (2011) suggest that the Muskoka domain recorded heterogeneous ductile flow during the convergent evolution of the Grenville Province. Rivers and Schwerdtner (2015) suggest that the metamorphic and structural features of the Muskoka domain result from retrogression and strain during orogenic collapse where the Muskoka domain acted as a ductile detachment zone between the underlying Central Gneiss Belt and the overlying CAB. While these two models are not necessarily mutually exclusive, it is unclear what the metamorphic and geochronological data record; convergence and heating, or cooling and exhumation. This is the main tectonic question that is addressed in this paper.

### 2.3.3 Sample descriptions

Four samples that contain large volumetric proportions of zircon were chosen from a suite of samples across the Central Gneiss Belt; three were collected from the Muskoka domain (20SD06, 20SD17A, 21SD68) and one from the Opeongo domain (22SD55E; Fig. 2.1 B). These samples come from rare occurrences of weakly foliated meta-granitoids that are part of the anorthosite-mangerite-charnockite-granite suite. Compared to the more common amphibole-biotite rich stromatic and patchy migmatite, these are more homogenous, with less leucosome. Leucosome has similar mineral assemblages to the host rocks which are generally more quartz and feldspar rich than the dominant lithologies of the region.

Sample 20SD06 is from a weakly foliated, massive, homogenous garnet-bearing meta-monzogranite. It contains infrequent parallel and crosscutting coarse-grained leucosome that has diffuse boundaries with the surrounding host-rock (Fig. 2.2 A). Leucosome contains variable amounts of plagioclase, alkali feldspar, quartz, and clinopyroxene with rims of amphibole.

Sample 20SD17A is from a weakly foliated garnet-bearing meta-monzogranite from a weakly-deformed granitoid body with a heterogeneous composition, varying from diorite to monzogranite. Pegmatites with amphibole-rich reaction selvedges crosscut the unit. Pods of mafic amphibolite are common. Crosscutting and foliation parallel leucosome is common, containing variable amounts of alkali feldspar, plagioclase, magnetite, clinopyroxene, biotite, and amphibole (Fig. 2.2 B). Magnetite-rich selvedges rarely occur at the edge of the leucosome.

Sample 21SD68 is from a ∼2 m wide homogenous pod of fayalite-clinopyroxene-bearing meta-quartz-monzonite. It is fine-grained with alkali feldspar porphyroclasts up to 1 cm in length. A weak fabric is present with rare parallel and crosscutting coarse-grained leucosome. The leucosome contains variable amounts of alkali feldspar, plagioclase, and quartz (Fig. 2.2 C).

Sample 22SD55E is from a pod of weakly deformed garnet-bearing meta-quartz-monzonite and is surrounded by stromatic meta-granodiorite and meta-diorite gneisses. Some crosscutting pegmatites are present with amphibole-rich reaction selvedges. No obvious leucosome is present within the garnet-rich portion of the outcrop that was sampled, however leucosome occurs in immediately adjacent rocks that contain little to no garnet (Fig. 2.2 D).

## 2.4 Methods

### 2.4.1 Whole-rock geochemistry

Whole-rock geochemistry of the four samples was conducted at ActLabs (Ancaster, Ontario) using their 4LithoResearch package. Samples were dissolved using lithium metaborate and lithium tetraborate fusion. Molten material was dissolved in 5% nitric acid, and this solution was then analyzed. Major element concentrations were measured using an Agilent Technologies Varian 735 Emission Spectrometer and trace elements were measured using an PerkinElmer Elan 9000 inductively coupled plasma mass spectrometer (ICP-MS). Ferrous iron ($Fe^{+2}$) was measured using titration with a cold digestion of ammonium metavanadate and hydrofluoric acid. Ferrous ammonium sulphate was added after digestion and potassium dichromate was used as the titrating agent.

### 2.4.2 Zircon imaging

Internal zircon textures and morphology were analyzed in polished thin sections using a petrographic microscope as well as back-scattered electron (BSE) and cathodoluminescence (CL) imaging. BSE imaging was done using an FEI Quanta Feg 250 ESEM operating at 20 kV. CL imaging was done using a Zeiss LEO 1530 scanning electron microscope (SEM) operating at 20 kV and 0.5–1 nA with an aperture size of 120 µm.

### 2.4.3 Mineral compositions

Major element mineral compositions were determined using electron probe microanalysis (EPMA) with a JEOL JXA8230 5-WDS electron microprobe at the University of Toronto Department of Earth Sciences EPMA lab. Minerals were analyzed using 1-10 µm spot sizes with an accelerating voltage of 15 keV and current of 20 nA and acquisition times were 2-4 min. On peak and background collection times for each element measured in each mineral are presented in Table A.1. Calibration was done prior to the start of analyses on natural and synthetic standards.

Trace element mineral compositions were measured using laser ablation inductively-coupled plasma mass spectrometry (LA-ICP-MS) with an Agilent 8800 QQQ-ICP-MS in sequence with an Analyte G2 193 nm Excimer laser ablation unit system in the Metal Isotope Geochemistry Lab at the University of Waterloo. Minerals were preablated with a 65 µm single shot operating at 4 $\frac{\text{J}}{\text{cm}^2}$. Ablation was performed with 50 µm spot size and a fluence of 4 $\frac{\text{J}}{\text{cm}^2}$ (measured at sample surface) with a repetition rate of 8 Hz. Ablated material was moved from the laser sample chamber using He as a carrier gas (0.8 L/min) with Ar added to the aerosol (0.85 L/min). Samples were analyzed using standard–sample bracketing (reference materials run every ∼10 unknowns). NIST612 was used as the external reference material for all silicate minerals and apatite, NIST610 was used as a secondary reference material for silicates and fragments of Durango apatite were used as a secondary reference material for apatite (e.g. Chew et al., 2016). Magnetite and ilmenite were analyzed using BC-28 as the primary reference material (Dare et al., 2014) and BHVO-2G (Jochum et al., 2005) as the secondary reference material. EPMA analyses at or near the laser spots were used as internal standards for all minerals except zircon, titanite, and allanite. Si was used as the internal standard for silicate minerals, Fe was used for magnetite and ilmenite, and Ca was used for apatite. Assumed concentrations of Si were used for titanite (14.2 wt%), and allanite (14 wt%). Data was processed using Iolite (v.4). Full analytical conditions are shown in Table A.2.

Concentrations of Ti in zircon were measured, but measurements could not be differentiated from the background signal and are therefore not included.

### 2.4.4 Zircon geochronology

Zircon was analyzed *in situ* in polished thin sections using an Analyte G2 laser ablation system coupled with a NuPlasma II multicollector-ICP-MS. Zircon was pre-ablated using 50 µm wide lines across grains from rim to rim or core to rim. Ablation was performed

with 20 µm wide lines and a fluence of 4 $\frac{J}{cm^2}$ with a repetition rate of 8 Hz and moving at 2 $\frac{\mu m}{s}$. Ablated material was transported from the laser sample chamber using He as a carrier gas (0.7 L/min) with $N_2$ added to the aerosol (0.003 L/min). Samples were run using standard–sample bracketing (reference materials run every ∼5 unknowns). The masses measured were 206, 207, 208, 232, and 238. The external standard used was 91500 (Wiedenbeck et al., 2004) with Plesovice (Sláma et al., 2008), DD85-17 (Davis et al., 2005), and DD91-1 (Davis, 2002) as secondary reference materials (Fig. A.1, Table A.4). The measured age of the secondary reference materials are: 337.3 ± 1.9 Ma (2s; MSWD = 0.63, concordia + equivalence) for Plesovice (Expected age: 337 ± 0.37 Ma), 2999 ± 12 Ma (2s; MSWD = 2.2, concordia + equivalence) for DD85-17 (Expected age: 3000 Ma), and 2687 ± 12 Ma (2s; MSWD = 2, concordia + equivalence) for DD91-1 (Expected age: 2682.4 ± 2.0 Ma). Data reduction was done using Iolite (v.4) (Paton et al., 2011). Discordance was calculated using the concordia distance method (Vermeesch, 2021) and dates with values between -3 and 5 were considered concordant. Single-measurement concordia dates were calculated using IsoplotR (Vermeesch, 2018). Kernal density estimates of these concordia dates are used to compare and discuss the average zircon date of each sample rather than a weighted mean age as the overdispersion of dates did not permit a statistically robust single age. Results were plotted using IsoplotR. Full analytical conditions are shown in Table A.3.

### 2.4.5 Phase equilibrium modelling

Phase equilibrium modelling was done with the software Perple_X (Connolly, 2005). The thermodynamic data from Holland and Powell (2011) was used in the $Na_2O$-CaO-$K_2O$-FeO-MgO-$Al_2O_3$-$SiO_2$-$H_2O$-$TiO_2$-$Fe_2O_3$ system. Calculations were done using solution models from White et al. (2014a) for garnet, biotite, white mica, chlorite, ilmenite, and orthopyroxene, Green et al. (2016) for clinoamphibole, augite, and melt, White et al. (2002) for spinel, Holland and Powell (2003) for feldspar, Holland and Powell (1998) for olivine, and Holland and Powell (2011) for epidote. For 20SD06, 20SD17A, and 22SD55E $H_2O$ was estimated based on T-$X_{H_2O}$ diagrams at expected pressures of melting to better reproduce observed assemblages. For 21SD68, the T-X diagram used was at 4 kbar due to the lower pressure stability of olivine predicted in the model. The $H_2O$ content was chosen to just stabilize the observed assemblage at the solidus at the modelled pressure (e.g. Yakymchuk et al., 2020).

### 2.4.6 Mineral–melt Zr partition modelling

Suprasolidus concentrations of Zr in silicate melt and the abundance of zircon were calculated following the methodology of Kelsey et al. (2008) using experimentally and empirically derived mineral–melt partition coefficients (Table A.5) and zircon saturation models from (Watson and Harrison, 1983). Melt composition and modal phase abundances calculated during phase equilibrium modelling with Perple_X (Connolly, 2005) were used as parameters for the mineral–melt Zr partition models. At each modelled pressure and temperature, theoretical Zr concentration of melt was calculated using bulk partition coefficients and measured bulk rock Zr concentration. The theoretical Zr concentration was compared against the calculated concentration Zr in melt at zircon saturation and the lower of the two values was used as the concentration of Zr in melt. This Zr concentration was used with the partition coefficients of each mineral to calculate the concentration of Zr in those minerals. Finally, the modelled total Zr contained in each phase was subtracted from the total measured Zr in the system to calculate the amount of Zr that remains available, which is assumed to be contained in zircon and is used to calculate the weight fraction of zircon in the system. The code used for this modelling has been made available in the Migmatites.jl Julia package at `https://github.com/sc-dyer/Migmatites.jl`.

## 2.5 Results

### 2.5.1 Whole rock chemical compositions

Major element composition of the selected samples (Table 2.1) shows they are alkali-rich intermediate rocks which can be classified with the IUGS QAPF classification monzogranites (20SD06, 20SD17A) and quartz monzonites (21SD68, 22SD55E). All samples have remarkably low concentrations of MgO (<0.4 wt%), which contrasts with their relatively high FeO + $Fe_2O_3$ content (>5 wt%). Trace element concentrations (Table A.6) are varied, but all show elevated concentrations of Zr (>900 $\frac{\mu g}{g}$, Table 2.1).

### 2.5.2 Mineral assemblages and microstructures

#### 20SD06

This sample is composed of, in decreasing order of abundance: alkali feldspar, plagioclase, quartz, clinopyroxene, garnet, magnetite, amphibole, and ilmenite with minor amounts

of zircon, apatite, and allanite and trace calcite, chalcopyrite, and pyrite. The rock is dominated by xenoblastic alkali feldspar, plagioclase, and quartz with a grain size range of 0.1-2 mm, alkali feldspar is commonly perthitic and occasionally occurs as rounded, elongate porphyroblasts up to 6 mm across, with fine-grained recrystallized quartz and feldspar at the edges. Garnet, clinopyroxene, magnetite, ilmenite and zircon most commonly occur clustered together within discontinuous bands and lenses <1 cm thick, however all of these minerals are distributed throughout the rock. Garnet porphyroblasts are hypidioblastic to xenoblastic with a size range of 0.5–5 mm and occur more commonly in the melanocratic bands and commonly occurs as an overgrowth on magnetite and ilmenite (Fig. 2.3 B). Garnet contains inclusions of quartz, alkali feldspar, zircon, allanite, apatite, ilmenite, and magnetite (Fig. 2.3 A). Clinopyroxene typically occurs as fine-grained (50–200 µm) clusters within the Fe-rich lenses and rarely occurs as an overgrowth on magnetite. Amphibole is only present as an overgrowth on magnetite or clinopyroxene. Clinopyroxene also occurs outside these lenses as xenoblastic 0.3–0.8 mm grains throughout the matrix. Magnetite is typically xenoblastic and up to 1 cm across. Magnetite commonly occurs with exsolution lamellae of ilmenite (Fig. 2.3 C) that range in thickness from several µm to 0.2 mm. Ilmenite also occurs within magnetite as discontinuous, irregular bands. Ilmenite most commonly occurs as larger, continuous grains <0.6 mm adjacent to magnetite. Gahnite and other Al-spinels are commonly located at magnetite-ilmenite grain boundaries (Fig. 2.3 C). Rare, thin (<0.1 mm), and discontinuous overgrowths of alkali feldspar on magnetite are present.

Zircon is distributed throughout the matrix and included in garnet and magnetite as 20–600 µm grains that are typically hypidioblastic or rounded. Zircon overgrowths up to 120 µm thick are most clearly seen in CL imaging (Fig. 2.4 A, B) but are also apparent as zones with distinct birefringence and separated from the more metamict core by a microstructural discontinuity. Rare zircon overgrowths occur as irregular abutments onto adjacent ilmenite or magnetite grains (Fig. 2.3 D). There are variable inclusions in zircon including apatite, plagioclase, alkali feldspar, quartz, biotite, pyrite, ilmenite, and rare monazite.

### 20SD17A

This sample contains a mineral assemblage of alkali feldspar, plagioclase, quartz, magnetite, clinopyroxene, garnet, titanite, and ilmenite, with minor amounts of zircon, apatite, and amphibole and trace chalcopyrite and pyrite. The rock is dominated by xenoblastic alkali feldspar, plagioclase, and quartz with a grain size of 0.1–2.5 mm. Alkali feldspar is commonly perthitic. Plagioclase and quartz are rarely myrmykitic. Magnetite and ilmenite are disseminated throughout the rock with a grain size <1.5 mm and commonly occur in

elongate clusters or stringers. Ilmenite occurs both as exsolution lamellae and needles in magnetite and as separate grains adjacent to magnetite (Fig. 2.3 F). Gahnite and other Al-spinels are included in magnetite and along ilmenite-magnetite grain boundaries. Garnet forms xenoblastic porphyroblasts 0.2–1.2 mm across, and as narrow (<0.2 mm) overgrowths on magnetite and ilmenite (Fig. 2.3 D). Thin overgrowths (<0.1 mm) of plagioclase on magnetite and ilmenite are common (Fig. 2.3 G). Titanite occurs as <0.2 mm overgrowths on magnetite and ilmenite (Fig. 2.3 F). Altered xenoblastic clinopyroxene is sparsely disseminated throughout the rock with a grain size of 0.1–1.5 mm.

Zircon is disseminated throughout the rock and included in garnet and magnetite as 20–500 µm grains that are typically hypidioblastic or rounded (Fig. 2.3 E). Zircon overgrowths up to 50 µm thick are apparent in CL imaging (Fig. 2.4 C, D). There are variable inclusions in zircon including apatite, plagioclase, alkali feldspar, and quartz.

### 21SD68

This sample contains a mineral assemblage of alkali feldspar, plagioclase, quartz, clinopyroxene, fayalite, ilmenite, and amphibole with minor amounts of zircon, biotite, and apatite, and trace allanite, pyrite, and chalcopyrite. The rock is dominated by granoblastic alkali feldspar, plagioclase, and quartz with grains <0.5 mm. Alkali feldspar is commonly perthitic and occasionally occurs as round elongate porphyroclasts 2–6 mm in size. Clinopyroxene, fayalite, ilmenite, magnetite, and amphibole are disseminated throughout the rock and commonly occur together as aggregates of <1 mm xenoblastic and polygonal grains (Fig. 2.3 H). Ilmenite is more abundant than magnetite in this sample and unlike the other samples in this study, commonly occurs without any shared grain boundaries with magnetite (Fig. 2.3 I). Clinopyroxene commonly contains inclusions of ilmenite and magnetite and has rare orthopyroxene exsolution lamellae (Fig. 2.3 J). Fayalite is typically pristine, even when adjacent to quartz, with no apparent reaction rims (Fig. 2.3 H). Amphibole typically appears as overgrowths on magnetite, ilmenite, and clinopyroxene and occasionally appears to be replacing clinopyroxene. Biotite is rare and typically <0.5 mm and occurs both with vermicular quartz intergrowths and without.

Zircon is disseminated throughout the rock, it is typically hypidioblastic and has grain sizes up to 0.5 mm across (Fig. 2.3 I). Zircon overgrowths up to 40 µm thick are apparent in CL imaging (Fig. 2.4 E, F). There are variable inclusions in zircon including apatite, plagioclase, alkali feldspar, quartz, and clinopyroxene (Fig. 2.3 I).

### 22SD55E

This sample contains a mineral assemblage of alkali feldspar, plagioclase, quartz, garnet, clinopyroxene, amphibole, magnetite, ilmenite, and biotite, with minor amounts of zircon and apatite, and trace calcite, pyrite, chalcopyrite, and allanite. The rock is dominated by xenoblastic alkali feldspar, plagioclase, and quartz, with grains <1 mm in size. Alkali feldspar commonly contains blebby exsolutions of plagioclase; more rarely, alkali feldspar is perthitic. Garnet occurs as xenoblastic to idioblastic grains 0.5–2 mm. Garnet also occurs as overgrowths on magnetite <0.3 mm thick and will often appear with a vermicular intergrowth with quartz (Figs. 2.3 K, L). Quartz inclusions in garnet mimic this vermicular texture and will often occur in a spiral inclusion pattern. Thin quartz overgrowths <50 µm are present most commonly on xenoblastic grains with vermicular quartz intergrowth but also occur on idioblastic grains more rarely (Figs. 2.3 J, K). Inclusions of zircon and clinopyroxene in garnet also rarely occur. Clinopyroxene and amphibole are xenoblastic to hypidioblastic <0.5 mm grains disseminated throughout the rock. Amphibole commonly occurs as overgrowths on magnetite and ilmenite (Figs. 2.3 J, K) and occasionally clinopyroxene. Amphibole commonly contains inclusions of magnetite. Magnetite and ilmenite are typically xenoblastic and occasionally polygonal <2 mm across. Ilmenite exsolutions in magnetite are common and ilmenite typically only occurs adjacent to magnetite (Fig. 2.3 K). Biotite typically occurs as xenoblastic to hypidioblastic grains <0.1 mm and with rare vermicular intergrowths with quartz.

Zircon is disseminated throughout the matrix and included in garnet and magnetite and is typically hypidioblastic or rounded and has grain sizes up to 150 µm. Zircon overgrowths up to 40 µm thick are apparent in CL imaging (Fig. 2.4 C, D). There are variable inclusions in zircon including apatite, plagioclase, alkali feldspar, quartz, and magnetite.

### Zircon textures

Zircon morphology and internal zoning patterns are variable within individual samples. Therefore, we imaged >30 zircon of various sizes in various microstructural settings for each thin section to obtain a representative set of CL images for each sample. One caveat of this approach is that grains are randomly oriented in thin section, and we do not consider the third dimension. Nevertheless, the large number of imaged zircon from each sample provides a reasonable indicator of zircon variability in different microstructural settings. Furthermore, since the foliation is weak in each sample, variation in the third dimension is not expected.

Zircon is most commonly hypidioblastic, often exhibiting rounded (e.g. Fig. 2.4 D, G) or multi-faceted edges (e.g. Fig. 2.4 A, H). Occasionally, zircon occurs with an idioblastic shape, this is most frequently observed as a square-shaped cross-section of a zircon, and is rarely observed in elongate cross-sections where at least one crystal terminus can be seen.

In the CL images of zircon (Fig. 2.4), distinct cores and rims are ubiquitous in every zircon. Cores typically exhibit oscillatory zoning, but patchy zones in cores are also common. Metamict cores have a speckled appearance in CL or appear almost entirely homogenous with little or no CL response. Zircon core shapes vary from very irregular (most common; e.g. Fig. 2.4 A, B, D, F, G, H) to nearly euhedral (rare; e.g. Fig. 2.4 C). Irregular core edges commonly truncate oscillatory zones (e.g. Fig. 2.4 A, B, D), whereas straight core edges are commonly parallel to oscillatory zones (e.g. Fig. 2.4 C).

Zircon rims vary in thickness across a thin-section and within individual zircons. Thicknesses range from 1 to 120 µm but average 10–20 µm. Cores are commonly completely surrounded by these rims; exposed cores are rare but do occur (e.g. Fig. 2.4 B, F, H). The CL response of zircon rims show 2–5 alternating dark and light bands. These bands do not have a uniform distribution or thickness around the zircon. They are typically sub-parallel (e.g. Fig. 2.4 A) but commonly exhibit complex patterns, particularly around more resorbed cores (e.g. Fig. 2.4 B, D). The first band typically occurs around the more irregular edges of the core zircon to create a hypidioblastic internal shape. Towards the edge of most zircons, outer bands partially or completely surround the inner bands and core.

The shape and size of zircon rims do not correlate with proximity to different minerals, except that when zircon is adjacent to magnetite or ilmenite, the rims are typically thickest adjacent to the oxide mineral (e.g. Figs. 2.4 B, C, F, G, H) and very rarely show distinct magnetite or ilmenite overgrowth (Fig. 2.3 D).

### Evidence of melting

The primary evidence that melting occurred in these rocks are the appearance of leucosome (Fig. 2.2). Leucosome typically has diffuse edges with rare melanosome present only in the outcrop of 20SD17A, suggesting this represents *in situ* melting rather than melt injection (Sawyer, 2008). In addition, possible melt films in the form of feldspar overgrowths are present around magnetite and ilmenite in 20SD06 and 20SD17A (Fig. 2.3 G).

### 2.5.3 Major mineral compositions

Average compositions of major minerals in each sample are shown in Table A.7. The following is a summary of that data for all samples, ranges indicate variation between samples as mineral compositions do not vary much within individual samples and show little evidence of compositional zoning. Garnet, clinopyroxene, and fayalite are all rich in Fe and very low in Mg. Garnet has relatively high Mn ranging from 4-11 wt% MnO across samples. Fayalite in 21SD68 has an average 0.90 wt% MgO but also contains relatively high Mn with an average ∼3.4 wt% MnO. Alkali feldspar is always K-rich (Ab/[Ab + Or]= 7–14) and plagioclase is always albite rich (An/[An + Ab]= 7–22). Magnetite has low concentrations of Ti, typically <1 wt% $TiO_2$, and never more than 2 wt% $TiO_2$. Ilmenite is close to stoichiometric ilmenite with more molar Ti than Fe and up to 3 wt% MnO.

### 2.5.4 Concentration of Zr in major and accessory minerals

Zirconium concentrations are relatively consistent in the major minerals across the four samples (Fig. 2.5). The exception is titanite in 20SD17A with an average concentration of 760 $\frac{\mu g}{g}$, all major minerals have low concentrations of Zr. Clinopyroxene and amphibole consistently contain the highest average Zr concentration ranges of 25–53 $\frac{\mu g}{g}$ and 30–35 $\frac{\mu g}{g}$ respectively. Allanite in 20SD06 has the next highest average Zr concentration at ∼6 $\frac{\mu g}{g}$. The rest of the major and accessory minerals have Zr concentrations <4 $\frac{\mu g}{g}$. Alkali feldspar in all samples except 20SD17A had too few measurements above the detection limit (<1 $\frac{\mu g}{g}$) to be included, as did plagioclase in all samples.

### 2.5.5 U-Pb zircon geochronology

Concordia plots of zircon U-Pb ages reveal a complex mix of dates from both cores and rims (Fig. 2.4). Several dates were excluded due to high degree of discordance, including reverse discordance (Fig. 2.4 grey ellipses). Wetherill plots and concordia kernel density estimates (Fig. 2.6) indicate a clear division in dates between cores and rims in all samples except 21SD68 which shows a less distinct date separation between cores and rims. In every sample, zircon core dates spread from ca. 1500 and ca. 1200 Ma (Single zircon ages; Fig. 2.6), and rim dates show a general spread between ca. 1150 and ca. 1000 Ma (Single zircon ages; Fig. 2.6). Sample 20SD06 has two distinct concordia peaks at ca. 1350 Ma, and 1070 Ma. Sample 20SD17A has two distinct peaks at ca. 1380 Ma and 1100 Ma. Sample 22SD55E has two distinct peaks at ca. 1310 Ma and 1080 Ma. Kernel density estimates for

sample 21SD68 show only one distinct peak at ca. 1180 Ma likely due to a large proportion of relatively young (ca. 1200 Ma) core dates. On the Wetherill diagram of sample 21SD68, ca. 1180 Ma separates zircon core dates and zircon rim dates. Single zircon concordia dates show the same distinct age differences observed in aggregate in all samples (Fig. 2.4).

### 2.5.6 Equilibrium phase relations

Pseudosections are remarkably consistent across these four samples (Fig. 2.7). They all predict the garnet-in reaction line with a positive slope, with garnet stable on the high pressure side of the reaction with no garnet present at high temperatures and lower pressures. The modelled solidus occurs between 650–750 °C depending on pressure. The models predict an increase in volumetric proportion of spinel and with higher Ti concentrations at higher temperatures, along with lower volumetric proportions of ilmenite (Fig. 2.8). The unique assemblage of quartz + fayalite present in sample 21SD68 appears in the pseudosection which shows olivine stable with quartz below 6 kbar. In 20SD17A, the only sample with titanite present in the thin section, the pseudosection shows titanite is stable below 650 °C and ∼5 kbar. Alkali feldspar and plagioclase are present at all modelled temperatures and pressures except above 850 °C and 12 kbar in 20SD06 and 21SD68. The interpreted peak phase assemblages including melt are stable at >700–750 °C and <7 kbar in 20SD06, >750 °C and 6–10 kbar in 20SD17A, >700–750 °C and <6 kbar in 21SD68, and >750 °C and <8 kbar in 22SD55E.

### 2.5.7 Zr reservoirs during melting

All four samples show similar trends in the mineral–melt Zr partitioning models (Fig. 2.9). The high concentration of Zr and limited amount of melt predicted in each system means that even at 950 °C, zircon contains >80% of the Zr by weight. Zircon excluded, melt, ilmenite, and magnetite are the dominant Zr reservoirs when garnet is not present. The proportion of Zr in each of these phases is dominantly temperature dependent, increasing at higher T with higher Zr concentration in melt due to higher zircon saturation. At <850 °C, melt, magnetite, and ilmenite contain similar proportions of Zr in the system of 0.25–1% of Zr by weight.

## 2.6 Discussion

### 2.6.1 Model limitations

The following discussion depends on the interpretation of the phase equilibrium models and mineral–melt partition models(Figs 2.7, 2.8, 2.9), so it is important to discuss their limitations. There are inherent uncertainties in all phase equilibrium modelling due to uncertainty in solution models (Powell and Holland, 2008) and in the effective bulk rock composition of a modelled equilibration volume (Palin et al., 2016). The latter is particularly relevant in this paper as we are focusing the discussion on retrograde metamorphism where kinetics is often slower than prograde metamorphism and equilibration volumes may be smaller than the sample analyzed for bulk rock composition or even smaller than a thin section (Palin et al., 2016; Lanari and Engi, 2017). In addition to these generalized limitations, the chemical system that we used does not contain MnO as it is excluded from the solution models described by Green et al. (2016). Mn is known to significantly modify garnet stability (e.g. White et al., 2014b) and considering that average garnet composition ranges from 4 to 11 wt% MnO, it is likely that the garnet stability fields shown in Fig. 2.7 are at artificially higher pressures than in natural systems. Stability fields of olivine are also likely to be modified by the presence of Mn. This could raise the maximum pressure of olivine stability; for example, 21SD68 has an average 3.4 wt% MnO in fayalite that could increase its stability. Beyond the Mn issue, Green et al. (2016) solution models are optimized for metabasites that are basaltic to andesitic in composition, and the samples we analyze in this paper are monzonites and quartz monzonites. These are nevertheless the most appropriate solution models to use as the White et al. (2014b) solution models do not include clinopyroxene, amphibole, or olivine, three phases seen in our samples. There are also clear limitations on the spinel model in its ability to fully predict the occurrence of titanomagnetite, particularly in sample 20SD17A, which does not have high amounts of Ti predicted in spinel in the modelled P–T range (Fig. 2.8 B), which disagrees with the occurrence of ilmenite lamallae in magnetite observed throughout that sample. Based on the occurrence of exsolution of Al-spinel minerals such as Gahnite (Zn-spinel) in magnetite, it is likely there are additional end-members in the spinel solution that are not accounted for in the available solution models that influence the amount of Ti that can be incorporated into spinel. Despite these limitations, the pseudosections generated (Fig. 2.7) still produce phase stability fields that align with the observed mineral assemblages. Therefore, we consider the model results fit for purpose to evaluate the general prograde and retrograde mineral assemblages in these rocks.

In addition to the limitations on the phase equilibrium models, the mineral–melt Zr

partition models have further limitations. The partition coefficients used were taken from experimental and empirical measurements on samples that do not have identical mineral and bulk rock composition as those in these samples and are likely different from the true partition coefficients of the minerals present in these systems. This is particularly relevant in magnetite as Zr partition coefficients have been shown to be strongly dependent on Ti content of magnetite (Nielsen and Beard, 2000). Furthermore, these models do not account for the impact of the breakdown of minerals that contained high amounts of Zr prior to melting (e.g. garnet or ilmenite) that might result in zircon growth during heating (e.g. Yakymchuk, 2023). Finally, there is an assumption of melt connectivity throughout each sample to allow efficient mixing and equilibrium between melt and the other phases present in the rock. These simplified models are still a useful indicator of relative Zr content in different phases present and provide a baseline for understanding the primary Zr reservoirs during melting.

### 2.6.2 Metamorphic zircon

The distinct textural characteristics of the oscillatory zoned zircon cores and the patchy and banded zoning of the zircon rims suggests at least two stages of zircon growth. Oscillatory zoning in zircon cores is common during growth from silicate melt (Corfu, 2003) and interpreted to record crystallization of the igneous protolith. The generally hypidioblastic and rounded shape of zircon and the patchy and banded zoning pattern of their rims suggest that the later stage of zircon growth occurred during metamorphism (Corfu, 2003; Rubatto, 2017). This is further supported by distinct age differences between the rims and the cores (Fig. 2.6). These generally align with previously measured dates of igneous protolith crystallization and metamorphism in the Allochthonous Belt of the Grenville Province (1470–1340 Ma Ketchum and Davidson, 2000). Furthermore, the general age gap (∼200 Myr) between rims and cores would be difficult to explain because of resorption and late regrowth of zircon during original melt crystallization. Concordia dates of rims are generally between 1100 and 1000 Ma, which coincides with the Ottawan phase of the Grenville orogeny (Rivers, 2008). Since these metamorphic rims are typically large (>10 µm) and zircon is so abundant, the Zr required for metamorphic zircon growth must be coming from a large reservoir in the rock.

Phases that are frequently proposed as Zr sources that are or have been present in these rocks are garnet (Fraser et al., 1997; Degeling et al., 2001; Tomkins et al., 2005), amphibole (Fraser et al., 1997; Kohn et al., 2015), ilmenite (Bingen, 2001; Morisset and Scoates, 2008; Beckman et al., 2017), and anatectic melt (Kohn et al., 2015; Yakymchuk, 2023).

Our models indicate that garnet is not stable in any samples at higher temperatures and lower pressures where melting occurs (Fig. 2.7) so the occurrence of garnet in these samples is more likely a result of retrograde metamorphism. Furthermore, the occurrence of zircon inclusions with metamorphic rims within garnet (Fig. 2.3 A, E, 2.4 B) and the very low concentrations of Zr in garnet (1–2 $\frac{\mu g}{g}$; Fig. 2.5) suggests garnet grew in an environment with very little available Zr, either after or during zircon growth. The low measured concentrations of Zr in garnet are also consistent with low-temperature garnet growth of ∼1–4 $\frac{\mu g}{g}$ for garnet in rocks that record peak temperatures of 400–700 °C (Kohn et al., 2015). For these reasons, we can exclude garnet as a potential source of Zr.

Amphibole has higher Zr concentrations than garnet, but they are still relatively low (30–35 $\frac{\mu g}{g}$; Fig. 2.5). In addition, amphibole occurs as overgrowths on clinopyroxene, fayalite (Fig. 2.3 H), garnet (Fig, 2.3 K), magnetite, and ilmenite, indicating that it is also a product of retrograde metamorphism. We therefore also exclude amphibole as a potential source of Zr.

The common occurrence of zircon rims that abut against magnetite and ilmenite (e.g. Figs. 2.3 D, G, 2.4 B, C, D, F, G) is the strongest petrographic evidence indicating a potential source of Zr for zircon growth. The extremely low concentration of Zr (<4 $\frac{\mu g}{g}$; Fig. 2.5) in ilmenite and magnetite implies that they were not sources of Zr. However, in contradiction of this, in 20SD17A titanite rims on ilmenite and magnetite (Fig. 2.3 F) have the highest measured Zr concentration of any mineral besides zircon(∼760 $\frac{\mu g}{g}$; Fig. 2.5). The pseudosection for this sample (Fig. 2.7 B) shows titanite is stable at lower temperatures and pressures, indicating that it likely formed during retrogression. This suggests that ilmenite and magnetite once had elevated concentrations of Zr but that it was lost after or during the formation of titanite and prior to the growth of garnet at lower temperatures, resulting in low Zr concentration in garnet. The frequent co-occurrence of ilmenite and magnetite and appearance of ilmenite lamellae in magnetite (Figs. 2.3 C, F, I, L) indicates that they are byproducts of the breakdown of another phase, likely a titanomagnetite (Buddington and Lindsley, 1964; Sauerzapf et al., 2008; Tan et al., 2016). This is supported by our models (Fig. 2.8), which show an increasing abundance of spinel (magnetite), a decreasing abundance of ilmenite, and a greater Ti content in spinel at higher temperatures and lower pressures. Sample 20SD17A is an exception where our models do not show high Ti in magnetite over the modelled P–T range (Fig. 2.8B), but the occurrence of ilmenite exsolution in magnetite and Zr-rich titanite rims around magnetite suggest that titanomagnetite did occur in this sample and the available solution models for spinel do not adequately describe this sample. While there have been no studies that indicate that titanomagnetite could contain high concentrations of Zr, Ti-rich minerals like rutile, ilmenite, and titanite are commonly reported to have high Zr concentrations (e.g. Bea et al.,

2006) as the 4+ charge and ionic radius of Ti allows Zr to substitute for Ti very effectively. Furthermore, experimental studies of magnetite–melt partition coefficients show that the partition coefficient of Zr in magnetite increases with higher Ti content (Nielsen and Beard, 2000). These observations are further supported by our mineral–melt Zr partition models (Fig. 2.9), which indicate that at the expected peak temperature of 750–850 °C, magnetite, ilmenite, and melt all contain similar proportions of the Zr in the system (0.25–0.75% by weight). We therefore consider titanomagnetite as one significant source of Zr for zircon growth in these samples.

The high abundance of zircon in these samples (∼0.2 vol. %), which all have resorbed oscillatory-zoned (i.e. igneous) cores (Fig. 2.4) suggests that prior to metamorphism, zircon was the primary Zr reservoir in these rocks (Fig. 2.10 - Stage 1). The break-down of zircon would have made Zr available to other phases such as titanomagnetite that would be able to contribute to zircon growth later in the P–T history. Considering that the rocks underwent high-temperature metamorphism and potentially partial melting as evidenced by the presence of leucosomes (Fig. 2.2), feldspar films around other minerals (Fig. 2.3 G), and evidence of extensive melting in the local area (Timmerman et al., 2002; Slagstad et al., 2005), the simplest explanation for the breakdown of zircon is melting during prograde metamorphism (Fig. 2.10 - Stage 2). Zircon is expected to dissolve when its host silicate melt is undersaturated in Zr (with respect to zircon) and this is a function of melt composition and temperature (Watson and Harrison, 1983). Thermodynamic phase equilibrium models that incorporate Zr end-members show that as temperature increases above the solidus, zircon is expected to dissolve into the melt when the melt is undersaturated in Zr (e.g. Kelsey and Powell, 2011; Kohn et al., 2015). However, if a Zr-rich source (other than zircon) breaks down during heating and melting, this can lead to oversaturation of the melt and zircon growth during suprasolidus prograde metamorphism (e.g. Yakymchuk, 2023). Ilmenite is one potentially Zr-rich phase (e.g. Bingen, 2001; Morisset and Scoates, 2008; Beckman et al., 2017) that our models predict to breakdown during heating at temperatures where melting is expected to occur (Figs. 2.7, 2.8), but ilmenite breakdown is counterbalanced by the growth of more spinel (magnetite) and an increase in its Ti-content (Fig. 2.8), making it titanomagnetite. This increase in titanomagnetite volume is associated with an increase in the total Zr contained within the spinel phase at the same time that total Zr in ilmenite is reduced (Fig. 2.9). This enrichment of Zr in titanomagnetite would have prevented Zr over-saturation in melt and therefore suppressed prograde zircon growth (Fig. 2.10 - Stage 2).

During cooling, anatectic melt will crystallize Zr-poor cotectic minerals (e.g. quartz, feldspar) until the melt becomes supersaturated in Zr and allows zircon growth. The presence of clinopyroxene and amphibole in some leucosomes in our samples (Fig. 2.2)

suggests these were either peritectic or cotectic minerals. These contain up to 53 $\frac{\mu g}{g}$ Zr (Fig. 2.5), which is higher than most other minerals present in the rock, but with a modal abundance <5 vol%, it is not high enough to be a possible Zr sink during melt crystallization and therefore unlikely to suppress zircon growth. Zircon rims are therefore a likely by-product of melt crystallization during cooling (Fig. 2.10 - Stage 3).

Zircon grains with rounded or irregular overgrowths (e.g. Figs. 2.3 D, 2.4 D, E, F) and frequently observed CL pattern of a dark inner band followed by bright outer bands (Fig. 2.4 B, D, E, H) are more consistent with sub-solidus zircon growth than melt-present zircon growth, which is more consistent with weak oscillatory zoning (Fig. 2.4 A) (Corfu, 2003; Hoskin and Schaltegger, 2003; Rubatto, 2017). This suggests that zircon growth from melt alone is unlikely. Furthermore, magnetite and ilmenite are predicted to contain similar proportions of Zr as melt at the expected peak temperature of 750–850 °C (Fig. 2.9). While it is likely that titanomagnetite lost some Zr during suprasolidus cooling, diffusion of Zr in these phases is slow (Sievwright et al., 2020), and it is therefore unlikely that complete loss of Zr occurred prior to melt crystallization. Furthermore, metamorphic zircon growth during protracted cooling is consistent with the spread in zircon rim ages of up to 100 Myr in each sample (Fig. 2.6).

In samples 20SD06, 20SD17A, and 22SD55E, garnet coronae around ilmenite and magnetite (Fig. 2.3 B, E, K, L) are likely a product of titanomagnetite breakdown (Fig. 2.10 - Stage 4). The proposed simplified reaction for garnet growth during titanomagnetite breakdown is:

$$\overbrace{(\underset{Magnetite}{Fe_3O_4} + \underset{Ulvospinel}{Fe_2TiO_4})}^{Titanomagnetite} + \underset{Anorthite}{CaAl_2Si_2O_8} + \underset{Quartz}{SiO_2} = \overbrace{(\underset{Ilmenite}{FeTiO_3} + \underset{Hematite}{Fe_2O_3})}^{Ilmenite} + \underset{Garnet}{Fe_2CaAl_2Si_3O_{12}} \quad (2.1)$$

The low Zr concentrations in garnet suggest that this reaction occurred either after titanomagnetite already lost its Zr (i.e. zircon already formed) or that zircon was a byproduct of this reaction. Either scenario is supported by the presence of zircon with metamorphic rims fully or partially included in garnet (Fig. 2.3 A, B, C, E, L, 2.4 B).

In brief, the most reasonable sequence of events of zircon formation is: (1) Formation of the protolith (Fig. 2.10 - Stage 1); (2) Breakdown of zircon and other Zr-bearing minerals during prograde metamorphism and melting, Zr is primarily hosted in melt and titanomagnetite (Fig. 2.10 - Stage 2); (3) Growth of zircon during cooling and melt crystallization, Zr moves from melt and titanomagnetite into zircon (Fig. 2.10 - Stage 3); (4) Cooling continues, titanomagnetite continues to breakdown with titanite (in 20SD17A) as the first reactant followed by garnet (in 20SD06, 20SD17A, and 22SD55E) as a later reactant, any Zr that was present in titanomagnetite after melt crystallization enters titanite

and contributes to further zircon growth (Fig. 2.10 - Stage 4). This mineral growth sequence informs our interpretation of the P–T–t history of these rocks.

### 2.6.3 P–T–t constraints on Grenvillian metamorphism

Zircon rims grew during cooling that accompanied melt crystallization and titanomagnetite breakdown, which indicates that the dates retrieved from the rims record the post-peak metamorphic history. This is in contrast with how a majority of metamorphic dates are interpreted in the Central Gneiss Belt, which are often assumed to be prograde or "peak" ages without clear evidence or because they are dates from zircons sourced from leucosome (see Rivers (2008) for summary). While predicted stability fields for P–T sensitive minerals are large (e.g. garnet, clinopyroxene, titanite) in the pseudosections (Fig. 2.7), there are several key reactions that can be used to provide general constraints on the P–T path of retrograde metamorphism. The minimum peak temperature can be determined using the solidus, which constrains each sample to >650 °C (Fig. 2.11). This is also the minimum temperature of suprasolidus zircon growth for these samples.

Linking metamorphic reactions that produce zircon with the P–T evolution of these rocks requires an assessment of the temperatures (and pressures) of titanomagnetite breakdown. Based on volume and Ti models, this process occurs continuously as temperatures decrease (Fig. 2.8). The modelled Ti content and volume of spinel (magnetite) is highest in all samples at suprasolidus temperatures and lower pressures (Fig. 2.8). Considering regional constraints on peak P and T estimates of 9–12 kbar (Anovitz and Essene, 1990; Timmerman et al., 2002) and 750–850 °C (Timmerman et al., 2002) (Fig. 2.11), the presence of titanomagnetite implies that melting started at or near peak pressure and continued during decompression towards the P–T conditions with the highest Ti content in spinel. Such a decompression path is further supported by the occurrence of olivine in 21SD68 (Fig. 2.3 H) and titanite in 20SD17A (Fig. 2.3 F) which are not predicted to be stable above 6 kbar (Fig. 2.7 B, C). Furthermore, due to its high Zr content, titanite likely grew close to the solidus at lower pressures (<5 kbar, Fig. 2.11). Isothermal decompression at higher temperatures means that cooling occurred at lower pressures. In samples with garnet present (20SD06, 20SD17A, and 22SD55E), the garnet stability field (Fig. 2.7 A, B, and C) further supports zircon growth during cooling based on reaction 2.1 and inclusions of zircon in garnet (Fig. 2.3 A, E). Zircon rim dates are interpreted to record this cooling.

Zircon rim dates vary (Fig. 2.4), and are spread out from ca. 1150 Ma to ca. 1000 Ma (Fig. 2.6). The spread in dates may be a result of partial resetting during the Rigolet phase of the Grenville orogeny (1005–980 Ma), or it may be a result of continuous zircon

growth during protracted cooling resulting in overdispersion of ages (e.g. Klein and Eddy, 2023). Differentiating the cause of the 100–150 Myr spread in metamorphic zircon dates is challenging due to the long-duration of Grenvillian metamorphism that could lead to protracted crystallization, or protracted Pb loss during residence at high temperature after zircon crystallization (e.g. Kirkland et al., 2020). The KDE plots (Fig. 2.6) show where zircon dates cluster and provide a generalized date to compare samples with each other and ages from other works. The concordia dates cluster at ca. 1070 Ma in 20SD06, ca. 1100 Ma in 20SD17A, and ca. 1080 Ma in 22SD55E. The 1170 Ma date in 21SD68 is unclear and may be a result of mixed signal, or more extensive partial resetting of core dates. The other dates align with previously measured dates for metamorphism in the Muskoka domain (Fig. 2.1 B) from analysis of zircon separates (Timmermann et al., 1997; Slagstad et al., 2005; Marsh and Culshaw, 2014). These previous dates provide reasonable constraints to metamorphism, and have been linked to prograde metamorphism (Marsh and Culshaw, 2014) or are sourced from leucosome and broadly tied to partial melting (Timmermann et al., 1997; Slagstad et al., 2005). In contrast, our work ties these zircon dates to retrograde metamorphic reactions. While these samples are located relatively far apart from each other (Fig. 2.1 B), general similarities in phase topology, mineral assemblage, field relations, and apparent reactions suggest that these rocks have similar P–T histories (Fig. 2.11).

Numerical modelling of zircon in high-temperature metamorphic rocks predicts that zircon should only grow during retrograde metamorphism (Kelsey et al., 2008; Kelsey and Powell, 2011; Kohn et al., 2015) except perhaps a very minor amount of prograde zircon at temperatures just above the solidus (Yakymchuk, 2023). Considering these new dates of 1100 Ma, 1080 Ma, and 1070 Ma are tied directly to retrograde reactions, we interpret them to represent cooling after the metamorphic peak in the Muskoka domain. This has important tectonic implications for understanding the tectonothermal history of the Grenville orogen.

In our current understanding of the Grenville orogeny the Ottawan phase began ca. 1090 Ma (Rivers, 2008). The dominant opinion is that this period represents the onset of continent-continent collision between Laurentia and another continent, possibly Amazonia (Carr et al., 2000; Rivers, 2008; Rivers et al., 2012). This paradigm has been recently challenged by Gervais et al. (2023), who use tectonic, geochemical, and igneous and detrital geochronological data as evidence that the Ottawan was not the primary orogenic phase. They propose instead that a distinct continent called Shawanaga was formed earlier (ca. 1200–1150 Ma) and was built up further in the Ottawan phase via a rapid subduction of Oceanic crust that brought it towards Laurentia before colliding with it during the Rigolet at ca. 1030 Ma. If the Ottawan phase began ca. 1090 Ma, crustal thickening and heating should follow the onset of orogenesis by at least 20 Myr (Jamieson and Beaumont, 2013).

However, our zircon dates are as old as ca. 1100 Ma (Fig. 2.6); these are from zircon rims that record growth from melt crystallization and/or titanomagnetite breakdown; both require cooling from the metamorphic peak. This would require thickening and heating prior to the formation of these metamorphic zircons and therefore orogeny would have to occur earlier than ca. 1100 Ma. It may be that the onset of the Ottawan phase of orogeny was earlier than previously thought at ca. 1120 Ma, but an alternate model is that there was a seperate, earlier orogeny resulting in the formation of Shawiniga, a continent proposed by Gervais et al. (2023) to have been formed at 1.2–1.15 Ga prior to collision with Laurentia, which they suggest occurred at 1.03–0.96 Ga.

Dates of metamorphic zircon in this study match up well with other measured zircon ages in the region (Fig. 2.1 B). Zircons in migmatites have ages of $1064 \pm 18$ Ma (Thermal ionization mass spectrometry Timmermann et al., 1997) and $1067 \pm 9$ Ma (Secondary ion mass spectrometry Slagstad et al., 2004). These dates, both interpreted as near-peak temperature ages and representing timing close to peak pressures can be reinterpreted as melt crystallization ages at lower pressures as indicated by our models (Fig. 2.11).

Tectonically, this suggests a very early burial of the Muskoka domain, likely earlier than 1100 Ma. It is difficult to constrain how much time passed between burial and cooling, as these rocks could have potentially been sitting in the high-temperature lower crust for an extended time period prior to decompression and cooling as is seen in other orogenies such as the Himalayas (>20 Myr Singh, 2019) and the Napier complex (>100 Myr Clark et al., 2018). Earlier onset of orogenesis is supported by evidence in related domains. The Shawanaga domain is genetically related to the Muskoka domain with protolith ages of 1470–1340 Ma and a similar metamorphic history (Fig. 2.1; Ketchum and Davidson, 2000; Wodicka et al., 2000; Slagstad et al., 2004). In the Shawanaga domain, the crystallization age of a post-deformational granite-pegmatite suggest deformation and metamorphism in this domain began prior to ca. 1089 Ma (Fig. 2.1 B; Slagstad et al., 2004). In addition, cryptic metamorphic dates of ca. 1120 Ma in the Shawanaga domain are interpreted to represent early thrusting of the Parry Sound domain on top of the Shawanaga domain (Wodicka, 1994; Wodicka et al., 2000). The Parry Sound domain is a klippe of the Composite Arc Belt that is structurally below the Muskoka Domain (Culshaw et al., 1997; White et al., 2000) with metamorphic signals at ca. 1160 Ma and 1080 Ma and depositional ages in some units as young as 1140–1120 Ma (Wodicka et al., 1996). The ca. 1100 Ma zircon dates in 20SD17A could be a result of cooling and exhumation after a ca. 1120 Ma collision with the Composite Arc Belt. Cooling ages of ca. 1100–1070 Ma align with proposed timing of thrusting of the Muskoka domain on top of the Parry Sound domain (ca. 1090–1050 Ma Wodicka et al., 2000).

There are also early to pre-Ottawan U–Pb zircon ages of 1097–1085 Ma from eclogite

pods in domains that immediately underlie the Muskoka and Shawanaga domains (Fig. 2.1 B) and are interpreted to represent prograde metamorphism, possibly up to peak pressure (Marsh and Culshaw, 2014). The timing of burial lines up with our earliest cooling ages in the Muskoka domain of ca. 1100 Ma, which likely occurred during or after some exhumation to higher levels of the crust. This suggests that structurally lower units experienced burial at around the same time that the Muskoka domain was being exhumed and cooled. This could be explained if the Muskoka and Shawanaga domains were being thrusted on top of these lower units concomitantly with erosion of overlying units.

Previous metamorphic zircon dates in the Muskoka domain were considered to represent the peak of the Ottawan phase (1090–1020 Ma) of the Grenville orogeny (Carr et al., 2000; Rivers, 2008; Rivers et al., 2012), our new data suggests an earlier orogeny, with cooling dates as early as ca. 1100 Ma. This would suggest that the metamorphism recorded in the Muskoka domain might not be a record of "Ottawan" metamorphism at all but the protracted cooling of an earlier orogenic phase, possibly during collision between the Allochthonous Belt and the Composite Arc Belt at ca. 1120 Ma. Alternatively, it is possible that the Muskoka domain and its equivalents experienced two separate orogenic phases at ca. 1120 Ma and <1100 Ma. The first phase would be the accretion of the Composite Arc Belt onto the Muskoka and Shawanaga domain. The second phase would be the assembly of the Allochthonous belt with the Parautochthonous belt during which the Muskoka domain was exhumed and cooled. An earlier orogeny with protracted cooling does fit with the tectonic model proposed by Gervais et al. (2023), although final assembly of the proposed off-board continent would be at ca. 1120 Ma rather than ca. 1150 Ma. Conversely, the two phase model better explains the occurrence of Ottawan-aged metamorphism in the underlying Parautochthonous Belt.

The results of this study potentially call into question previous interpretations of Ottawan dates in this part of the Grenville Province, as ages that may have once been considered "peak" metamorphic ages of zircon outside their textural context may record cooling. In future developments of tectonic models of the Grenville and other orogenies, interpretations of metamorphic zircon dates should be treated with caution because many are missing microstructural context related to metamorphic reactions.

Understanding the zircon-forming reaction is critical to placing it in the P–T history of a rock to construct P–T–t paths. As every rock has different conditions of formation, we do not provide a geochemical or morphological indicator to help determine the zircon-forming reaction that has occurred in any individual rock. Rather, we suggest that careful petrographic analysis in the context of the regional geology and the specific sample under consideration—as we have done here—is required to adequately understand what a metamorphic zircon date means. This applies whether the zircon is being analyzed *in*

*situ* or in separates, as the textural context of the zircon will influence the interpretation of measured dates. Future analytical developments such as U-Pb isotope mapping of zircons (e.g. Cottle and Stearns, 2018) should allow more zircon geochronology to be conducted *in situ*—such as in this study—and allow for a more robust link between zircon dates, the processes that grow zircon in metamorphic systems, and the resultant tectonic interpretations.

## 2.7 Conclusions

Metamorphic zircon may grow during prograde, peak, or retrograde portions of a P–T evolution. Here we conduct *in situ* zircon geochronology and careful analysis of petrographic relationships to demonstrate that zircon can grow during retrograde metamorphism as a result of titanomagnetite breakdown and/or melt crystallization. Our results indicate that the Muskoka domain in the Grenville Province experienced retrograde metamorphism and cooling in a time period that has previously been considered the onset of the largest tectonic phase of the Grenville orogeny. This has significant implications to our understanding of the tectonics of the region, and can only be explained by an additional earlier orogenic phase at ca. 1120 Ma, or by shifting the onset of the Ottawan orogeny up to 30 Myr earlier. These results also raise an important question as to the validity of the interpretation of metamorphic zircon ages collected without any textural context. Are these ages truly representative of prograde or peak metamorphism? Or has there been a systematic mischaracterization of retrograde metamorphic ages? Reinterpretation of previous data and new *in situ* techniques may provide answers to these questions that are crucial for unravelling the nature and timing of orogenic events throughout Earth's history.

# References


Anovitz, L. M. and Essene, E. J. (1990). Thermobarometry and Pressure-Temperature Paths in the Grenville Province of Ontario. *Journal of Petrology*, 31(1):197–241.

Bea, F., Montero, P., and Ortega, M. (2006). A LA-ICP-MS evaluation of zr reservoirs in common crustal rocks: Implications for Zr and Hf geochemistry, and zircon-forming processes. *The Canadian Mineralogist*, 44(3):693–714.

Beckman, V., Möller, C., Söderlund, U., and Andersson, J. (2017). Zircon Growth during Progressive Recrystallization of Gabbro to Garnet Amphibolite, Eastern Segment, Sveconorwegian Orogen. *Journal of Petrology*, 58(1):167–187.

Bingen, B. (2001). Ilmenite as a Source for Zirconium during High-grade Metamorphism? Textural Evidence from the Caledonides of Western Norway and Implications for Zircon Geochronology. *Journal of Petrology*, 42(2):355–375.

Buddington, A. F. and Lindsley, D. H. (1964). Iron-Titanium Oxide Minerals and Synthetic Equivalents. *Journal of Petrology*, 5(2):310–357.

Carr, S. D., Easton, R. M., Jamieson, R. A., and Culshaw, N. G. (2000). Geologic transect across the Grenville orogen of Ontario and New York. *Canadian Journal of Earth Sciences*, 37:27.

Cesare, B., Rubatto, D., and Gómez-Pugnaire, M. T. (2009). Do extrusion ages reflect magma generation processes at depth? An example from the Neogene Volcanic Province of SE Spain. *Contributions to Mineralogy and Petrology*, 157(2):267–279.

Chew, D. M., Babechuk, M. G., Cogné, N., Mark, C., O'Sullivan, G. J., Henrichs, I. A., Doepke, D., and McKenna, C. A. (2016). (LA,Q)-ICPMS trace-element analyses of Durango and McClure Mountain apatite and implications for making natural LA-ICPMS mineral standards. *Chemical Geology*, 435:35–48.

Cisneros de León, A., Schmitt, A. K., and Weber, B. (2022). Multi-episodic formation of baddeleyite and zircon in polymetamorphic anorthosite and rutile-bearing ilmenitite from the Chiapas Massif Complex, Mexico. *Journal of Metamorphic Geology*, page jmg.12683.

Clark, C., Taylor, R. J. M., Kylander-Clark, A. R. C., and Hacker, B. R. (2018). Prolonged (>100 Ma) ultrahigh temperature metamorphism in the Napier Complex, East Antarctica: A petrochronological investigation of Earth's hottest crust. *Journal of Metamorphic Geology*, 36(9):1117–1139.

Connolly, J. (2005). Computation of phase equilibria by linear programming: A tool for geodynamic modeling and its application to subduction zone decarbonation. *Earth and Planetary Science Letters*, 236(1-2):524–541.

Corfu, F. (2003). Atlas of Zircon Textures. *Reviews in Mineralogy and Geochemistry*, 53(1):469–500.

Cottle, J. M. and Stearns, M. A. (2018). Application of Single-Shot Laser Ablation Split-Stream Inductively Coupled Plasma Mass Spectrometry to Accessory Phase Petrochronology. In Moser, D. E., Corfu, F., Darling, J. R., Reddy, S. M., and Tait, K., editors, *Geophysical Monograph Series*, pages 91–111. Wiley, 1 edition.

Culshaw, N., Foster, J., Marsh, J., Slagstad, T., and Gerbi, C. (2016). Kiosk domain, Central Gneiss Belt, Grenville Province, Ontario: A Labradorian palimpsest preserved in the ductile deep crust. *Precambrian Research*, 280:249–278.

Culshaw, N., Van De Kerckhove, S., Slagstad, T., Marsh, J., and Easton, R. M. (2023). Crustal evolution of the Laurentian continental margin from the Paleo- through Mesoproterozic: A zircon U–Pb and Hf transect through the western Grenville Province, Ontario, Canada. *Precambrian Research*, 386:106963.

Culshaw, N. G., Jamieson, R. A., Ketchum, J. W. F., Wodicka, N., Corrigan, D., and Reynolds, P. H. (1997). Transect across the northwestern Grenville orogen, Georgian Bay, Ontario: Polystage convergence and extension in the lower orogenic crust. *Tectonics*, 16(6):966–982.

Dare, S. A. S., Barnes, S.-J., Beaudoin, G., Méric, J., Boutroy, E., and Potvin-Doucet, C. (2014). Trace elements in magnetite as petrogenetic indicators. *Mineralium Deposita*, 49(7):785–796.

Davis, D., Amelin, Y., Nowell, G., and Parrish, R. (2005). Hf isotopes in zircon from the western Superior province, Canada: Implications for Archean crustal development and evolution of the depleted mantle reservoir. *Precambrian Research*, 140(3-4):132–156.

Davis, D. W. (2002). U–Pb geochronology of Archean metasedimentary rocks in the Pontiac and Abitibi subprovinces, Quebec, constraints on timing, provenance and regional tectonics. *Precambrian Research*, 115(1-4):97–117.

Degeling, H., Eggins, S., and Ellis, D. J. (2001). Zr budgets for metamorphic reactions, and the formation of zircon from garnet breakdown. *Mineralogical Magazine*, 65(6):749–758.

Dickin, A., Strong, J., Arcuri, G., Van Kessel, A., and Krivankova-Smal, L. (2017). A revised model for the crustal structure of the SW Grenville Province, Ontario, Canada. *Geological Magazine*, 154(4):903–913.

Ewing, T. A., Hermann, J., and Rubatto, D. (2013). The robustness of the Zr-in-rutile and Ti-in-zircon thermometers during high-temperature metamorphism (Ivrea-Verbano Zone, northern Italy). *Contributions to Mineralogy and Petrology*, 165(4):757–779.

Fraser, G., Ellis, D., and Eggins, S. (1997). Zirconium abundance in granulite-facies minerals, with implications for zircon geochronology in high-grade rocks. *Geology*, 25(7):607.

Gervais, F., Beaudry, A., Kavanagh-Lepage, C., Moukhsil, A., Larson, K. P., and Guilmette, C. (2023). Far from boring: A new Grenvillian perspective on Mesoproterozoic tectonics. *Earth and Planetary Science Letters*, 610:118129.

Green, E. C. R., White, R. W., Diener, J. F. A., Powell, R., Holland, T. J. B., and Palin, R. M. (2016). Activity-composition relations for the calculation of partial melting equilibria in metabasic rocks. *Journal of Metamorphic Geology*, 34(9):845–869.

Holland, T. and Powell, R. (2003). Activity–composition relations for phases in petrological calculations: An asymmetric multicomponent formulation. *Contributions to Mineralogy and Petrology*, 145(4):492–501.

Holland, T. J. B. and Powell, R. (1998). An internally consistent thermodynamic data set for phases of petrological interest: An internally consistent thermodynamic data set. *Journal of Metamorphic Geology*, 16(3):309–343.

Holland, T. J. B. and Powell, R. (2011). An improved and extended internally consistent thermodynamic dataset for phases of petrological interest, involving a new equation of state for solids: Thermodynamic dataset for phases of petrological interest. *Journal of Metamorphic Geology*, 29(3):333–383.

Hoskin, P. W. O. and Schaltegger, U. (2003). The Composition of Zircon and Igneous and Metamorphic Petrogenesis. *Reviews in Mineralogy and Geochemistry*, 53(1):27–62.

Jamieson, R. A. and Beaumont, C. (2011). Coeval thrusting and extension during lower crustal ductile flow - implications for exhumation of high-grade metamorphic rocks. *Journal of Metamorphic Geology*, 29(1):33–51.

Jamieson, R. A. and Beaumont, C. (2013). On the origin of orogens. *Geological Society of America Bulletin*, 125(11-12):1671–1702.

Jochum, K. P., Willbold, M., Raczek, I., Stoll, B., and Herwig, K. (2005). Chemical Characterisation of the USGS Reference Glasses GSA-1G, GSC-1G, GSD-1G, GSE-1G, BCR-2G, BHVO-2G and BIR-1G Using EPMA, ID-TIMS, ID-ICP-MS and LA-ICP-MS. *Geostandards and Geoanalytical Research*, 29(3):285–302.

Kelsey, D. E., Clark, C., and Hand, M. (2008). Thermobarometric modelling of zircon and monazite growth in melt-bearing systems: Examples using model metapelitic and metapsammitic granulites. *Journal of Metamorphic Geology*, 26(2):199–212.

Kelsey, D. E. and Powell, R. (2011). Progress in linking accessory mineral growth and breakdown to major mineral evolution in metamorphic rocks: A thermodynamic approach in the $Na_2O$-CaO-$K_2O$-FeO-MgO-$Al_2O_3$-$SiO_2$ -$H_2O$-$TiO_2$-$ZrO_2$ system. *Journal of Metamorphic Geology*, 29(1):151–166.

Ketchum, J. W. F. and Davidson, A. (2000). Crustal architecture and tectonic assembly of the Central Gneiss Belt, southwestern Grenville Province, Canada: A new interpretation. *Canadian Journal of Earth Sciences*, 37:18.

Kirkland, C., Johnson, T., Kinny, P., and Kapitany, T. (2020). Modelling U-Pb discordance in the Acasta Gneiss: Implications for fluid–rock interaction in Earth's oldest dated crust. *Gondwana Research*, 77:223–237.

Klein, B. Z. and Eddy, M. P. (2023). What's in an age? Calculation and interpretation of ages and durations from U-Pb zircon geochronology of igneous rocks. *Geological Society of America Bulletin*.

Kohn, M. J., Corrie, S. L., and Markley, C. (2015). The fall and rise of metamorphic zircon. *American Mineralogist*, 100(4):897–908.

Lanari, P. and Engi, M. (2017). Local Bulk Composition Effects on Metamorphic Mineral Assemblages. *Reviews in Mineralogy and Geochemistry*, 83(1):55–102.

Marsh, J. H. and Culshaw, N. G. (2014). Timing and conditions of high-pressure metamorphism in the western Grenville Province: Constraints from accessory mineral composition and phase equilibrium modeling. *Lithos*, 200–201:402–417.

McMullen, S. M. (1999). *Tectonic Evolution of the Bark Lake Area, Eastern Central Gneiss Belt, Ontario Grenville: Constraints from Geology, Geochemistry and U-Pb Geochronology*. BSc Thesis, Carleton University.

Morisset, C.-E. and Scoates, J. S. (2008). Origin of zircon rims around ilmenite in mafic plutonic rocks of proterozoic anorthosite suites. *The Canadian Mineralogist*, 46(2):289–304.

Nielsen, R. L. and Beard, J. S. (2000). Magnetite–melt HFSE partitioning. *Chemical Geology*, 164(1-2):21–34.

Palin, R. M., Weller, O. M., Waters, D. J., and Dyck, B. (2016). Quantifying geological uncertainty in metamorphic phase equilibria modelling; a Monte Carlo assessment and implications for tectonic interpretations. *Geoscience Frontiers*, 7(4):591–607.

Pape, J., Mezger, K., and Robyr, M. (2016). A systematic evaluation of the Zr-in-rutile thermometer in ultra-high temperature (UHT) rocks. *Contributions to Mineralogy and Petrology*, 171(5):44.

Paton, C., Hellstrom, J., Paul, B., Woodhead, J., and Hergt, J. (2011). Iolite: Freeware for the visualisation and processing of mass spectrometric data. *Journal of Analytical Atomic Spectrometry*, 26(12):2508.

Powell, R. and Holland, T. J. B. (2008). On thermobarometry. *Journal of Metamorphic Geology*, 26(2):155–179.

Rivers, T. (2008). Assembly and preservation of lower, mid, and upper orogenic crust in the Grenville Province—Implications for the evolution of large hot long-duration orogens. *Precambrian Research*, 167(3-4):237–259.

Rivers, T. (2012). Upper-crustal orogenic lid and mid-crustal core complexes: Signature of a collapsed orogenic plateau in the hinterland of the Grenville Province. *Canadian Journal of Earth Sciences*, 49(1):1–42.

Rivers, T., Culshaw, N. G., Hynes, A., Indares, A., Jamieson, R. A., and Martignole, J. (2012). The Grenville Orogen–A post-LITHOPROBE perspective. In *Tectonic Styles in Canada: The LITHOPROBE Perspective*, number 49 in Geological Association of Canada Special Paper, pages 97–236. Geological Association of Canada.

Rivers, T. and Schwerdtner, W. (2015). Post-peak Evolution of the Muskoka Domain, Western Grenville Province: Ductile Detachment Zone in a Crustal-scale Metamorphic Core Complex. *Geoscience Canada*, 42(4):403.

Rubatto, D. (2017). Zircon: The Metamorphic Mineral. *Reviews in Mineralogy and Geochemistry*, 83(1):261–295.

Sauerzapf, U., Lattard, D., Burchard, M., and Engelmann, R. (2008). The Titanomagnetite–Ilmenite Equilibrium: New Experimental Data and Thermo-oxybarometric Application to the Crystallization of Basic to Intermediate Rocks. *Journal of Petrology*, 49(6):1161–1185.

Sawyer, E. W. (2008). *Atlas of Migmatites*. Number 9 in The Canadian Mineralogist. Special Publication. NRC research press, Ottawa.

Schneider, D., Cope, N., and Holm, D. (2013). Thermochronology of the Mont Laurier terrane, southern Canadian Grenville Province, and its bearing on defining orogenic architecture. *Precambrian Research*, 226:43–58.

Sievwright, R. H., O'Neill, H. St. C., Tolley, J., Wilkinson, J. J., and Berry, A. J. (2020). Diffusion and partition coefficients of minor and trace elements in magnetite as a function of oxygen fugacity at 1150 ºC. *Contributions to Mineralogy and Petrology*, 175(5):40.

Singh, S. (2019). Protracted zircon growth in migmatites and In situ melt of Higher Himalayan Crystallines: U–Pb ages from Bhagirathi valley, NW Himalaya, India. *Geoscience Frontiers*, 10(3):793–809.

Slagstad, T. (2003). *Muskoka and Shawanaga Domains, Central Gneiss Belt, Grenville Province, Ontario: Geochemical and Geochronological Constraints on Pre-Grenvillian and Grenvillian Geological Evolution*. PhD thesis, Dalhousie University, Halifax, Nova Scotia.

Slagstad, T., Hamilton, M. A., Jamieson, R. A., and Culshaw, N. G. (2004). Timing and duration of melting in the mid orogenic crust: Constraints from U–Pb (SHRIMP) data, Muskoka and Shawanaga domains, Grenville Province, Ontario. *Canadian Journal of Earth Sciences*, 41:27.

Slagstad, T., Jamieson, R. A., and Culshaw, N. G. (2005). Formation, Crystallization, and Migration of Melt in the Mid-orogenic Crust: Muskoka Domain Migmatites, Grenville Province, Ontario. *Journal of Petrology*, 46(5):893–919.

Sláma, J., Košler, J., Condon, D. J., Crowley, J. L., Gerdes, A., Hanchar, J. M., Horstwood, M. S., Morris, G. A., Nasdala, L., Norberg, N., Schaltegger, U., Schoene, B., Tubrett, M. N., and Whitehouse, M. J. (2008). Plešovice zircon — A new natural reference material for U–Pb and Hf isotopic microanalysis. *Chemical Geology*, 249(1-2):1–35.

Tan, W., Liu, P., He, H., Wang, C. Y., and Liang, X. (2016). Mineralogy and Origin of Exsolution In Ti-Rich Magnetite From Different Magmatic Fe-Ti Oxide-Bearing Intrusions. *The Canadian Mineralogist*, 54(3):539–553.

Timmerman, H., Jamieson, R. A., Parrish, R. R., and Culshaw, N. G. (2002). Coeval migmatites and granulites, Muskoka domain, southwestern Grenville Province, Ontario. *Canadian Journal of Earth Sciences*, 39:239–258.

Timmermann, H., Jamieson, R. A., Culshaw, N. G., and Parrish, R. R. (1997). Time of metamorphism beneath the Central Metasedimentary Belt boundary thrust zone, Grenville Orogen, Ontario: Accretion at 1080 Ma? *Canadian Journal of Earth Sciences*, 34(7):1023–1029.

Tomkins, H. S., Williams, I. S., and Ellis, D. J. (2005). *In Situ* U–Pb dating of zircon formed from retrograde garnet breakdown during decompression in Rogaland, SW Norway. *Journal of Metamorphic Geology*, 23(4):201–215.

Vermeesch, P. (2018). IsoplotR: A free and open toolbox for geochronology. *Geoscience Frontiers*, 9(5):1479–1493.

Vermeesch, P. (2021). On the treatment of discordant detrital zircon U–Pb data. *Geochronology*, 3(1):247–257.

Volante, S., Blereau, E., Guitreau, M., Tedeschi, M., Van Schijndel, V., and Cutts, K. (2024). Current applications using key mineral phases in igneous and metamorphic geology: Perspectives for the future. *Geological Society, London, Special Publications*, 537(1):57–121.

Watson, E. B. and Harrison, T. M. (1983). Zircon saturation revisited: Temperature and composition effects in a variety of crustal magma types. *Earth and Planetary Science Letters*, 64(2):295–304.

White, D. J., Forsyth, D. A., Asudeh, I., Carr, S. D., Wu, H., Easton, R. M., and Mereu, R. F. (2000). A seismic-based cross-section of the Grenville Orogen in southern Ontario and western Quebec. *Canadian Journal of Earth Sciences*, 37.

White, R. W., Powell, R., and Clarke, G. L. (2002). The interpretation of reaction textures in Fe-rich metapelitic granulites of the Musgrave Block, central Australia: Constraints from mineral equilibria calculations in the system $K_2O$–FeO–MgO–$Al_2O_3$–$SiO_2$–$H_2O$–$TiO_2$–$Fe_2O_3$. *Journal of Metamorphic Geology*, 20(1):41–55.

White, R. W., Powell, R., Holland, T. J. B., Johnson, T. E., and Green, E. C. R. (2014a). New mineral activity–composition relations for thermodynamic calculations in metapelitic systems. *Journal of Metamorphic Geology*, 32(3):261–286.

White, R. W., Powell, R., and Johnson, T. E. (2014b). The effect of Mn on mineral stability in metapelites revisited: New a–x relations for manganese-bearing minerals. *Journal of Metamorphic Geology*, 32(8):809–828.

Whitney, D. L. and Evans, B. W. (2010). Abbreviations for names of rock-forming minerals. *American Mineralogist*, 95(1):185–187.

Wiedenbeck, M., Hanchar, J. M., Peck, W. H., Sylvester, P., Valley, J., Whitehouse, M., Kronz, A., Morishita, Y., Nasdala, L., Fiebig, J., Franchi, I., Girard, J.-P., Greenwood, R., Hinton, R., Kita, N., Mason, P., Norman, M., Ogasawara, M., Piccoli, P., Rhede, D., Satoh, H., Schulz-Dobrick, B., Skår, O., Spicuzza, Mj., Terada, K., Tindle, A., Togashi, S., Vennemann, T., Xie, Q., and Zheng, Y.-F. (2004). Further Characterisation of the 91500 Zircon Crystal. *Geostandards and Geoanalytical Research*, 28(1):9–39.

Wodicka, N. (1994). *Middle Proterozoic Evolution of the Parry Sound Domain, Southwestern Grenville Orogen, Ontario: Structural, Metamorphic, U/Pb, and 40Ar/39 Ar Constraints*. PhD thesis, Dalhousie University.

Wodicka, N., Jamieson, R. A., and Parrish, R. R. (1996). The Parry Sound domain: A far-travelled allochthon? New evidence from U–Pb zicon geochronology. *Canadian Journal of Earth Sciences*, 33(7):1087–1104.

Wodicka, N., Ketchum, J. W., and Jamieson, R. A. (2000). Grenvillian metamorphism of monocyclic rocks, georgian bay, ontario, canada: Implications for convergence history. *The Canadian Mineralogist*, 38(2):471–510.

Yakymchuk, C. (2023). Prograde zircon growth in migmatites. *Journal of Metamorphic Geology*, 41(5):719–743.

Yakymchuk, C. and Brown, M. (2014). Behaviour of zircon and monazite during crustal melting. *Journal of the Geological Society*, 171(4):465–479.

Yakymchuk, C., Kirkland, C., Hollis, J., Kendrick, J., Gardiner, N., and Szilas, K. (2020). Mesoarchean partial melting of mafic crust and tonalite production during high-T–low-P stagnant tectonism, Akia Terrane, West Greenland. *Precambrian Research*, 339:105615.

**Table 2.1:** Bulk rock composition in weight %

| **Sample** | **$SiO_2$** | **$Al_2O_3$** | **$Fe_2O_3$** | **FeO** | **MnO** | **MgO** | **CaO** | **$Na_2O$** | **$K_2O$** | **$TiO_2$** | **$P_2O_5$** | **LOI** | **Total** | **Zr ($\frac{\mu g}{g}$)** |
|---|---|---|---|---|---|---|---|---|---|---|---|---|---|---|
| 20SD06 | 66.24 | 13.24 | 2.79 | 3.7 | 0.190 | 0.210 | 2.09 | 3.28 | 5.19 | 0.640 | 0.10 | 0.77 | 98.4 | 1001 |
| 20SD17A | 68.60 | 13.26 | 3.55 | 2.2 | 0.123 | 0.15 | 1.38 | 2.88 | 5.45 | 0.526 | 0.06 | 0.50 | 98.7 | 924 |
| 21SD68 | 60.95 | 14.87 | 2.60 | 6.1 | 0.263 | 0.24 | 2.82 | 4.77 | 5.32 | 0.799 | 0.13 | 0.38 | 99.2 | 2290 |
| 22SD55E | 59.38 | 16.33 | 3.77 | 6.1 | 0.185 | 0.33 | 3.17 | 4.20 | 5.33 | 0.710 | 0.14 | 0.89 | 100.5 | 1664 |

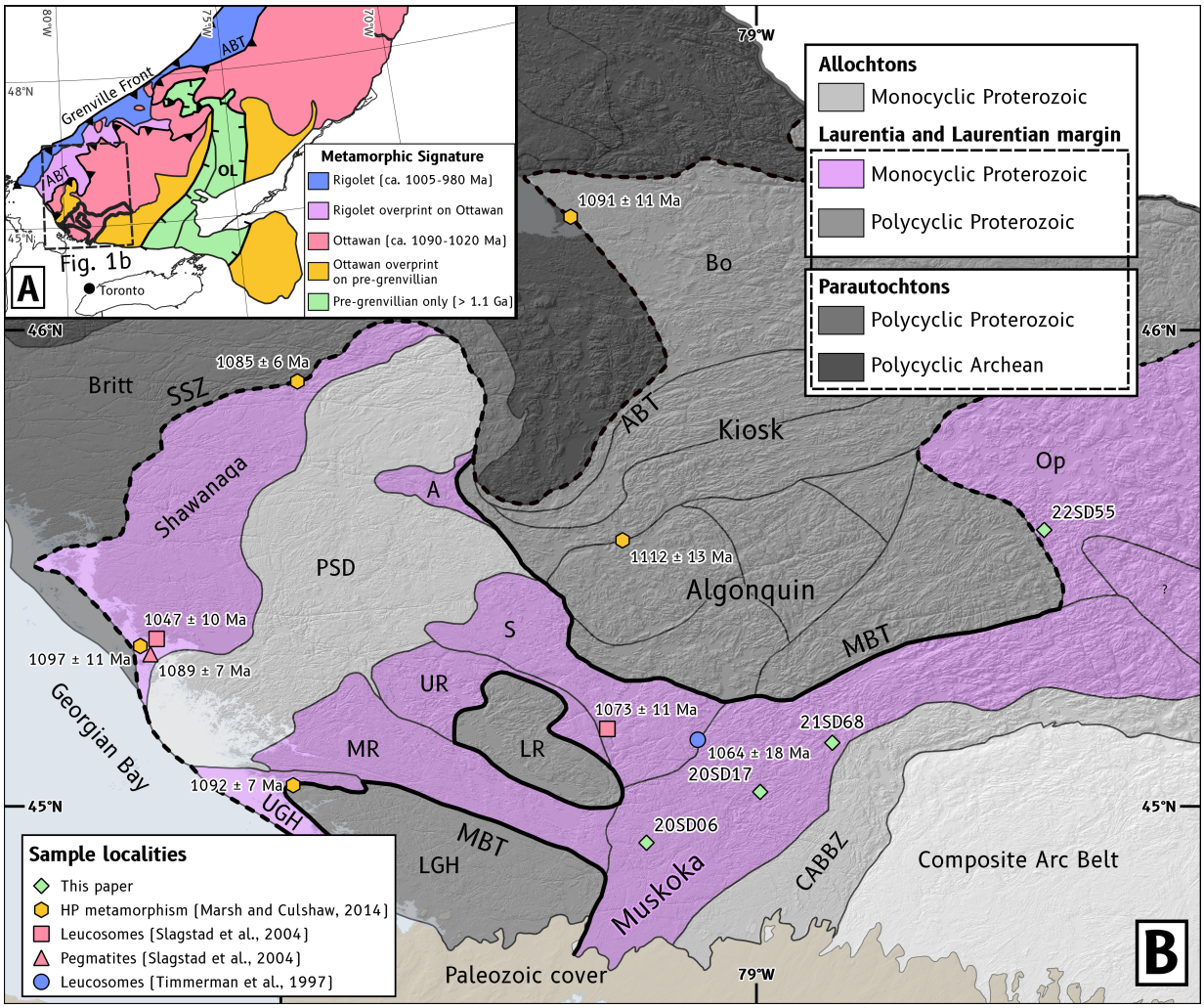


**Figure 2.1: (A)**: Overview map of the Grenville Province showing metamorphic affinity of different regions in the Grenville (Modified after Rivers (2008)) Abbreviations: OL = Orogenic Lid; ABT = Allochthon Boundary Thrust. **(B)**: Map of the Central Gneiss Belt in Ontario with the Muskoka domain highlighted (Modified after Culshaw et al. (2016)). Important sample locations and measured ages from Marsh and Culshaw (2014), Slagstad et al. (2004), and Timmermann et al. (1997) are also shown. Abbreviations: MBT = Monocyclic Boundary Thrust; SSZ = Shawanaga shear zone; CABBZ = Composite Arc Belt Boundary Zone; UGH, LGH, UR, LR, A, Op = upper-, lower Go Homme, upper-, lower Rosseau, Ahmic, Opeongo domains; MR, S = Moon River, Seguin subdomains; PSD = Parry Sound domain; Bo = Bonfield domain. Sample coordinates shown in Table A.13

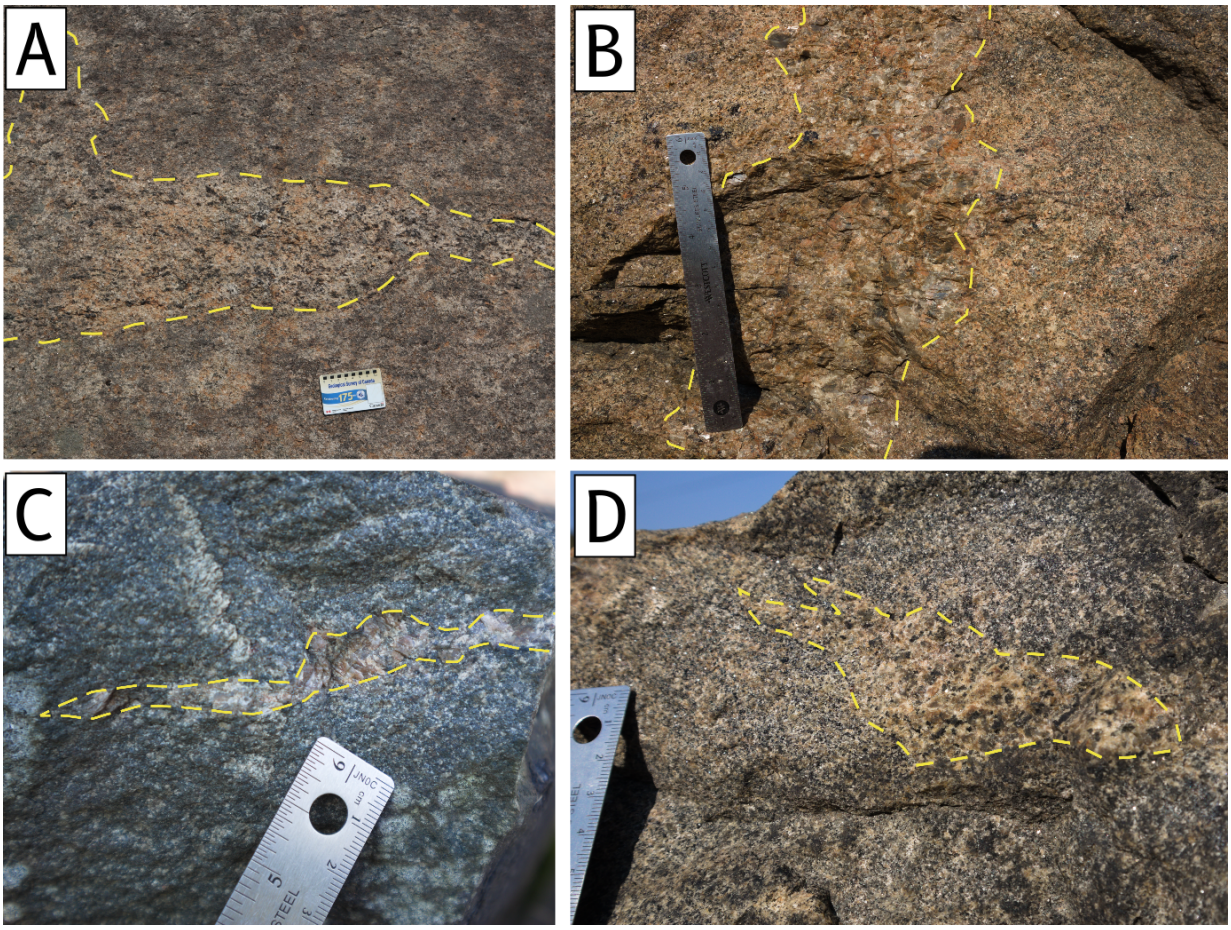


**Figure 2.2:** Field photos of source outcrops of **(A)**: 20SD06, **(B)**: 20SD17A, **(C)**: 21SD68, and **(D)**: 22SD55E. Dashed lines outline leucosomes.

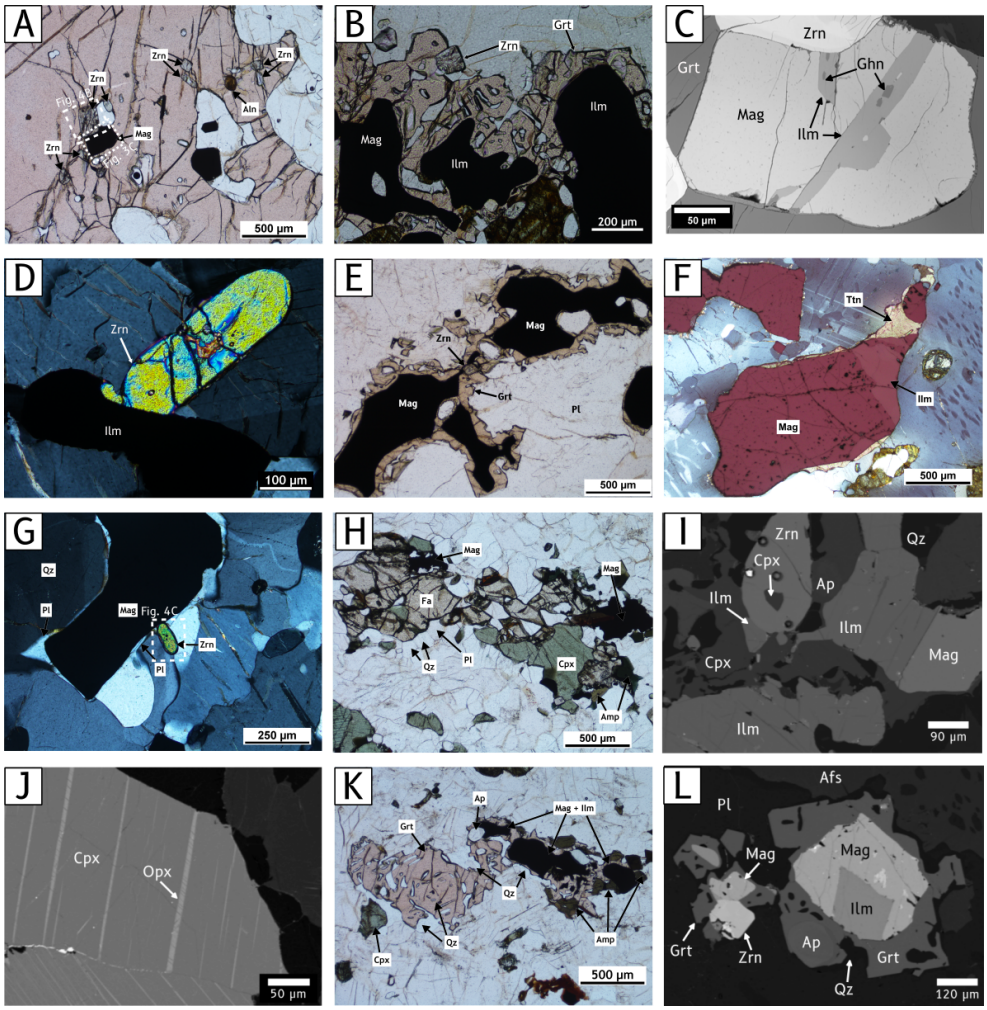


**Figure 2.3:** Photomicrographs of mineral assemblages and microstructures of samples. Abbreviations are after Whitney and Evans (2010) **(A)**: Plane polarized light (PPL) image of zircon, allanite, and magnetite inclusions in garnet in 20SD06. **(B)**: PPL image of garnet and quartz intergrowths overgrowing magnetite and ilmenite with partial overgrowth of zircon in 20SD06 **(C)**: BSE image of magnetite inclusion with garnet adjacent to zircon with ilmenite lamallae that contain the Zn-spinel gahnite (Ghn) in 20SD06. **(D)**: Cross-polarized light (XPL) image of zircon with irregular overgrowth onto adjacent ilmenite in 20SD06. **(E)**: PPL image of garnet overgrowths on magnetite and zircon in 20SD17A **(F)**: Reflected light partial XPL image of titanite overgrowths on magnetite and ilmenite in 20SD17A. **(G)**: XPL image of zircon attached to magnetite grain alongside plagioclase overgrowths on magnetite in 20SD17A. **(H)**: PPL image of fayalite and clinopyroxene cluster with quartz and magnetite in 21SD68. **(I)**: Back scattered electron (BSE) image of zircon with a clinopyroxene inclusion and rounded edges abutting against ilmenite and clinopyroxene in 21SD68. Also shows occurrence of ilmenite with magnetite and independent ilmenite grains. **(J)**: BSE image of orthopyroxene exsolution lamallae in clinopyroxene in 21SD68. **(K)**: PPL image of garnet and amphibole overgrowths on magnetite and vermicular intergrowths of quartz and garnet. **(L)**: BSE image showing garnet overgrowths of ilmenite and magnetite and partial overgrowth on zircon that abuts on magnetite with a straight edge.

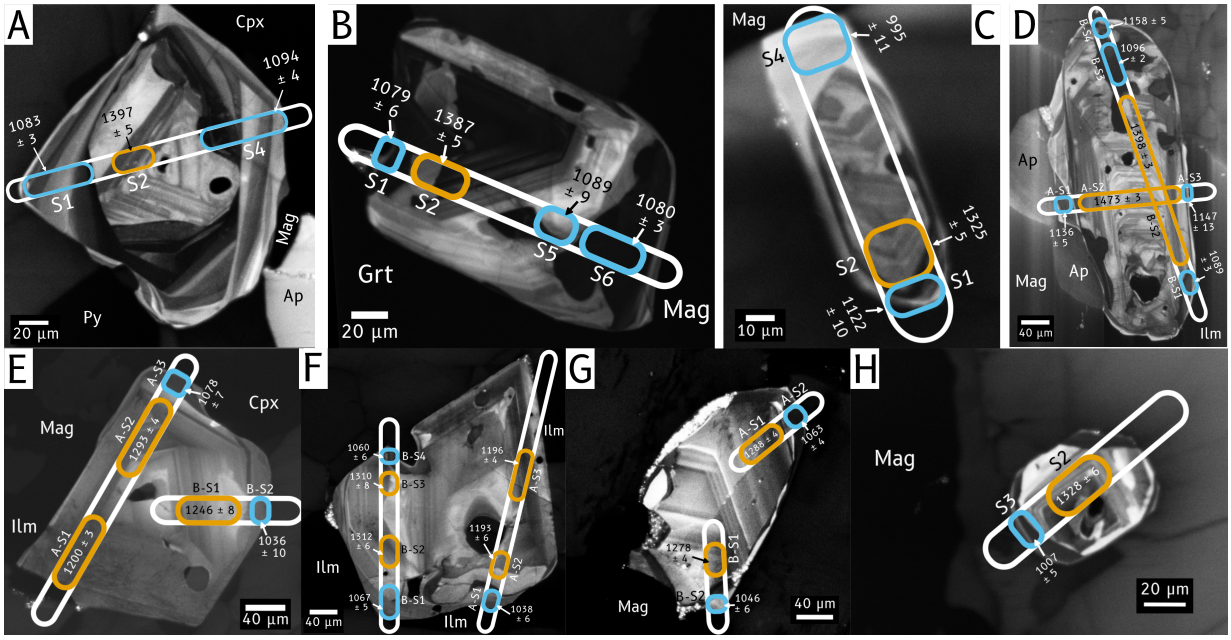


**Figure 2.4:** Cathodoluminescence photos of select zircons: **(A)**: 20SD06-Zrn10,**(B)**: 20SD06-Zrn26,**(C)**: 20SD17A-Zrn25, **(D)**: 20SD17A-Zrn4, **(E)**: 21SD68-Zrn8, **(F)**: 21SD68-Zrn27, **(G)**: 22SD55E-Zrn16, **(H)**: 22SD55E-Zrn30. Full laser lines that were analyzed are outlined, with specific selections coloured and indicated with their corresponding concordia date in Ma with 1s error. Colours correspond to those in Fig. 2.6. Zircon imaged in B and C corresponds to the zircon in Fig. 2.3 A and G respectively. Zircon shown in B, C, F, and G have younger ages in texturally distinct rims that abut on magnetite or ilmenite. Each selection is labelled with corresponding label in Table A.11

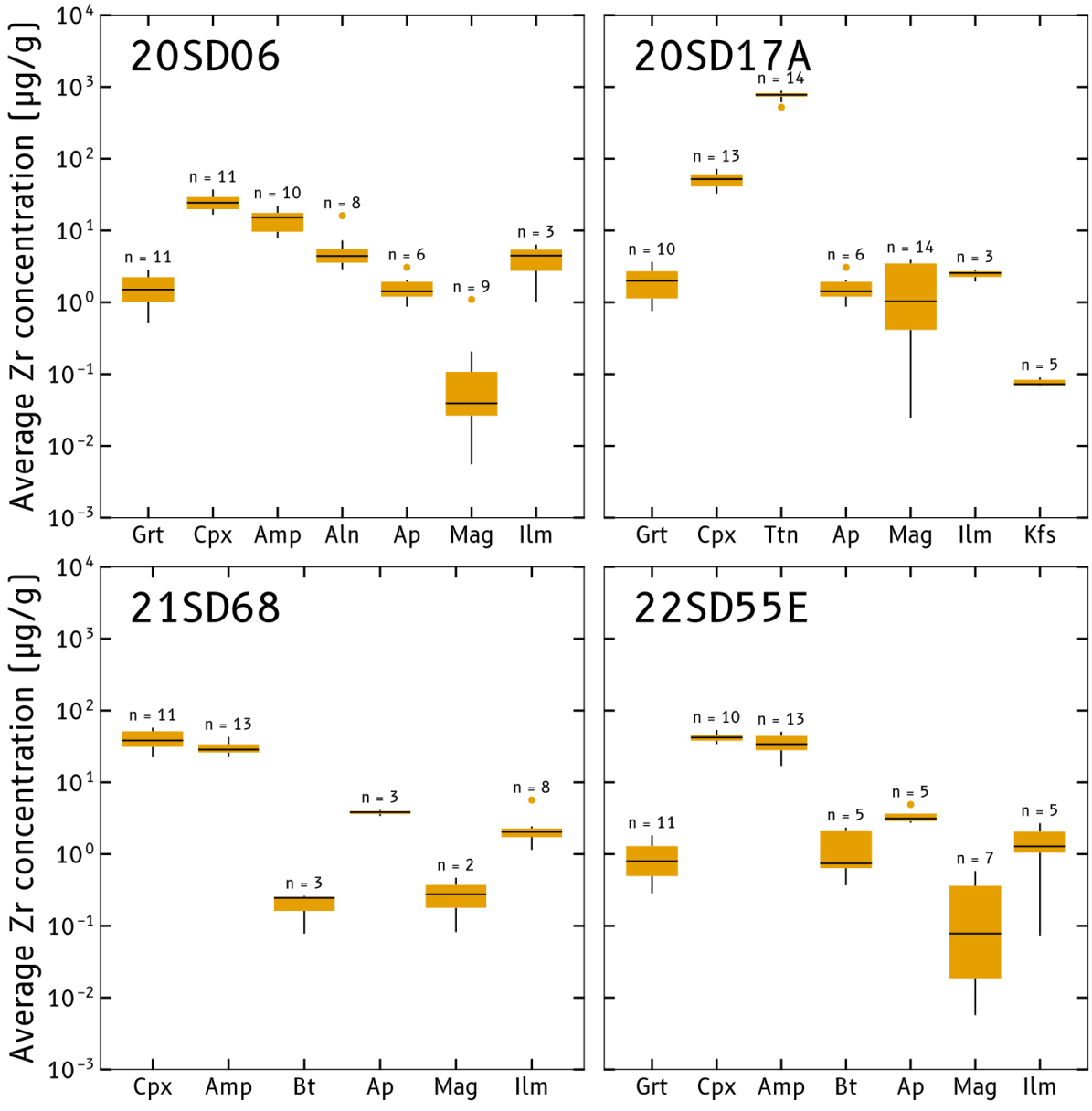


**Figure 2.5:** Zr concentrations in major minerals with measurements above detection limit measured using LA-ICP-MS.

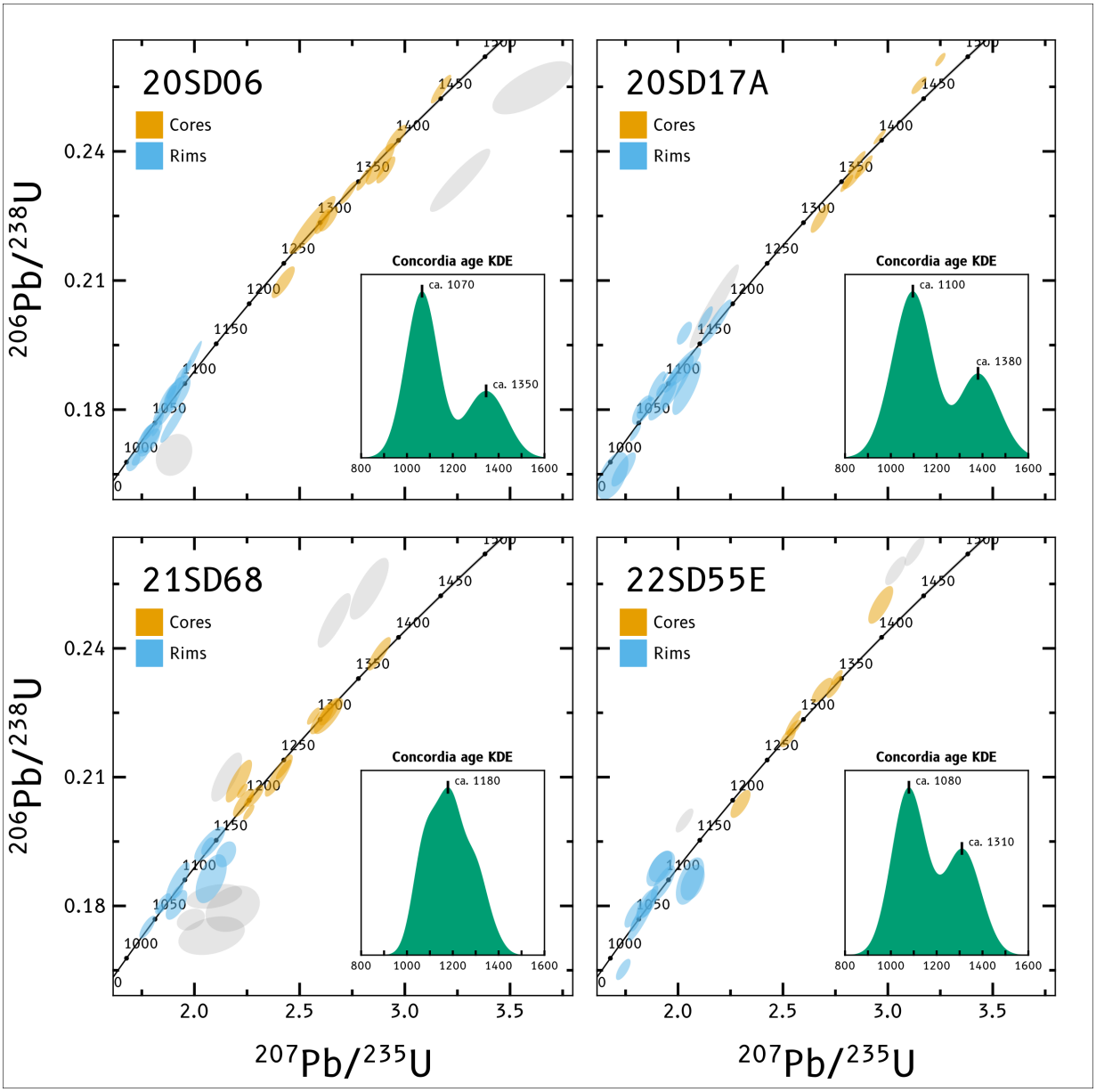


**Figure 2.6:** Wetherill plots of all selected LA-MC-ICP-MS data. Cores and rims were differentiated by age, trace elements, and cathodoluminescence textures. Discordant analyses shown in grey, concordance defined as a value between -3 and 5 using the concordia distance method (Vermeesch, 2021). Kernel density estimates (KDE) of concordia dates are inset in each plot

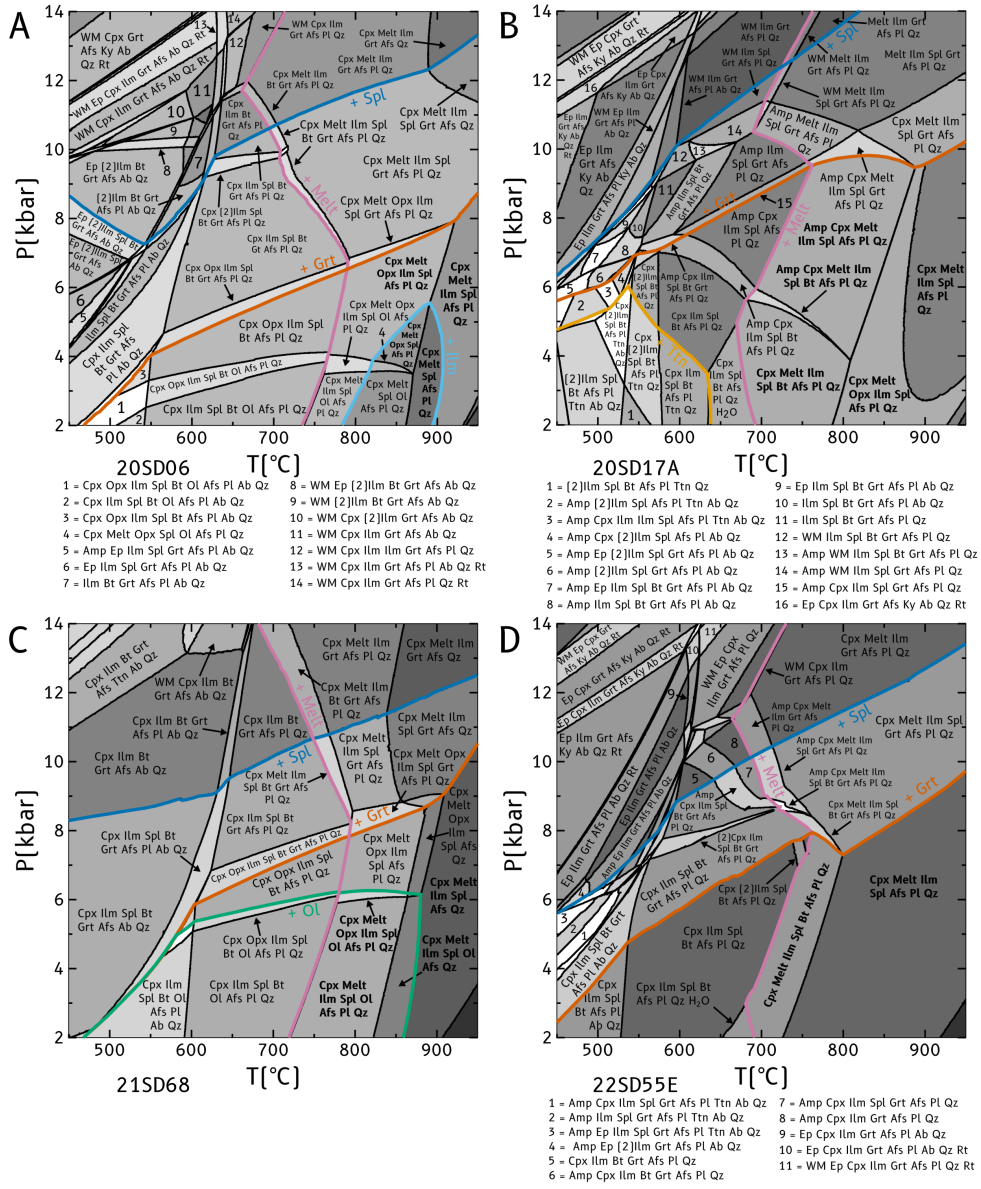


**Figure 2.7:** Pseudosections of each sample with key field boundaries highlighted in **(A)**: 20SD06, **(B)**: 20SD17A, **(C)**: 21SD68, and **(D)**: 22SD55E. Possible peak assemblages are indicated with bold text. Abbreviations after Whitney and Evans (2010), WM = White mica, (2)Ilm indicates stability of 2 immiscible ilmenite phases, one $Fe^{3+}$-rich and one Ti-rich. Sp is closest to magnetite in composition with variable amounts of Ti (See Fig. 2.8 for more details)

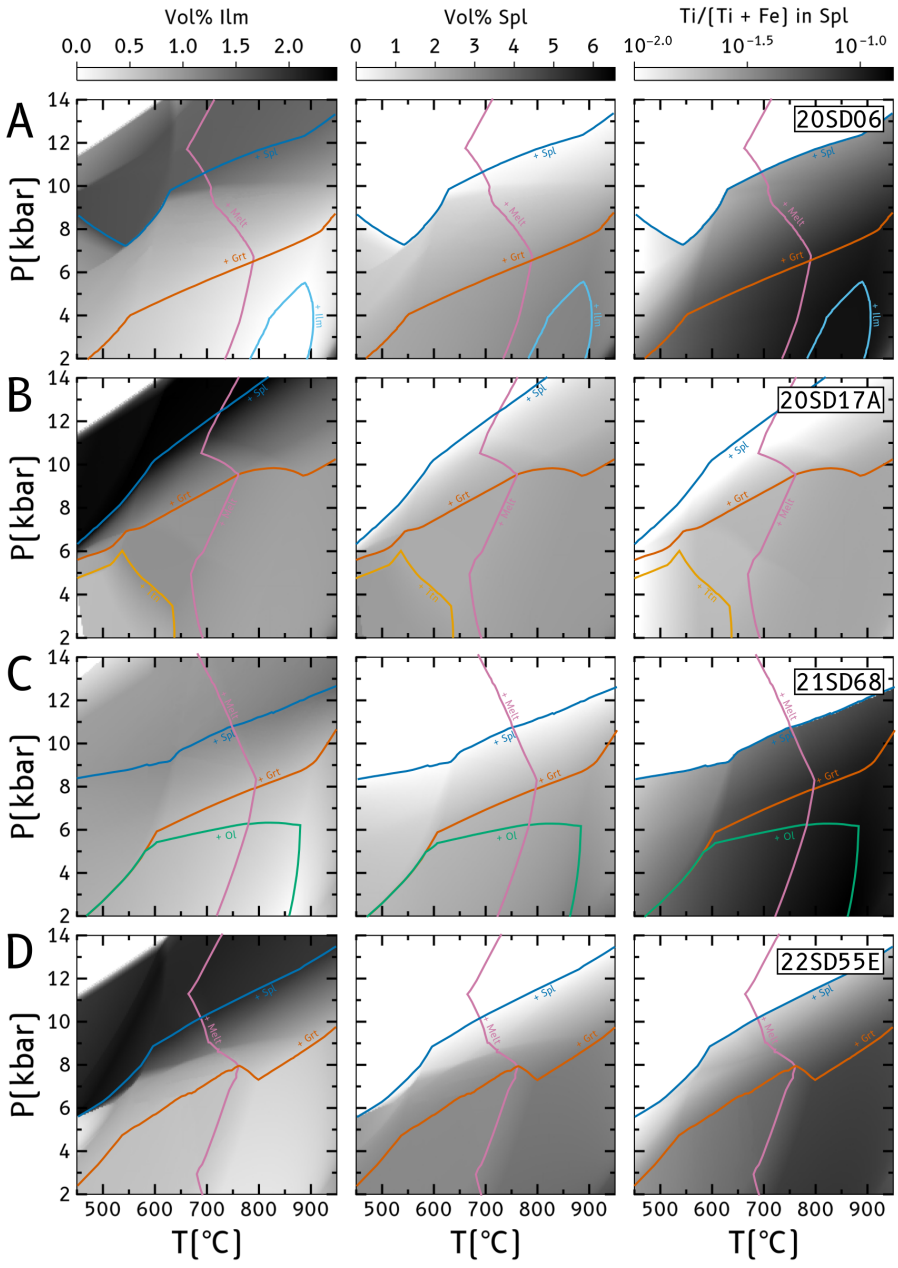


**Figure 2.8:** Heatmaps showing variation of volumetric proportion of ilmenite and spinel, and molar Ti concentration in spinel with pressure and temperature in **(A)**: 20SD06, **(B)**: 20SD17A, **(C)**: 21SD68, and **(D)**: 22SD55E. Key field boundaries are overlain.

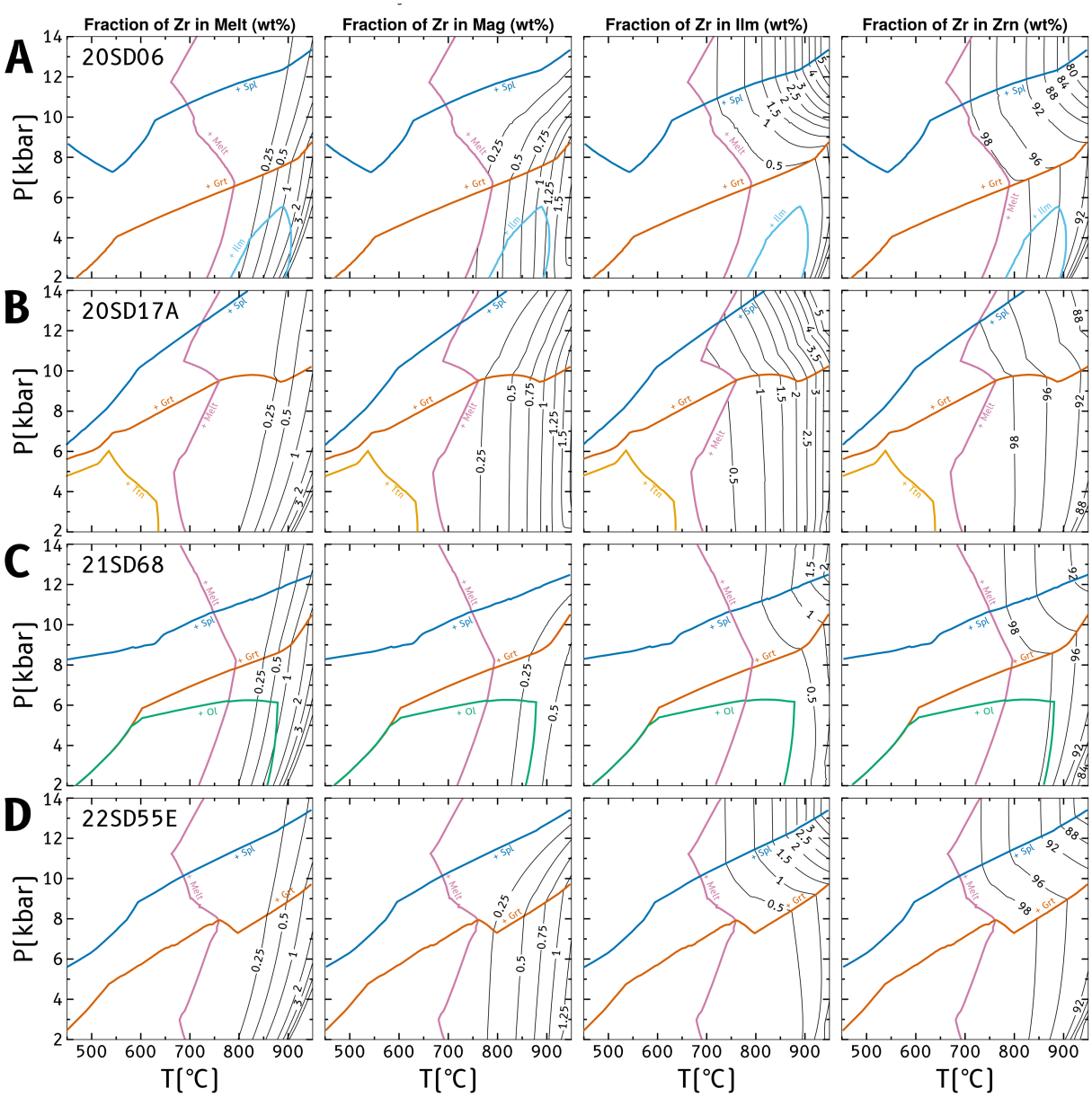


**Figure 2.9:** Contours of proportion of the Zr in the system (wt%) calculated to be in melt, magnetite (Mag), ilmenite (Ilm), and zircon (Zrn) during melting. **(A)**: 20SD06, **(B)**: 20SD17A, **(C)**: 21SD68, and **(D)**: 22SD55E. Key field boundaries are overlain

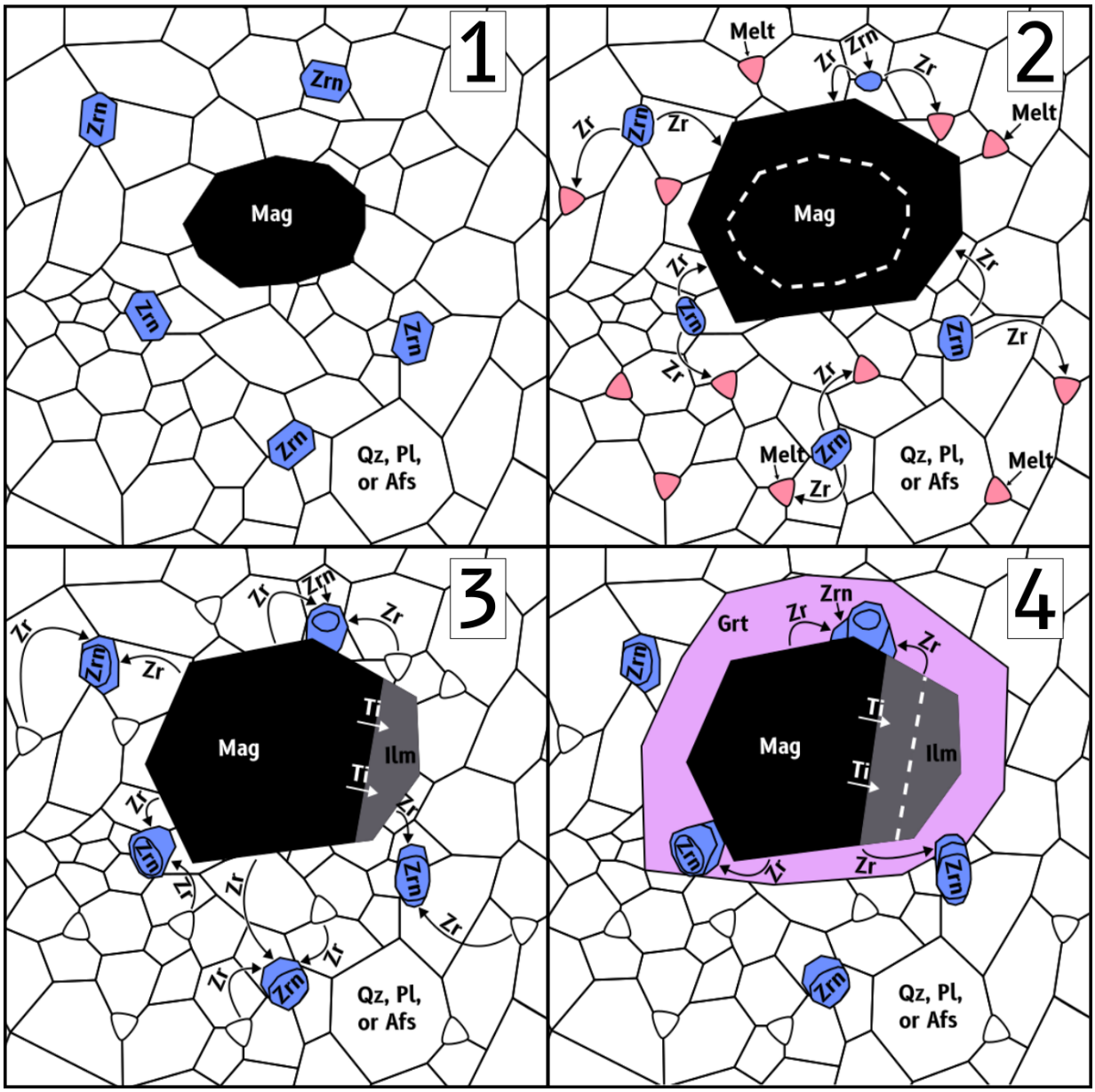


**Figure 2.10:** Schematic sketch illustrating the possible growth sequence of zircon and movement of Zr during metamorphism: **Stage 1**: Initial formation of the igneous protolith with igneous zircon and magnetite present; **Stage 2**: Prograde metamorphism resulting in melt formation and the growth of more magnetite. This magnetite is more Ti-rich and can incorporate some Zr lost from zircon dissolution during melting, Zr also enters the melt; **Stage 3**: Melt crystallization and loss of Ti from magnetite result in Zr loss from melt and magnetite and cause metamorphic zircon to grow over resorbed relict igneous zircon grains; **Stage 4**: Further breakdown of titanomagnetite to make garnet and ilmenite result in more loss of Zr from magnetite to make zircon.

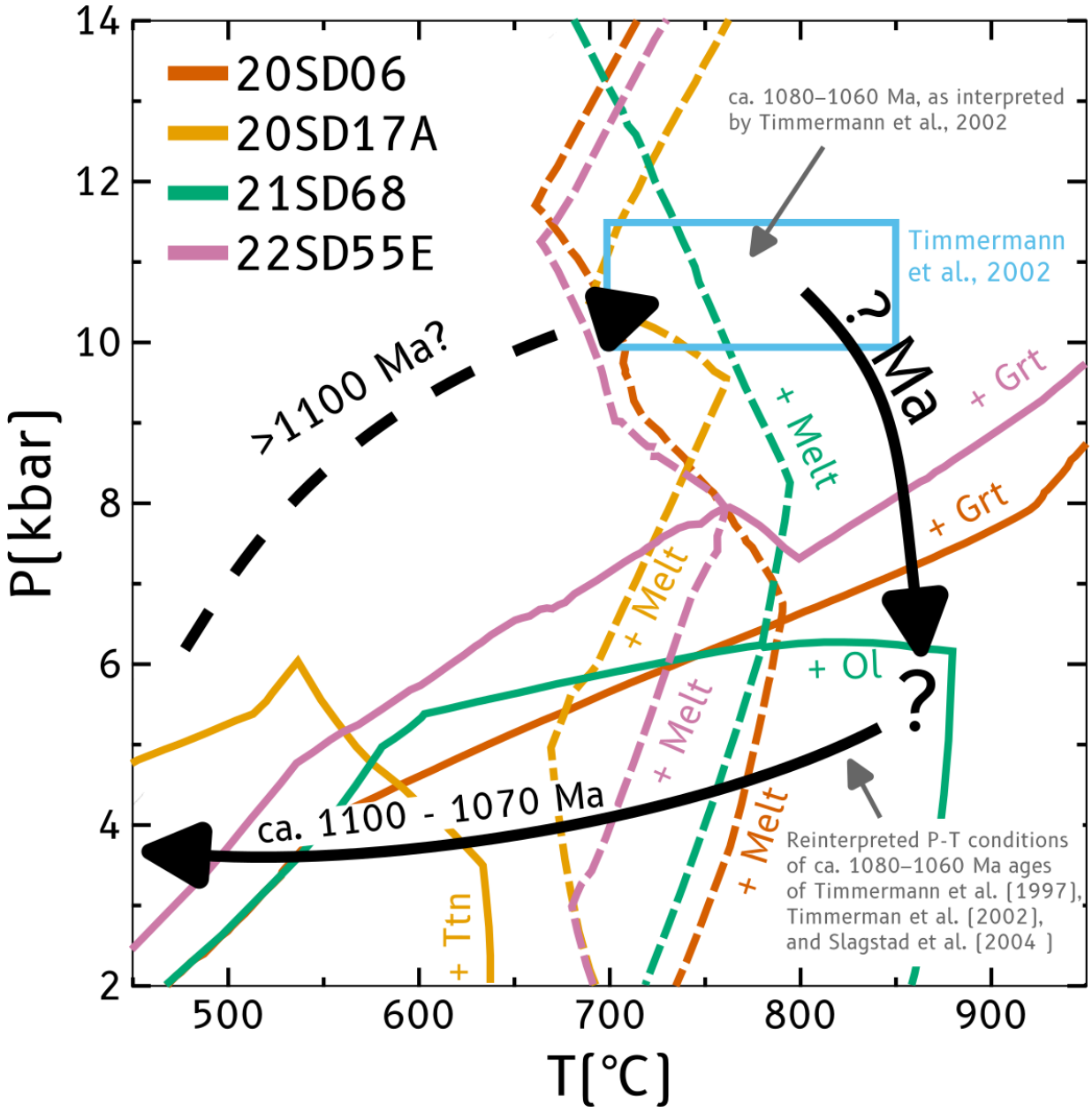


**Figure 2.11:** Generalized P–T path of samples in this study including stability fields of some key minerals. Prograde path and timing are uncertain. Peak P conditions are from Timmerman et al. (2002). Original and new interpretations of P–T conditions for ages from Timmermann et al. (1997), Timmerman et al. (2002) and Slagstad et al. (2004) are indicated. Date range for retrograde path is from this study.

# Chapter 3

# Sluggish mobility of trace elements in suprasolidus metamorphic systems: implications for zircon petrochronology

## 3.1 Summary

Trace elements serve as the fingerprints to the source of fluids and melts and give us important insights into tectonic processes and the long-term evolution of the continental crust. Applying equilibrium trace element partitioning between minerals, fluids, and melt to natural metamorphic systems requires assessment of kinetic limits to equilibrium. We present empirical evidence that diffusion of Hf, Y, Th, U and HREE is too slow to establish thin-section scale equilibrium in metamorphic rocks at high temperatures (>700 °C), even in the presence of melt. *In situ* analysis of zircon that grew during melt crystallization shows differences in trace element concentrations and zoning patterns that suggest intergranular diffusion of these trace elements is slower than rates of zircon growth. The occurrence of these differences in Y, Th, U and HREE concentration in zircon grains immediately adjacent to each other imply scales of equilibrium for these elements are generally less than a millimeter during melt crystallization. Consequently, the utility of popular chemical and isotopic indicators of zircon petrogenesis—such as $\varepsilon$Hf, Th/U, and HREE—may be limited by slow intergranular diffusion of these elements. The slow intergranular diffusion rates of trace elements implied by this study suggest that these important chemical indicators in

metamorphic zircon are controlled by heterogeneity in the protolith and interpretation and models of trace elements in zircon need to account for variability of zircon composition as a result of sluggish diffusion. The potential kinetic hindrances to trace element equilibration may be reflected by variable melt compositions in sources, which leads to complications for linking trace element compositions and isotope ratios to granite petrogenesis and for zircon petrochronology. While slow intergranular diffusion may limit the utility of bulk-rock analyses and models, it elevates the utility of millimeter-scale analysis to study high-temperature metamorphic processes.

## 3.2 Introduction

Petrological processes in the deep crust and their impact on the long-term evolution of the continental crust are tracked by the trace elements, stable, and radioactive isotopes in igneous rocks (e.g. Hanson, 1980; Blichert-Toft and Albarède, 1997; Eiler, 2001; Laurent et al., 2020; Mulder et al., 2021). Trace element concentrations in whole-rock samples and accessory minerals are frequently used to connect granitoids and other igneous rocks to a specific tectonic setting or melt-generating process in the deep crust (e.g. McCulloch and Gamble, 1991; Davidson et al., 2007; Laurent et al., 2020; Zhang et al., 2024a; Smit and Kooijman, 2024; Kendrick et al., 2022). To reasonably make such connections, we must first understand the petrological processes that control melt generation and the resulting melt composition in the anatectic source. Modelling the concentrations of trace elements in melt generated in the crust at high temperatures has been a major focus of studies on source migmatites and the resulting igneous rocks (e.g. Johnson et al., 2017) and accessory minerals (e.g. Roberts et al., 2024). Understanding how trace elements partition between minerals, melt, and fluid is crucial for applying equilibrium-based models to natural petrological processes. Accessory minerals in metamorphic and igneous systems have minor abundances, but disproportionately concentrate trace elements; these include the rare earth elements (REE), U, Th, and Hf, which are widely used geochemical monitors of the nature of the source rocks and protoliths (Bea, 1996b). Numerical models of zircon, monazite, allanite, apatite, and titanite growth have been the focus of many trace element modelling studies (e.g. Kelsey et al., 2008; Spear, 2010; Kohn et al., 2015; Yakymchuk, 2017; Taylor et al., 2017; Yakymchuk, 2023; Cioffi et al., 2019; Kirkland et al., 2020; Krneta et al., 2018; Kinney et al., 2024). However, the applicability of these models to natural systems is dependent on reaching chemical equilibrium, which is rarely established for individual samples, as indicated by ubiquitous trace element zoning in zircon and other accessory minerals (e.g. Kelly and Harley, 2005; Harley and Kelly, 2007; Sláma et al., 2007).

A hand-sample scale (up to $\sim 100$ cm$^3$) equilibration volume—that is the volume within which all phases are in equilibrium with each other (Powell and Holland, 2008)—is generally considered a reasonable assumption for suprasolidus systems. In such systems, diffusion is assumed to be faster than crystal growth or breakdown at melting temperatures and if melt connectivity is achieved; melt is assumed to be a more efficient transport medium than dry grain boundaries (White and Powell, 2002). However, a majority of diffusion data in silicate melt are from systems that are entirely composed of melt (Zhang et al., 2010; Zhang and Gan, 2022). Experimental studies of major element diffusion in system with low modal proportions of melt suggest that these elements can be heterogeneously distributed in melt as a result of diffusion-controlled melting (Acosta-Vigil et al., 2006a,b, 2012b, 2017). Of the trace elements, only Sr diffusion has been investigated experimentally in systems with low proportions of melt (Hammouda et al., 1996) and heterogeneous isotope ratios in the melt were found to be a result of slow diffusion of Sr. The Sr isotope ratios of the melt were locally variable and strongly influenced by the variable concentration and isotope ratios of Sr in different minerals that participated in the partial melting reaction (Hammouda et al., 1996).

In comparison with major elements, which are present in variable proportions in most minerals that participate in partial melting reactions, many key trace elements like Zr, U, Th, Y, and HREE partition most strongly into accessory minerals (Bea, 1996a). Concentrations of these elements in melt are therefore more sensitive to the behaviour of accessory minerals. Considering that these key trace elements also diffuse slower than most major elements in silicate melt (Zhang and Gan, 2022), trace element concentrations in melt may vary locally based on the relative local abundance of accessory minerals interacting with the melt. Empirical studies of trace element distribution in migmatites and granitoids support slow diffusion during partial melting for a variety of trace elements including Zr (Zhang et al., 2024b), Hf (Zhang et al., 2024b; Tang et al., 2014; Zhang et al., 2020; Wang et al., 2018; Farina et al., 2014; Finch et al., 2021), Sr (Farina and Stevens, 2011; McLeod et al., 2012), and the REE (Acosta-Vigil et al., 2012a; Taylor et al., 2017). Most of these empirical studies are based on analyses of zircon separates and provide little indication of the equilibration volume during melting. Studies with *in situ* analyses of glass in migmatites (McLeod et al., 2012; Acosta-Vigil et al., 2012a) indicate trace element equilibration volumes the scale of cubic millimetres or less.

Partial melting that generates silicate liquid with different major and trace element compositions that locally vary due to small equilibration volumes (cubic millimetre-scale) is typically referred to as "disequilibrium melting". When disequilibrium melting occurs, melt homogenization requires timescales ranging from decades to hundreds of thousands of years (Hammouda et al., 1996; Acosta-Vigil et al., 2006a,b, 2012b,a). Whether equilibrium or

disequilibrium melting occurs is based on a confluence of factors, including: (1) the reaction rate of melting, (2) the rate of diffusion in the melt, (3) the rate of intracrsytalline diffusion in reactant and accessory minerals, and (4) the composition and zoning of the reactant and accessory minerals (Acosta-Vigil et al., 2006a, 2017; Hammouda et al., 1996; Acosta-Vigil et al., 2012a). Disequilibrium melting may introduce heterogeneities in both the isotopic composition of granitoids (Tang et al., 2014; Zhang et al., 2020; Wang et al., 2018; Farina and Stevens, 2011; Farina et al., 2014; Finch et al., 2021) and in zircon formed during melt crystallization (Finch et al., 2021; Zhang et al., 2024b). Whereas *in situ* studies (McLeod et al., 2012; Acosta-Vigil et al., 2012a) have empirically shown isotopic and compositional heterogeneity can occur in melt during partial melting of deep crustal rocks, the residence time of melt in these rocks remains uncertain, and samples may represent snapshots of transitional states. Therefore, it is uncertain if melt heterogeneity is retained until melt crystallization and how this impacts the composition of accessory minerals that formed during melt crystallization.

Here we address several questions that remain about disequilibrium melting. How does slow diffusion in the melt impact the concentrations of trace elements in zircon? What is the spatial extent of equilibrium for the trace elements that are key petrogenetic indicators like U, Th, Hf, Y, and HREE? We show that diffusion of these trace elements is slow enough in anatectic melt to result in significant differences in zircon composition across sub-millimetric length scales. This has important implications for the use of accessory minerals (specifically zircon) as petrogenetic indicators, and for linking trace element compositions of granitoids to their source rocks. We also demonstrate how detailed analysis of zircon can provide key insights into trace element mobility in anatectic systems.

## 3.3 Regional context and petrography

We focus on a metamonzogranite sample with abundant zircon (20SD06) that was previously analyzed in Chapter 2 to assess zircon forming reactions and understand the regional metamorphic history. The sample is from the Muskoka Domain in the Grenville Province in Ontario, Canada. The Muskoka domain first reached peak pressures of 10–11.5 kbar, followed by peak temperatures of 750–850 °C (Timmerman et al., 2002). U–Pb geochronology in a polished thin section of sample 20SD06 using laser ablation inductively-coupled plasma mass spectrometry showed that zircon contains ca. 1350 Ma igneous cores and ca. 1070 Ma metamorphic rims (Chapter 2). Metamorphic rims formed during retrogression as a result of melt crystallization and titanomagnetite breakdown during protracted cooling between ca. 1100 Ma and 1000 Ma.

This sample is composed of: alkali feldspar (∼38 vol%), plagioclase (∼30 vol%), quartz (∼20 vol%), clinopyroxene (∼4 vol%), garnet (∼3 vol%), magnetite (∼3 vol%), amphibole (∼1 vol%), and ilmenite (∼1 vol%) with minor amounts of zircon, apatite, and allanite and trace calcite, chalcopyrite, pyrite, sphalerite, (Ce, La, Nd)-oxide, and monazite. The modal abundance of zircon in this sample is anomalously high (∼0.15 vol%).

The metamonzogranite is heterogeneous at the hand sample scale. Alternating discontinuous 5–10 mm thick melanocratic bands have higher proportions of clinopyroxene, garnet, magnetite, ilmenite, amphibole, allanite, apatite, and zircon (Fig. 3.1B). Alkali feldspar, plagioclase, and quartz are predominantly xenoblastic with grain sizes ranging from 0.1 to 2 mm. Alkali feldspar is commonly perthitic and occasionally occurs as rounded, elongate porphyroblasts up to 6 mm across, with fine-grained recrystallized quartz and feldspar at the edges. Garnet, clinopyroxene, magnetite, ilmenite and zircon are distributed throughout the rock but most commonly cluster within discontinuous melanocratic bands and lenses <1 cm thick (Fig. 3.1B). Garnet porphyroblasts are hypidioblastic to xenoblastic with sizes of 0.5–5 mm and are more common in melanocratic bands. In addition to porphyroblasts, garnet also occurs as overgrowths on magnetite and ilmenite. Garnet contains inclusions of quartz, alkali feldspar, zircon, allanite, apatite, ilmenite, and magnetite. Clinopyroxene typically occurs as fine-grained (50–200 µm) clusters within the melanocratic bands and rarely as overgrowths on magnetite. Clinopyroxene also occurs outside the melanocratic bands as isolated xenoblastic 0.3–0.8 mm grains. Amphibole is only present as an overgrowth on magnetite or clinopyroxene. Magnetite is typically xenoblastic and up to 1 cm across. Magnetite and ilmenite commonly occur together: ilmenite typically occurs as <0.6 mm xenoblastic grains with at least one grain boundary with magnetite and as exsolution lamallae in magnetite that range in thickness from several µm to 0.2 mm. Micron-scale (<50 µm) gahnite and other Al-spinels are commonly located at magnetite-ilmenite grain boundaries. Discontinuous <0.1 mm overgrowths of alkali feldspar on magnetite are also present but are only observed on ∼5 grains distributed throughout the thin section.

Zircon occurs as hypidioblastic and rounded grains and are described in more detail below. Apatite typically occurs as hypidioblastic grains (20–100 µm) that are most concentrated in the melanocratic bands. Allanite occurs as small (20–50 µm) xenoblastic grains around and included in mafic minerals, or as larger (50–200 µm) more isolated grains with a hypidioblastic form. Allanite is highly fractured and has a mottled appearance with undulose extinction indicative of partial or complete recrystallization. (Ce, La, Nd)-oxides (<5 µm) are rare but do occur near the edges of allanite and along cracks and fractures in allanite. Monazite only occurs as a <5 µm layer at rare interfaces of apatite and allanite grains.

## 3.4 Analytical methods

### 3.4.1 SEM and cathodoluminescence imaging

Zircon modes, microtextures, and internal zoning in a polished thin section were determined using a combination of backscatter imaging and cathodoluminescence (CL) imaging using a Zeiss LEO 1530 scanning electron microscope (SEM) operating at 20 kV and 0.5–1 nA with an aperture size of 120 µm. A total of 168 zircons were identified and imaged. Zircon cores were visually determined in all but three zircon grains using the CL images. The cross-sectional area of zircon cores and core plus rims were measured manually with ImageJ. The grain size parameters $a_0$ and $a$ were calculated from the cross-sectional area $A_0$ and $A$ of the cores and total grains respectively with the formula $a = \sqrt{A}$ and $a_0 = \sqrt{A_0}$ (as in Miyazaki et al., 2018).

#### Trace element analysis of zircon

We analyzed the trace element compositions of selected zircons in the same thin section as for SEM and CL imaging. From the 168 identified zircons, seven were chosen for trace element analysis to compare the compositions of zircons that are both close together and far apart to observe differences in trace element compositions at multiple length scales. The closest pair of zircons are adjacent to each other (Fig. 3.1A), while the pair that are the farthest from each other are >35 mm apart (Fig. 3.1B).

Trace elements were measured using laser ablation inductively-coupled plasma mass spectrometry (LA-ICP-MS) with an Agilent 8800 QQQ-ICP-MS in sequence with an Analyte G2 193 nm Excimer laser ablation unit system in the Metal Isotope Geochemistry Laboratory at the University of Waterloo. Ablation was performed with 20 µm wide lines on top of the lines previously ablated for analysis with the MC-ICP-MS described later. The laser had a fluence of 4 $\frac{\text{J}}{\text{cm}^2}$ (measured at the sample surface) with a repetition rate of 8 Hz and was moving at 2 $\frac{\mu\text{m}}{\text{s}}$. Ablated material was moved from the laser sample chamber using He as a carrier gas (0.8 L/min) with Ar added to the aerosol (0.8 L/min). Samples were analyzed using standard–sample bracketing (reference materials run every ∼5 unknowns). NIST612 was used as the external reference material, 91500 (Wiedenbeck et al., 2004) and BCR-2G (Jochum and Stoll, 2008) were used as a secondary reference materials. $^{29}$Si + $^{90}$Zr was used as internal standard for data reduction using an assumed combined value of 65.1 wt%. We focus on four key trace elements here (Y, Yb, U, and Th), but the entire dataset and evaluation of the secondary reference materials are included in the supplemental material. Integration time of each measured mass was 0.01 s. A full list

of conditions and analyzed elements are shown in Table B.1. Measurements in each Y and Yb profile were averaged in segments such that each segment consists of 10% of the length of the profile that extends from the core–rim interface to the outer edge of the grain.

Uranium, Th, and Pb were also analyzed semi-quantitatively in the same 7 zircons using an Analyte G2 laser ablation system coupled with a NuPlasma II multicollector-inductively-coupled plasma mass spectrometry (MC-ICP-MS) with U and Th measured on Faraday detectors and Pb isotopes on ion counters. Although there is no way to account for laser induced fractionation by using an internal standard using a multi-collector array, the semi-quantitative data obtained through this approach provides a higher-resolution record of U, Th and Pb zoning across individual zircon grains. In this paper we focus on the relative U and Th concentration in zircon, but the geochronological data and its implications are discussed in greater detail in Chapter 2. Zircon was pre-ablated using 50 µm wide lines across grains from rim to rim or core to rim. Ablation was performed with 20 µm wide lines and a fluence of 4 $\frac{\mathrm{J}}{\mathrm{cm}^2}$ with a repetition rate of 8 Hz and moving at 2 $\frac{\mu\mathrm{m}}{\mathrm{s}}$. Ablated material was transported from the laser sample chamber using He as a carrier gas (0.7 L/min) with $N_2$ added to the aerosol (0.003 L/min). Samples were run using standard–sample bracketing (reference materials run every $\tilde{5}$ unknowns). The masses measured were 206, 207, 208, 232, and 238. The external standard used was 91500 (Wiedenbeck et al., 2004) with Plesovice (Sláma et al., 2008), DD85-17 (Davis et al., 2005), and DD91-1 (Davis, 2002) as secondary reference materials. Data reduction was done using Iolite (v.4) (Paton et al., 2011). Full analytical conditions—including Faraday cup and ion counter configurations—are shown in Table B.2.

A combination of the trace element data from LA-ICP-MS and LA-MC-ICP-MS was used to evaluate internal U and Th zoning in zircon grains. Considering that the multi-collector approach does not include an internal standard needed for quantitative analysis, the background-corrected counts per second for U and Th were converted into approximate (semi-quantitative) concentrations by direct comparison with the LA-ICP-MS data from laser ablation lines measured over the same regions of the zircon grains. This was done by applying a scaling factor to the MC-ICP-MS data to match it to the QQQ-ICP-MS data using U counts and concentrations, respectively. The scaling factor was calculated through linear regression between the MC-ICP-MS data and the QQQ-ICP-MS data for each transect. The resulting profiles are still semi-quantitative but better show the subtle variability in U and Th zoning across individual trends (Fig. B.1).

Data from zircon cores were differentiated from zircon rims using U concentration (from LA-ICP-MS) and CL patterns (Fig. 3.2) as well as U-Pb dates (Fig. B.1, Chapter 2). This was done based on the assumption that all metamorphic zircon grew at approximately the same Timmermann1997 but oblique cuts through zircon grains and anisotropic mineral

growth would have resulted in different rim sizes that should have similar zoning patterns at different length scales (Costa et al., 2008). The data we present is scaled horizontally so that data from the core–rim interface for each transect are aligned and the length of each zircon rim profile is comparable with one another and to minimize the impact of variable growth rates along different crystallographic axes. One exception is Zrn26, which is included in garnet and does not exhibit the same U zoning pattern as the other zircon grains. Consequently, Zrn26 was rescaled to 40% the length of the other zircon rim profiles based on the matching portion of the U zoning pattern.

### 3.4.2 Electron Probe Microanalysis

Concentrations of Si, Zr, and Hf were analyzed in 4 out of the 7 zircons using electron probe microanalysis (EPMA) with a JEOL JXA8230 5-WDS electron microprobe at the University of Toronto Department of Earth Sciences EPMA lab. Minerals were analyzed using 1 µm spot sizes with an accelerating voltage of 15 keV and current of 10 nA and acquisition times were 4 min. Spot spacing varies from 2 to 5 µm. On peak and background collection times for each element measured are presented in Table B.3. Calibration was done prior to the start of analyses on synthetic standards.

## 3.5 Results

### 3.5.1 Zircon textures

Zircon occurs as 20–600 µm hypidioblastic or rounded grains that are distributed throughout the matrix but often clusters in the millimetric-scale melanocratic domains (Fig. 3.1B). Zircon is also frequently included in garnet and magnetite. Zircon contains variable inclusion assemblages of apatite, plagioclase, alkali feldspar, quartz, biotite, pyrite, ilmenite, and rare monazite. In the CL images of zircon (Fig. 3.2), distinct cores and rims are ubiquitous in every zircon. Cores typically exhibit oscillatory zoning, but patchy zones in cores are also common. Darker or entirely homogenous cores with little or no CL response are uncommon and are likely metamict. The outer edges of most zircon cores are dark under CL, likely as a result of high U concentrations measured near the core–rim interface. Zircon core shapes vary from irregular (most common; e.g. Fig. 3.2 Zrn10, Zrn26, Zrn37, Zrn41, Zrn43) to nearly euhedral (rare; e.g. Fig. 3.2 Zrn33, Zrn40). Irregular core edges commonly truncate oscillatory zones (e.g. Fig. 3.2 Zrn10), whereas straight core edges are commonly parallel to oscillatory zones (e.g. Fig. 3.2 Zrn33).

Observed zircon rims are on average 10–20 µm thick but can be as thick as 120 µm. Typically, rims completely envelope cores, but exposed portions of zircon core, while uncommon, do occur (e.g. Fig. 3.2 Zrn40). On average, zircon rims make up $\sim$ 45% of each grain. Zircon rims are typically bright in CL with 1–5 annuli of variable brightness (Fig. 3.2). These annuli are typically sub-parallel but commonly exhibit complex patterns, particularly around more resorbed cores. Total zircon grain size, $a$, increases linearly with zircon core size, $a_0$, with a line of best fit that diverges away from $a = a_0$ at larger grain sizes with a slope of 1.07 (Fig. 3.3).

The shape and thickness of zircon rims do not correlate with proximity to different minerals, except uncommon occurrences of zircon adjacent to magnetite or ilmenite with rims that are thicker adjacent to the oxide mineral and very rarely show distinct irregular overgrowths on magnetite or ilmenite.

### 3.5.2 U and Th zoning

Uranium zoning in zircon rims (Fig. 3.4 A) show a consistent pattern across all measured grains except Zrn26, which is included in garnet. Each U pattern begins with a peak at the inner edge of the rim followed by a steep decrease in concentration, typically to a local minimum (zone Z1, Fig. 3.5). This is followed by a shallow increase up to a plateau and a short and shallow decrease in concentration away from the core to the outer edge of the zircon grain (zone Z2, Fig. 3.5). While this zoning pattern is consistent, the exact horizontal positioning and concentrations of local minima and maxima can vary between zircon grains. The highest U concentration at the core–rim interface in zone Z1 is $\sim$3.5 times higher than the lowest U concentration at the core–rim interface. This extreme difference is seen between individual grains and between different sections of the rim in the same zircon (e.g. Fig. 3.4A; Zrn43 R1 vs R2). At the local maximum in zone Z2 near the edge of the rim, U concentration is up to 4 times higher in the rim with the highest U compared to the rim with the lowest concentration. There are also several zircon rims (e.g. Fig. 3.4 A; Zrn10 R2 and Zrn33) that have similar U concentrations and zoning profiles across the entire rim.

The Th profiles of zircon rims (Fig. 3.4 B) show a greater degree of complexity than U. Analyzed zircons can be separated into four groups based on distinct patterns in the Th profiles that are not correlated to the position of the zircon in the thin section (Fig. 3.1 B). Group 1 zircons show a peak in Th concentration at the core–rim interface (Fig. 3.4 B; Zrn37, Zrn40, and Zrn41) with steeply decreasing concentration away from the core in zone Z1 in the rim (Fig. 3.5). Zone Z2 in the rim (Fig. 3.5) is a plateau or

shallowly decreasing concentration up to the edge of the rim–matrix interface. Group 2 is only Zrn43-R2 which has a peak at the core–rim interface with a steep decrease in Th concentration away from the core to a local minimum (corresponds with zone Z1 Fig. 3.5). This is followed by an increase in concentration to a local maximum followed by a shallow decrease in concentration towards the rim–matrix interface (corresponds with zone Z2 Fig. 3.5). This local maximum appears to horizontally align with plateaus in group 1.

Group 3 zircons (Fig. 3.4 B; Zrn10-R2, Zrn26, Zrn33) have Th concentrations at the core–rim interface that are 3–6 times lower than the Th concentration at the corresponding position in group 1 and 2 zircons. These more Th depleted rims have flatter compositional profiles that show a shallow decrease in concentration away from the core–rim interface. Group 4 zircons (Fig. 3.4 B; Zrn10-R1, Zrn43-R1) also have a low Th concentration at the core–rim interface but instead increase in concentration away from the core–rim interface with a peak near the rim–matrix interface, followed by decreasing concentration toward the rim–matrix interface.

Since Th zoning is highly variable between zircons and there already exists significant variability in U profiles, it follows that a similar degree of variability can be seen in Th/U profiles (Fig. 3.4 C). The degree of variability can be quite extreme for Th/U with values ranging at the core–rim interface from <0.01 to 0.3 and a similar range at the rim–matrix interface. The Th/U profiles have similar trends of increasing away from the core–rim interface to a peak then decreasing towards the rim–matrix interface. Variability of Th/U ratios within individual metamorphic zircon rim profiles also show large value ranges with the most extreme range of ∼0.05–∼0.4.

### 3.5.3 Y and Yb zoning

Yttrium and Yb—a proxy for HREE—profiles (Fig, 3.4 D and E) are relatively noisy and show variable zoning patterns. Significant differences in Y and Yb concentration can be seen between different zircon rims, both near the core–rim interface in zone Z1 (Fig. 3.5) and near the rim–matrix interface in zone Z2 (Fig. 3.5). The difference in Y concentration can be up to 4 times higher at the core–rim interface and up to 2 times higher near the rim–matrix interface. The difference in Yb concentration is more significant; up to 6 times higher at the core–rim interface and 4-6 times higher near the rim–matrix interface.

### 3.5.4 Hf zoning

Hafnium concentration profiles (Fig. 3.4 F) are also relatively noisy, but display clear differences in concentration near the core–rim interface in zone Z1 (Fig. 3.5) and near the rim–matrix interface in zone Z2 (Fig. 3.5). At the core–rim interface, there is a contrast in Hf concentration and profile shape of Zrn26 and the others, with a ∼0.35 wt% difference between Zrn26 and the other zircon rims. At the rim–matrix interface, the distribution pattern and concentration of Hf in Zrn37 is distinct from Zrn41 and Zrn43, which are adjacent to each other (Fig. 3.1A). Zrn37 shows a decreasing concentration of Hf towards the rim while Zrn41 and Zrn43 both show increasing concentrations, amounting to a difference of ∼0.25 wt% between Zrn37 and Zrn43 on the outermost edge of the rim.

## 3.6 Discussion

### 3.6.1 Zircon growth mechanisms

In the analysis of zircon and its relationship to diffusion of elements in melt and matrix, Zr is perhaps the most important element to understand. While Zr is a trace element in this rock and has tracer diffusivity in rhyolitic melt that is comparable to U and Hf and slower than Y and REE (Zhang and Gan, 2022), Zr is an essential structural constituent of zircon and the rate of Zr diffusion relative to zircon interface reactions will significantly impact how zircon grows. If the rate of diffusion of Zr is slow compared to interface reactions, it will strongly influence the rate and location of new zircon growth (Diffusion-controlled growth). If, instead, diffusion rates of Zr are fast compared to zircon interface reactions, then the rate and location of new zircon growth will be controlled by those interface reactions (Interface-controlled growth).

Since there are no other significant major components that substitute for Zr in zircon grains in this sample, we cannot use Zr concentration in zircon to assess whether its growth is diffusion-controlled or interface-controlled as is done with other minerals such as garnet (e.g. George and Gaidies, 2017). However, since we have original zircon size prior to metamorphism we can compare relative size changes of zircon grains to assess whether zircon growth is interface-controlled or diffusion-controlled (following Miyazaki et al., 2018). If zircon growth is diffusion-controlled, we expect that zircon grains with a smaller original size (lower $a_0$) to have a higher growth rate than larger grains, and for the $a_0$ vs $a$ plot to diverge from $a = a_0$ (Fig. 3.3 inset), or for the slope of the best-fit line to be less than one. If zircon growth is interface-controlled, we expect that zircon grains all grow at the same

rate regardless of the original size and for the best-fit line in the $a_0$ vs $a$ plot to be parallel to $a = a_0$ (Fig. 3.3 inset). The resulting best-fit line has a slope of 1.07, indicating that zircon grains with a larger original size (higher $a_0$) actually had a higher growth rate than smaller grains. This is not a scenario anticipated by Miyazaki et al. (2018), however it is indicative of size-dependent interface controlled growth, which has been suggested to occur in garnets during prograde Barrovian metamorphism (Gaidies and George, 2021; Yogi et al., 2025).

Gaidies and George (2021) suggested that size-dependent interface-controlled growth of garnet implies a small chemical driving force for garnet growth, which is expected in garnet grown close to equilibrium. If this same principle can be extended to zircon growth, then zircon grown during melt-crystallization will have a composition representative of equilibrium with local melt. Differences in trace element concentration between zircon grains grown at the same time during melt crystallization (i.e. zone Z1 zircon Fig. 3.5) can therefore be attributed to heterogeneity of melt composition in the sample. In this context, zircon is used in this study as a proxy for melt composition. While zircon growth in this sample occurred during cooling and subsolidus zircon growth did occur (Chapter 2), zircon grew first from melt crystallization, and so we assume that the concentration of trace elements in zircon at the core–rim interface (Zone Z1, Fig. 3.5) are representative of this first stage of zircon growth.

### 3.6.2 Trace element mobility

### 3.6.3 Analytical smoothing of profiles

In the interpretation of elements analyzed using LA-ICP-MS, it is important to note the relative thickness of most zircon rims compared to the size of the laser spot size. Since the profiles of U, Th, Y, and Yb are produced by a continuously moving laser line with a spot size of 20 µm, the resulting profiles are effectively moving averages with a 20 µm sampling window. This will result in an artificial smoothing of trace element profiles, particularly because zircon rims are thin and discrete chemical changes will represent proportionally small portions of the profile. For example, zircon zone Z1 in Zrn37 is only slightly larger than the spot size itself (Fig. 3.5 A). This smoothing is exacerbated by variations in zoning at depth that are incorporated by the depth of ablation, as well as averaging due to laser lines that are oblique to compositional gradients, which are apparent when laser line paths are overlain the CL images (Fig. 3.2). As a result of this analytical smoothing, U, Th, Y, and Yb profiles cannot be considered representative of chemical gradients within zircon grains, hence we focus our discussion on relative comparisons of local minima and maxima.

### Uranium

Zircon growth was interpreted to have occurred in this sample during cooling as a result of both melt crystallization and subsolidus titanomagnetite breakdown (Chapter 2). The consistency and alignment of the U zoning pattern (Fig. 3.4 A) in zircon rims across the thin section and their significant differences in concentration suggests that all analyzed zircons except Zrn26 experienced the same approximate growth history in which U came from the same phases breaking down from the same reactions occurring throughout sample, but U was not diffusing quickly enough to establish equilibrium across the sample and melt composition was heterogeneous. This implies that zircon growth did not occur in pulses within transient melt pockets that migrate through the sample, but rather during a continuous process of melt crystallization that occurred throughout the sample simultaneously.

The initial U peak (∼100–350 $\frac{\mu g}{g}$) followed by a steep decrease in U concentration (Zone Z1 Fig. 3.5) may be caused by Rayleigh fractionation during zircon crystallization from melt (e.g. Zhong et al., 2021). The increase in U concentration to the second peak (∼20–90 $\frac{\mu g}{g}$; zone Z2 Fig. 3.5) is likely a result of the breakdown of a U-bearing phase during zircon growth. This could have been a result of recrystallization, re-equilibration, or partial breakdown of allanite or apatite (e.g. to monazite or a (Ce,La,Nd)-oxide), both minerals that are still present in the rock, or complete breakdown of another U-bearing phase like monazite. These phases are generally expected to grow during melt crystallization (Kelsey et al., 2008; Yakymchuk, 2017) so it is likely their breakdown occurred at subsolidus conditions. In addition, the zircon included in garnet (Zrn26) does not exhibit zone Z2 in its rim, suggesting that it was trapped prior to the breakdown of the U source mineral. Phase equilibrium modelling of this sample suggests that garnet growth occurred below the solidus during cooling (Chapter 2), so it is most likely that zone Z2 (Fig. 3.5) zircon growth was subsolidus. The variance in horizontal positioning of peaks and troughs in the U profiles (Fig. 3.4 A) can in part be attributed to imprecise differentiation between zircon cores and rims as a result of signal mixing during ablation along a line.

### Thorium

Like U, Th concentrations in zircon at the core–rim interface are up to six times higher in the zircon with the highest concentration Th compared to the zircon with the lowest concentration (Fig. 3.4 B). This variability in Th concentration and zoning in zircon rims throughout this sample can only be explained as a result of limited Th diffusion.

The differences in Th concentration at the core–rim interface in zone Z1 (Fig. 3.5)—the segment of zircon expected to have grown in the presence of melt—suggest that Th was

heterogeneously distributed and slow diffusing in the melt during melt crystallization. These differences in Th zoning between zircon grains could be attributed to lower compatibility in zircon than in the other relatively Th-rich accessory minerals. For example, if apatite and allanite were growing at the same time as zircon during melt crystallization, zircon grains with more apatite and allanite nearby would have more competition for diffusion-limited Th, resulting in more Th-depleted zircon similar to how monazite has been suggested to reduce Th concentration in co-crystallizing zircon (Yakymchuk et al., 2018). Later in the metamorphic history, breakdown, recrystallization, or re-equilibration of these more Th enriched apatite or allanite grains could have contributed to the increase in Th concentration observed in the group 2 and group 4 zircons in zone Z2, near the rim–matrix interface (Fig. 3.4 B). Regardless of the cause of the different zoning patterns and concentrations of Th, it is clear that concentrations of Th in zircon are decoupled from U between grains and between rim segments from different parts of individual zircon grains that likely grew at the same time. This is further supported by the Th/U ratios (Fig. 3.4 C), which show significant variance in zoning pattern and ratio values across zircon grains. Decoupled Th and U concentrations is likely a result of Th and U having different sources and sinks throughout the growth history of zircon. This decoupling of Th and U and the resulting discrepancy of Th/U ratios between individual zircons might be the culprit of highly variable Th/U ratios observed in other studies of metamorphic zircon (e.g. Möller et al., 2003; Kunz et al., 2018). Many segments of these Th/U profiles on most zircon grains are over 0.1, the often quoted number used to differentiate between igneous and metamorphic zircon (e.g. Kelly and Harley, 2005; Rubatto, 2017), further corroborating the interpretation of Yakymchuk et al. (2018) that Th/U ratios may not be an effective differentiator for igneous and metamorphic zircon.

### Y and HREE

While there is less spatial resolution on the Y (Fig. 3.4 D) and HREE (Fig. 3.4 E) profiles, the variance in concentration of these elements is still apparent at multiple different segments of the profile including the core–rim interface in zone Z1 (Fig. 3.5) where the concentration of Y in the zircon with the highest Y is four times higher than the zircon with the lowest Y and concentration of Yb in the zircon with the highest Yb is six times higher than the zircon with the lowest Yb. At the core–rim interface (Zone Z1 Fig. 3.5), where we expect zircon grew as a result of melt crystallization, these large compositional differences indicate that concentrations of Y and the REE in zircon are limited by diffusion. The potential sources and sinks for Y and HREE in this sample are varied, so it is challenging to distinguish how the distribution of other phases may have influenced the Y and HREE

profiles of zircon.

#### Hafnium

With more limited spatial resolution, fewer analyzed zircons, and high degree of fluctuations in the compositional profiles, variations in Hf concentration and zoning (Fig. 3.4 F) are not as clear. The profile of Zrn26 is unique with a higher Hf concentration in zone Z1 (Fig. 3.5) at the core–rim interface (∼1.45 wt% vs ∼1.20 wt% in others) with a steep decrease towards the rim to the lowest Hf concentration measured in metamorphic zircon rims in this sample (∼0.95 wt%). As with the other trace elements, these differences in Hf concentration indicate Hf concentration in melt is heterogeneous and diffusion is slow. However, the profiles of Zrn37, Zrn41, and Zrn43 (Fig. 3.4 F) are similar, and these grains are no more than a couple mm apart from each other (Fig. 3.1 B) compared to Zrn26 which is over 20 mm away and in a separate melanocratic domain. This suggests that Hf may have a larger equilibration volume in melt than other trace elements. Besides melt, zircon is the primary reservoir of Hf and so Hf heterogeneity in melt is likely linked to the distribution and dissolution of zircon during melting. In addition, there would likely be no other phases competing for Hf during zircon growth and influencing local concentrations of Hf.

### 3.6.4 Diffusion limited trace elements in zircon

Compositional profiles (Fig. 3.4) in zircon suggest Concentrations of U, Th, Y, HREE, and Hf in metamorphic zircon in these samples are limited by diffusion and heterogeneous distribution of these trace elements in melt and in the subsolidus matrix. Since large differences in trace element concentrations occur even between rims on opposite ends of the same grain, it is likely that the concentrations of trace elements in zircon are based on the availability and concentrations of these elements from reacting phases immediately adjacent to zircon. This appears to be the case for both the first stage of zircon growth (Zone Z1 Fig. 3.5) that occurred in the presence of melt (Chapter 2) and the second stage, which (Zone Z2 Fig. 3.5) which occurred partially or completely at subsolidus conditions.

It is important to consider the potential causes of heterogeneity and slow diffusion of these trace elements. It may seem reasonable to assume that since the diffusion coefficient of Zr has been measured to be similar to Hf and U, and lower than REE and Y (Zhang and Gan, 2022), that these should have similar rates of diffusion in a natural sample when zircon is growing. By this reasoning, if zircon growth is interface-controlled, then Zr diffusion is

fast relative to the cooling rate of the rock and Hf, U, REE, and Y diffusion should all be fast too. Our observations contradict this assumption and imply that Zr diffusivity is faster than Hf, U, REE, and Y diffusivity. However, rates of diffusion depend on multiple factors beyond diffusion coefficients, diffusion is driven by chemical potential gradients which arise from compositional heterogeneity as well as mineral growth and breakdown. These gradients can therefore be influenced by the growth of competing minerals that partition important trace elements more strongly than zircon. This might be an explanation for why Hf concentrations in zircon appear more consistent compared to U, Th, HREE, and Y as there appears to be no other phase to compete for Hf that was growing at the same time as zircon (Chapter 2), whereas apatite, allanite, and garnet growth may significantly influence the chemical potential gradient of U, Th, HREE, and Y. Since this occurred during cooling, and particularly during melt crystallization, this means we cannot necessarily assume that the apparent heterogeneity in melt composition inferred from zircon occurred during melt generation and that these heterogeneities may have developed as a result of crystallization of multiple phases. What can be concluded however, is that the intercrystalline diffusion of U, Th, Hf, HREE, and Y is slow during zircon growth—including in the presence of melt—and not representative of thin-section scale equilibrium. This conclusion can be extended to other low-$H_2O$ granitic melt bearing rocks where zircon crystallization occurs during cooling, as kinetic processes like diffusion are most strongly controlled by melt composition and in particular by $H_2O$ content of the melt (Mungall, 2002; Watson, 1981).

### 3.6.5 Implications

Sluggish intercrystalline diffusion of U, Th, Hf, Y, and HREE in silicate melt-bearing rocks has a number of significant implications in the study of zircon. First, the high variability of Th/U values (Fig. 3.4 C) across zircon grains suggest that this may be an inadequate indicator for differentiation of metamorphic from igneous zircon. While the majority of measured Th/U in the metamorphic portion of the zircon does not exceed 0.4 (median Th/U reported for metamorphic zircon based on the database of Yakymchuk et al. (2018)), the range of Th/U values at the core–rim interfaces of <0.1–0.3 indicate that Th/U is not correlated with any meaningful extensive variable in the system. The decoupling of Th/U ratios could explain measured variability in zircon by other authors (e.g. Möller et al., 2003; Kunz et al., 2018). This certainly merits further investigation in other rock types and metamorphic grades as the data presented by Kunz et al. (2018) suggests lower variability of Th/U in metamorphic zircon formed at lower temperatures in subsolidus rocks and would imply that intercrystalline diffusion of Th and U are slower at higher temperatures in suprasolidus rocks. Experiments suggest that diffusion of Fe in fluid-bearing systems

can be higher than diffusion in melt-bearing systems at the same temperature (Watson, 1991). The same may be true for Th and U, considering their slower diffusion rates than Fe in melt (Zhang et al., 2010). Furthermore, if metamorphic zircon growth occurs primarily during retrogression (e.g. Chapter 2, Kohn et al., 2015), zircon may record similar growth temperatures in rocks with variable peak temperatures.

The second implication of these results relates to how zircon Y and HREE compositions are interpreted. Taylor et al. (2017) have observed the occurrence of a high variance of REE in metamorphic zircon of similar ages in similar rocks in long-lived granulite terranes and suggested this to be a result of sluggish diffusion and lack of melt connectivity. The sluggish diffusion of Y and HREE suggested by their high variability in metamorphic zircon in our study (Fig. 3.4 D, E) supports the interpretation proposed by Taylor et al. (2017). We suggest that future studies that utilize REE arrays (e.g. Taylor et al., 2017) or other analytical tools that utilize HREE composition of zircon (e.g. Hermann and Rubatto, 2003) should use line profiles across metamorphic zones in zircon grains as a simple and rapid way to assess whether the equilibration volume of HREE is reflected in zircon across individual samples.

There are further implications of sluggish Y and HREE diffusion for the modelling of zircon growth during metamorphism. Since models of accessory minerals in migmatites assume sample scale equilibrium (Kelsey et al., 2008), the lack of sample scale equilibrium for important trace elements like HREE and Zr can potentially result in significant divergence of models from reality (Lanari and Engi, 2017; Palin et al., 2016). Such divergence could include incorrect estimates of HREE composition of not just zircon but potentially any mineral in the system. In addition, there is the potential for a significant impact on the amount of accessory minerals grown during melt crystallization as the local equilibrium conditions will vary and affect the stability of these phases (Lanari and Engi, 2017). This is unlikely to significantly impact the amount of zircon grown as there is usually little competition for Zr in most rocks.

Heterogeneous $\varepsilon$Hf values measured in migmatitic zircon (e.g. Finch et al., 2021; Zhang et al., 2024b) are also consistent with sluggish diffusion of Hf in melt. Since zircon is the primary reservoir for Hf in most rocks, heterogeneity in Hf concentration in zircon formed during melt crystallization would most likely be a result of heterogeneity inherited from the melt which was in turn sourced from the primary zircon dissolved during melting. Garnet and apatite can also provide sources of highly radiogenic Hf (e.g. Chen et al., 2023; Zhang et al., 2023). Since Hf isotopes (e.g. $^{176}$Hf and $^{177}$Hf) are not expected to diffuse at different rates from each other in high-temperature metamorphic systems, the resulting $\varepsilon$Hf and any variability observed in $\varepsilon$Hf in zircon would be inherited and partially homogenized from the original source of Hf (Finch et al., 2021). It follows from this that variability in

Hf concentration in zircon and variability in $\varepsilon$Hf are inextricably linked. Therefore, the observed variability of Hf concentration in zircon in the sample described in this study implies variability in $\varepsilon$Hf. This is consistent with the observations of heterogeneous $\varepsilon$Hf values in zircon observed by others (e.g. Finch et al., 2021; Zhang et al., 2024b) and indicates that disequilibrium melting occurred in the sample described in this study (e.g. Acosta-Vigil et al., 2012a; Finch et al., 2021; McLeod et al., 2012). A similar argument can be made for disequilibrium melting based on the variability of U in zircon formed during melt crystallization as zircon was likely to be the dominant host of U during prograde metamorphism (Bea, 1996b). However, the influence of co-crystallizing U-bearing phases like apatite and allanite cannot be discounted. If disequilibrium melting contributes to the heterogeneity of Hf and U concentration in zircon, it will probably also influence the heterogeneity of Th, Y, and HREE as these all have similar or lower tracer diffusivity in melt (Zhang and Gan, 2022).

The broader implications of disequilibrium melting on granitoid petrogenesis and inferring tectonic processes have been discussed at length by others (Zhang et al., 2024b; Tang et al., 2014; Zhang et al., 2020; Wang et al., 2018; Farina et al., 2014; Finch et al., 2021; Acosta-Vigil et al., 2006a,b, 2012a; Farina and Stevens, 2011; McLeod et al., 2012). The results of this study further suggest that disequilibrium melting and slow rates of diffusion will impact the U, Th, Hf, Y, and HREE composition of melt and accessory minerals. This may need to be taken into account when modelling partial melting of rocks, the resulting trace element composition of those melts, and the accessory minerals formed (e.g. Kinney et al., 2024; Kelsey et al., 2008; Yakymchuk and Brown, 2014; Taylor et al., 2017). While the low diffusivity of these trace elements may limit their use as indicators of ancient tectonic processes, better constraints on their intergranular diffusivity can potentially open new avenues to understanding petrological processes and developing trace element-based thermometers. This could be accomplished by measuring and modelling local rock composition with tools like Bingo-Antidote in combination with detailed trace element maps (Lanari and Hermann, 2021; Duesterhoeft and Lanari, 2020). Such an approach could potentially be used to estimate the duration of anatexis in a migmatite or the timescales of granite crystallization using diffusion geochronometry (Chakraborty, 2008) of elements that partition strongly into zircon such as Hf or U.

## 3.7 Conclusions

Variable concentrations of U, Th, Y, Hf, and HREE in metamorphic zircon that grew at the same time in a single rock is most reasonably explained as a result of slow intergranular

diffusion of these elements. Such variance in zircon that grew during melt crystallization implies that diffusion of these elements is slow enough that melt did not homogenize during melt production. Slow diffusion of these elements in melt aligns with previous studies that posit disequilibrium melting is common in anatectic systems. While others have focused on how the process of disequilibrium melting impacts the resulting melt, we have shown that such a process can have significant influence on the trace element composition of zircon, including Th/U ratios. This provides a simple explanation for observed heterogeneity in Th/U and HREE of anatectic zircon that cannot be explained with an equilibrium model. Concentrations of trace elements in minerals and silicate melt cannot be modelled in the same way as major elements, especially in systems without free fluid. While a limited range of diffusion does restrict our ability to use traditional bulk rock modelling tools for accessory minerals, it allows the modelling accessory minerals using local rock composition and opens possible novel applications of diffusion geochronometry to understanding melting processes in metamorphic rocks.

# References


Acosta-Vigil, A., Buick, I., Cesare, B., London, D., and Morgan, G. B. (2012a). The Extent of Equilibration between Melt and Residuum during Regional Anatexis and its Implications for Differentiation of the Continental Crust: A Study of Partially Melted Metapelitic Enclaves. *Journal of Petrology*, 53(7):1319–1356.

Acosta-Vigil, A., London, D., and Morgan, G. B. (2006a). Experiments on the kinetics of partial melting of a leucogranite at 200 MPa H2O and 690–800°C: Compositional variability of melts during the onset of H2O-saturated crustal anatexis. *Contributions to Mineralogy and Petrology*, 151(5):539–557.

Acosta-Vigil, A., London, D., and Morgan, G. B. (2012b). Chemical diffusion of major components in granitic liquids: Implications for the rates of homogenization of crustal melts. *Lithos*, 153:308–323.

Acosta-Vigil, A., London, D., Morgan, G. B., Cesare, B., Buick, I., Hermann, J., and Bartoli, O. (2017). Primary crustal melt compositions: Insights into the controls, mechanisms and timing of generation from kinetics experiments and melt inclusions. *Lithos*, 286–287:454–479.

Acosta-Vigil, A., London, D., Morgan, G. B., and Dewers, T. A. (2006b). Dissolution of Quartz, Albite, and Orthoclase in H2O-Saturated Haplogranitic Melt at 800°C and 200 MPa: Diffusive Transport Properties of Granitic Melts at Crustal Anatectic Conditions. *Journal of Petrology*, 47(2):231–254.

Bea, F. (1996a). Controls on the trace element composition of crustal melts. *Earth and Environmental Science Transactions of the Royal Society of Edinburgh*, 87(1-2):33–41.

Bea, F. (1996b). Residence of REE, Y, Th and U in Granites and Crustal Protoliths; Implications for the Chemistry of Crustal Melts. *Journal of Petrology*, 37(3):521–552.

Blichert-Toft, J. and Albarède, F. (1997). The Lu-Hf isotope geochemistry of chondrites and the evolution of the mantle-crust system. *Earth and Planetary Science Letters*, 148(1-2):243–258.

Chakraborty, S. (2008). Diffusion in Solid Silicates: A Tool to Track Timescales of Processes Comes of Age. *Annual Review of Earth and Planetary Sciences*, 36(1):153–190.

Chen, L., Yakymchuk, C., Zhao, K., Zhao, Z., Li, D., Gao, P., Chen, Y., Sun, G., and Liu, Z. (2023). The garnet effect on hafnium isotope compositions of granitoids during crustal anatexis. *Geology*, 51(5):439–443.

Cioffi, C. R., Campos Neto, M. D. C., Möller, A., and Rocha, B. C. (2019). Titanite petrochronology of the southern Brasília Orogen basement: Effects of retrograde net-transfer reactions on titanite trace element compositions. *Lithos*, 344–345:393–408.

Costa, F., Dohmen, R., and Chakraborty, S. (2008). Time Scales of Magmatic Processes from Modeling the Zoning Patterns of Crystals. *Reviews in Mineralogy and Geochemistry*, 69(1):545–594.

Davidson, J., Turner, S., Handley, H., Macpherson, C., and Dosseto, A. (2007). Amphibole "sponge" in arc crust? *Geology*, 35(9):787.

Davis, D., Amelin, Y., Nowell, G., and Parrish, R. (2005). Hf isotopes in zircon from the western Superior province, Canada: Implications for Archean crustal development and evolution of the depleted mantle reservoir. *Precambrian Research*, 140(3-4):132–156.

Davis, D. W. (2002). U–Pb geochronology of Archean metasedimentary rocks in the Pontiac and Abitibi subprovinces, Quebec, constraints on timing, provenance and regional tectonics. *Precambrian Research*, 115(1-4):97–117.

Duesterhoeft, E. and Lanari, P. (2020). Iterative thermodynamic modelling—Part 1: A theoretical scoring technique and a computer program ( Bingo-Antidote). *Journal of Metamorphic Geology*, 38(5):527–551.

Eiler, J. M. (2001). Oxygen Isotope Variations of Basaltic Lavas and Upper Mantle Rocks. *Reviews in Mineralogy and Geochemistry*, 43(1):319–364.

Farina, F. and Stevens, G. (2011). Source controlled 87Sr/86Sr isotope variability in granitic magmas: The inevitable consequence of mineral-scale isotopic disequilibrium in the protolith. *Lithos*, 122(3-4):189–200.

Farina, F., Stevens, G., Gerdes, A., and Frei, D. (2014). Small-scale Hf isotopic variability in the Peninsula pluton (South Africa): The processes that control inheritance of source 176Hf/177Hf diversity in S-type granites. *Contributions to Mineralogy and Petrology*, 168(4):1065.

Finch, M., Weinberg, R., Barrote, V., and Cawood, P. (2021). Hf isotopic ratios in zircon reveal processes of anatexis and pluton construction. *Earth and Planetary Science Letters*, 576:117215.

Gaidies, F. and George, F. R. (2021). The interfacial energy penalty to crystal growth close to equilibrium. *Geology*, 49(8):988–992.

George, F. R. and Gaidies, F. (2017). Characterisation of a garnet population from the Sikkim Himalaya: Insights into the rates and mechanisms of porphyroblast crystallisation. *Contributions to Mineralogy and Petrology*, 172(7):57.

Hammouda, T., Pichavant, M., and Chaussidon, M. (1996). Isotopic equilibration during partial melting: An experimental test of the behaviour of Sr. *Earth and Planetary Science Letters*, 144(1-2):109–121.

Hanson, G. N. (1980). Rare Earth Elements in Petrogenetic Studies of Igneous Systems. *Annual Review of Earth and Planetary Sciences*, 8(1):371–406.

Harley, S. and Kelly, N. (2007). The impact of zircon–garnet REE distribution data on the interpretation of zircon U–Pb ages in complex high-grade terrains: An example from the Rauer Islands, East Antarctica. *Chemical Geology*, 241(1-2):62–87.

Hermann, J. and Rubatto, D. (2003). Relating zircon and monazite domains to garnet growth zones: Age and duration of granulite facies metamorphism in the Val Malenco lower crust. *Journal of Metamorphic Geology*, 21(9):833–852.

Jochum, K. P. and Stoll, B. (2008). Reference materials for elemental and isotopic analyses by LA-(MC)-ICP-MS: Successes and outstanding needs. *Laser ablation ICP-MS in the Earth sciences: Current practices and outstanding issues*, 40:147–168.

Johnson, T. E., Brown, M., Gardiner, N. J., Kirkland, C. L., and Smithies, R. H. (2017). Earth's first stable continents did not form by subduction. *Nature*, 543(7644):239–242.

Kelly, N. M. and Harley, S. L. (2005). An integrated microtextural and chemical approach to zircon geochronology: Refining the Archaean history of the Napier Complex, east Antarctica. *Contributions to Mineralogy and Petrology*, 149(1):57–84.

Kelsey, D. E., Clark, C., and Hand, M. (2008). Thermobarometric modelling of zircon and monazite growth in melt-bearing systems: Examples using model metapelitic and metapsammitic granulites. *Journal of Metamorphic Geology*, 26(2):199–212.

Kendrick, J., Duguet, M., and Yakymchuk, C. (2022). Diversification of Archean tonalite-trondhjemite-granodiorite suites in a mushy middle crust. *Geology*, 50(1):76–80.

Kinney, C., Kendrick, J., Duguet, M., and Yakymchuk, C. (2024). Redistribution of heat-producing elements during melting of Archean crust. *Journal of Metamorphic Geology*, 42(2):197–224.

Kirkland, C., Yakymchuk, C., Gardiner, N., Szilas, K., Hollis, J., Olierook, H., and Steenfelt, A. (2020). Titanite petrochronology linked to phase equilibrium modelling constrains tectono-thermal events in the Akia Terrane, West Greenland. *Chemical Geology*, 536:119467.

Kohn, M. J., Corrie, S. L., and Markley, C. (2015). The fall and rise of metamorphic zircon. *American Mineralogist*, 100(4):897–908.

Krneta, S., Ciobanu, C., Cook, N., and Ehrig, K. (2018). Numerical Modeling of REE Fractionation Patterns in Fluorapatite from the Olympic Dam Deposit (South Australia). *Minerals*, 8(8):342.

Kunz, B. E., Regis, D., and Engi, M. (2018). Zircon ages in granulite facies rocks: Decoupling from geochemistry above 850 °C? *Contributions to Mineralogy and Petrology*, 173(3):26.

Lanari, P. and Engi, M. (2017). Local Bulk Composition Effects on Metamorphic Mineral Assemblages. *Reviews in Mineralogy and Geochemistry*, 83(1):55–102.

Lanari, P. and Hermann, J. (2021). Iterative thermodynamic modelling—Part 2: Tracing equilibrium relationships between minerals in metamorphic rocks. *Journal of Metamorphic Geology*, 39(6):651–674.

Laurent, O., Björnsen, J., Wotzlaw, J.-F., Bretscher, S., Pimenta Silva, M., Moyen, J.-F., Ulmer, P., and Bachmann, O. (2020). Earth's earliest granitoids are crystal-rich magma reservoirs tapped by silicic eruptions. *Nature Geoscience*, 13(2):163–169.

McCulloch, M. and Gamble, J. (1991). Geochemical and geodynamical constraints on subduction zone magmatism. *Earth and Planetary Science Letters*, 102(3-4):358–374.

McLeod, C. L., Davidson, J. P., Nowell, G. M., and De Silva, S. L. (2012). Disequilibrium melting during crustal anatexis and implications for modeling open magmatic systems. *Geology*, 40(5):435–438.

Miyazaki, K., Mori, Y., Nishiyama, T., Suga, K., and Shigeno, M. (2018). Determination of reaction kinetics using grain size: An application for metamorphic zircon growth. *Terra Nova*, 30(2):162–168.

Möller, A., O'Brien, P. J., Kennedy, A., and Kröner, A. (2003). Linking growth episodes of zircon and metamorphic textures to zircon chemistry: An example from the ultrahigh-temperature granulites of Rogaland (SW Norway). *Geological Society, London, Special Publications*, 220(1):65–81.

Mulder, J. A., Nebel, O., Gardiner, N. J., Cawood, P. A., Wainwright, A. N., and Ivanic, T. J. (2021). Crustal rejuvenation stabilised Earth's first cratons. *Nature Communications*, 12(1):3535.

Mungall, J. E. (2002). Empirical models relating viscosity and tracer diffusion in magmatic silicate melts. *Geochimica et Cosmochimica Acta*, 66(1):125–143.

Palin, R. M., Weller, O. M., Waters, D. J., and Dyck, B. (2016). Quantifying geological uncertainty in metamorphic phase equilibria modelling; a Monte Carlo assessment and implications for tectonic interpretations. *Geoscience Frontiers*, 7(4):591–607.

Paton, C., Hellstrom, J., Paul, B., Woodhead, J., and Hergt, J. (2011). Iolite: Freeware for the visualisation and processing of mass spectrometric data. *Journal of Analytical Atomic Spectrometry*, 26(12):2508.

Powell, R. and Holland, T. J. B. (2008). On thermobarometry. *Journal of Metamorphic Geology*, 26(2):155–179.

Roberts, N. M. W., Yakymchuk, C., Spencer, C. J., Keller, C. B., and Tapster, S. R. (2024). Revisiting the discrimination and distribution of S-type granites from zircon trace element composition. *Earth and Planetary Science Letters*, 633:118638.

Rubatto, D. (2017). Zircon: The Metamorphic Mineral. *Reviews in Mineralogy and Geochemistry*, 83(1):261–295.

Sláma, J., Košler, J., Condon, D. J., Crowley, J. L., Gerdes, A., Hanchar, J. M., Horstwood, M. S., Morris, G. A., Nasdala, L., Norberg, N., Schaltegger, U., Schoene, B., Tubrett, M. N., and Whitehouse, M. J. (2008). Plešovice zircon — A new natural reference material for U–Pb and Hf isotopic microanalysis. *Chemical Geology*, 249(1-2):1–35.

Sláma, J., Košler, J., and Pedersen, R. B. (2007). Behaviour of zircon in high-grade metamorphic rocks: Evidence from Hf isotopes, trace elements and textural studies. *Contributions to Mineralogy and Petrology*, 154(3):335–356.

Smit, M. A. and Kooijman, E. (2024). A common precursor for global hotspot lavas. *Nature Geoscience*, 17(10):1053–1058.

Spear, F. S. (2010). Monazite–allanite phase relations in metapelites. *Chemical Geology*, 279(1-2):55–62.

Tang, M., Wang, X.-L., Shu, X.-J., Wang, D., Yang, T., and Gopon, P. (2014). Hafnium isotopic heterogeneity in zircons from granitic rocks: Geochemical evaluation and modeling of "zircon effect" in crustal anatexis. *Earth and Planetary Science Letters*, 389:188–199.

Taylor, R. J. M., Clark, C., Harley, S. L., Kylander-Clark, A. R. C., Hacker, B. R., and Kinny, P. D. (2017). Interpreting granulite facies events through rare earth element partitioning arrays. *Journal of Metamorphic Geology*, 35(7):759–775.

Timmerman, H., Jamieson, R. A., Parrish, R. R., and Culshaw, N. G. (2002). Coeval migmatites and granulites, Muskoka domain, southwestern Grenville Province, Ontario. *Canadian Journal of Earth Sciences*, 39:239–258.

Wang, D., Wang, X.-L., Cai, Y., Goldstein, S. L., and Yang, T. (2018). Do Hf isotopes in magmatic zircons represent those of their host rocks? *Journal of Asian Earth Sciences*, 154:202–212.

Watson, E. B. (1981). Diffusion in magmas at depth in the Earth: The effects of pressure and dissolved H2O. *Earth and Planetary Science Letters*, 52(2):291–301.

Watson, E. B. (1991). Diffusion in fluid-bearing and slightly-melted rocks: Experimental and numerical approaches illustrated by iron transport in dunite. *Contributions to Mineralogy and Petrology*, 107(4):417–434.

White, R. W. and Powell, R. (2002). Melt loss and the preservation of granulite facies mineral assemblages. *Journal of Metamorphic Geology*, 20(7):621–632.

Wiedenbeck, M., Hanchar, J. M., Peck, W. H., Sylvester, P., Valley, J., Whitehouse, M., Kronz, A., Morishita, Y., Nasdala, L., Fiebig, J., Franchi, I., Girard, J.-P., Greenwood, R., Hinton, R., Kita, N., Mason, P., Norman, M., Ogasawara, M., Piccoli, P., Rhede, D., Satoh, H., Schulz-Dobrick, B., Skår, O., Spicuzza, Mj., Terada, K., Tindle, A., Togashi, S., Vennemann, T., Xie, Q., and Zheng, Y.-F. (2004). Further Characterisation of the 91500 Zircon Crystal. *Geostandards and Geoanalytical Research*, 28(1):9–39.

Yakymchuk, C. (2017). Behaviour of apatite during partial melting of metapelites and consequences for prograde suprasolidus monazite growth. *Lithos*, 274–275:412–426.

Yakymchuk, C. (2023). Prograde zircon growth in migmatites. *Journal of Metamorphic Geology*, 41(5):719–743.

Yakymchuk, C. and Brown, M. (2014). Behaviour of zircon and monazite during crustal melting. *Journal of the Geological Society*, 171(4):465–479.

Yakymchuk, C., Kirkland, C. L., and Clark, C. (2018). Th/U ratios in metamorphic zircon. *Journal of Metamorphic Geology*, 36(6):715–737.

Yogi, M. T. A. G., Gaidies, F., Heldwein, O. K. A., and Rice, A. H. N. (2025). The Distribution of Major and Trace Elements Across a Garnet Population From the Kalak Nappe Complex (Finnmark, Scandinavian Caledonides): Evidence for Size-Dependent Growth and Compositional Equilibration in the Garnet Zone. *Journal of Metamorphic Geology*, page jmg.12820.

Zhang, C., Chen, T.-W., and Vervoort, J. D. (2023). An optimized chromatography method and MC-ICP-MS technique for apatite Lu–Hf geochronology. *Journal of Analytical Atomic Spectrometry*, 38(12):2636–2647.

Zhang, C., Liu, D., Zhang, X., Spencer, C., Tang, M., Zeng, J., Jiang, S., Jolivet, M., and Kong, X. (2020). Hafnium isotopic disequilibrium during sediment melting and assimilations. *Geochemical Perspectives Letters*, pages 34–39.

Zhang, J.-B., Liu, Y.-S., Foley, S. F., Moynier, F., Zhao, L., Xu, R., and Wang, C.-Y. (2024a). Widespread two-layered melt structure in the asthenosphere. *Nature Geoscience*, 17(5):472–477.

Zhang, Y. and Gan, T. (2022). Diffusion in Melts and Magmas. *Reviews in Mineralogy and Geochemistry*, 87(1):283–337.

Zhang, Y., Guo, L., Zhang, W., Zhang, H., and Luo, T. (2024b). Zircon Zr Hf isotope disequilibrium during crustal anatexis: A record from the Mesozoic migmatite in the eastern Gangdese arc, South Tibet. *Chemical Geology*, 659:122144.

Zhang, Y., Ni, H., and Chen, Y. (2010). Diffusion Data in Silicate Melts. *Reviews in Mineralogy and Geochemistry*, 72(1):311–408.

Zhong, S., Li, S., Seltmann, R., Lai, Z., and Zhou, J. (2021). The influence of fractionation of REE-enriched minerals on the zircon partition coefficients. *Geoscience Frontiers*, 12(3):101094.

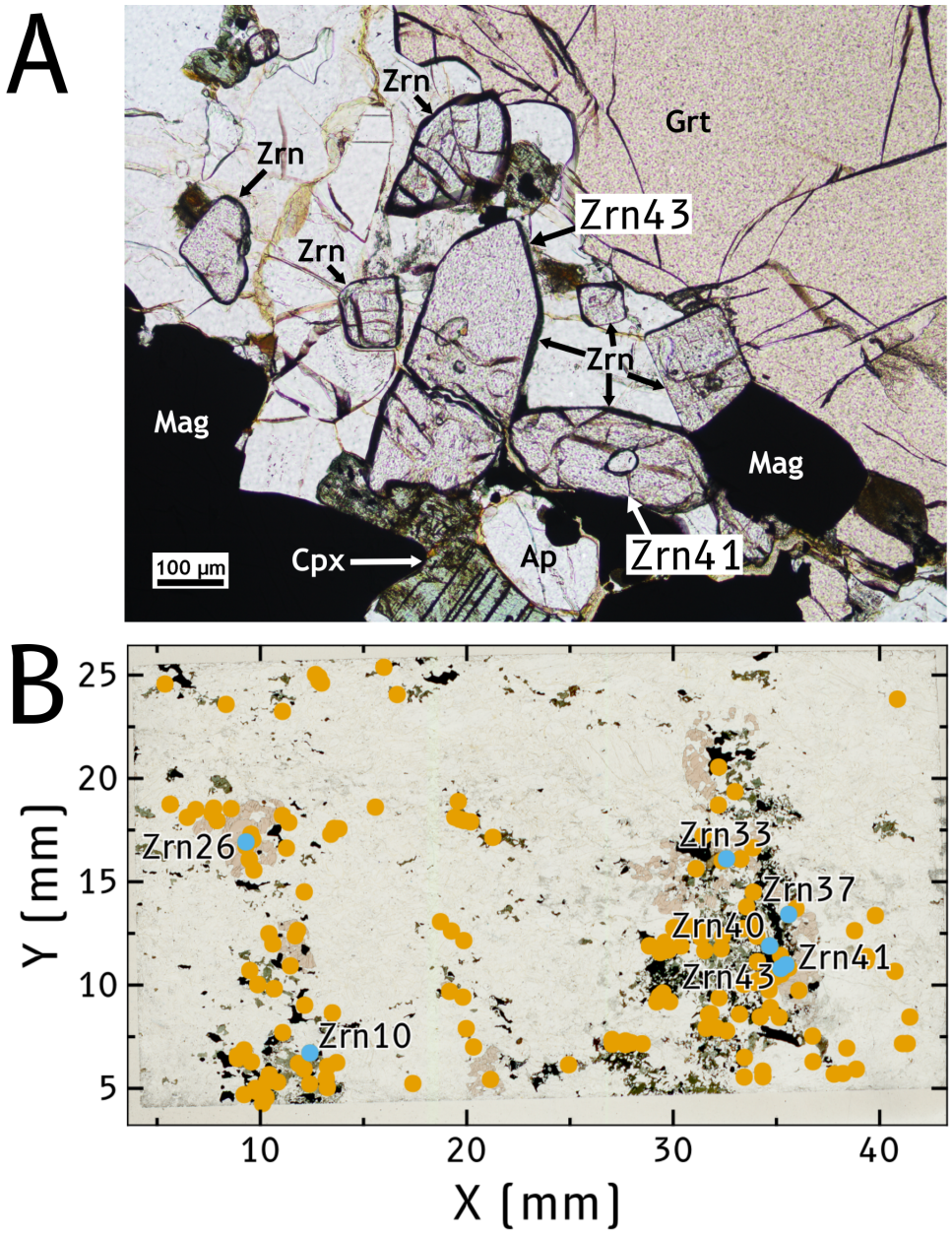


**Figure 3.1:** **A**: Photomicrograph of zircon cluster in thin section including Zrn41 and Zrn43. **B**: Plot of positions of all the zircons in a single thin section with the analyzed zircons highlighted and labelled. Overlain on scan of the thin section emphasizing the clustering of zircon in melanocratic regions.

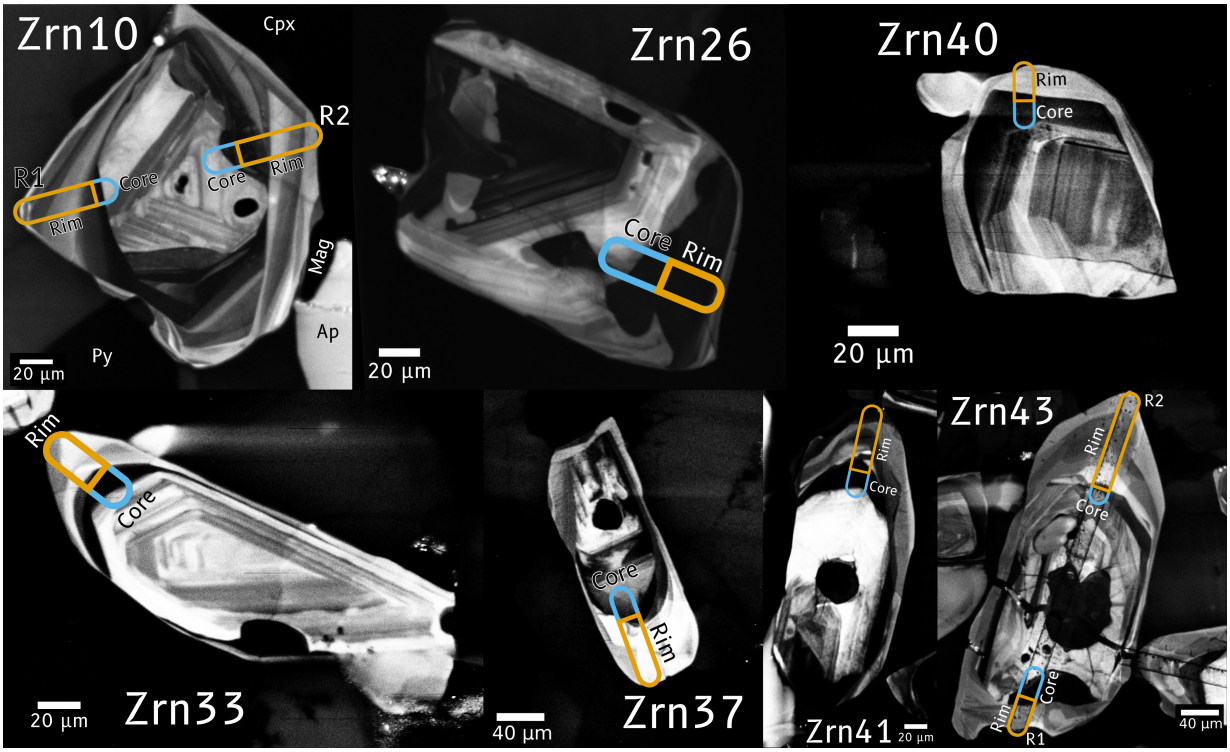


**Figure 3.2:** Cathodoluminescence images of select zircons in thin section. Coloured polygons indicate the extent of LA-ICP-MS analyses shown in Figure 3.4. Microprobe profile lines are close or parallel to LA-ICP-MS lines and shown in Fig. B.2

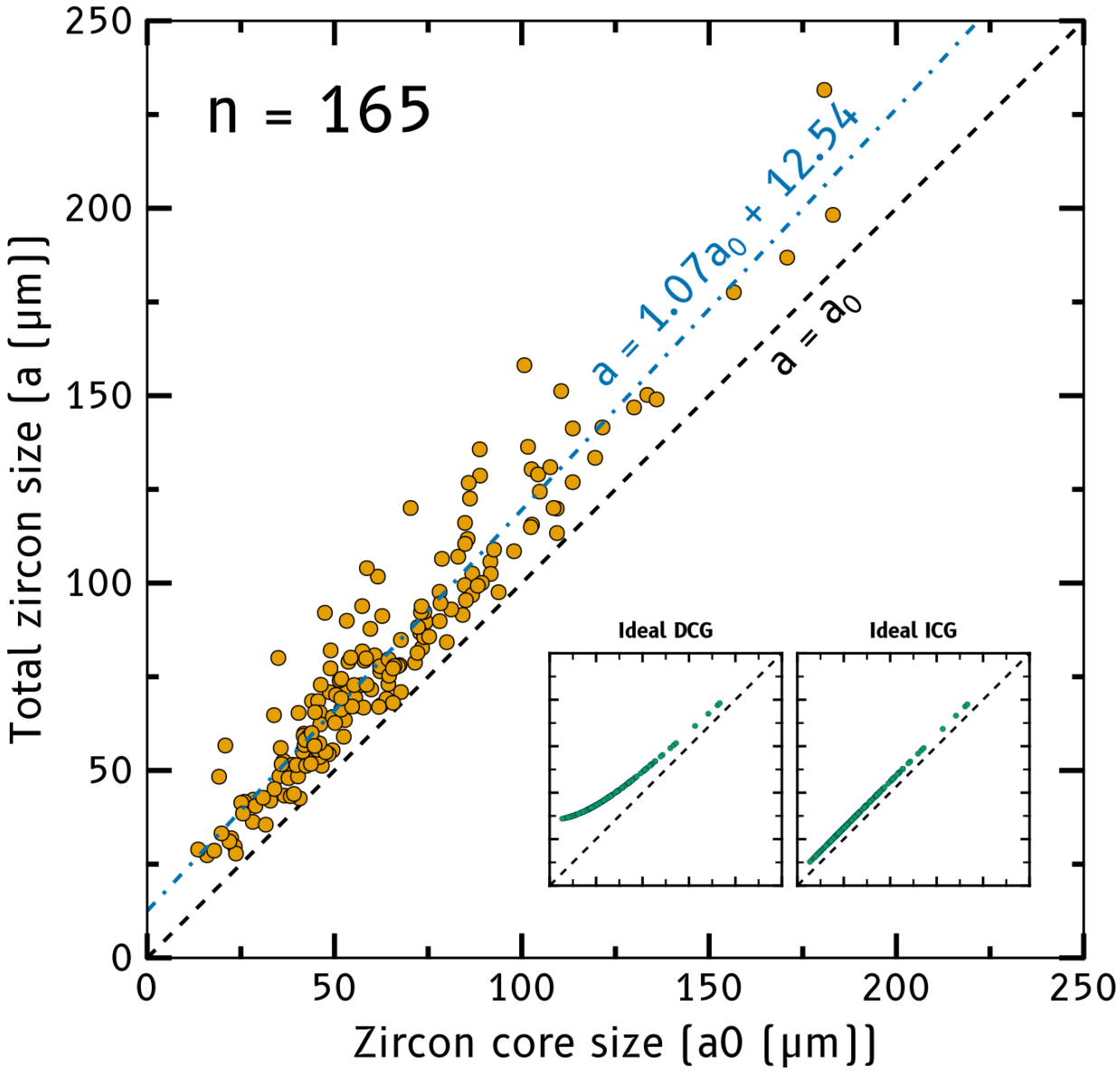


**Figure 3.3:** Grain size plots of zircon cores ($a_0$) vs total zircon grain size ($a$). Best-fit line shown as green dashed line with equation of $a = 1.07a_0 + 12.54$. Insets show the total zircon grain sized ($a$) in ideal diffusion-controlled growth (DCG) and interface-controlled growth (ICG) scenarios described by Miyazaki et al. (2018). Axes and zircon core sizes ($a_0$) of insets are identical to the main figure.

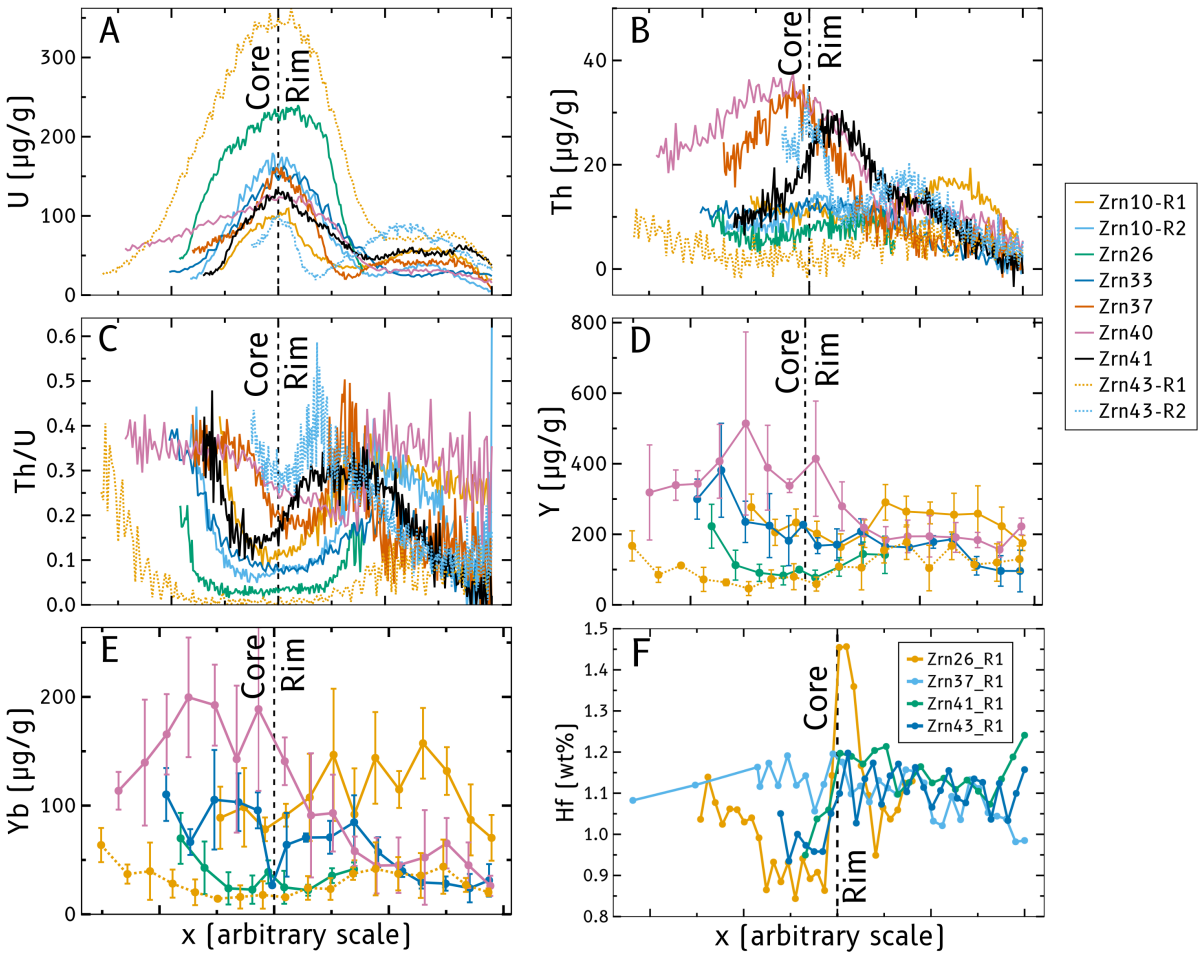


**Figure 3.4:** U **(A)**, Th **(B)**, Th/U **(C)**, Y **(D)**, Th/U **(E)**, and Hf **(F)** profiles of select zircons. Spatial extent of all profiles except Hf are indicated in Figure 3.2. Dashed lines indicate core/rim interface. Points on Y and Yb profiles are average concentration and $1\sigma$ of multiple measurements in an interval. Intervals have 10% of the measurements between the core-rim interface and rim edge. Some analyses are left out of Y and Yb profiles for clarity and can be found in Fig. B.3.

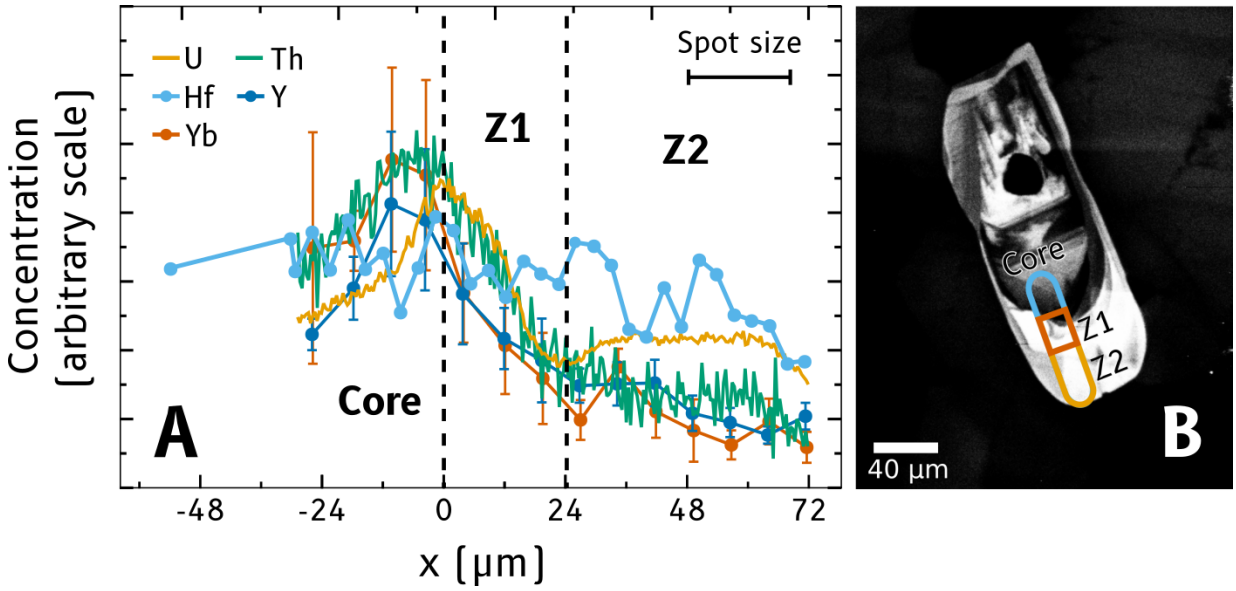


**Figure 3.5:** **A**: Overlay of each key trace element in Zrn37 showing where the two distinct zones (Z1 and Z2) observed in the trace element profile are demarcated in this grain **B**: The cathodoluminescence image of Zrn37 with the extent of the LA-ICP-MS lines indicated with coloured polygons and labelled according to their corresponding zones. The microprobe line for this zircon is along the same path as the LA-ICP-MS line (Fig. B.2)

# Chapter 4

# Regionally extensive $H_2O$-fluxed melting in the Grenville Province

## 4.1 Summary

The Muskoka domain in the Grenville Province contains abundant migmatites that formed via $H_2O$-fluxed partial melting, yet its is unclear if the $H_2O$ is coming from within the orogen (i.e. lower in the crust) or external to the orogen (e.g. the mantle). Pegmatites that intruded these migmatites while they were still partially molten crystallized at ca. 1070–1030 Ma. The migmatites have leucosome-rich reaction selvages adjacent to pegmatites, which suggests a genetic link between pegmatite intrusion and $H_2O$ transport and $H_2O$-fluxed melting. We present petrographic and geochemical evidence as well as thermodynamic models that support the interpretation that these locally preserved reaction selvages represent less-deformed equivalents of migmatites across the Muskoka domain. We then use a two-stage partial melting and chemical-potential equilibration model to show that reaction selvages and the migmatites in the region developed through diffusive $H_2O$-fluxed melting via hydrous silicate melt generated from hydrate-breakdown melting at greater depth. The results of these models are used to justify a simple tectonic model of one unit thrusted over another unit that is undergoing hydrate-breakdown melting with the resulting melt transporting $H_2O$ into the overriding slab. This generic tectonic model can explain regional-scale $H_2O$-fluxed melting without the input of fluids external to the orogen and can be applied to a variety of tectonic environments. With this model, we provide a possible explanation for the $H_2O$-fluxed melting seen in many regions across the globe.

## 4.2 Introduction

The role of regional scale fluid-fluxed melting in orogenic systems is contentious. There are limited amounts of free fluid in lower crustal rocks (Brown, 2013; Clemens and Vielzeuf, 1987; Clemens, 2006), yet there is an abundance of rocks with petrographic evidence for fluid-fluxed melting (Weinberg and Hasalová, 2015). Significant volumes of melt generated by the addition of $H_2O$ has been proposed for a range of tectonic environments, in rocks of various ages, and at temperatures ranging from the wet granite solidus up to $\sim$ 800 °C (e.g. Slagstad et al., 2005; Holk and Taylor, 2000; Sawyer, 2010; Le Fort et al., 1987; Berger et al., 2008; Yardley and Barber, 1991; Collins et al., 1989). While there are different conceptual models for $H_2O$ infiltration into deep crustal rocks (e.g. via shear zones), there are very few tectonic frameworks that incorporate regionally extensive fluid-fluxed melting in the deep crust. The primary challenge for any explanatory model of regional-scale fluid-present melting lies in the limited availability of free hydrous fluid due to the low permeability of the deep crust and its progressive loss through subsolidus dehydration reactions during burial prior to reaching the deep crust (Yardley and Valley, 1997). The limited availability of free fluids is often circumvented by suggesting that fluids are coming from the mantle (e.g. Xia et al., 2025; Volante et al., 2025; Errázuriz-Henao et al., 2024; Vanardois et al., 2024), but many localities do not show evidence of the ingress of mantle fluids.

Hydrous silicate melts—as opposed to hydrous fluids—are an alternative medium for $H_2O$ transport through the crust that may permeate more easily through the deep crust through a variety of transport mechanisms, including diking and porosity propogation through a ductile medium (Brown, 2004, 2007; Plunder et al., 2022). There are many localities with evidence of silicate magmas that released free hydrous fluids during crystallization that induced melting in adjacent rocks (e.g. Holk and Taylor, 2000; Yardley and Barber, 1991; Collins et al., 1989). It is typically assumed that intruding hydrous magmas lose $H_2O$ to the country rock during exsolution upon ascent (e.g. Glazner, 2019), however $H_2O$ may be transferred into relatively dry host rocks by diffusion when chemical potential gradients are equialized between intruding $H_2O$-rich magma and $H_2O$-poor due to the equalization of chemical potential gradients between silicate melt and wall rock (Tafur and Diener, 2020). Diffusive $H_2O$-fluxed melting permits scenarios—such as lower crustal melting—that are unlikely with free fluids or even exsolution of fluids from crystallizing hydrous melt. While it is possible for hydrous silicate melt to release water while rising through the crust via adiabatic ascent (Glazner, 2019) or upon isobaric cooling (Annen and Burgisser, 2021), it still needs to reach its water-present solidus for free hydrous fluid to be liberated, which is typically at relatively low temperatures (ca. 650 °C) in the middle to lower crust (Johannes and Holtz, 1996; Tuttle and Bowen, 1958). By contrast, diffusive $H_2O$-fluxed melting can

potentially occur anywhere a hydrous silicate melt is in contact with a rock with low $\mu_{H_2O}$ (i.e. low proportions of hydrous minerals within the host).

Although diffusive $H_2O$-fluxed melting may be feasible under several common scenarios (Tafur and Diener, 2020), it has not yet been tested or applied to areas interpreted to record regional-scale fluid-present partial melting. Here, we evaluate the applicability of diffusive $H_2O$-fluxed melting in the Muskoka domain in the Grenville Province where extensive $H_2O$-fluxed melting has been proposed (Slagstad et al., 2005). We demonstrate that diffusive $H_2O$-fluxed melting is the most reasonable cause for the extensive, protracted, regional melting that has been observed throughout the Muskoka domain. Our petrological model for $H_2O$-fluxed melting is then integrated into the regional tectonic framework that considers both long-term duration and large regional extent of $H_2O$-fluxed melting during Grenvillian orogenesis.

## 4.3 Geological setting

### 4.3.1 Grenville Province

The Grenville Province is the remnant of the ca 1.1–1.0 Ga Grenville orogeny that is contiguously exposed from Lake Huron in Ontario to the eastern coast of Labrador (e.g. Rivers et al., 2012). The Grenville Province is composed of multiple tectonic belts and terranes with distinct tectonometamorphic histories (Fig. 4.1 A). The Central Gneiss Belt is a tectonic belt that dominates the Ontario extent of the Grenville Province extending from the Composite Arc Boundary thrust zone in the southeast to the Grenville Front Tectonic Zone in the northwest (Fig. 4.1 B). The Central Gneiss Belt is divided by the allochthon boundary thrust into the parautochthonous belt and allochthonous belt. The dominant metamorphic signature in the Central Gneiss Belt is Grenvillian (*sensu stricto*) in age (ca. 1.1–1.0 Ga), with the allochthonous belt metamorphosed only during the Ottawan phase (ca. 1090–1020 Ma) and the parautochthonous belt overprinted by the Rigolet phase (ca. 1005–980 Ma) (Rivers, 2008; Rivers et al., 2012). The allochthonous belt is further subdivided into a granulite-facies Allochthonous Polycyclic Belt that contains evidence for pre-Grenvillian metamorphism (>1.1 Ga) and the amphibolite-facies Allochthonous Monocyclic Belt that contains no discernible evidence for pre-Genvillian metamorphism (Ketchum and Davidson, 2000). Each belt is composed of multiple domains distinguished primarily by metamorphic history and separated by shear zones. These domains are interpreted to represent thrust sheets that developed during orogenesis (Culshaw et al.,

1997; Jamieson et al., 2010). The focus of this study is the Muskoka domain and the related Opeongo domain in the Allochthonous Monocyclic Belt.

### 4.3.2 Muskoka domain

The Muskoka domain is a ∼7 km thick package of amphibolite-facies orthogneiss structurally below the Composite Arc Boundary thrust zone (Fig. 4.1 B) and structurally above the Algonquin, Rosseau, and Go-Home domains (Rivers, 2008; Jamieson and Beaumont, 2011; Dickin et al., 2017; Rivers and Schwerdtner, 2015). In the western extent, the Muskoka domain includes the Moon River and Seguin subdomains. The eastern extent of the Muskoka domain is less clear and may transition into the Opeongo domain which has similar lithology and metamorphic history (Chapter 2, Culshaw et al., 2016). While the eastern extent of the Opeongo domain is unknown, Nd model ages have been used to group the Muskoka and Opeongo domains into a single allochthon called the Muskoka allochthon that extends into western Quebec with a full orogen-parallel length of ∼ 300 km (Dickin et al., 2017; Dickin and Strong, 2019; Dickin, 2025).

The units that make up the Muskoka and Opeongo domains are the ≥ 1460 Ma calc-alkaline suite containing meta-tonalite, meta-granodiorite and meta-gabbro; a 1460–1430 Ma anorthosite-mangerite-charnockite-granite suite containing meta-monzonite, meta-monzodiorite, meta-gabbro, and meta-anorthosite; 1170–1150 Ma coronitic metagabbros; syn-deformational syenite and granite pegmatite dikes (1100–1050 Ma); and post-deformational (∼1000 Ma) granite pegmatite dykes that crosscut both the calc-alkaline suite and the anorthosite-mangerite-charnockite-granite suite (Ketchum and Davidson, 2000; Slagstad, 2003; Rivers and Schwerdtner, 2015; Culshaw et al., 2016). The calc-alkaline suite is the dominant lithology and occurs primarily as stromatic and patch migmatites (Slagstad et al., 2005). The lithological units of the Muskoka and Opeongo domains are similar to those present in the underlying Allochthonous Polycyclic Belt rocks of the Algonquin, Rosseau, and Go-Home domains. Metamorphic grade is the primary differentiating factor; the Muskoka and Opeongo domains are dominated by amphibolite-facies assemblages with an abundance of hydrous minerals such as amphibole and biotite whereas the underlying Allochthonous Polycyclic Belt rocks have granulite-facies assemblages with dominantly anhydrous ferromagnesian minerals (e.g. garnet, orthopyroxene, and clinopyroxene). The Allochthonous Polycyclic Belt rocks are further differentiated from Allochthonous Monocyclic Belt rocks by the occurrence of pre-Grenvillian metamorphism (>1.1 Ga) (Ketchum and Davidson, 2000) and older Nd model ages (Ketchum and Davidson, 2000; Dickin et al., 2017).

Metamorphism in the Muskoka domain has been estimated to reach with a peak pressure of 9–12 kbar (Anovitz and Essene, 1990; Timmerman et al., 2002), followed by a peak temperature of 750–850 °C (Chapter 2, Timmerman et al., 2002). The exact timing of peak metamorphism remains uncertain, however multiple cooling ages have been measured: U–Pb dates of zircon in leucosome in the calc-alkaline rocks can be interpreted to record melt crystallization at ca. 1070–1060 Ma (Fig. 4.1 B; Slagstad et al., 2004; Timmerman et al., 2002) and retrograde U-Pb zircon dates that indicate cooling began as early as ca. 1100 Ma and possibly continued until ca. 1000 Ma (Chapter 2).

Two tectonic models have been proposed for the Muskoka domain that explain the structural placement of the domain and strong extensional deformation observed throughout the domain. One model suggests that the Muskoka domain developed during convergence in which the ductile flow occurred in the domain as it was thrusted over the underlying units (Jamieson et al., 2007). In this model, melting and deformation occurred during continent–continent convergence and crustal thickening. An alternative model suggests that deformation and partial melting of the Muskoka domain dominantly occurred during extension where the Muskoka domain acted as a detachment zone between the Central Gneiss Belt and the Composite Arc Belt (Rivers and Schwerdtner, 2015). Chapter 2 suggested that cooling in the Muskoka domain was coeval with eclogite-facies metamorphism (Marsh and Culshaw, 2014) in the underlying domains; this is best explained by the convergent ductile flow model. In this model, the Muskoka domain would have been undergoing ductile extension during convergence, allowing for the creation of space for melt flow to readily occur throughout the domain.

### 4.3.3 Migmatites

There are two morphologies of migmatites in the Muskoka domain: stromatic migmatites and patch migmatites (Slagstad et al., 2005; Timmerman et al., 2002). Stromatic migmatites are migmatites in which the leucosome, mesosome, and melanosome occur as continuous and parallel layers of variable thickness (Sawyer, 2008). Patch migmatites are migmatites with discrete leucosome that typically form *in situ* (Sawyer, 2008).

Stromatic migmatites with concordant granodioritic mesosome and granitic leucosome are the dominant rock type in the Muskoka domain (Fig. 4.2 A, B)(Slagstad et al., 2005). Leucosome in the stromatic migmatites are typically 0.5–5 cm thick and contain coarse grained alkali-feldspar and quartz with rare amphibole and biotite porphyroblasts. Amphibole- and biotite-rich selvages are uncommon but do occur on the edges of some leucosome. Concordant leucosome is commonly in petrographic continuity with discordant

leucosome (Fig. 4.2 A). Discordant leucosome are typically localized in small shear bands and, along with coarse-grained leucosome in boudin necks (Fig. 4.2 B), indicates that melt was present and mobilized during deformation (Timmerman et al., 2002; Slagstad et al., 2005). Stromatic migmatites typically contain very high proportions of leucosome (typically 20–30 vol.%, up to 40–50 vol.%) that are not consistent with the amount of melt expected to be generated by granodiorite at the peak temperatures (750–850 °C) of the Muskoka domain (<10 vol.%) or the proportion of melanosome present, suggesting that not all leucosome formed from *in situ* partial melting and these migmatites contain a component of melt injection (Slagstad et al., 2005).

Patch migmatites are less common and occur in weakly strained rocks that are typically dioritic in composition but do occur in more granodioritic rocks (Fig. 4.2 C, D) (Slagstad et al., 2005). Granitic leucosome is typically 5–20 cm wide, anastamosing through the host rock (Fig. 4.2 C), or as diffuse lenses (Fig. 4.2 D). Leucosome can have either sharp (Fig. 4.2 C) or diffuse edges (Fig. 4.2 D), or a combination of both. Amphibole and biotite porphyroblasts are common in the leucosome of patch migmatites (Fig. 4.2 C, D). These amphibole porphyroblasts have been suggested to be peritectic (Slagstad et al., 2005). Coarse grained amphibole porphyroblasts (up to 1 cm in length) are also common in the host rock close to the leucosome (Fig. 4.2 C). Amphibole-rich melanosome has been observed in many patch migmatites in dioritic host rocks in the region (Slagstad et al., 2005). Smaller proportions of patch leucosome also occur in weakly deformed pyroxene-bearing monzonitic host rocks that are rare throughout the Muskoka and Opeongo domains (Chapter 2). One occurrence of this monzonite contains coarse-grained garnet porphyroblasts in the leucosome (23SD20; Fig. 4.2 E, F).

### 4.3.4 Pegmatites

Granitic pegmatite dykes of variable size and age are common throughout the Muskoka domain (Fig. 4.3) (Slagstad et al., 2004, 2005; Rivers and Schwerdtner, 2015). They are typically 10–50 cm wide and frequently have offshoots that gradually transition into leucosome in the host rock (Fig. 4.3 G) (Slagstad et al., 2005). Pegmatites are dominated by alkali feldspar, quartz, and plagioclase and commonly contain 1–3 cm amphibole and biotite grains. No published dates exist for granitic pegmatites in the Muskoka domain, but orthopyroxene-bearing syenitic pegmatites have been dated with two distinct ages of $1077 \pm 2$ Ma (U-Pb zircon; Timmermann et al., 1997) and $1035 \pm 7$ Ma (U-Pb zircon; Slagstad et al., 2004). Granitic pegmatites in the related Shawanaga domain have an older crystallization age of $1089 \pm 4$ Ma (U-Pb zircon; Slagstad et al., 2004). In the related Ahmic domain, granitic pegmatites have slightly younger dates of ca. 1080 Ma (U-Pb zircon; Bussy

et al., 1995). Granitic pegmatites most commonly crosscut the dominant foliation at high angles and occur as either tabular bodies with sharp boundaries and few offshoots (Fig. 4.3 B, C, D, F, H) or anastamosing dykes with sharp or diffuse boundaries and more offshoots (Fig. 4.3 G).

The genetic relationship between pegmatites and the stromatic migmatites is obscured by high amounts of strain and large proportions of leucosome. It is unclear from field relationships if the host rock is the source of leucosome or if it represents injected melt. Rare occurrences of pegmatites cutting through low strain and leucosome-poor host rocks of monzonitic and granodioritic composition (Fig. 4.3 A, B, C, D, E, F, H) that are analogous to the higher-strained stromatic migmatites provide insight into the relative timing of injection and melting in the host rock. These pegmatites are typically undeformed with straight enveloping surfaces (Fig. 4.3 B, C, D, F, H) but rare, deformed pegmatites do occur (Fig. 4.3 A). Reaction selvages that are ∼5–150 cm thick are present in the host rock surrounding these pegmatites and commonly contain amphibole or biotite porphyroblasts and alkali feldspar rich leucosome lenses (Fig. 4.3 A, B, C, H, I). A discontinuous foliation is common in the wider selvages in the form of compositional banding (Fig. 4.3 A, I). The orientation of this foliation is consistent with the foliation of the host rock (Fig. 4.3 I). Alkali feldspar + quartz + plagioclase + amphibole ± biotite is the common assemblage seen in the selvage; garnet is present in some selvages only when it is found in the neighbouring host rock. In host rocks that contain amphibole, amphibole in the selvage typically appears coarser grained. Reaction selvages typically have diffuse but distinct edges at the contact the host rock. By contrast, the contact between the pegmatite and host rock are sharp and only rarely contain offshoots that transition into more diffuse leucosome (Fig. 4.3 E).

## 4.4 Methods

### 4.4.1 Whole-rock geochemistry

Whole-rock geochemistry was measured at ActLabs (Ancaster, Ontario) using their 4LithoResearch package. Samples were dissolved using lithium metaborate and lithium tetraborate fusion. Molten material was dissolved in 5% nitric acid, and this solution was then analyzed. Major element concentrations were measured using an Agilent Technologies Varian 735 Emission Spectrometer and trace elements were measured using an PerkinElmer Elan 9000 inductively coupled plasma mass spectrometer (ICP-MS). Ferrous iron $Fe^{2+}$ was measured using titration with a cold digestion of ammonium metavanadate and hydrofluoric acid.

Ferrous ammonium sulphate was added after digestion and potassium dichromate was used as the titrating agent.

### 4.4.2 Amphibole compositions

Major element amphibole compositions were determined using electron probe microanalysis (EPMA) with a JEOL JXA8230 5-WDS electron microprobe at the University of Toronto Department of Earth Sciences EPMA lab. Amphibole was analyzed using a 10 µm spot size with an accelerating voltage of 15 keV and current of 20 nA and acquisition times were 2 min. On peak and background collection times for each element measured are presented in Table C.1. Calibration was done prior to the start of analysis on natural and synthetic standards.

Trace element mineral compositions were measured using laser ablation inductively-coupled plasma mass spectrometry (LA-ICP-MS) with an Agilent 8800 QQQ-ICP-MS in sequence with an Analyte G2 193 nm Excimer laser ablation unit system in the Metal Isotope Geochemistry Lab at the University of Waterloo. Amphibole was preablated with a 65 µm single shot operating at 2.5 $\frac{\text{J}}{\text{cm}^2}$ (measured at sample surface). Ablation was performed with 65 µm spot size and a fluence of 2.5 $\frac{\text{J}}{\text{cm}^2}$ with a repetition rate of 8 Hz for 30 s. Ablated material was moved from the laser sample chamber using He as a carrier gas (0.9–1.0 L/min) with Ar added to the aerosol (0.9–1.2 L/min). Samples were analyzed using standard–sample bracketing (reference materials run every ∼10 unknowns). NIST612 was used as the external reference material, NIST610, and BHVO-2G were used as a secondary reference materials. Si measured on EPMA was used as the internal standard. Data was processed using Iolite (v.4). Full analytical conditions are shown in Table C.2 and QAQC is shown in Table C.4.

### 4.4.3 Zircon U–Pb geochronology

Zircon grains were separated from pegmatite samples by mechanical crushing, gravity, magnetic, and heavy liquid separation methods. Zircon grains were handpicked and mounted on epoxy mounts except for 22SD55D in which zircon grains were analyzed *in situ* in thin section (Fig. 4.4 C). Zircon was then imaged using a Zeiss LEO 1530 scanning electron microscope (SEM) operating at 20 kV and 0.5–1 nA with an aperture size of 120 µm. Zircon grains were analyzed using laser ablation inductively-coupled plasma mass spectrometry (LA-ICP-MS) with an Agilent 8800 QQQ-ICP-MS in sequence with an Analyte G2 193 nm Excimer laser ablation unit system in the Metal Isotope Geochemistry

Lab at the University of Waterloo. Zircon was pre-ablated using 65 µm single shot operating at 2.5 $\frac{J}{cm^2}$. Ablation was performed with 65 µm spot size and a fluence of 2.5 $\frac{J}{cm^2}$ (measured at sample surface) with a repetition rate of 8 Hz for 30 s. Ablated material was moved from the laser sample chamber using He as a carrier gas (1.0 L/min) with Ar added to the aerosol (0.9 L/min). Samples were analyzed using standard–sample bracketing (reference materials run every ∼8 unknowns). The masses measured were 29, 88, 206, 207, 232, and 238. The external standard used was 91500 (Wiedenbeck et al., 2004) with Plesovice (Sláma et al., 2008) as a secondary reference material (Fig. C.1, Table C.5). The measured age of Plesovice was: 334.0 ± 4.9 Ma (2s; MSWD = 0.18, concordia + equivalence), which is within uncertainty of the expected age (337 ± 0.37 Ma). The error on the secondary reference material was propagated to the unknown samples using quadrature averaging (e.g. Horstwood et al., 2016). Data was processed using Iolite (v.4) and the data reduction procedure outlined by Paton et al. (2010). Analyses with a discordance of -3–5 measured using the concordia distance method (Vermeesch, 2021) were not included in calculation of concordia age for samples. Analyses with single-zircon concordia dates >1200 Ma were also excluded from the calculation of concordia age as they were assumed to be xenocrysts from the host rock. Results were plotted using IsoplotR (Vermeesch, 2018). Full analytical conditions are shown in Table C.3.

### 4.4.4 Phase equilibrium modelling

Phase equilibrium modelling for the purpose of understanding how $H_2O$ modifies mineral content and melt proportions was done with the software Perple_X (Connolly, 2005). The thermodynamic data from Holland and Powell (2011) was used in the $Na_2O$–CaO–$K_2O$–FeO–MgO–$Al_2O_3$–$SiO_2$–$H_2O$–$TiO_2$–$Fe_2O_3$ system. Calculations were done using solution models from White et al. (2014a) for garnet, biotite, white mica, chlorite, ilmenite, and orthopyroxene, Green et al. (2016) for clinoamphibole, augite, and melt, White et al. (2002) for spinel, Holland and Powell (2003) for feldspar, Holland and Powell (1998) for olivine, and Holland and Powell (2011) for epidote. The T–$X_{H_2O}$ models of host rocks were run at fixed pressures of 9 kbar for 23SD03B, 22SD55E, 23SD20A, and 8 kbar for 23SD02A based on the iteratively calculated stable pressures of minerals present in the host rocks.

### 4.4.5 $H_2O$-fluxed melting models

To test whether diffusive $H_2O$-fluxed melting is plausible in the Muskoka domain, we present a two-stage thermodynamic equilibrium model that starts with (predominantly fluid-absent)

melting in the source rock considering variable initial proportions of $H_2O$, and is followed by consideration of moving the melt fraction shallower in the crust and equilibrating $H_2O$ chemical potential gradients to generate further melting. This is similar to the conceptual Holk and Taylor (2000) model of catalytic melting wherein hydrous melt generated at greater depth crystallizes upon ascent and releases fluids to induce melting at shallower crustal levels, however we ground our model using quantitative thermodynamic calculations and observations from the Muskoka domain.

We start with a granodiorite composition (23SD03B) representative of the granodioritic mesosome present in stromatic migmatites and some patch migmatites that dominate the Muskoka domain as an initial melt source. Considering that the amount of anatectic melt will be a product of the initial $H_2O$ content (e.g. White et al., 2007), we model four concentrations of $H_2O$ (0.32, 0.63, 1.3, and 2.8 wt% or 2, 3, 5, and 10 mol%) chosen to show a range of low to moderate initial $H_2O$ concentrations in the granodiorite protolith. An isobaric heating path was modelled for each scenario from 600 to 1000 °C at 10 kbar. When melt volume exceeded 7 vol% of the rock, 6 vol% was extracted (as in Yakymchuk and Brown, 2014) to be used in the next stage of the model and the residual composition was used in the remaining heating path. When the melt extraction threshold is reached, this melt is then used as a starting point for the second stage calculations. Melt extracted during each melt loss event will have different major element compositions, and importantly, different concentrations of $H_2O$.

The second stage of the model followed the method described by Tafur and Diener (2020) that equilibrates chemical potential gradients of $H_2O$ between an intruding silicate melt (analogous to our pegmatites) and a host rock. The chemical potential of $H_2O$ ($\mu_{H_2O}$) of each extracted melt composition from the first stage was recalculated at 9 kbar and both 750 °C and 800 °C; these are the approximate P–T conditions of $H_2O$-fluxed partial melting of stromatic migmatites in the Muskoka domain based on regional temperature estimates (Chapter 2, Slagstad et al., 2005; Timmerman et al., 2002). We then take our host rocks at the same P–T conditions and increase the chemical potential of $H_2O$ until it matches that of each of the extracted melt compositions; the result is an estimate of volumetric proportion of melt generated and the concentration of $H_2O$ in the host rock (which includes residual minerals and the newly formed anatectic melt). Two different host rocks were chosen for comparison, 23SD03B to represent the granodiorites that dominate the region, and 23DS20A to represent the rare leucosome-poor granulite-facies monzonites that we have observed in the region. These two compositions represent the two rock types observed to host the pegmatites and associated migmatite reaction selvages (Fig. 4.3 F and H for granodiorite and monzonite hosts respectively).

## 4.5 Results

### 4.5.1 Petrography

#### Granodiorite host rock

The granodiorite host rocks (Fig. 4.4 G) are similar to the granodioritic mesosome described by Slagstad et al. (2005). These rocks contain in decreasing order of abundance: plagioclase, alkali feldspar, quartz, amphibole, biotite, magnetite, ilmenite, and clinopyroxene (if present) with trace amounts of zircon and apatite. Average grain size is ∼0.5–1 mm and minerals are generally xenoblastic to hypidioblastic. Amphibole contains variable inclusions of quartz, magnetite, and rarely clinopyroxene. Biotite commonly have vermicular intergrowths with quartz. Blebby albite exsolution is common in alkali feldspar.

#### Granodiorite selvages

Reaction selvages crosscutting granodiorite host rocks (Fig. 4.4 H, I) contain: plagioclase, alkali feldspar, quartz, amphibole, biotite, magnetite, and ilmenite with trace amounts zircon and apatite. The proportions of minerals vary according to proximity to the pegmatite but follow the general trend of plagioclase + alkali feldspar >quartz >amphibole + biotite >magnetite + ilmenite with an average grain size of ∼1–3 mm, coarsening towards the pegmatite. Closest to the pegmatites, alkali feldspar dominates over plagioclase and amphibole dominates over biotite (Fig. 4.4 I), further from the pegmatites, plagioclase dominates over alkali feldspar and in one selvage biotite dominates over amphibole (Fig. 4.4 H). Biotite commonly has vermicular intergrowths with quartz. Amphibole contains variable inclusions of quartz, biotite, magnetite, and plagioclase. Blebby albite exsolution in alkali feldspar is common. Myrmekite intergrowths between quartz and alkali feldspar are common in the parts of the selvages closest to the pegmatite.

#### Monzonite host rock

Monzonitic host rocks including 22SD55E (Fig. 4.4 A), 23SD02A, 23SD20A (Fig. 4.4 D), 23SD20B, and 23SD20G consist of: alkali feldspar + plagioclase + quartz + clinopyroxene + magnetite + ilmenite + amphibole + biotite ± garnet ± orthopyroxene with trace amounts of zircon and apatite. The abundance of minerals varies between outcrops but follow the trend of: alkali feldspar >plagioclase >quartz >clinopyroxene + amphibole

>magnetite + ilmenite >garnet + orthopyroxene >biotite. Grain size is relatively consistent with an average size of ∼0.5–1 mm and no grain larger than 3 mm. Alkali feldspar, plagioclase, quartz, clinopyroxene, amphibole, biotite, and orthopyroxene are xenoblastic to hypidioblastic. Garnet, magnetite, and ilmenite are hypidioblastic to idioblastic. Blebby plagioclase exsolution in alkali feldspar is common. Garnet and biotite commonly have vermicular intergrowths with quartz (Fig. 4.4 A, D). Garnet and amphibole overgrowths on magnetite and ilmenite are common as are amphibole overgrowths on garnet (Fig. 4.4 A) and clinopyroxene (Fig. 4.4 D).

### Monzonite selvages

Reaction selvages around pegmatites crosscutting monzonitic hosts including 22SD55B (Fig. 4.4 B), 23SD03C (Fig. 4.4 E), 23SD03D (Fig. 4.4 F), 23SD20F, and 23SD02B consist of: alkali feldspar + plagioclase + quartz + magnetite + ilmenite + amphibole + biotite ± garnet with trace amounts of apatite, allanite, and zircon. The relative proportions of minerals varies between outcrops, but follow the general trend of alkali feldspar >quartz >amphibole + biotite >plagioclase >garnet. Grain size varies between outcrops, outcrops 22SD55 and 23SD20 have an average grain size of ∼0.5–1 mm and outcrop 23SD02 has an average grain size of ∼2–3 mm. Alkali feldspar, plagioclase, quartz, and garnet are xenoblastic to hypidioblastic. Amphibole, biotite, magnetite, and ilmenite are hypidioblastic to idioblastic. Amphibole and biotite rarely occur as overgrowths on garnet (Fig. 4.4 B, E, F). Amphibole may occur with variable inclusions of quartz, plagioclase, biotite, and allanite. Biotite commonly have vermicular intergrowths with quartz in all outcrops as does amphibole in outcrop 23SD20 (Fig. 4.4 E). Blebby albite exsolution is common in alkali feldspar. In comparison to the host rocks, when garnet is present, it has more irregular crystal faces, especially when overgrown by amphibole (Fig. 4.4 B), or closer to the pegmatite (Fig. 4.4 F). In outcrop 23SD20, amphibole is not present closest to the pegmatite (Fig. 4.4) and the rock has higher proportions of alkali feldspar, quartz, and plagioclase.

### Pegmatites

Pegmatites that crosscut both monzonitic and granodioritic hosts are similar. They contain in decreasing order of abundance: alkali feldspar, quartz, amphibole and/or biotite, plagioclase, and magnetite with trace amounts of zircon, apatite, and allanite. Grain size is highly variable with grains up as coarse as 3 cm. Crystals are typically subhedral to euhedral. Clinopyroxene occurs only in pegmatite 23SD02C, and is always overgrown

and partially replaced by amphibole. Amphibole does not occur in pegmatite 23SD20E. Amphibole contains variable inclusions of biotite, quartz, apatite, allanite, zircon, and magnetite. Myrmekite intergrowths between quartz and alkali feldspar are common. Where zircon is seen in thin section, it occurs as subhedral to euhedral grains as large as 2 mm. One occurrence of a $\sim$ 1 mm cluster of zircon grains is present in 22SD55D (Fig. 4.4 C).

### 4.5.2 Whole rock geochemistry

Host rocks, pegmatites, and selvages can be broadly classified as granitic, monzonitic, or granodioritic. Major element compositions of these rocks (Table C.6) are variable, but some similarities persist between these groups. Major element compositions of host rocks, pegmatites, and selvages (Table C.6) broadly classify as granitic, monzonitic, or granodioritic.

The granodiorite host rocks investigated here have major element compositions that are almost identical to the granodiorite mesosomes in stromatic migmatites that dominate the Muskoka domain (Figs. 4.5, 4.6; Slagstad et al., 2005). Monzonite host rocks have more variable major element compositions but all plot within the "granite" field in the normative Ab-Or-An plot (Fig. 4.6), between the granodioritic mesosomes and stromatic leucosomes (Slagstad et al., 2005). Except for one outlier (23SD02A) anomalously enriched in Fe*+Mg+Ti (Fe* = Total Fe), the monzonitic host rocks are more K-rich and Na and Ca-poor than the granodiorite host rocks and mesosomes but more rich in Fe*+Mg+Ti than the stromatic leucosomes (Fig. 4.5). There are no consistent patterns between the host rocks and reaction selvages, in some cases the selvage is more Or-rich than the host rock (e.g. 22SD55B vs 22SD55E; Fig. 4.6) and in others it is more Or-poor (e.g. 23SD20D vs 23SD20A; Fig. 4.6). These trends are mirrored in the K–(Fe* + Mg + Ti)–(Na + Ca) plot (Fig. 4.5) where selvages are either enriched in K compared to the host (e.g. 22SD55B vs 22SD55E) or depleted in K compared to the host (e.g. 23SD20D vs 23SD20A). Pegmatites in this study also have variable major element compositions but are similar to stromatic leucosomes (Fig. 4.5, 4.6).

### 4.5.3 Amphibole compositions

A common mineral in leucosome and melanosome is amphibole, which can be an important tracker of metamorphic grade and melt–rock interaction (e.g. Stuart et al., 2017). Major cation composition of nearly all analyzed amphiboles can be classified as pargasite (Fig. 4.7) following the classification scheme of Hawthorne et al. (2012). Trace element analyses of

amphibole (Fig. 4.8) reveal several different trends in the chondrite-normalized REE patterns depending on the host rock. For samples of pegmatites and the surrounding host rock, amphibole was measured in samples taken from the pegmatites, the surrounding reaction selvages, and the unmodified host rocks. This includes amphibole in one granodiorite outcrop (Fig. 4.8 A), two monzonite outcrops (Fig. 4.8 B, C). Amphibole analyses from several stromatic migmatites are also shown for comparison (Fig. 4.8 D)

Amphibole in granodiorite at variable distances from pegmatite 23SD03E (Fig. 4.3 F) have generally consistent trace element patterns regardless of distance from the pegmatite (Fig. 4.8 A). While the pattern is consistent, average concentrations of nearly every trace element increases as samples get closer to the pegmatite and are highest in the pegmatite. Except for a few analyses in the host (23SD03C-3), a negative Eu anomaly ($Eu/Eu^* = Eu_N/\sqrt{Sm_N \times Gd_N}$) is present in each amphibole. A small positive slope on chondrite-normalized diagrams is present in the LREE from La to Pr in most samples, except a few analyses in the pegmatite (23SD03E) which have a steeper positive slope between La and Sm. All amphibole in the granodiorite have flat chondrite-normalized HREE trends.

Amphibole from one outcrop of migmatitic monzonite (host and selvage) and intruded pegmatite (outcrop 22SD55, Fig. 4.3 B) has variable trace element trends (Fig. 4.8 B). All amphibole in this outcrop show negative Eu anomalies, but it is less negative in the host (22SD55E) than the selvage (22SD55B-3) and pegmatite (22SD55D). The chondrite-normalized LREE have a positive slope between La and Sm, this slope is similar in the amphibole in the host and selvage and steeper in the amphibole in the pegmatite. The chondrite-normalized HREE have a negative slope between Gd and Lu, which is steeper in the host amphibole and a few analyses in the selvage.

Amphibole from another migmatitic monzonite (host and selvage) and the intruded pegmatite (outcrop 23SD20, Fig. 4.3 H, I), trace element trends also have a high degree of variability (Fig. 4.8 C). A negative Eu anomaly is present in amphibole in most samples except the selvage closest to the pegmatite (23SD20F), in which most analyses have a positive Eu anomaly. The Eu anomaly is also less negative in the selvage amphibole from the other side of the pegmatite (23SD20C) compared to the hosts (23SD20B, 23SD20G). The chondrite-normalized LREE have a positive slope between La and Sm in most amphibole except a few analyses in 23SD20F, the slope is shallower and concentration of LREE lower in the selvage amphibole (23SD20C, 23SD20F) than the amphibole in the host rocks (23SD20B, 23SD20G). The HREE have a negative slope between Gd and Lu in the host amphibole and a positive or nearly flat slope in the selvage amphibole.

In amphibole in stromatic migmatites (Fig. 4.2 A, B; samples collected from Slagstad

(2003)), trace element trends (Fig. 4.8 D) are less variable and similar to amphibole around pegmatite 23SD03E (Fig. 4.8 A). A negative Eu anomaly is present in all samples except four analyses in sample 2M02061A from a large amphibole grain within a leucosome. The chondrite-normalized LREE have a positive slope between La and Sm in all samples except 2M0506-16_3B and the leucosome amphibole in 2M02061A. The chondrite-normalized HREE have a relatively flat trend in all samples except the leucosome amphibole in 2M02061A which has a positive slope between Gd and Lu.

### 4.5.4 Pegmatite U–Pb zircon geochronology

Sample 22SD55D is a granitic pegmatite crosscutting a monzonite host rock and has an associated reaction selvage (Fig. 4.3 B). Zircon grains from this sample were measured *in situ* in thin section (Fig. 4.4 C) and range in size from $\sim$ 20 to $\sim$ 700 µm. Zircon grains are typically euhedral and commonly have distinct cores with bright, patchy zones under CL and oscillatory zoned mantles (Fig. 4.9 A). Two zircon grains with spots in the cores have single-analysis concordia dates of >1200 Ma and are interpreted to be xenocrystic. Ten analyses are discordant and are not considered further. Eighteen analyses are concordant and yield dates of ca. 1010–1190 Ma and give a weighted mean age of $1052 \pm 18$ Ma (2s; MSWD = 0.91 concordia + equivalence), this is interpreted as the crystallization age of the pegmatite.

Sample 23SD02C is a deformed granitic pegmatite crosscutting a monzonite host rock and has an associated reaction selvage (Fig. 4.3 A). Zircons were analyzed as separates and range in size from $\sim$ 50 to $\sim$ 1000 µm. Zircon grains are typically euhedral with oscillatory zoned cores under CL and bright homogenous or patchy rims (Fig. 4.9 B). One zircon grain has a single-analysis concordia date of ca. 1600 Ma and is interpreted to be xenocrystic. Sixteen analyses are discordant and are not considered further. Thirteen analyses are concordant and yield dates of ca. 1030–1120 Ma and give a weighted mean age of $1071 \pm 21$ Ma (2s; MSWD = 0.20 concordia + equivalence), this is interpreted as the crystallization age of the pegmatite.

Sample 23SD03E is a granitic pegmatite crosscutting a granodiorite host rock and has an associated reaction selvage (Fig. 4.3 F). Zircons were analyzed as separates and range in size from $\sim$ 50 to $\sim$ 700 µm. Zircon grains are typically euhedral with oscillatory or sector zoned cores under CL and bright homogenous or patchy rims (Fig. 4.9 C). Ten analyses are discordant and are not considered further. Twenty analyses are concordant and yield dates of ca. 1100–1000 Ma and give a weighted mean age of $1033 \pm 17$ Ma (2s; MSWD = 0.16 concordia + equivalence), this is interpreted as the crystallization age of the pegmatite.

Sample 23SD03K is a deformed granitic pegmatite crosscutting a stromatic granodioiritic gneiss host rock (Fig. 4.3 G). Zircons were analyzed as separates and range in size from $\sim$ 60 to $\sim$ 800 µm. Zircon grains are typically euhedral with dark oscillatory zoned cores under CL and bright homogenous or patchy rims (Fig. 4.9 D). Three zircon grains with spots in the cores have single-analysis concordia dates of >1200 Ma and are interpreted to be xenocrystic. Nine analyses are discordant and are not considered further. Eighteen analyses are concordant and yield dates of ca. 960–1090 Ma and give a weighted mean age of $1044 \pm 17$ Ma (2s; MSWD = 0.45 concordia + equivalence), this is interpreted as the crystallization age of the pegmatite.

### 4.5.5 T–X diagrams

Temperature–composition (T–$X_{H_2O}$) diagrams are used to evaluate the changes in mineral assemblages and compositions and melt proportions as a function of $H_2O$ in the rock. Four samples were investigated as representative of the host rock composition of each outcrop where pegmatites with reaction selvages are found. The T–$X_{H_2O}$ diagrams of all four investigated samples show similar phase topologies and trends (Fig. 4.10). The mineral assemblage is similar between each and the temperature of the solidus decreases with increasing $H_2O$ until the water-saturated solidus becomes stable at $\sim$ 650 °C. Orthopyroxene is typically stable at high T or low $X_{H_2O}$ and above the solidus, as temperature decreases, the orthopyroxene-out reaction is closely associated with the amphibole-in reaction. Garnet has variable stability fields in the different samples. It is only predicted in the garnet bearing samples, 22SD55E (Fig. 4.10 C) and 23SD20A (Fig. 4.10 D). Below the solidus, garnet decreases in proportion with increasing $X_{H_2O}$ in both samples but above the solidus are two different trends. In 22SD55E, suprasolidus garnet increases in proportion as T decreases towards the $H_2O$-saturated solidus and $X_{H_2O}$ does not have a significant impact on garnet proportions. In 23SD20A, below the amphibole-in reaction, garnet volume decreases in proportion as T decreases or as $X_{H_2O}$ increases. In every sample except 23SD02A, clinopyroxene reacts out with decreasing temperatures $\sim$ 10–20 °C above the $H_2O$-saturated solidus. With increasing $X_{H_2O}$, each sample exhibits an increasing proportion of melt up to 20 vol% at 800 °C at high $X_{H_2O}$. Above the solidus, increasing $X_{H_2O}$ only marginally increases the proportion of amphibole present. In contrast, decreasing T at suprasolidus $X_{H_2O}$ increases the proportion of amphibole up to 3 vol% on the low end in sample 22SD55E (Fig. 4.10 C) and up to 16 vol% on the high end in 23SD02A (Fig. 4.10 A). This trend typically inverts near the water saturated solidus where biotite is stable in each sample except 23SD02A.

### 4.5.6 $H_2O$-fluxed melting models

In the first stage of the model, for the lowest water content (0.32 wt% $H_2O$), two melt extraction thresholds were reached, one at ~ 890 °C and one at ~ 960 °C. For the two intermediate $H_2O$ contents (0.63 and 1.3 wt% $H_2O$), three events occurred (~ 810, ~ 900, and ~ 960 °C) for the 0.63 wt% $H_2O$ composition, and four events (~ 640, ~ 820, ~ 890, and ~ 960 °C). The source with the highest $H_2O$ content (2.8 wt%) yielded five melt extraction events (~ 630, ~ 730, ~ 870, ~ 910, and ~ 980 °C).

In the second stage of the model, beginning with the low-$H_2O$ source, (0.32 wt% $H_2O$), the silicate melt produced at ~ 890 °C reacts with the host rock at 750 °C to generate ~ 75 vol% melt in the host (Fig. 4.12). No melt is generated in the host rock at 800 °C. The melt generated in the source at ~ 960 °C is too dry to induce melting in the host rock at 750 or 800 °C.

At 0.63 wt% $H_2O$ in the source the ~ 810 °C melt induces host partial melting at both 750 °C and 800 °C; the ~ 900 °C melt induces melting in both host rocks only at 750 °C; and no melting occurs in either host rock at either temperature for the melt generated at ~ 960 °C (Fig. 4.12). The proportion of melt generated in the host rock (second stage) decreases based on the temperature of the melt extraction event (first stage). Up to 80 vol% melt is generated in the second stage.

At 1.3 wt% $H_2O$ in the source, free $H_2O$ appears in the subsolidus source and the first batch of melt is extracted at ~ 640 °C (Fig. 4.12). Melt extracted at this temperature would require an inverted geothermal gradient to achieve the P–T conditions of the host rock. However, the three subsequently extracted melts follow the same trends observed in the 0.63 wt% $H_2O$ source scenario with up to ~ 90 vol% melt generated during the second stage.

At 2.8 wt% $H_2O$ in the source rock (Fig. 4.12), trends are similar to the 1.3 wt% $H_2O$ source scenario. One notable difference is that the temperature of the second extracted melt is ~ 730 °C rather than ~ 820 °C. In addition, the melt extracted at ~ 910 °C does not induce melting in either host rocks at 800 °C.

The composition of melt extracted from the source rock is granitic (Fig. 4.6) and varies along a single trend line depending on the extraction temperature and independent of the initial $H_2O$ (Figs. 4.5, 4.6). Extracted melt composition is most similar to stromatic leucosome composition (Slagstad et al., 2005) and pegmatite compositions (Fig. 4.5, 4.6).

In summary, for diffusive $H_2O$-fluxed melting to occur in either granodiorite or monzonite host rocks, a sufficiently hydrous melt can be generated in source rocks at greater depth with low amounts of $H_2O$ (as low as 0.32 wt% $H_2O$). Diffusive $H_2O$-fluxed melting occurs under a

greater range of model conditions (i.e. source $H_2O$ content and melt extraction temperature) when the host rock is at 750 °C than at 800 °C. At higher $H_2O$ content in the source rock ($\geq$ 1.3 wt%), early melts generated in the source rock at lower temperatures (<700 °C) would require an inverted geotherm to reach the temperature of the host rock. There is no evidence for an inverted geotherm in the Muskoka domain so these low-temperature melts in the source rock are not considered further.

## 4.6 Discussion

### 4.6.1 Model limitations

It is important to note the limits of the T–$X_{H_2O}$ equilibrium models (Fig. 4.10) in their application to the rocks considered in this study. As in all phase equilibrium modelling, there is an inherent uncertainty due to the uncertainty in the activity composition models used (Powell and Holland, 2008; Palin et al., 2016). More specific to the phase equilibrium models presented here is that the Green et al. (2016) activity composition models we employ are optimized for metabasites that are basaltic to andesitic, these are not as felsic as the granodiorite and monzonite rock compositions that we have modelled. These activity composition models are still the most appropriate ones that are currently available as the White et al. (2014b) activity composition models do not include clinopyroxene or amphibole.

Some consideration also needs to be given to the limitations of the $H_2O$-fluxed melting model. There is uncertainty in the P–T conditions of both the source (first stage) and the host (second stage); Chapter 2 has shown that the region began to cool as early as 1100 Ma and this possibly continued until 1000 Ma, during which some migmatites have already crystallized (ca. 1070 Ma; Slagstad et al., 2005). With pegmatites as young as ca. 1035 Ma (Fig. 4.9 C), it is unclear at what P or T that the observed reaction selvages formed, although they are likely in the amphibolite to granulite facies. We simplified the P–T path for the first stage to isobaric heating of the source rock. This was chosen as a simplification to ensure that the melt generated at the source would be deeper than the host rock without the need of assuming a more complex P–T path based on limited metamorphic data. Furthermore, the main melt-producing reactions are not expected to be sensitive to pressure over permissible P–T range based on regional data (e.g. Slagstad et al., 2005).

Our two-stage model also does not account for modifications of the source-generated melt upon ascent to the host such as fractional crystallization, which would likely increase $H_2O$ in the melt or reaction during transport, which could likely decrease $H_2O$ and therefore

$\mu_{H_2O}$ in the melt. There is also an assumption that external (stage 1) melt is constantly produced and flows continuously through the host rock. This assumption allows a fixed $\mu_{H_2O}$ of the external melt in stage 2 of the model, and consequently the composition of the external melt does not change during equilibration with the host rock, either through $H_2O$ loss as a result of mass balance or magma mixing. In reality, the external melt would continuously lose $H_2O$ to the host rock during diffusive $H_2O$-fluxed melting, and there would be mixing of the original melt and the new melt generated in the host rock. The simplifying assumption that only $H_2O$ is the only mobile component is not likely to be reflective of reality as components like K and Na can have fast rates of diffusion (Zhang and Gan, 2022) and will also depress melting temperatures (Aranovich et al., 2013). Finally, since these are partially-open system models, there is assumption that melt is continuously generated at depth and constantly replenishes the magma reacting with the host rock and that there is no mixing between melt generated at depth and melting in the host rock. This is not reflective of the real limitations on melt generation in the source rock and diffusion in the host rock that will limit the amount of $H_2O$ that is available to the host to progress the $H_2O$-fluxed melting reaction or the complicating factor of melt loss and magma mixing that would result from a completely open system model. While factoring these processes into the model would likely reduce the amount of melt produced in the host rock compared to what the current model predicts, the predicted melt production is so high that even 1/3 of the predicted melting would result in >20 vol% melt in the host rock, which is still a very high proportion of melt and close to the volume of leucosome typically observed in the Muskoka domain migmatites (20–30 vol. %).

### 4.6.2 Evidence for $H_2O$-fluxed melting

Partial melting of silicate rocks at high temperatures due to the influx of $H_2O$ is a contentious subject (e.g. Weinberg and Hasalová, 2015; Clemens, 2006; Clemens et al., 2020). Differences in terminology related to the source of $H_2O$ and/or fluids and mechanisms that allow $H_2O$ to move through the crust can also cause confusion. Here, we use the term "fluid-fluxed melting" to refer to melting with a free fluid involved including fluids exsolved from silicate melt, "$H_2O$-fluxed melting" to refer generally to any melting involving the addition of $H_2O$, and "diffusive $H_2O$-fluxed melting" to refer to $H_2O$-fluxed melting from diffusion of $H_2O$ from a hydrous melt (following Tafur and Diener, 2020).

Slagstad et al. (2005) suggested that the amphibole-bearing migmatites that are common throughout the Muskoka domain most likely formed from the addition of $H_2O$. Their primary evidence was: 1) The high volume of leucosome present in the migmatites that can only be accounted for through fluid-fluxed melting and the addition of melts sourced externally

from the Muskoka domain, 2) The occurrence of large, possibly peritectic amphibole porphyroblasts within leucosomes that is not expected in hydrate breakdown melting, and 3) Geochemical evidence suggesting the rocks were infiltrated by K-bearing fluids (Slagstad et al., 2005). However, the highly strained nature of the stromatic migmatites in the Muskoka domain (Fig. 4.2 A, B) make it challenging to assess how $H_2O$ could infiltrate and react with the protoliths to induce partial melting prior to pervasive ductile deformation. High strain can also mask if a coarse-grained leucosome is truly intrusive or generated *in situ*. We examine low strain outcrops where the primary relationships between host rocks, leucosome, and pegmatites are preserved and this provides important constraints on the potential movement of $H_2O$ through the crust.

The investigated pegmatites (Fig. 4.3 A, B, C, D, E, F, H, I) show evidence that varying proportions of partial melt was produced within the reaction selvage surrounding them. Macroscopic evidence permissive of partial melting include leucosome in the reaction selvages (23SD02, 22SD55, 23SD20; Fig. 4.3 A, B, C, H, I). Partial melting is further supported by mineral assemblages and textures present in the host rocks and reaction selvages. Where garnet, orthopyroxene, or clinopyroxene are present in the host rock (e.g. garnet in 22SD55E, 23SD20A; Fig. 4.4 A, D), the selvage either does not contain the anhydrous mineral, or it is present in lower abundance with resorbed textures (e.g. garnet in 22SD55B, 23SD20C, 23SD20D; Fig. 4.4 B, E, F). By contrast, coarse-grained amphibole is more abundant in the reaction selvage compared to the host rock (22SD55B, 23SD20C, 21SD51F; Fig. 4.4 B, E, I). Amphibole overgrowths on garnet in reaction selvages (Fig. 4.4 D, E) suggest that it is growing at the expense of anhydrous ferromagnesian minerals. These same trends are predicted in the T–$X_{H_2O}$ pseudosections of every sample, where amphibole increases in abundance with decreasing temperature towards the water-saturated solidus at $\sim 650$°C. As the amphibole-out reaction occurs at higher $X_{H_2O}$ close to the water-saturated solidus, it is likely that melt loss and melt crystallization allowed the preservation of large amphibole porphyroblasts in the reaction selvages. Conversely, anhydrous minerals like garnet, orthopyroxene, and clinopyroxene have the inverse trend with reducing modal abundance or complete consumption during cooling at higher $X_{H_2O}$. The presence of biotite (23SD20C, 23SD20D, 21SD51E; Fig. 4.4 E, F, H) in reaction selvages is also explained by the pseudosections (23SD03B, 23SD20A; Fig. 4.10 B, D) where biotite is shown to join the stable assemblage near the water-saturated solidus, indicating that it formed in the reaction selvage as a result of hydrous melt crystallization. This interpretation is further supported by the vermicular intergrowth of biotite and quartz (Fig. 4.4 E, H) that has been associated with melt crystallization in other studies (e.g. Guernina and Sawyer, 2003; Brown and Raith, 1996). An observed reduction in the proportion of plagioclase and increase in the proportion of alkali feldspar in the selvage compared to the host is

possibly a result of the crystallization of a granitic melt that was produced in the reaction selvage. This apparent consumption of plagioclase in the reaction selvages aligns with the suggested melting reaction proposed by Slagstad et al. (2005) of: Bt + Pl + Qtz + Fluid = Hbl + Granitic melt. Interpreting the alkali feldspar as crystallization products is further supported by the occurrence of myrmekites in some reaction selvages, which other studies have suggested to be a melt crystallization texture (e.g. Kohn et al., 1997). On balance, the observed microstructures and mineral assemblages from host to selvage coupled with the results from phase equilibrium modelling are interpreted to represent $H_2O$-fluxed partial melting (Fig. 4.10). Overall, the increase in the proportion of hydrous minerals—and decrease in anhydrous mineral modes—towards the pegmatites in the samples and in the model results suggest an influx of $H_2O$ that has resulted in the production of melt.

Amphibole trace element compositions in outcrops 23SD20 and 22SD55 (Fig. 4.8 B, C) also link with variable mineral assemblages between the selvage and the host rocks, and are suggestive of growth in the presence of melt. Amphibole in the reaction selvages (22Sd55B, 23SD20C, 23SD20F) do not have HREE depletion expected if they grew or equilibrated with garnet; but HREE depletion is present in amphiboles in the host that contain garnet (22SD55E, 23SD20B, 23SD20G). In outcrop 21SD51/23SD03 (Fig. 4.8 A), amphibole contains increasing concentrations of REE from host to selvage to pegmatite. In the absence of other major REE reservoirs like garnet, increasing REE concentration in amphibole is indicative of a reduction of abundance of accessory minerals such as apatite (typically high in LREE and MREE) and zircon (typically high in HREE) before or during the growth of amphibole. A reduction in accessory mineral abundance could be attributed to dissolution in increasing proportions of partial melt present during amphibole growth. In the selvages within monzonitic host rocks (22SD55 and 23SD20; Fig. 4.8 B and C), less depletion of HREE from the host to the selvage further supports amphibole forming at the expense of garnet during melting as indicated by the textures described above; the pseudosection (Fig. 4.10 D) also shows an inverse correlation between garnet and amphibole proportions at suprasolidus conditions. The Eu anomaly in amphibole in samples from outcrop 23SD20 increases from $\sim 0.21$ in the host to $\sim 1.32$ in the selvage (Fig. 4.8 C), which is attributed to release of $Eu^{2+}$ from plagioclase breakdown and incorporation into growing amphibole. This is consistent with the proposed partial melting reaction of Slagstad et al. (2005) where biotite, plagioclase, quartz, and fluid are consumed to produce hornblende and melt.

Although petrographic evidence, trace elements in amphibole, and modelling results are compatible with partial melting due to $H_2O$-fluxed melting, the specific temperature is unclear. The occurrence of leucosome in the monzonitic host rocks (Chapter 2) (Fig. 4.2 E) and the occurrence of orthopyroxene in the hosts of outcrop 23SD02 and 23SD20 suggest temperatures reached at least 875 °C based on the pseudosection stability fields (Fig. 4.10

A, D). The influx of $H_2O$ into these rocks likely occurred during cooling with the upper temperature limit bounded by the amphibole-in reaction at $\sim$ 875–750 °C and the lower temperature limit bounded by the $H_2O$-saturated solidus at $\sim$ 650 °C. Regardless of the temperature when $H_2O$ was added to these rocks, <1.5 wt% $H_2O$ is required to generate >10 vol% melt at any temperature above 650°C (Fig. 4.10).

In summary, $H_2O$-fluxed melting is the most reasonable explanation for the following observations: 1) Large proportions of leucosome and amphibole in the reaction selvages surrounding pegmatites, 2) Reduced proportions of garnet, orthopyroxene, and clinopyroxene and overgrowth of amphibole on these minerals in reaction selvages, 3) REE trends in amphibole that suggest that it grew during garnet and/or plagioclase breakdown during $H_2O$-fluxed melting by thermodynamic models and proposed reactions based on mass balance (Slagstad et al., 2005).

### 4.6.3 Sources of $H_2O$

The spatial relationship between pegmatites, hydrated selvage, and adjacent anhydrous granulite-facies assemblages indicate that the pegmatites were the source of $H_2O$ responsible for partial melting and amphibole growth. Given that the addition of $H_2O$ occurred in a ductile regime (Rivers and Schwerdtner, 2015), the pegmatite dikes likely intruded as hydrous silicate magmas that provided the $H_2O$ to the surrounding host rock and induced melting via exsolution of a hydrous fluid (e.g. White et al., 2005; Holk and Taylor, 2000) or diffusion (e.g. Tafur and Diener, 2020)

$H_2O$ transported as a free fluid is the method of transport that is normally considered in $H_2O$-fluxed melting in crustal rocks (Weinberg and Hasalová, 2015). There are a number of issues, however, with fluid-fluxed melting on meaningfully large scales (e.g. tens to hundreds of kilometers) in the mid to lower crust. Low permeability at higher pressures is a major restriction on the flow of free fluids in the lower crust (Yardley and Valley, 1997), meaning that fluid flow will be restricted to fractures and shear zones, which reduces the possible regional extent of fluid-flux melting (Clemens and Vielzeuf, 1987). At suprasolidus conditions, dilational zones or pore spaces are preferential sites for melt accumulation; either internally- or externally-derived melt (Sawyer, 2010). This limits the amount of fluid that can recharge the conduits. For fluid-fluxed melting to occur, the fluid itself must not significantly react with other rocks while being transported to the host rock. For instance, melting reactions with deeper rocks will not occur if the fluid has a low $a_{H_2O}$ such as high salinity or $CO_2$-rich fluids (Aranovich et al., 2013; Manning, 2018), or in an inverted geothermal gradient where surrounding rocks get hotter as fluid rises through the crust (Genier et al., 2008; Finch et al., 2014).

An alternative method of $H_2O$ transport is as a soluble constituent in silicate melt; this obviates the challenges with the movement of free $H_2O$ in the deep crust at higher temperatures. Melt strongly partitions $H_2O$ during hydrate-breakdown melting (Fig. 4.11 A), which is expected at upper-amphibolite to granulite-facies conditions in the deep crust (Clemens, 2006), making it an effective carrier for $H_2O$ at depth. Melting itself generates porosity in the rock and the accumulated magma generates space and permeability during dike ascent (Fig. 4.11 B) (Brown, 2007). Whether $H_2O$-fluxed melting occurs through exsolution or diffusion, if a large portion of melt persists in the intruding dikes, it will provide an easily accessed conduit for the new melt to be transported (Fig. 4.11 D). This melt extraction could even be promoted by melt suction resulting from continuous flow of melt through the conduits (e.g. Liang and Parmentier, 2010). Finally, if hydrous melt is the source of $H_2O$ in the $H_2O$-fluxed partial melting reactions, it allows the possibility for the melting to propagate further beyond the initial site of $H_2O$-fluxed melting after the newly generated melt is mobilized to higher crustal levels. This could result in a positive feedback loop where $H_2O$ is the catalyst driving partial melting at shallower and shallower conditions (e.g. Holk and Taylor, 2000)

Hydrous melt is a candidate for transporting water in the lower crust in general, but we must verify that such a scenario is possible in the Muskoka domain given the geological constraints. Several important questions need to be answered: 1) How much $H_2O$ is needed in the source rock to generate a hydrous melt that can induce appreciable amounts of melting in the host rock? 2) Does the resulting melt exsolve any fluid when transported to the host? 3) Does melting occur in the host rock at lower temperatures? These are addressed by our $H_2O$-fluxed melting model, which is grounded in petrological observations from the Muskoka domain.

### 4.6.4 $H_2O$-fluxed melting models

#### Interpretation of model results

There are a few notable and counterintuitive trends observed in the modelling results. First, more anatectic melt is generated during the second stage in the lower temperature host rock than at higher temperatures. This is likely a result of higher $\mu_{H_2O}$ in the melt generated in stage one (i.e. from the source rock). The cause of this higher $\mu_{H_2O}$ is probably the higher proportion of anhydrous solids present in the system and therefore a higher concentration of $H_2O$ in the melt. The other notable trend is that higher weight fractions of $H_2O$ in the source rock require an inverted geothermal gradient to generate melt during the second stage. This is an artifact of the modelling due to the temperatures of 750 and 800 °C

assumed for the Muskoka domain compared with the relatively low temperatures of initial melting (near wet solidus) for the high-$H_2O$ source compositions (1.3 and 2.8 wt% $H_2O$). This scenario would require underthrusting of relatively high-$H_2O$ material that is fertile for partial melting (stage 1 in the model) that is thermally out of equilibrium with the overlying material via an inverted thermal gradient. While an inverted geotherm is possible, no evidence has been found for one in the Muskoka domain and so this scenario will not be considered further. Therefore, we focus on the results of the 0.32 and 0.63 wt% $H_2O$ sources, although we acknowledge that the source for the first stage could be slightly more hydrated than we modelled (but less than 1.3 wt% H2O).

Based on these models, very little $H_2O$ is required in the source rock to produce a hydrous melt that can generate large volumes of melt (60–80 vol%) in the given host rocks at conditions seen in the Muskoka domain. In addition, free $H_2O$ was not predicted in the phase equilibrium modelling of any melts generated at the source above 800 °C. Our results support the possibility of diffusive $H_2O$-fluxed melting from hydrous melts occurring within the Muskoka Domain.

### 4.6.5 Comparison with migmatites

The pegmatites and partially melted reaction selvages observed in the field and modelled here are rare features due to pervasive ductile deformation across the region. The Muskoka domain is largely dominated by stromatic migmatites with granodioritic mesosomes (Slagstad et al., 2005). Our sample 23SD03B is within the compositional range of the granodiorite mesosomes throughout the Muskoka domain (Fig. 4.5, 4.6) and we assume that it is broadly representative of the dominant rock type. The high volume of leucosome (typically 20–30 vol. % up to 40–50 vol. %) observed in these migmatites is too high to be produced by hydrate-breakdown melting alone at the predicted temperatures (Slagstad et al., 2005). Furthermore, geochemical evidence suggests that melt was continuously drained from these migmatites (Slagstad et al., 2005). While it is unlikely that all leucosome formed at the same time, it is clear that the stromatic migmatites underwent substantial partial melting over a protracted P–T history. Slagstad et al. (2005) suggested that the high volumes of leucosome records a combination of $H_2O$-fluxed melting and a result of intrusion of melt derived externally to the Muskoka domain. As we have shown in our models of the granodiorite host rock (Fig. 4.12), an externally derived melt generated at greater depth via hydrate-breakdown can easily provide the requisite amount of $H_2O$ to generate large volumes of melt in a similar rock type.

Similarities between the reaction selvages and migmatites further support a genetic relationship between them. Both selvages and migmatites contain granitic leucosome with

and large amphibole porphyroblasts. The composition of these amphibole porphyroblasts provide some insight into the relationship between these units. While major element compositions are similar between host rock and reaction selvage (Fig. 4.7), variations in trace elements (Fig. 4.8) provide additional insight. The most notable comparison is between monzonite selvage (Fig. 4.8 C) and the stromatic migmatite (sample 2M02061A, Fig. 4.8 D). Similar to the monzonite selvage, the Eu anomaly in select amphibole analyses is close to 1.0 in the stromatic migmatite (Fig. 4.8 D) which may indicate a breakdown of plagioclase during or prior to the growth of the amphiboles. As these specific analyses are from a larger amphibole porphyroblast within the leucosome, this is consistent with the interpretation of large amphibole prophyroblasts in Muskoka migmatites as peritectic products of a plagioclase-consuming melting reaction(Slagstad et al., 2005).

The similarities of mineral assemblages, amphibole compositions (Figs. 4.7, 4.8), and whole rock compositions (Figs. 4.5, 4.6) between the stromatic migmatites that dominate the region and the rare pegmatites with reaction selvages implies that they may be genetically related. We suggest that the pegmatites and reaction selvages represent less deformed equivalents of leucosome and melanosome in the stromatic migmatites. In this scenario, the granodioritic mesosome represents the original host rock before the addition of $H_2O$ and melting; the variety of stromatic leucosomes represent mixtures of injected melt and locally generated melt from $H_2O$-fluxed melting (i.e. Fig 4.11 E). If this is the case however, then why did the pegmatites and selvages not develop into migmatites like the rest of the Muskoka domain? The key difference is likely the extent of deformation. The stromatic migmatites are highly deformed and the relationship between intruded magma and reaction selvage is no longer recognizable extensive deformation and rescrystallization. By contrast, the hosts of pegmatites with preserved reaction selvages are less deformed and may be within large-scale low-strain boudins (Schwerdtner et al., 2014) that may have inhibited melt injection.

Pegmatites investigated in this study have crystallization ages of ca. 1070 to 1030 Ma (Fig. 4.9). All the ages overlap with each other and with leucosome ages in the granodiorites in the Muskoka domain (ca. 1070–1060 Ma; Timmerman et al., 2002; Slagstad et al., 2004). This overlap in ages indicates that the pegmatites and leucosome had similar crystallization ages and suggests that they could be remnants of a similar petrological process, except deformation and recrystallization obscured primary relationships in the (now) stromatic leucosome.

### 4.6.6 Tectonic implications

The ages of stromatic leucosome (ca. 1070–1060 Ma; Slagstad et al., 2004; Timmerman et al., 2002) and that of pegmatites inferred here to be drivers of $H_2O$-fluxed melting (ca. 1070–1030 Ma; Fig 4.9) occurred during cooling of the Muskoka domain (ca. 1100–1070 Ma, Chapter 2). Although these are all crystallization ages, they point to melt generated in the deep crust and moving through the rocks now exposed at the surface for at least a few tens of millions of years ($\sim$ 30–70 Myr). Considering that the dominant partial melting reaction included influx of $H_2O$ derived externally to the Muskoka domain (e.g. via pegmatites), this long duration would have required a persistent source of $H_2O$-rich material melting at depth. While this might include magma from other parts of the Muskoka domain, it is unlikely that such a process could be sustained over a protracted period of cooling in a single unit without generating a large volume of restitic material, which has not been reported in the Muskoka domain. It is instead more likely that an underlying unit is being heated and melted, and that melt is transported upward into the Muskoka domain to maintain the cycle of $H_2O$-fluxed melting. The underlying Algonquin and related domains consist largely of granulite-facies migmatites, with frequent occurrence of mafic or quartz-poor granitoids (Lumbers and Vertolli, 2003) that may be the restitic remains after partial melt was mobilized upward into the Muskoka domain. Cooling dates as early as ca. 1100 Ma (Chapter 2) that are synchronous with prograde eclogite ages in underlying units (ca. 1090 Ma; Marsh and Culshaw, 2014), indicating that the Muskoka domain was underthrusted by the Algonquin and related domains and its exhumation began as early as ca. 1100 Ma. Deformation in the Muskoka domain occurred at least as early as ca. 1070 Ma based on the age of the deformed pegmatite 23SD02C (Fig. 4.3 A) and continued in some localities at least until ca. 1040 Ma based on the age of the deformed pegmatite 23SD03K (Fig. 4.3 G) and likely ceased shortly after at ca. 1030 Ma based on the age of the undeformed pegmatite 23SD03E in the same outcrop (Fig. 4.3 F) and likely ceased in other localities further east at ca. 1050 Ma based on the age of the undeformed pegmatite 22SD55D (Fig. 4.3 B).

A simplified tectonic model to account for the long duration of $H_2O$-fluxed melting and that the Muskoka domain was—as a whole—generally cooling by ca. 1100 Ma (Chapter 2) relies on the interaction with the underlying domains. The Muskoka domain was underthrusted by the underlying Algonquin domain during the Ottawan phase of the Grenville orogen (ca. 1090–1020 Ma) where hydrate-breakdown melting initiated in the footwall (Fig. 4.13 A). Hydrous melt produced in the footwall was transported into the overlying Muskoka domain where $H_2O$-fluxed melting initiated (Fig. 4.13 B). The region of melting in the hanging wall is weakened, which promotes further thrusting over the

underlying domains (Fig. 4.13 C). The region of highly strained migmatites is continuously transported to higher crustal levels, allowing it to cool coeval with continuous burial and heating of fertile rock in the underlying domains. This model could be tested further with a regional study of the underlying Algonquin domain to determine if the geochemical composition of the restite present supports the mass balance required to generate sufficient volumes of hydrous magma to induce melting in the Muskoka domain.

Thermomechanical modelling the Muskoka domain also yields a similar tectonic evolution (Jamieson et al., 2007). While their model did not incorporate $H_2O$-fluxed melting, Jamieson et al. (2007) suggested that the Muskoka and related Shawanaga domain represent melt-weakened mid-crust that was continuously expelled through lateral tectonic forces in a process analogous to channel-flow that was proposed for the Himalayan Orogen (Beaumont et al., 2001). This model contrasts with—but does not necessarily preclude—the model of Rivers and Schwerdtner (2015), who suggest that the Muskoka domain represents a detachment zone that formed during orogenic collapse. During orogenic collapse, the Muskoka domain is expected to be cooling and exhuming at the same time as the underlying units, and it is not clear how $H_2O$-fluxed melting could be sustained under such conditions. Between these two models, the Jamieson et al. (2007) model is the one that is most consistent with the available petrochronological data for the central gneiss belt and the interpreted mechanisms for $H_2O$-fluxed melting operating in the Muskoka domain.

The generic tectonic model we have presented (Fig. 4.13) for $H_2O$-fluxed melting is applicable to a wide variety of tectonic environments. It requires no unique circumstances such as inverted geotherms and no sources of fluid external to the orogen (e.g. the mantle). This model only requires the continuous underthrusting of rocks with moderate amounts of $H_2O$ that can be expected in most crustal rocks. These conditions can be reasonably obtained in most orogens and so this model could be invoked in many of the regions found across the world showing evidence for extensive $H_2O$-fluxed melting (Weinberg and Hasalová, 2015).

## 4.7 Conclusion

$H_2O$-fluxed melting occurred in the Muskoka domain of the Grenville Province over >100 $km^2$. We propose that hydrous melts generated at greater depths induced diffusive $H_2O$-fluxed melting and generated high volumes of melts that are now preserved as stromatic leucosome. This process occurred continuously over >35 Myr as the Muskoka domain cooled, turning it into a migmatite-rich and easily deformed horizon that likely influenced the development of the Grenville orogen. The continuous movement between the Muskoka

domain and the underlying domains undergoing hydrate-breakdown melting provided a replenishing source of hydrous melts that intruded into and caused partial melting in the overlying granitoid rocks now found in the Muskoka domain. This model for regional-scale $H_2O$-fluxed melting only involves cycling of $H_2O$ within the orogen itself without the addition of additional $H_2O$ from another source (e.g. the mantle). The relatively low amount of $H_2O$ needed and simple tectonic process of thrusting suggests that this model may be applicable to other regions that record $H_2O$-fluxed melting over large areas and provides a case study into deconvoluting complex migmatite terranes to understand the drivers of anatexis in the deep crust.

# References


Annen, C. and Burgisser, A. (2021). Modeling water exsolution from a growing and solidifying felsic magma body. *Lithos*, 402–403:105799.

Anovitz, L. M. and Essene, E. J. (1990). Thermobarometry and Pressure-Temperature Paths in the Grenville Province of Ontario. *Journal of Petrology*, 31(1):197–241.

Aranovich, L., Newton, R., and Manning, C. (2013). Brine-assisted anatexis: Experimental melting in the system haplogranite–H2O–NaCl–KCl at deep-crustal conditions. *Earth and Planetary Science Letters*, 374:111–120.

Barker, F. (1979). Trondhjemite: Definition, Environment and Hypotheses of Origin. In *Developments in Petrology*, volume 6, pages 1–12. Elsevier.

Beaumont, C., Jamieson, R. A., Nguyen, M. H., and Lee, B. (2001). Himalayan tectonics explained by extrusion of a low-viscosity crustal channel coupled to focused surface denudation. *Nature*, 414(6865):738–742.

Berger, A., Burri, T., Alt-Epping, P., and Engi, M. (2008). Tectonically controlled fluid flow and water-assisted melting in the middle crust: An example from the Central Alps. *Lithos*, 102(3-4):598–615.

Brown, M. (2004). The mechanism of melt extraction from lower continental crust of orogens. *Earth and Environmental Science Transactions of the Royal Society of Edinburgh*, 95(1-2):35–48.

Brown, M. (2007). Crustal melting and melt extraction, ascent and emplacement in orogens: Mechanisms and consequences. *Journal of the Geological Society*, 164(4):709–730.

Brown, M. (2013). Granite: From genesis to emplacement. *Geological Society of America Bulletin*, 125(7-8):1079–1113.

Brown, M. and Raith, M. (1996). First evidence of ultrahigh-temperature decompression from the granulite province of southern India. *Journal of the Geological Society*, 153(6):819–822.

Bussy, F., Krogh, T. E., Klemens, W. P., and Schwerdtner, W. M. (1995). Tectonic and metamorphic events in the westernmost Grenville Province, central Ontario: New results from high-precision U–Pb zircon geochronology. *Canadian Journal of Earth Sciences*, 32(5):660–671.

Clemens, J. and Vielzeuf, D. (1987). Constraints on melting and magma production in the crust. *Earth and Planetary Science Letters*, 86(2-4):287–306.

Clemens, J. D. (2006). Melting of the continental crust: Fluid regimes, melting reactions, and source-rock fertility. In Brown, M. and Rushmer, T., editors, *Evolution and Differentiation of the Continental Crust*, pages 297–331. Cambridge University Press, Cambridge, UK ; New York.

Clemens, J. D., Stevens, G., and Bryan, S. E. (2020). Conditions during the formation of granitic magmas by crustal melting – Hot or cold; drenched, damp or dry? *Earth-Science Reviews*, 200:102982.

Collins, W., Flood, R., Vernon, R., and Shaw, S. (1989). The Wuluma granite, Arunta Block, central Australia: An example of in situ, near-isochemical granite formation in a granulite-facies terrane. *Lithos*, 23(1-2):63–83.

Connolly, J. (2005). Computation of phase equilibria by linear programming: A tool for geodynamic modeling and its application to subduction zone decarbonation. *Earth and Planetary Science Letters*, 236(1-2):524–541.

Culshaw, N., Foster, J., Marsh, J., Slagstad, T., and Gerbi, C. (2016). Kiosk domain, Central Gneiss Belt, Grenville Province, Ontario: A Labradorian palimpsest preserved in the ductile deep crust. *Precambrian Research*, 280:249–278.

Culshaw, N. G., Jamieson, R. A., Ketchum, J. W. F., Wodicka, N., Corrigan, D., and Reynolds, P. H. (1997). Transect across the northwestern Grenville orogen, Georgian Bay, Ontario: Polystage convergence and extension in the lower orogenic crust. *Tectonics*, 16(6):966–982.

Dickin, A. (2025). Nd isotope mapping in the Go Home region of Georgian Bay: A misunderstood key to the geology of the Central Gneiss Belt, Grenville Province of Ontario. *Canadian Journal of Earth Sciences*, 62(2):119–130.

Dickin, A. and Strong, J. (2019). Nd isotope mapping of the Grenvillian Allochthon Boundary Thrust in Algonquin Park, Ontario. *Canadian Journal of Earth Sciences*, 56(2):101–110.

Dickin, A., Strong, J., Arcuri, G., Van Kessel, A., and Krivankova-Smal, L. (2017). A revised model for the crustal structure of the SW Grenville Province, Ontario, Canada. *Geological Magazine*, 154(4):903–913.

Errázuriz-Henao, C., Parolari, M., Gómez-Tuena, A., Gutiérrez-Aguilar, F., and García-RodrÍguez, H. (2024). Geochemical Evidence of Water-Fluxed Crustal Melting in the Northern Colombian Andes. *Journal of Petrology*, 65(7):egae073.

Finch, M., Hasalova, P., Weinberg, R. F., and Fanning, C. M. (2014). Switch from thrusting to normal shearing in the Zanskar shear zone, NW Himalaya: Implications for channel flow. *Geological Society of America Bulletin*, 126(7-8):892–924.

Gardien, V., Thompson, A. B., Grujic, D., and Ulmer, P. (1995). Experimental melting of biotite + plagioclase + quartz ± muscovite assemblages and implications for crustal melting. *Journal of Geophysical Research: Solid Earth*, 100(B8):15581–15591.

Gardien, V., Thompson, A. B., and Ulmer, P. (2000). Melting of Biotite + Plagioclase + Quartz Gneisses: The Role of H2O in the Stability of Amphibole. *Journal of Petrology*, 41(5):651–666.

Genier, F., Bussy, F., Epard, J.-L., and Baumgartner, L. (2008). Water-assisted migmatization of metagraywackes in a Variscan shear zone, Aiguilles-Rouges massif, western Alps. *Lithos*, 102(3-4):575–597.

Glazner, A. F. (2019). The ascent of water-rich magma and decompression heating: A thermodynamic analysis. *American Mineralogist*, 104(6):890–896.

Green, E. C. R., White, R. W., Diener, J. F. A., Powell, R., Holland, T. J. B., and Palin, R. M. (2016). Activity-composition relations for the calculation of partial melting equilibria in metabasic rocks. *Journal of Metamorphic Geology*, 34(9):845–869.

Guernina, S. and Sawyer, E. W. (2003). Large-scale melt-depletion in granulite terranes: An example from the Archean Ashuanipi Subprovince of Quebec. *Journal of Metamorphic Geology*, 21(2):181–201.

Hawthorne, F. C., Oberti, R., Harlow, G. E., Maresch, W. V., Martin, R. F., Schumacher, J. C., and Welch, M. D. (2012). Nomenclature of the amphibole supergroup. *American Mineralogist*, 97(11-12):2031–2048.

Holk, G. J. and Taylor, H. P. (2000). Water as a Petrologic Catalyst Driving 18O/16O Homogenization and Anatexis of the Middle Crust in the Metamorphic Core Complexes of British Columbia. *International Geology Review*, 42(2):97–130.

Holland, T. and Powell, R. (2003). Activity–composition relations for phases in petrological calculations: An asymmetric multicomponent formulation. *Contributions to Mineralogy and Petrology*, 145(4):492–501.

Holland, T. J. B. and Powell, R. (1998). An internally consistent thermodynamic data set for phases of petrological interest: An internally consistent thermodynamic data set. *Journal of Metamorphic Geology*, 16(3):309–343.

Holland, T. J. B. and Powell, R. (2011). An improved and extended internally consistent thermodynamic dataset for phases of petrological interest, involving a new equation of state for solids: Thermodynamic dataset for phases of petrological interest. *Journal of Metamorphic Geology*, 29(3):333–383.

Horstwood, M. S. A., Košler, J., Gehrels, G., Jackson, S. E., McLean, N. M., Paton, C., Pearson, N. J., Sircombe, K., Sylvester, P., Vermeesch, P., Bowring, J. F., Condon, D. J., and Schoene, B. (2016). Community-Derived Standards for LA - ICP - MS U-(Th-)Pb Geochronology – Uncertainty Propagation, Age Interpretation and Data Reporting. *Geostandards and Geoanalytical Research*, 40(3):311–332.

Jamieson, R. A. and Beaumont, C. (2011). Coeval thrusting and extension during lower crustal ductile flow - implications for exhumation of high-grade metamorphic rocks. *Journal of Metamorphic Geology*, 29(1):33–51.

Jamieson, R. A., Beaumont, C., Nguyen, M. H., and Culshaw, N. G. (2007). Synconvergent ductile flow in variable-strength continental crust: Numerical models with application to the western Grenville orogen. *Tectonics*, 26(5):2006TC002036.

Jamieson, R. A., Beaumont, C., Warren, C. J., and Nguyen, M. H. (2010). The Grenville Orogen explained? Applications and limitations of integrating numerical models with geological and geophysical data. *Canadian Journal of Earth Sciences*, 47(4):517–539.

Johannes, W. and Holtz, F. (1996). *The Haplogranite System Qz-Ab-Or*, volume 22, pages 18–57. Springer Berlin Heidelberg, Berlin, Heidelberg.

Ketchum, J. W. F. and Davidson, A. (2000). Crustal architecture and tectonic assembly of the Central Gneiss Belt, southwestern Grenville Province, Canada: A new interpretation. *Canadian Journal of Earth Sciences*, 37:18.

Kohn, M. J., Spear, F. S., and Valley, J. W. (1997). Dehydration-Melting and Fluid Recycling during Metamorphism: Rangeley Formation, New Hampshire, USA. *Journal of Petrology*, 38(9):1255–1277.

Le Fort, P., Cuney, M., Deniel, C., France-Lanord, C., Sheppard, S., Upreti, B., and Vidal, P. (1987). Crustal generation of the Himalayan leucogranites. *Tectonophysics*, 134(1-3):39–57.

Liang, Y. and Parmentier, E. M. (2010). A Two-Porosity Double Lithology Model for Partial Melting, Melt Transport and Melt-rock Reaction in the Mantle: Mass Conservation Equations and Trace Element Transport. *Journal of Petrology*, 51(1-2):125–152.

Lumbers, S. B. and Vertolli, V. M. (2003). Precambrian Geology, Kawagama Lake area; Ontario Geological Survey, Preliminary Map P. 3525.

Manning, C. E. (2018). Fluids of the Lower Crust: Deep Is Different. *Annual Review of Earth and Planetary Sciences*, 46(1):67–97.

Marsh, J. H. and Culshaw, N. G. (2014). Timing and conditions of high-pressure metamorphism in the western Grenville Province: Constraints from accessory mineral composition and phase equilibrium modeling. *Lithos*, 200–201:402–417.

McDonough, W. and Sun, S.-s. (1995). The composition of the Earth. *Chemical Geology*, 120(3-4):223–253.

Palin, R. M., Weller, O. M., Waters, D. J., and Dyck, B. (2016). Quantifying geological uncertainty in metamorphic phase equilibria modelling; a Monte Carlo assessment and implications for tectonic interpretations. *Geoscience Frontiers*, 7(4):591–607.

Paton, C., Woodhead, J. D., Hellstrom, J. C., Hergt, J. M., Greig, A., and Maas, R. (2010). Improved laser ablation U-Pb zircon geochronology through robust downhole fractionation correction. *Geochemistry, Geophysics, Geosystems*, 11(3):2009GC002618.

Plunder, A., Le Pourhiet, L., Räss, L., Gloaguen, E., Pichavant, M., and Gumiaux, C. (2022). Pegmatites as geological expressions of spontaneous crustal flow localisation. *Lithos*, 416–417:106652.

Powell, R. and Holland, T. J. B. (2008). On thermobarometry. *Journal of Metamorphic Geology*, 26(2):155–179.

Rivers, T. (2008). Assembly and preservation of lower, mid, and upper orogenic crust in the Grenville Province—Implications for the evolution of large hot long-duration orogens. *Precambrian Research*, 167(3-4):237–259.

Rivers, T., Culshaw, N. G., Hynes, A., Indares, A., Jamieson, R. A., and Martignole, J. (2012). The Grenville Orogen–A post-LITHOPROBE perspective. In *Tectonic Styles in Canada: The LITHOPROBE Perspective*, number 49 in Geological Association of Canada Special Paper, pages 97–236. Geological Association of Canada.

Rivers, T. and Schwerdtner, W. (2015). Post-peak Evolution of the Muskoka Domain, Western Grenville Province: Ductile Detachment Zone in a Crustal-scale Metamorphic Core Complex. *Geoscience Canada*, 42(4):403.

Sawyer, E. (2010). Migmatites formed by water-fluxed partial melting of a leucogranodiorite protolith: Microstructures in the residual rocks and source of the fluid. *Lithos*, 116(3-4):273–286.

Sawyer, E. W. (2008). *Atlas of Migmatites*. Number 9 in The Canadian Mineralogist. Special Publication. NRC research press, Ottawa.

Schwerdtner, W., Rivers, T., Zeeman, B., Wang, C., Tsolas, J., Yang, J., and Ahmed, M. (2014). Post-convergent structures in lower parts of the 1090–1050 Ma (early-Ottawan) thrust-sheet stack, Grenville Province of Ontario, southern Canadian Shield. *Canadian Journal of Earth Sciences*, 51(3):243–265.

Slagstad, T. (2003). *Muskoka and Shawanaga Domains, Central Gneiss Belt, Grenville Province, Ontario: Geochemical and Geochronological Constraints on Pre-Grenvillian and Grenvillian Geological Evolution*. PhD thesis, Dalhousie University, Halifax, Nova Scotia.

Slagstad, T., Hamilton, M. A., Jamieson, R. A., and Culshaw, N. G. (2004). Timing and duration of melting in the mid orogenic crust: Constraints from U–Pb (SHRIMP) data, Muskoka and Shawanaga domains, Grenville Province, Ontario. *Canadian Journal of Earth Sciences*, 41:27.

Slagstad, T., Jamieson, R. A., and Culshaw, N. G. (2005). Formation, Crystallization, and Migration of Melt in the Mid-orogenic Crust: Muskoka Domain Migmatites, Grenville Province, Ontario. *Journal of Petrology*, 46(5):893–919.

Sláma, J., Košler, J., Condon, D. J., Crowley, J. L., Gerdes, A., Hanchar, J. M., Horstwood, M. S., Morris, G. A., Nasdala, L., Norberg, N., Schaltegger, U., Schoene, B., Tubrett, M. N., and Whitehouse, M. J. (2008). Plešovice zircon — A new natural reference material for U–Pb and Hf isotopic microanalysis. *Chemical Geology*, 249(1-2):1–35.

Solar, G. S. and Brown, M. (2001). Petrogenesis of Migmatites in Maine, USA: Possible Source of Peraluminous Leucogranite in Plutons? *Journal of Petrology*, 42(4):789–823.

Stuart, C. A., Daczko, N. R., and Piazolo, S. (2017). Local partial melting of the lower crust triggered by hydration through melt–rock interaction: An example from Fiordland, New Zealand. *Journal of Metamorphic Geology*, 35(2):213–230.

Tafur, L. A. and Diener, J. F. A. (2020). Mineral equilibrium constraints on the feasibility of diffusive H2O-fluxed melting in the continental crust. *Journal of Metamorphic Geology*, 38(7):719–742.

Timmerman, H., Jamieson, R. A., Parrish, R. R., and Culshaw, N. G. (2002). Coeval migmatites and granulites, Muskoka domain, southwestern Grenville Province, Ontario. *Canadian Journal of Earth Sciences*, 39:239–258.

Timmermann, H., Jamieson, R. A., Culshaw, N. G., and Parrish, R. R. (1997). Time of metamorphism beneath the Central Metasedimentary Belt boundary thrust zone, Grenville Orogen, Ontario: Accretion at 1080 Ma? *Canadian Journal of Earth Sciences*, 34(7):1023–1029.

Tuttle, O. F. and Bowen, N. L. (1958). Origin of granite in the light of experimental studies in the system NaAlSi3O8–KAlSi3O8–SiO2–H2O. In *Geological Society of America Memoirs*, volume 74, pages 1–146. Geological Society of America.

Vanardois, J., Trap, P., and Marquer, D. (2024). Crucial role of water-present melting in metagranite: Implications for the instigation of crustal-scale shear zones. *Geology*, 52(3):199–204.

Vermeesch, P. (2018). IsoplotR: A free and open toolbox for geochronology. *Geoscience Frontiers*, 9(5):1479–1493.

Vermeesch, P. (2021). On the treatment of discordant detrital zircon U–Pb data. *Geochronology*, 3(1):247–257.

Volante, S., Pourteau, A., Li, Z.-X., Collins, W. J., Doucet, L. S., Olierook, H. K. H., Martin, L., and Smit, M. A. (2025). Oxygen isotope shifts reveal fluid-fluxed melting in continental anatexis. *Communications Earth & Environment*, 6(1):282.

Weinberg, R. F. and Hasalová, P. (2015). Water-fluxed melting of the continental crust: A review. *Lithos*, 212–215:158–188.

White, R. W., Pomroy, N. E., and Powell, R. (2005). An *in situ* metatexite–diatexite transition in upper amphibolite facies rocks from Broken Hill, Australia. *Journal of Metamorphic Geology*, 23(7):579–602.

White, R. W., Powell, R., and Clarke, G. L. (2002). The interpretation of reaction textures in Fe-rich metapelitic granulites of the Musgrave Block, central Australia: Constraints from mineral equilibria calculations in the system $K_2O$–FeO–MgO–$Al_2O_3$–$SiO_2$–$H_2O$–$TiO_2$–$Fe_2O_3$. *Journal of Metamorphic Geology*, 20(1):41–55.

White, R. W., Powell, R., and Holland, T. J. B. (2007). Progress relating to calculation of partial melting equilibria for metapelites. *Journal of Metamorphic Geology*, 25(5):511–527.

White, R. W., Powell, R., Holland, T. J. B., Johnson, T. E., and Green, E. C. R. (2014a). New mineral activity–composition relations for thermodynamic calculations in metapelitic systems. *Journal of Metamorphic Geology*, 32(3):261–286.

White, R. W., Powell, R., and Johnson, T. E. (2014b). The effect of Mn on mineral stability in metapelites revisited: New a–x relations for manganese-bearing minerals. *Journal of Metamorphic Geology*, 32(8):809–828.

Whitney, D. L. and Evans, B. W. (2010). Abbreviations for names of rock-forming minerals. *American Mineralogist*, 95(1):185–187.

Wiedenbeck, M., Hanchar, J. M., Peck, W. H., Sylvester, P., Valley, J., Whitehouse, M., Kronz, A., Morishita, Y., Nasdala, L., Fiebig, J., Franchi, I., Girard, J.-P., Greenwood, R., Hinton, R., Kita, N., Mason, P., Norman, M., Ogasawara, M., Piccoli, P., Rhede, D., Satoh, H., Schulz-Dobrick, B., Skår, O., Spicuzza, Mj., Terada, K., Tindle, A., Togashi, S., Vennemann, T., Xie, Q., and Zheng, Y.-F. (2004). Further Characterisation of the 91500 Zircon Crystal. *Geostandards and Geoanalytical Research*, 28(1):9–39.

Xia, Y.-S., Gao, P., Sun, G.-C., Zhao, Z.-F., Qin, L., Wen, G., Li, Z.-X., and Dai, L.-Q. (2025). Fluid-fluxed melting of juvenile lower crust traced by molybdenum isotopes. *Geology*, 53(2):125–129.

Yakymchuk, C. and Brown, M. (2014). Consequences of open-system melting in tectonics. *Journal of the Geological Society*, 171(1):21–40.

Yardley, B. W. D. and Barber, J. P. (1991). Melting reactions in the Connemara Schists: The role of water infiltration in the formation of amphibolite facies migmatites. *American Mineralogist*, 76:848–856.

Yardley, B. W. D. and Valley, J. W. (1997). The petrologic case for a dry lower crust. *Journal of Geophysical Research: Solid Earth*, 102(B6):12173–12185.

Zhang, Y. and Gan, T. (2022). Diffusion in Melts and Magmas. *Reviews in Mineralogy and Geochemistry*, 87(1):283–337.

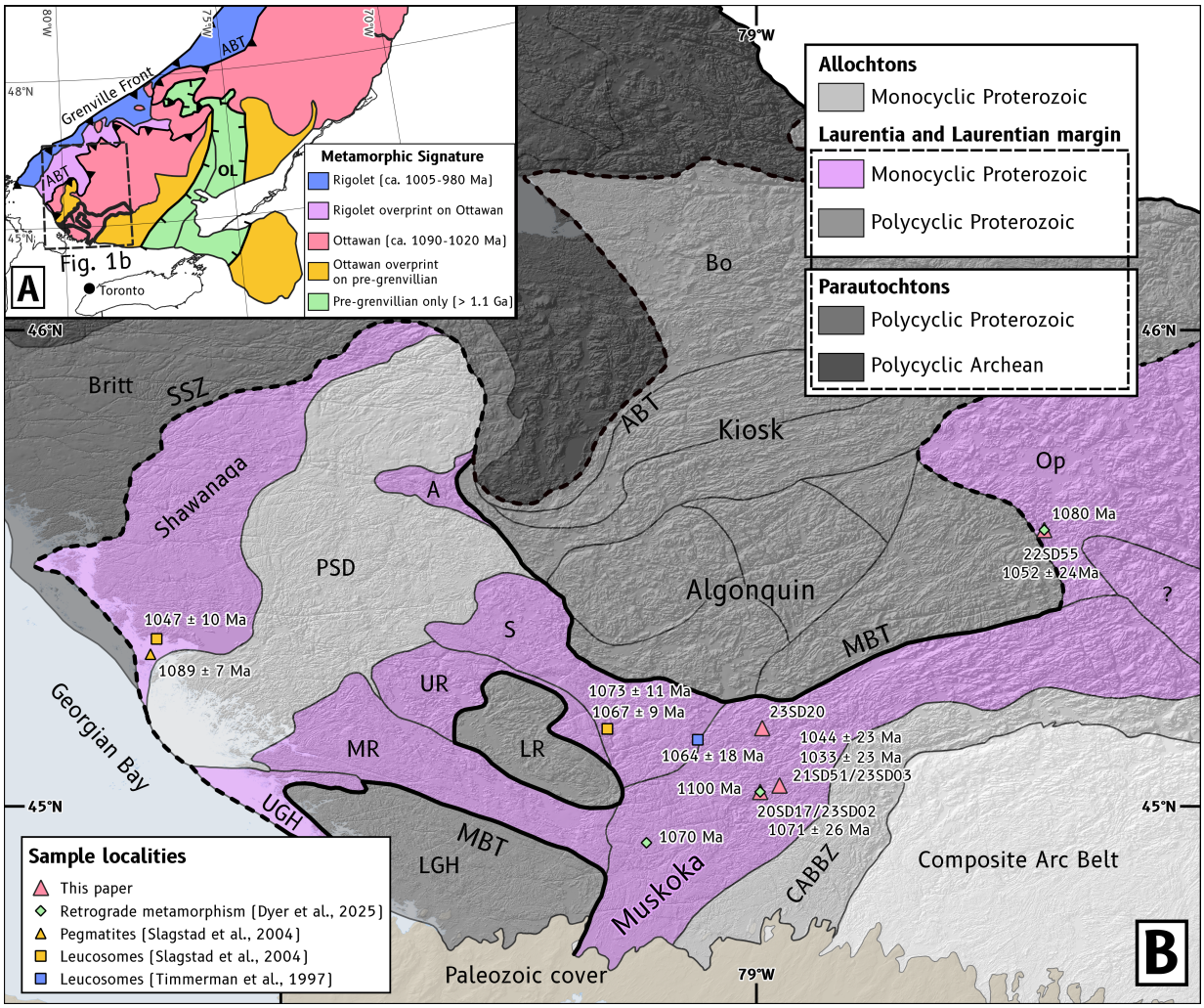


**Figure 4.1: (A)**: Overview map of the Grenville Province showing metamorphic affinity of different regions in the Grenville (Modified after Rivers (2008)) Abbreviations: OL = Orogenic Lid; ABT = Allochthon Boundary Thrust. **(B)**: Map of the Central Gneiss Belt in Ontario with the Muskoka domain highlighted (Modified after Culshaw et al. (2016)). Important sample locations and measured ages from Chapter 2, Slagstad et al. (2004), and Timmermann et al. (1997) are also shown. Location of pegmatites analyzed in this paper are shown with associated measured ages. Abbreviations: MBT = Monocyclic Boundary Thrust; SSZ = Shawanaga shear zone; CABBZ = Composite Arc Belt Boundary Zone; UGH, LGH, UR, LR, A, Op = upper-, lower Go Homme, upper-, lower Rosseau, Ahmic, Opeongo domains; MR, S = Moon River, Seguin subdomains; PSD = Parry Sound domain; Bo = Bonfield domain. Sample coordinates shown in Table C.7.

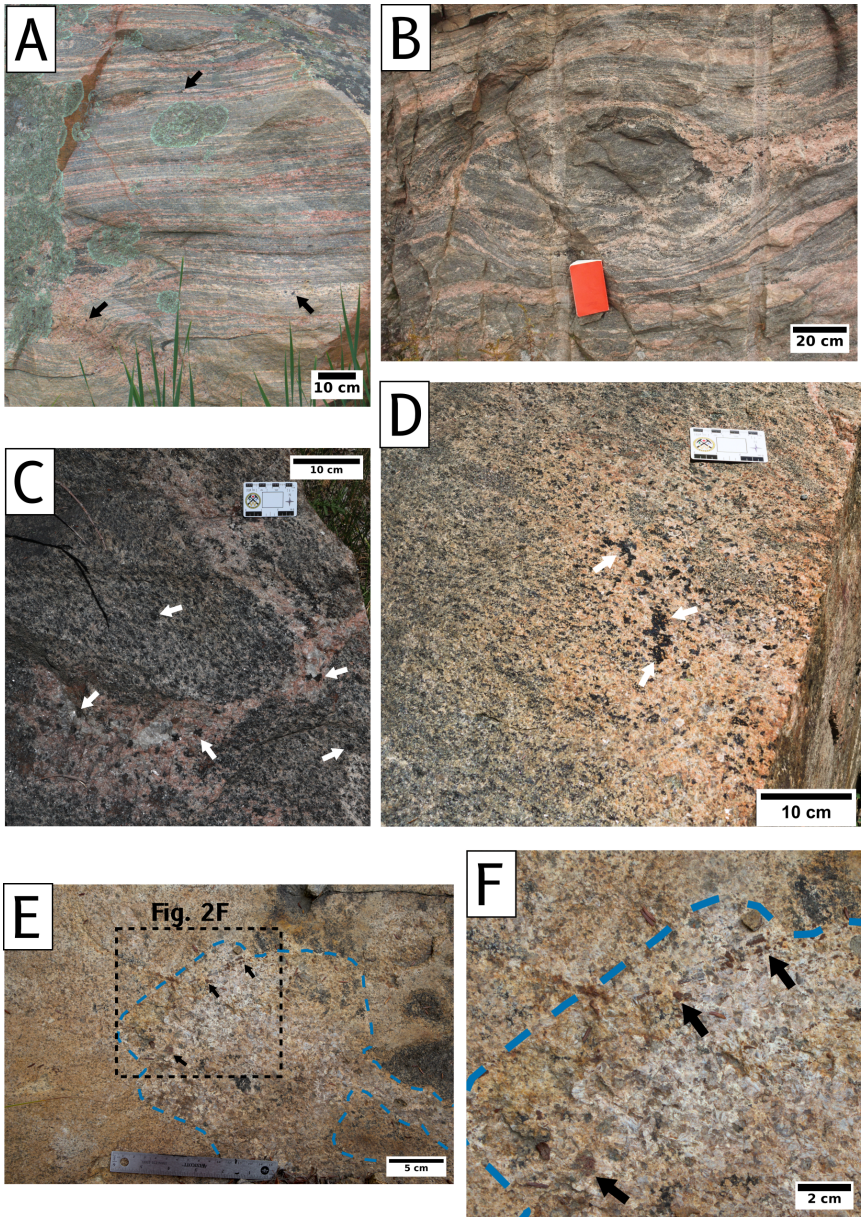


**Figure 4.2:** Example photos of common rock types in the Muskoka domain. **(A)**: Stromatic migmatite with granodiorite mesosome with rare amphibole porophyroblasts (arrows) present in the leucosome. **(B)**: Stromatic migmatite with amphibolite boudin. Leucosome is concentrated in the boudin necks. **(C)**: Patch migmatite with both gradational and sharp contacts between leucosome and host. Amphibole and biotite porphyroblasts (arrows) are present both in the leucosome and the surrounding rock. **(D)**: Patch migmatite with gradational contacts between leucosome and host. Leucosome contains amphibole porophyroblasts up to 2 cm long (arrows). **(E)**: Garnet-bearing (arrows) leucosome in the monzonitic host rock (sample 23SD20A) **(F)**: Close-up of garnet in leucosome in the monzonitic host rock (sample 23SD20).

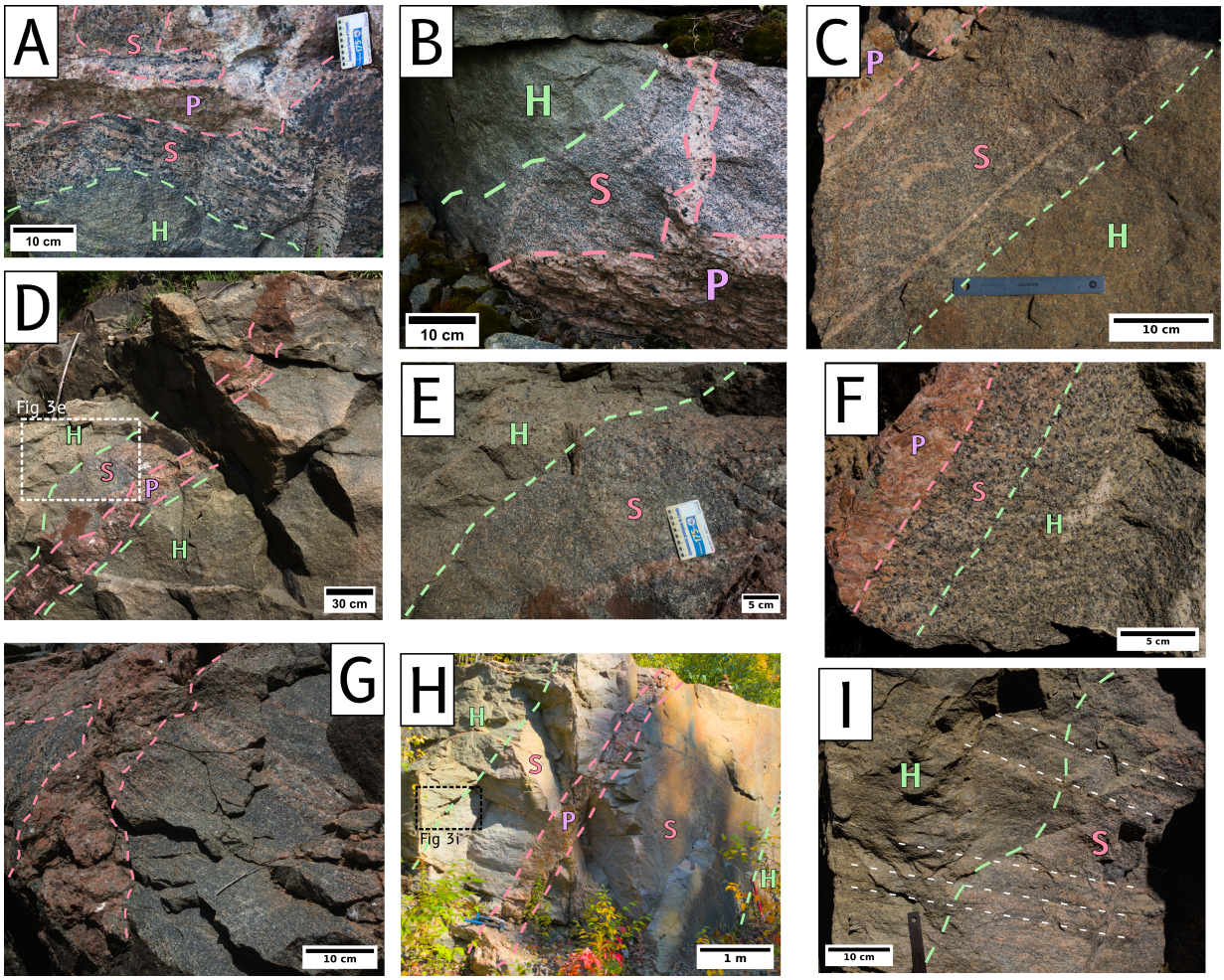


**Figure 4.3:** Example photos of pegmatites (P) crosscutting weakly deformed metagranodiorite and metamonzonite hosts (H) the reaction selvages (S) surrounding them that are occasionally preserved in the Muskoka domain. **(A)**: Pegmatite (Sample 23SD02C) crosscutting granulite facies metamonzonite (Sample 23SD02A). The pegmatite is deformed, and a foliation is present in the reaction selvage that is parallel to the foliation present in the host rock. The reaction selvage contains abundant amphibole and biotite and alkali-feldspar rich leucosomes. The host rock contains garnet and clinopyroxene. **(B & C)**: Pegmatite (Sample 22SD55D, Fig. 4.4 C) crosscutting granulite facies metamonzonite (Sample 22SD55E, Fig 4.4 A). Both pegmatites have sharp contacts with the reaction selvages (Sample 22SD55B Fig. 4.4 B). The reaction selvages contain abundant amphibole and alkali-feldspar rich leucosome lenses. **(D & E)**: Pegmatite crosscutting amphibolite facies metagranodiorite (Sample 21SD51D, Fig. 4.8 G). The reaction selvage (Sample 21SD51E) contains biotite porphyroblasts throughout (Fig. 4.4 H) and amphibole porphyroblasts (Fig. 4.4 I) at the margin of the pegmatite. **(F)**: Pegmatite (Sample 23SD03E) crosscutting amphibolite facies granodiorite (Sample 23SD03B). Reaction selvage (Sample 23SD03C) contains coarser grained amphibole porphyroblasts than the host rock and a greater abundance of pink alkali-feldspar. **(G)**: Deformed pegmatite (Sample 23SD03K) crosscutting amphibolite facies granodiorite. The host rock is more leucosome-rich with coarse grained amphibole occurring closer to the pegmatite margin. Numerous offshoots from the pegmatite occur with gradational contacts with the host rock. **(H)**: Pegmatite crosscutting granulite facies monzonite (Samples 23SD20A, 23SD20B, 23SD20G, Fig. 4.4 D). The reaction selvage (Samples 23SD20C, 23SD20F, Fig. 4.4 E & F) contains abundant amphibole and foliated alkali-feldspar rich leucosome. The foliation in the reaction selvage is continuous with the foliation present in the host rock **(I)**.

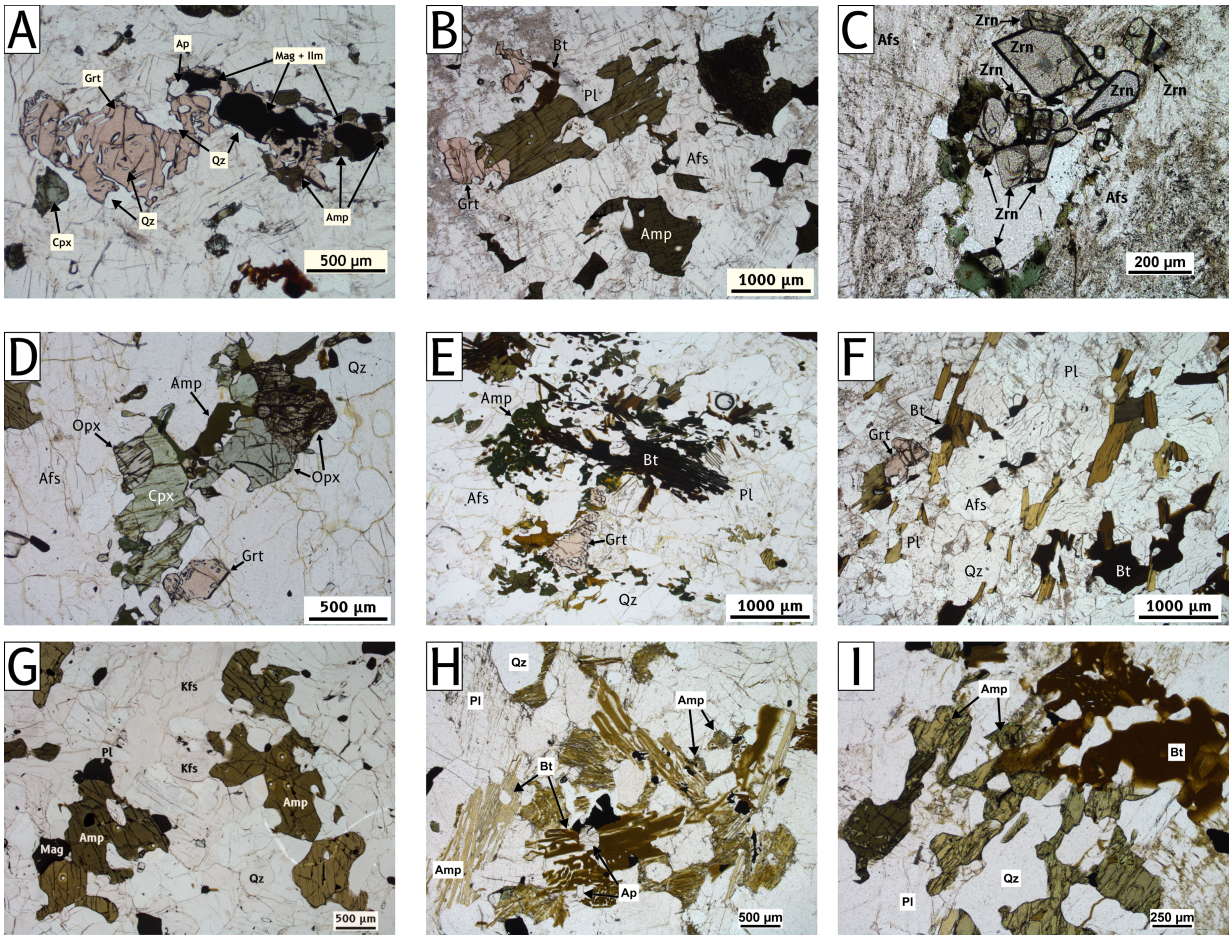


**Figure 4.4:** Transmitted light photomicrographs of select samples, abbreviations after Whitney and Evans (2010). **(A)**: Sample 22SD55E, representative of the host rock at that outcrop (Fig. 4.3 B). Abundant subhedral garnet is present. **(B)**: Sample 22SD55B, representative of the reaction selvage around pegmatites at that outcrop (Fig. 4.3 B). Garnet is still present in the selvage as it is in the host rock, but it is resorbed and rarely partially overgrown by amphibole. **(C)**: Occurrence of zircon in pegmatite 22SD55D (Fig. 4.3 B), occurrence of zircon in a vug indicates that zircon dates are not inherited. **(D)**: Sample 23SD20A, representative of the host rock at that outcrop (Fig. 4.3 H). This sample contains garnet, orthopyroxene, and clinopyroxene. **(E)**: Sample 23SD20C, from the reaction selvage around the pegmatite ∼1 m away from the pegmatite (Fig. 4.3 H). Contains abundant amphibole, biotite, and commonly partially resorbed garnet. **(F)**: Sample 23SD20D, the reaction selvage at the pegmatite margin(Fig. 4.3 H). Contains abundant biotite and rare highly resorbed garnet. **(G)**: Sample 21SD51D, representative of the host rock around pegmatite in that outcrop (Fig. 4.3 D). **(H)**: Sample 21SD51E, representative of the reaction selvage around the pegmatite in that outcrop (Fig. 4.3 D). Contains abundant biotite with vermicular intergrowth with quartz. **(I)**: Sample 21SD51F, representative of reaction selvage at pegmatite margin in that outcrop (Fig. 4.3 D). Contains abundant amphibole and biotite.

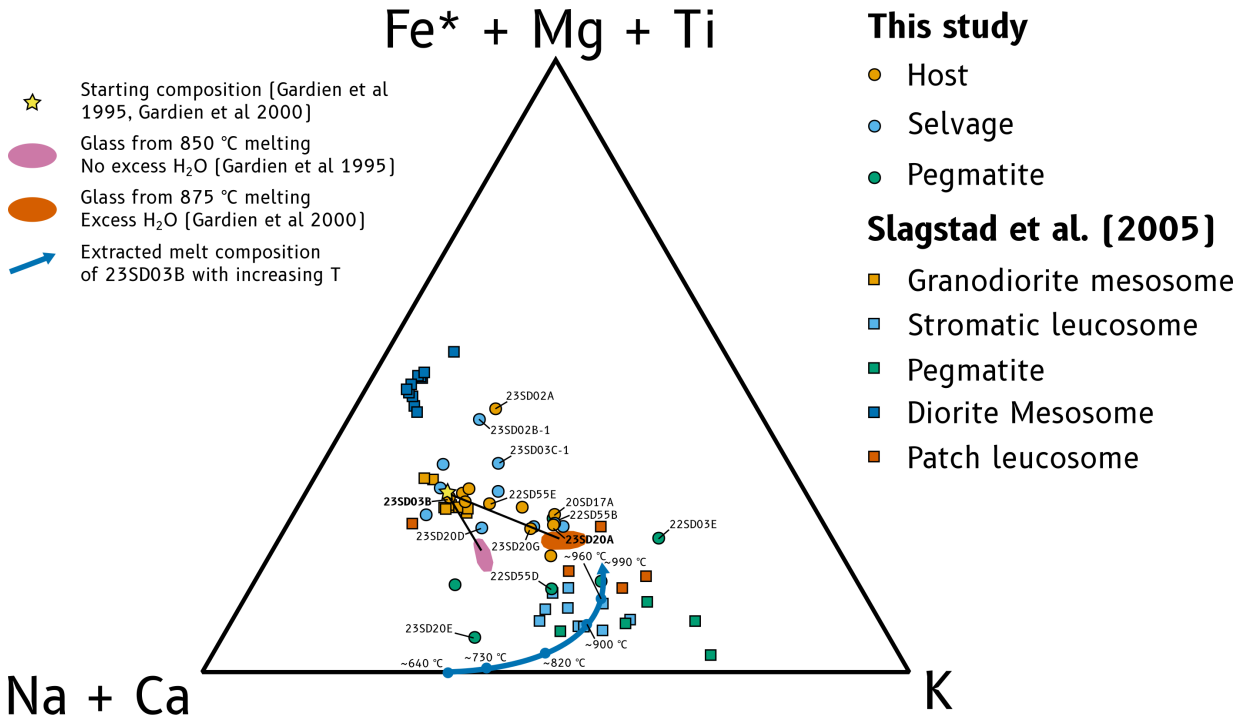


**Figure 4.5:** Molar Na + Ca, Fe* + Mg + Ti, K ternary diagram, Fe* = Total Fe (Solar and Brown, 2001) showing variability in bulk rock geochemistry of host rocks, pegmatites, and reaction selvages adjacent to pegmatites from this study as well as mesosome, leucosome, and pegmatite geochemistry from Slagstad et al. (2005). Select experimental results of melting of a granodiorite sample at 850 °C with no excess $H_2O$ (Gardien et al., 1995) and at 875 °C and 4 wt% $H_2O$ (Gardien et al., 2000). Arrow indicates the trend of melt composition generated in the first stage of modelled melting of sample 23SD03B (Fig. 4.12) from the lowest temperature of extracted melt ($\sim$ 630 °C) to the highest temperature ($\sim$ 990 °C), independent of the initial $H_2O$ content of the source rock, points with approximate extraction temperature are labelled.

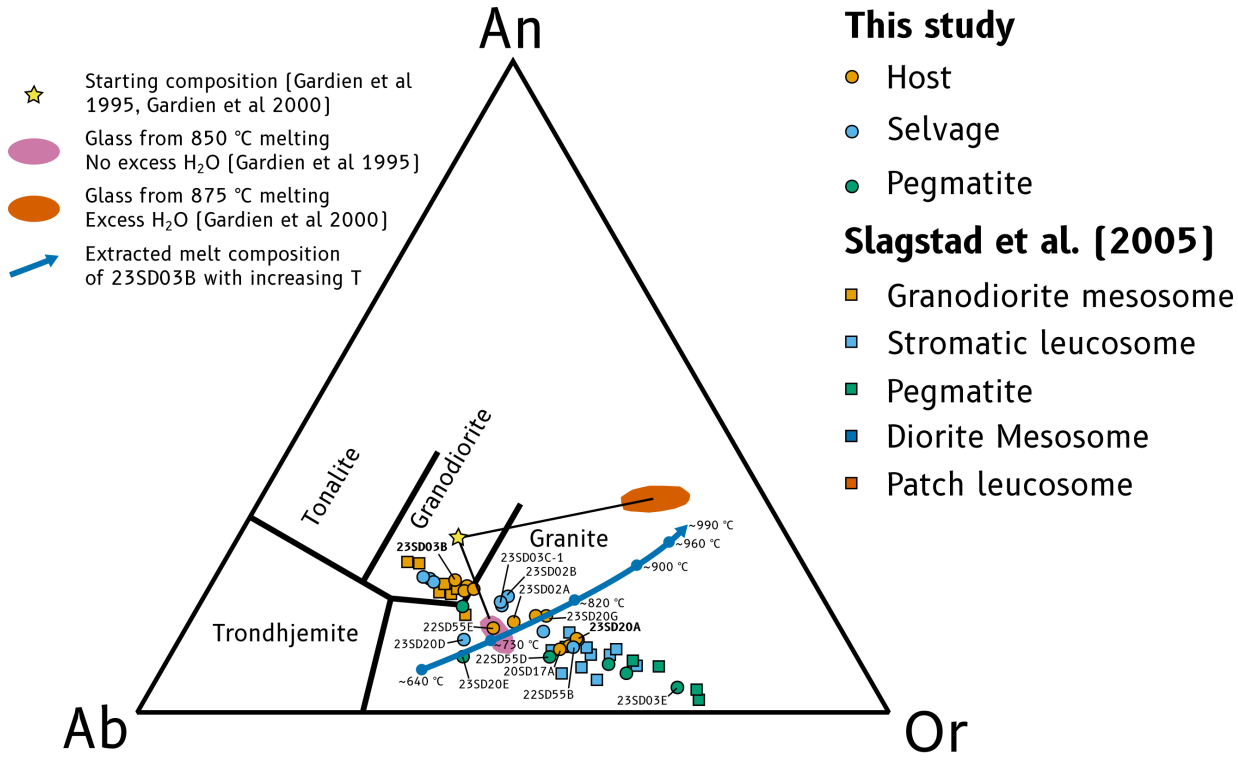


**Figure 4.6:** Normative An-Ab-Or ternary diagram (Barker, 1979) showing CIPW calculated variability in bulk rock mineral proportions of host rocks, pegmatites, and reaction selvages adjacent to pegmatites from this study as well as mesosome, leucosome, and pegmatite mineral proportions from Slagstad et al. (2005). Select experimental results of melting of a granodiorite sample at 850 °C with no excess $H_2O$ (Gardien et al., 1995) and at 875 °C and 4 wt% $H_2O$ (Gardien et al., 2000). Arrow indicates the trend of melt composition generated in the first stage of modelled melting of sample 23SD03B (Fig. 4.12) from lowest temperature of extracted melt ($\sim$ 630 °C) to the highest temperature ($\sim$ 990 °C), independent of the initial $H_2O$ content of the source rock, points with approximate extraction temperature are labelled.

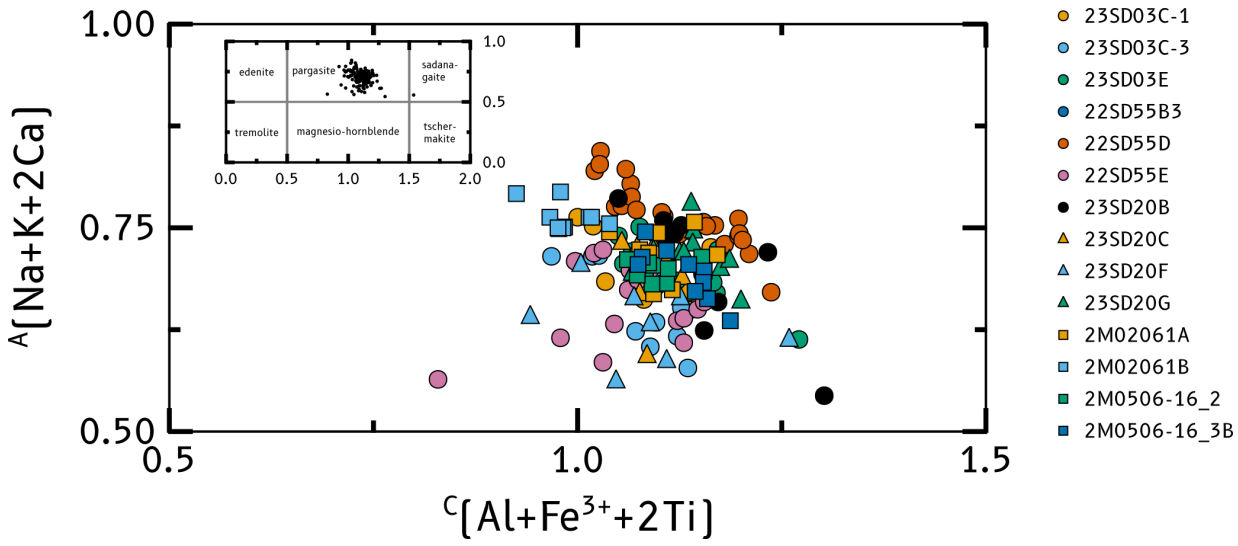


**Figure 4.7:** Calcium amphibole classification plot (Hawthorne et al., 2012) with electron microprobe analyses of amphiboles from hosts, selvages, and pegmatites (circles and triangles) as well as granodioritic migmatites samples collected by Slagstad et al. (2005) (squares).

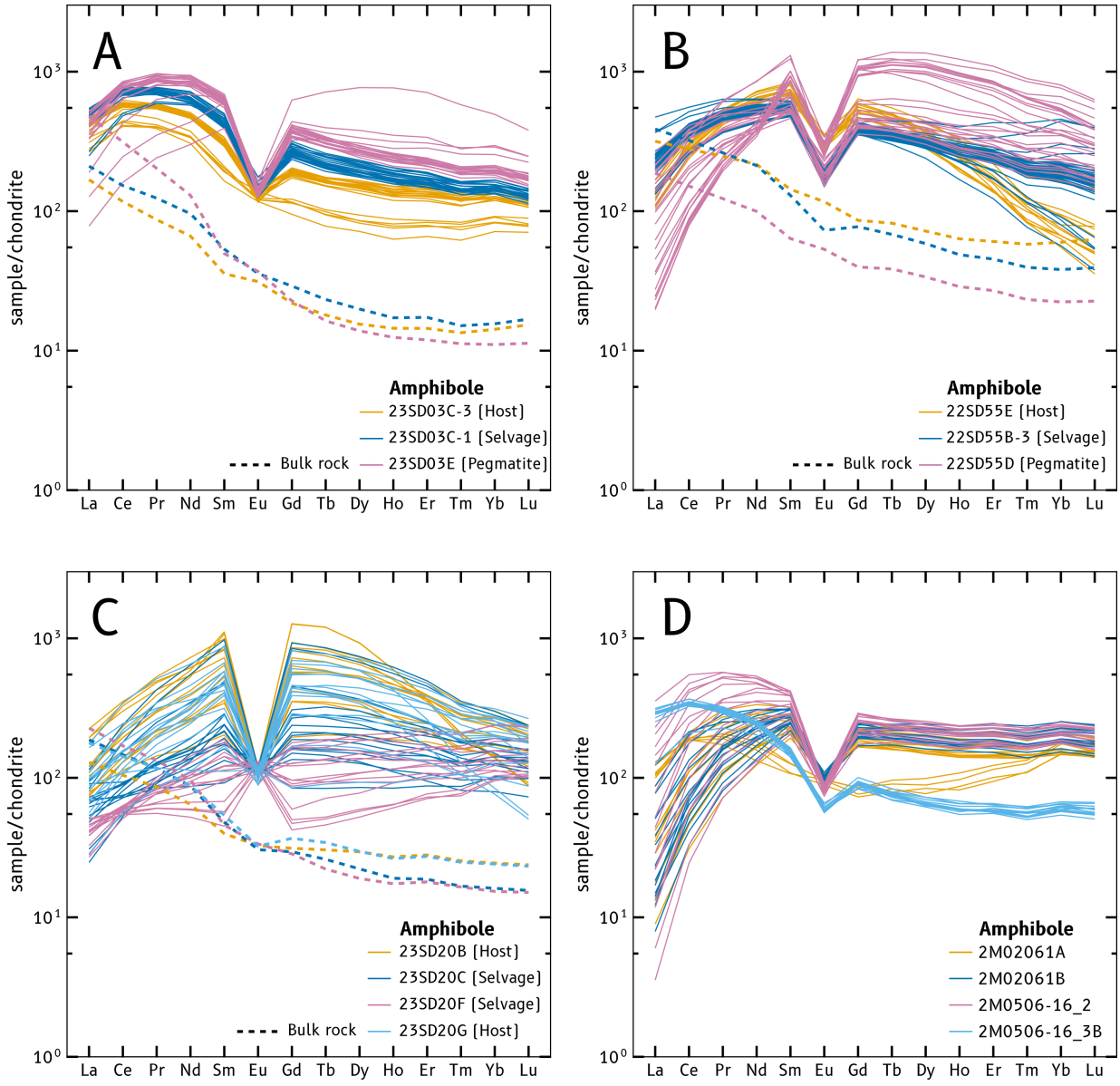


**Figure 4.8:** Chondrite-normalized (McDonough and Sun, 1995) REE plots for amphibole (solid lines) and whole rock (dashed lines). **(A)**: Samples from pegmatite crosscutting granodioritic host rock (outcrop 23SD03, Fig. 4.3 D, E, F, 4.4 G, H, I) **(B)**: Samples from pegmatite crosscutting monzonitic host rock (outcrop 22SD55 (Fig. 4.3 B, C, 4.4 A, B, C) **(C)**: Samples from pegmatite crosscutting monzonitic host rock (outcrop 23SD20 Fig. 4.3 G, H, I, 4.4 D, E, F) **(B)**: Samples from granodioritic stromatic migmatites discussed by Slagstad et al. (2005).

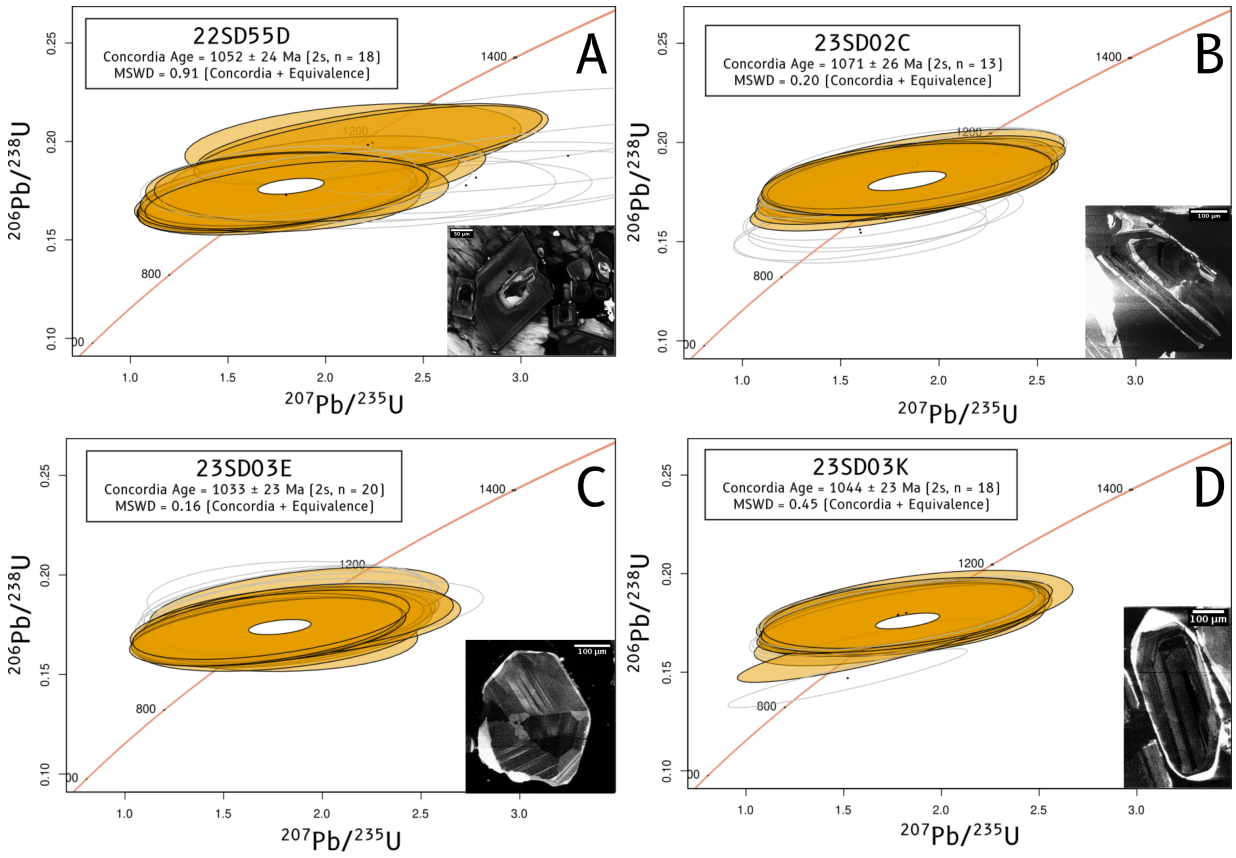


**Figure 4.9:** Wetherill plots of pegmatite zircons plotted using IsoplotR (Vermeesch, 2018) with representative cathodoluminescence images of zircon grains. Error ellipses show 2s error. Concordia age is shown with propogated error. Discordant analyses of 22SD55D, 23SD02C, 23SD03E, 23SD03K shown as empty ellipses, concordance is defined as a value between -3 and 5 using the concordia distance method (Vermeesch, 2021) **(A)**: Analyses of zircons *in situ* in thin section of sample 22SD55D including concordia age. **(B, C, D)**: Analyses of zircon separates of samples 23SD02C, 23SD03E, and 23SD03K respectively, including concordia ages.

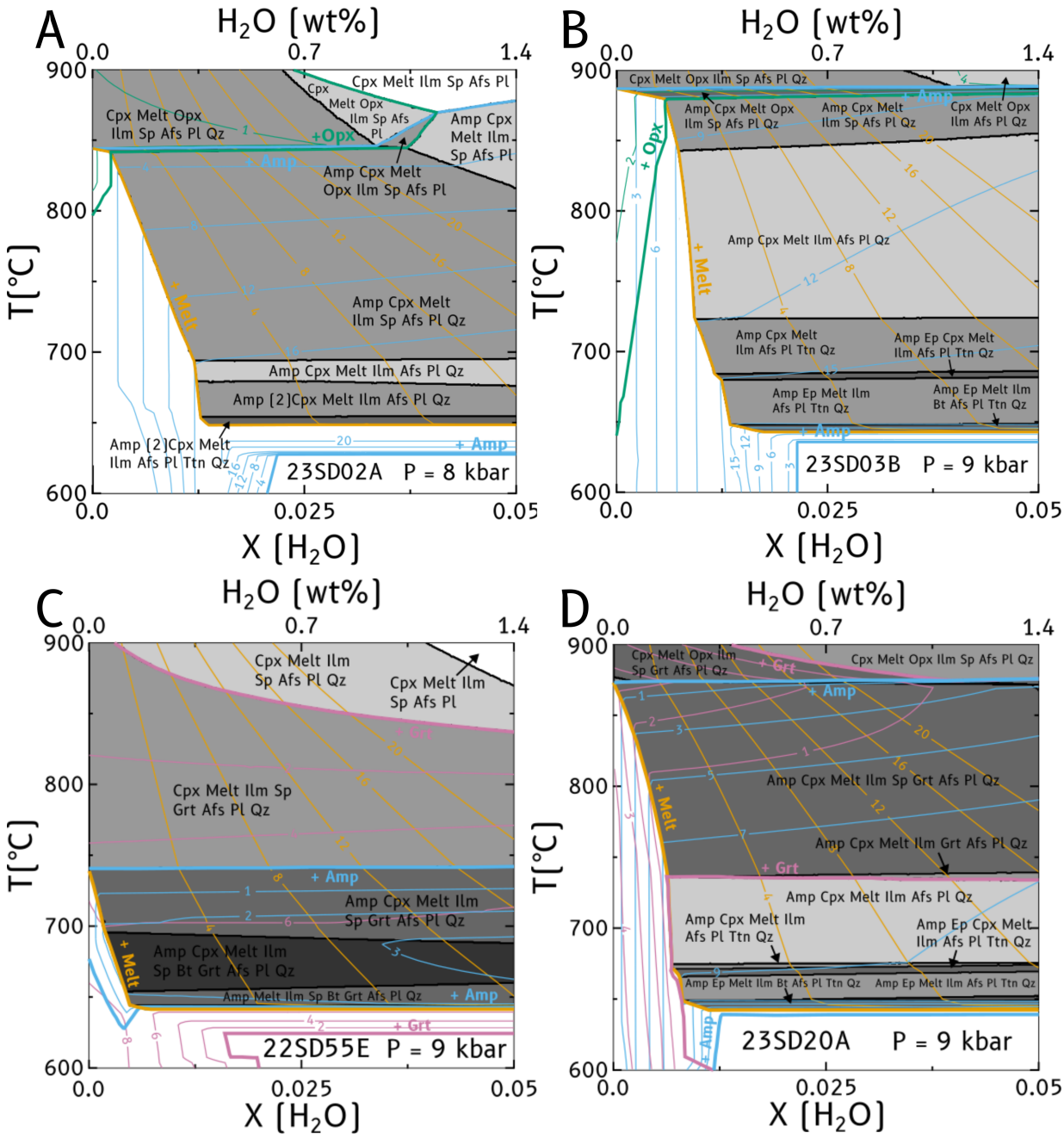


**Figure 4.10:** T–X pseudosections for select host rock compositions. **(A)**: 23SD02A at 8 kbar, corresponding to the host rock in Fig. 4.3 A. **(B)**: 23SD03B at 9 kbar, corresponding to the host rock in Fig. 4.3 E and F as well as granodiorite mesosome analyzed by Slagstad et al. (2005). **(C)**: 22SD55B at 9 kbar, corresponding to the host rock in Fig. 4.3 B and C. **(D)**: 23SD20A at 9 kbar, corresponding to the host rock in Fig. 4.3 H and I. Abbreviations after Whitney and Evans (2010).

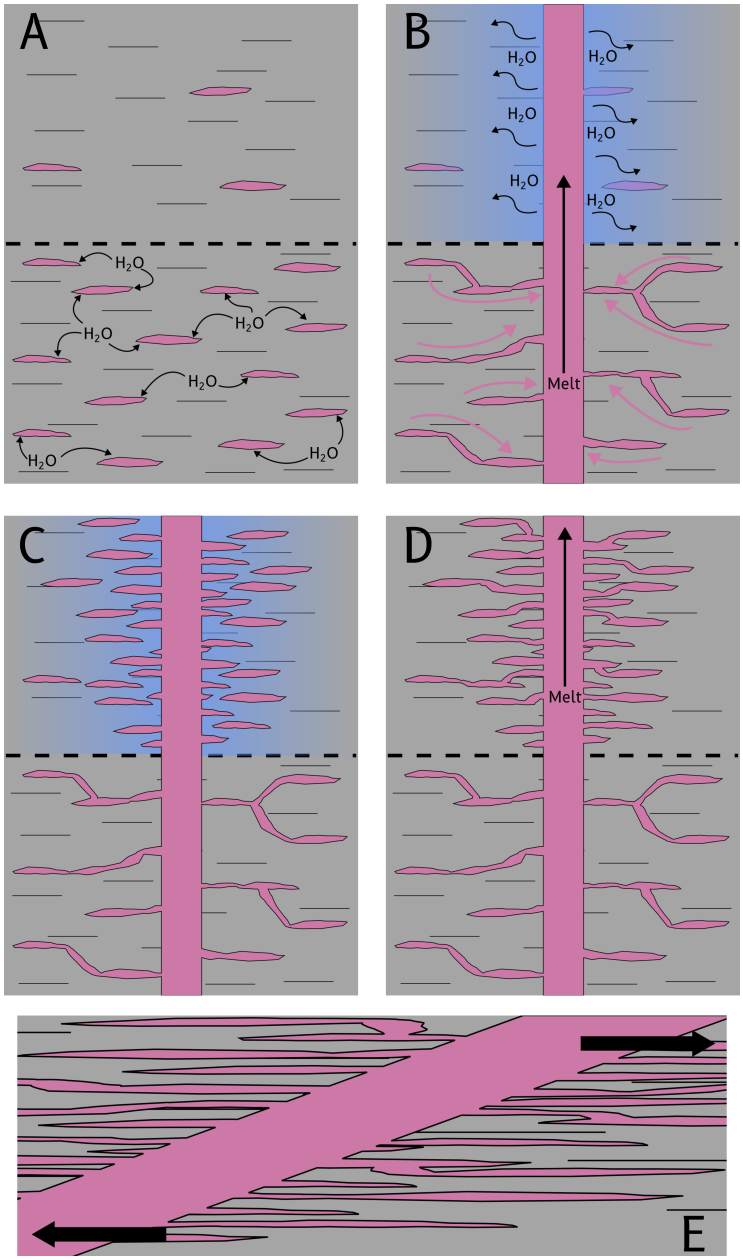


**Figure 4.11:** Schematic sketch showing how $H_2O$-fluxed melting would propagate through the crust. **(A)**: Hydrate breakdown melting occurs at depth resulting in $H_2O$ strongly partitioning into the melt phase **(B)**: Melt is voluminous enough to mobilize and is extracted from the source rock at depth and transported to higher levels. $H_2O$ diffuses from the hydrous melt into the relatively anhydrous host rock. **(C)**: Increasing $H_2O$ in the host rock induces high degrees of melting. **(D)**: Melt is mobilized and extracted, moving to higher levels to continue the cycle. **(E)**: The dike and leucosome are deformed into stromatic gneiss.

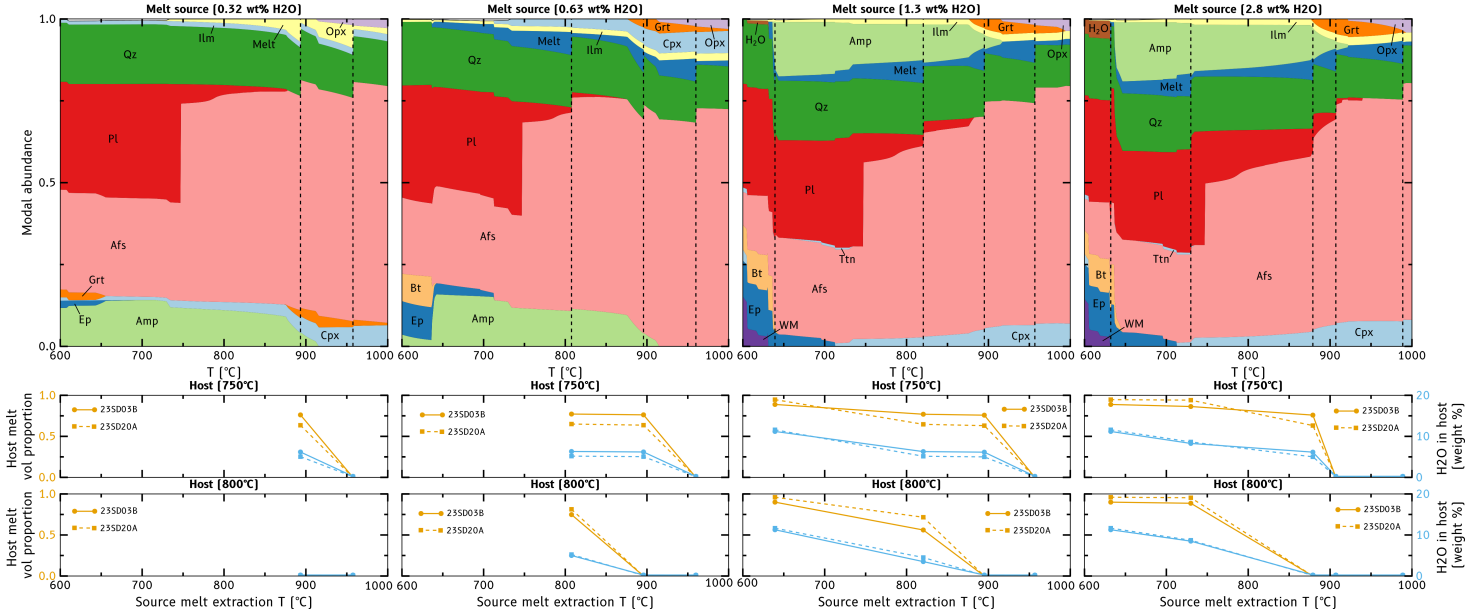


**Figure 4.12:** Results of $H_2O$-fluxed melting model. The source rock is sample 23SD03B, representing the granodiorite commonly found throughout the Muskoka domain with the same composition of mesosomes in the stromatic migmatites of Slagstad et al. (2005). Modebox diagrams of four different $H_2O$ contents in the source rock are shown in the first row, following an isobaric heating path at 10 kbar. Melt volume and resulting $H_2O$ in the host rock after $H_2O$ equilibration with the extracted melts are shown for 23SD03B and 23SD20A at 750°C and 800°C and 9 kbar in the bottom two rows. See text for more details. Abbreviations after Whitney and Evans (2010).

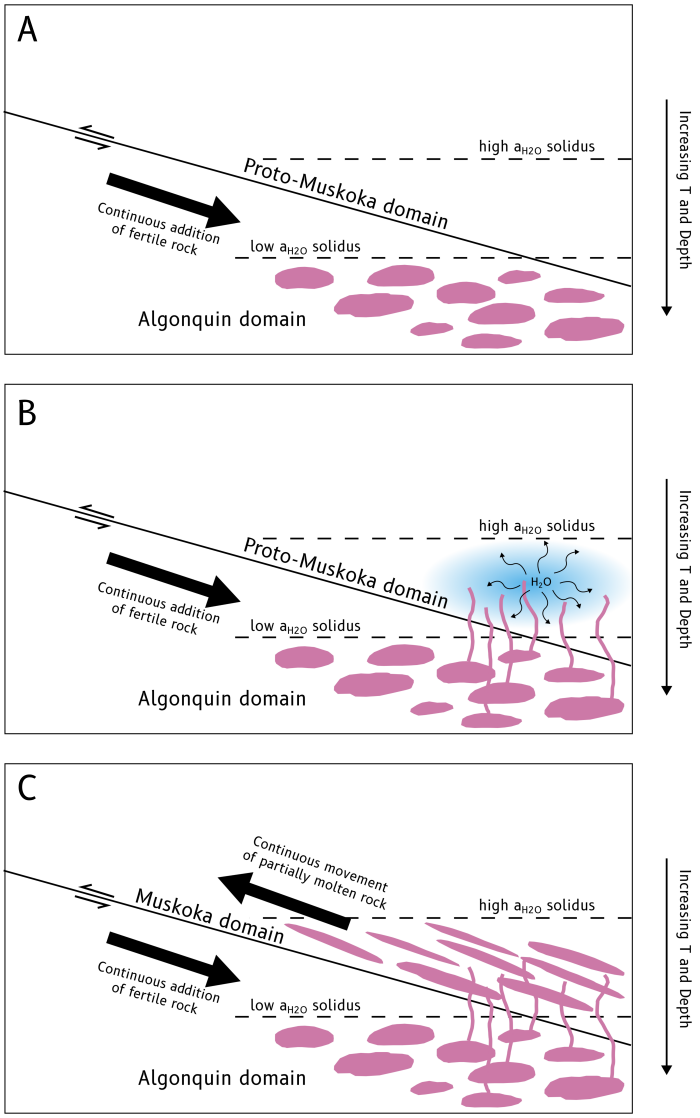


**Figure 4.13:** Schematic cross-section of a possible tectonic model for the Muskoka and related domains. **(A)**: The upper block (Muskoka domain) is thrusted over the lower block (Algonquin and related domains), and melting occurs at depth in the lower block. **(B)**: Melt is transported upward from the lower block into the upper block where $H_2O$ is lost as in Fig. 4.11. **(C)**: Melting occurs in the upper block, enhancing deformation and movement of the two blocks, continuous movement of these two blocks allows a constant influx of fertile rock in the lower block and continuous addition of $H_2O$ and melting in the upper block.

# Chapter 5

# Conclusions

## 5.1 Summary of research

This thesis addresses several important questions about metamorphic reactions at high temperatures at both the micro-scale and the macro-scale. The Muskoka domain was the common link between these disparate scales of investigation and was used to demonstrate how approaching metamorphic problems from multiple perspectives provides insight into both broad metamorphic processes and regional tectonic processes.

On the micro-scale, new zircon-forming reactions in meta-granitoids were determined (Chapter 2). Multiple examples of zircon-growth from the breakdown of titanomagnetite were found. This was established with a detailed analysis of textures in combination with trace element measurements of potential Zr source minerals and phase equilibrium modelling. Chapter 2 demonstrated that titanomagnetite was a likely source for Zr during zircon growth, it was concluded that this zircon growth occurred during retrogression. The measured dates of these zircons were then used based on this interpretation to provide new insight into the tectonics in the Grenville Province, suggesting that the orogeny may have began tens of millions of years earlier than previously thought.

The occurrence of a 165 zircon grains with metamorphic overgrowths in a single thin section allowed an investigation into the kinetics of zircon growth and the relative rate of diffusion of key trace elements during melt crystallization (Chapter 3). Using trace element analyses of zircon and measurements of internal zircon textures, zircon growth was shown to be interface-controlled and size dependent and that Hf, U, Th, Y, and heavy rare earth elements all diffuse slower than zircon growth during melt crystallization in a

migmatite. This work raises doubt on the reliability of trace element indicators of reaction co-products in metamorphic zircon, but allows for more comprehensive studies into trace element kinetics in migmatites using accessory minerals like zircon.

On the macro-scale, the problem of apparent regional-scale fluid-fluxed melting in the Muskoka domain of the Grenville province was addressed (Chapter 4). Previous work had established the extensive and expansive fluid-fluxed melting in the region (Slagstad et al., 2005), but as with many other known occurrences of $H_2O$-fluxed melting there was no clear fluid source and the mechanism for how the fluid infiltrated into the domain was uncertain. Field evidence was found that suggests that $H_2O$ was being transported into the Muskoka domain by hydrous melt. Using a two-step thermodynamic model, I demonstrated that this could have easily occurred with the $H_2O$ being lost only by diffusion and without free fluid being required. This model was combined with the insights provided by retrograde zircon dates that suggested relatively early cooling (Chapter 2) to produce a simple tectonic model of continuous thrusting of the Muskoka domain over the underlying Algonquin domain that melted at depth and provided a source of hydrous melt over tens of millions of years. This work further emphasizes the great research opportunities in the Grenvillian orogeny and the often-neglected Proterozoic tectonics. As more studies emerge to challenge (e.g. Gervais et al., 2023) the previously accepted models (Rivers et al., 2012), a better understanding of crustal melting processes is critical to determine how the Grenvillian orogeny developed and all orogens where $H_2O$-fluxed melting occurs.

## 5.2 Future work and recommendations

The research presented in this thesis opens many potential directions for future work related to accessory mineral reactions, trace element kinetics, and $H_2O$-fluxed melting in high temperature metamorphic systems. Zircon growth from titanomagnetite breakdown was proposed to have occurred during cooling (Chapter 2), which is contradictory to the interpretations of many metamorphic zircon ages, particularly in the Grenville Province. A re-evaluation of published metamorphic ages in the Grenville (e.g. summarized by Rivers, 2008) and targeted re-analysis of key samples using modern techniques to assess the relative timing of growth of the dated minerals would refine our understanding of the recently challenged tectonic model for the Grenville (Gervais et al., 2023) and provide greater insight into when metamorphism in the Grenvillian orogeny properly began.

### 5.2.1 Trace element mobility

Due to challenges in studying diffusion of trace elements during metamorphism, there remains much that is not known about trace element mobility. Chapter 3 has suggested that many Hf, U, Th, Y, and heavy rare earth elements diffuse slowly in melt during cooling, but there remain many open questions. What are the grain-boundary diffusion coefficients of trace elements in metamorphic rocks? How does trace element distribution and kinetics affect major mineral growth? How can we effectively model accessory mineral growth during metamorphism? Mineral growth and diffusion kinetics could be investigated more closely with multi-mineral trace element maps of small domains within a thin section using tools like BINGO-ANTIDOTE (Duesterhoeft and Lanari, 2020) coupled with high-resolution techniques like TOF-ICP-MS (e.g. Rubatto et al., 2020) or NanoSIMS (e.g. Didier et al., 2015). This would provide detailed information on where trace elements are distributed on a local-scale—including mineral zoning—which could be sufficient to test local-equilibrium models of accessory mineral growth.

### 5.2.2 $H_2O$-present melting

The proposed mechanism for $H_2O$-fluxed melting in the Muskoka domain (Chapter 4) provides a simple thermodynamic and tectonic explanation for the large-scale melting observed in the region. It also prompts many more questions about the process of diffusive $H_2O$-fluxed melting in general. How does this mechanically propagate through the Muskoka domain? A melt flow model that incorporates $H_2O$ transfer between host rock and melt would inform us on how much melt could be reasonably generated when mass balance and flow mechanics are adequately accounted for. How does it influence the tectonics of the Grenville? Previous numerical models of the Grenville orogen (Jamieson et al., 2010) did not incorporate regional scale $H_2O$-fluxed melting and it would be worthwhile to investigate how the additional weakening at higher crustal levels would impact the model.

More generally, a numerical model of how the strain would be partitioned and how the structure would develop in the simplified scenario proposed (Chapter 5) of $H_2O$-fluxed melting caused by melt transport from one unit being actively thrusted under another unit. There have been no in-depth studies into the melting processes of the immediately underlying domains to make a geochemical connection between those and the Muskoka domain. There should be an investigation done into the migmatites in the Algonquin domain to compare the timing and conditions of their formation as well as the geochemistry to see if this proposed link can be justified.

Developing an understanding of the regional scale $H_2O$-fluxed melting in the Grenville province will provide geologists a better foundation for applying this tectonic model to other regions such as the Cordiellera (Holk and Taylor, 2000; Collins et al., 2016), the Georgetown Inlier (Volante et al., 2025), the Dabie Orogen (Xia et al., 2025), or the Andes (Errázuriz-Henao et al., 2024). Further investigation should be done into other regions noted for high amounts of possible $H_2O$-fluxed melting (Weinberg and Hasalová, 2015) to see if the same tectonic model can be applied elsewhere. If this is a common, global process, then it needs to be considered in tectonic models that incorporate crustal melting and in the interpretation of geochemical data from igneous rocks as a potential melt-source.

High temperature metamorphic reactions are central to tectonics and our ability to determine both the drivers of tectonic processes and the movement of rocks through the crust as a result of these tectonic processes. Approaching metamorphic reactions from both the micro-scale and the macro-scale allows an interpretation of metamorphism from multiple geological perspectives as our understanding of the small scale processes informs our ability to understand the large scale processes and vice versa. Much remains to be discovered at both the micro-scale and the macro-scale, and in bridging these together in a holistic approach to metamorphic petrology that ultimately yields a greater understanding of the modern and ancient petrological processes in Earth's continental crust.

# References


Acosta-Vigil, A., Buick, I., Cesare, B., London, D., and Morgan, G. B. (2012a). The Extent of Equilibration between Melt and Residuum during Regional Anatexis and its Implications for Differentiation of the Continental Crust: A Study of Partially Melted Metapelitic Enclaves. *Journal of Petrology*, 53(7):1319–1356.

Acosta-Vigil, A., London, D., and Morgan, G. B. (2006a). Experiments on the kinetics of partial melting of a leucogranite at 200 MPa H2O and 690–800°C: Compositional variability of melts during the onset of H2O-saturated crustal anatexis. *Contributions to Mineralogy and Petrology*, 151(5):539–557.

Acosta-Vigil, A., London, D., and Morgan, G. B. (2012b). Chemical diffusion of major components in granitic liquids: Implications for the rates of homogenization of crustal melts. *Lithos*, 153:308–323.

Acosta-Vigil, A., London, D., Morgan, G. B., Cesare, B., Buick, I., Hermann, J., and Bartoli, O. (2017). Primary crustal melt compositions: Insights into the controls, mechanisms and timing of generation from kinetics experiments and melt inclusions. *Lithos*, 286–287:454–479.

Acosta-Vigil, A., London, D., Morgan, G. B., and Dewers, T. A. (2006b). Dissolution of Quartz, Albite, and Orthoclase in H2O-Saturated Haplogranitic Melt at 800°C and 200 MPa: Diffusive Transport Properties of Granitic Melts at Crustal Anatectic Conditions. *Journal of Petrology*, 47(2):231–254.

Annen, C. and Burgisser, A. (2021). Modeling water exsolution from a growing and solidifying felsic magma body. *Lithos*, 402–403:105799.

Anovitz, L. M. and Essene, E. J. (1990). Thermobarometry and Pressure-Temperature Paths in the Grenville Province of Ontario. *Journal of Petrology*, 31(1):197–241.

Aranovich, L., Newton, R., and Manning, C. (2013). Brine-assisted anatexis: Experimental melting in the system haplogranite–H2O–NaCl–KCl at deep-crustal conditions. *Earth and Planetary Science Letters*, 374:111–120.

Bader, T., Franz, L., De Capitani, C., and Zhang, L. (2014). The effect of water activity on calculated phase equilibria and garnet isopleth thermobarometry of granulites, with particular reference to Tongbai (east-central China). *European Journal of Mineralogy*, 26(1):5–23.

Barker, F. (1979). Trondhjemite: Definition, Environment and Hypotheses of Origin. In *Developments in Petrology*, volume 6, pages 1–12. Elsevier.

Bea, F. (1996a). Controls on the trace element composition of crustal melts. *Earth and Environmental Science Transactions of the Royal Society of Edinburgh*, 87(1-2):33–41.

Bea, F. (1996b). Residence of REE, Y, Th and U in Granites and Crustal Protoliths; Implications for the Chemistry of Crustal Melts. *Journal of Petrology*, 37(3):521–552.

Bea, F., Montero, P., and Ortega, M. (2006). A LA-ICP-MS evaluation of zr reservoirs in common crustal rocks: Implications for Zr and Hf geochemistry, and zircon-forming processes. *The Canadian Mineralogist*, 44(3):693–714.

Beaumont, C., Jamieson, R. A., Nguyen, M. H., and Lee, B. (2001). Himalayan tectonics explained by extrusion of a low-viscosity crustal channel coupled to focused surface denudation. *Nature*, 414(6865):738–742.

Beckman, V., Möller, C., Söderlund, U., and Andersson, J. (2017). Zircon Growth during Progressive Recrystallization of Gabbro to Garnet Amphibolite, Eastern Segment, Sveconorwegian Orogen. *Journal of Petrology*, 58(1):167–187.

Berger, A., Burri, T., Alt-Epping, P., and Engi, M. (2008). Tectonically controlled fluid flow and water-assisted melting in the middle crust: An example from the Central Alps. *Lithos*, 102(3-4):598–615.

Bingen, B. (2001). Ilmenite as a Source for Zirconium during High-grade Metamorphism? Textural Evidence from the Caledonides of Western Norway and Implications for Zircon Geochronology. *Journal of Petrology*, 42(2):355–375.

Blichert-Toft, J. and Albarède, F. (1997). The Lu-Hf isotope geochemistry of chondrites and the evolution of the mantle-crust system. *Earth and Planetary Science Letters*, 148(1-2):243–258.

Bohlen, S. R. and Mezger, K. (1989). Origin of Granulite Terranes and the Formation of the Lowermost Continental Crust. *Science*, 244(4902):326–329.

Brown, M. (2004). The mechanism of melt extraction from lower continental crust of orogens. *Earth and Environmental Science Transactions of the Royal Society of Edinburgh*, 95(1-2):35–48.

Brown, M. (2007). Crustal melting and melt extraction, ascent and emplacement in orogens: Mechanisms and consequences. *Journal of the Geological Society*, 164(4):709–730.

Brown, M. (2013). Granite: From genesis to emplacement. *Geological Society of America Bulletin*, 125(7-8):1079–1113.

Brown, M., Kirkland, C., and Johnson, T. (2020). Evolution of geodynamics since the Archean: Significant change at the dawn of the Phanerozoic. *Geology*, 48(5):488–492.

Brown, M. and Raith, M. (1996). First evidence of ultrahigh-temperature decompression from the granulite province of southern India. *Journal of the Geological Society*, 153(6):819–822.

Brudner, A., Jiang, H., Chu, X., and Tang, M. (2022). Crustal thickness of the Grenville orogen: A Mesoproterozoic Tibet? *Geology*, 50(4):402–406.

Buddington, A. F. and Lindsley, D. H. (1964). Iron-Titanium Oxide Minerals and Synthetic Equivalents. *Journal of Petrology*, 5(2):310–357.

Bussy, F., Krogh, T. E., Klemens, W. P., and Schwerdtner, W. M. (1995). Tectonic and metamorphic events in the westernmost Grenville Province, central Ontario: New results from high-precision U–Pb zircon geochronology. *Canadian Journal of Earth Sciences*, 32(5):660–671.

Carr, S. D., Easton, R. M., Jamieson, R. A., and Culshaw, N. G. (2000). Geologic transect across the Grenville orogen of Ontario and New York. *Canadian Journal of Earth Sciences*, 37:27.

Cesare, B., Rubatto, D., and Gómez-Pugnaire, M. T. (2009). Do extrusion ages reflect magma generation processes at depth? An example from the Neogene Volcanic Province of SE Spain. *Contributions to Mineralogy and Petrology*, 157(2):267–279.

Chakraborty, S. (2008). Diffusion in Solid Silicates: A Tool to Track Timescales of Processes Comes of Age. *Annual Review of Earth and Planetary Sciences*, 36(1):153–190.

Chen, L., Yakymchuk, C., Zhao, K., Zhao, Z., Li, D., Gao, P., Chen, Y., Sun, G., and Liu, Z. (2023). The garnet effect on hafnium isotope compositions of granitoids during crustal anatexis. *Geology*, 51(5):439–443.

Chen, Y., Ye, K., Liu, J.-B., and Sun, M. (2008). Quantitative $P - T - X$ constraints on orthopyroxene-bearing high-pressure granulites in felsic–metapelitic rocks: Evidence from the Huangtuling granulite, Dabieshan Orogen. *Journal of Metamorphic Geology*, 26(1):1–15.

Chew, D. M., Babechuk, M. G., Cogné, N., Mark, C., O'Sullivan, G. J., Henrichs, I. A., Doepke, D., and McKenna, C. A. (2016). (LA,Q)-ICPMS trace-element analyses of Durango and McClure Mountain apatite and implications for making natural LA-ICPMS mineral standards. *Chemical Geology*, 435:35–48.

Cioffi, C. R., Campos Neto, M. D. C., Möller, A., and Rocha, B. C. (2019). Titanite petrochronology of the southern Brasília Orogen basement: Effects of retrograde net-transfer reactions on titanite trace element compositions. *Lithos*, 344–345:393–408.

Cisneros de León, A., Schmitt, A. K., and Weber, B. (2022). Multi-episodic formation of baddeleyite and zircon in polymetamorphic anorthosite and rutile-bearing ilmenitite from the Chiapas Massif Complex, Mexico. *Journal of Metamorphic Geology*, page jmg.12683.

Clark, C., Taylor, R. J. M., Kylander-Clark, A. R. C., and Hacker, B. R. (2018). Prolonged (>100 Ma) ultrahigh temperature metamorphism in the Napier Complex, East Antarctica: A petrochronological investigation of Earth's hottest crust. *Journal of Metamorphic Geology*, 36(9):1117–1139.

Clemens, J. and Vielzeuf, D. (1987). Constraints on melting and magma production in the crust. *Earth and Planetary Science Letters*, 86(2-4):287–306.

Clemens, J. D. (2006). Melting of the continental crust: Fluid regimes, melting reactions, and source-rock fertility. In Brown, M. and Rushmer, T., editors, *Evolution and Differentiation of the Continental Crust*, pages 297–331. Cambridge University Press, Cambridge, UK ; New York.

Clemens, J. D., Stevens, G., and Bryan, S. E. (2020). Conditions during the formation of granitic magmas by crustal melting – Hot or cold; drenched, damp or dry? *Earth-Science Reviews*, 200:102982.

Clemens, J. D., Stevens, G., and Mayne, M. J. (2021). Do arc silicic magmas form by fluid-fluxed melting of older arc crust or fractionation of basaltic magmas? *Contributions to Mineralogy and Petrology*, 176(6):44.

Collins, W., Flood, R., Vernon, R., and Shaw, S. (1989). The Wuluma granite, Arunta Block, central Australia: An example of in situ, near-isochemical granite formation in a granulite-facies terrane. *Lithos*, 23(1-2):63–83.

Collins, W. J., Huang, H.-Q., and Jiang, X. (2016). Water-fluxed crustal melting produces Cordilleran batholiths. *Geology*, 44(2):143–146.

Collins, W. J., Murphy, J. B., Johnson, T. E., and Huang, H.-Q. (2020). Critical role of water in the formation of continental crust. *Nature Geoscience*, 13(5):331–338.

Connolly, J. (2005). Computation of phase equilibria by linear programming: A tool for geodynamic modeling and its application to subduction zone decarbonation. *Earth and Planetary Science Letters*, 236(1-2):524–541.

Corfu, F. (2003). Atlas of Zircon Textures. *Reviews in Mineralogy and Geochemistry*, 53(1):469–500.

Costa, F., Dohmen, R., and Chakraborty, S. (2008). Time Scales of Magmatic Processes from Modeling the Zoning Patterns of Crystals. *Reviews in Mineralogy and Geochemistry*, 69(1):545–594.

Cottle, J. M. and Stearns, M. A. (2018). Application of Single-Shot Laser Ablation Split-Stream Inductively Coupled Plasma Mass Spectrometry to Accessory Phase Petrochronology. In Moser, D. E., Corfu, F., Darling, J. R., Reddy, S. M., and Tait, K., editors, *Geophysical Monograph Series*, pages 91–111. Wiley, 1 edition.

Culshaw, N., Foster, J., Marsh, J., Slagstad, T., and Gerbi, C. (2016). Kiosk domain, Central Gneiss Belt, Grenville Province, Ontario: A Labradorian palimpsest preserved in the ductile deep crust. *Precambrian Research*, 280:249–278.

Culshaw, N., Van De Kerckhove, S., Slagstad, T., Marsh, J., and Easton, R. M. (2023). Crustal evolution of the Laurentian continental margin from the Paleo- through Mesoproterozic: A zircon U–Pb and Hf transect through the western Grenville Province, Ontario, Canada. *Precambrian Research*, 386:106963.

Culshaw, N. G., Jamieson, R. A., Ketchum, J. W. F., Wodicka, N., Corrigan, D., and Reynolds, P. H. (1997). Transect across the northwestern Grenville orogen, Georgian Bay,

Ontario: Polystage convergence and extension in the lower orogenic crust. *Tectonics*, 16(6):966–982.

Dare, S. A. S., Barnes, S.-J., Beaudoin, G., Méric, J., Boutroy, E., and Potvin-Doucet, C. (2014). Trace elements in magnetite as petrogenetic indicators. *Mineralium Deposita*, 49(7):785–796.

Davidson, J., Turner, S., Handley, H., Macpherson, C., and Dosseto, A. (2007). Amphibole "sponge" in arc crust? *Geology*, 35(9):787.

Davis, D., Amelin, Y., Nowell, G., and Parrish, R. (2005). Hf isotopes in zircon from the western Superior province, Canada: Implications for Archean crustal development and evolution of the depleted mantle reservoir. *Precambrian Research*, 140(3-4):132–156.

Davis, D. W. (2002). U–Pb geochronology of Archean metasedimentary rocks in the Pontiac and Abitibi subprovinces, Quebec, constraints on timing, provenance and regional tectonics. *Precambrian Research*, 115(1-4):97–117.

Degeling, H., Eggins, S., and Ellis, D. J. (2001). Zr budgets for metamorphic reactions, and the formation of zircon from garnet breakdown. *Mineralogical Magazine*, 65(6):749–758.

Dickin, A. (2025). Nd isotope mapping in the Go Home region of Georgian Bay: A misunderstood key to the geology of the Central Gneiss Belt, Grenville Province of Ontario. *Canadian Journal of Earth Sciences*, 62(2):119–130.

Dickin, A. and Strong, J. (2019). Nd isotope mapping of the Grenvillian Allochthon Boundary Thrust in Algonquin Park, Ontario. *Canadian Journal of Earth Sciences*, 56(2):101–110.

Dickin, A., Strong, J., Arcuri, G., Van Kessel, A., and Krivankova-Smal, L. (2017). A revised model for the crustal structure of the SW Grenville Province, Ontario, Canada. *Geological Magazine*, 154(4):903–913.

Didier, A., Bosse, V., Bouloton, J., Mostefaoui, S., Viala, M., Paquette, J. L., Devidal, J. L., and Duhamel, R. (2015). NanoSIMS mapping and LA-ICP-MS chemical and U–Th–Pb data in monazite from a xenolith enclosed in andesite (Central Slovakia Volcanic Field). *Contributions to Mineralogy and Petrology*, 170(5-6):45.

Diener, J. F. A. and Fagereng, Å. (2014). The influence of melting and melt drainage on crustal rheology during orogenesis. *Journal of Geophysical Research: Solid Earth*, 119(8):6193–6210.

Duan, W.-Y., Chen, S., Schertl, H.-P., and Li, X.-P. (2023). High-pressure/ultrahigh-temperature mafic and felsic granulites associated with magnetite deposits from the Jiaobei terrane, Jiao-Liao-Ji Belt, North China Craton. *Ore Geology Reviews*, 152:105252.

Duesterhoeft, E. and Lanari, P. (2020). Iterative thermodynamic modelling—Part 1: A theoretical scoring technique and a computer program ( Bingo-Antidote). *Journal of Metamorphic Geology*, 38(5):527–551.

Duesterhoeft, E., Quinteros, J., Oberhänsli, R., Bousquet, R., and De Capitani, C. (2014). Relative impact of mantle densification and eclogitization of slabs on subduction dynamics: A numerical thermodynamic/thermokinematic investigation of metamorphic density evolution. *Tectonophysics*, 637:20–29.

Dyer, S. C., Edgeworth, I., Kendall, B., and Yakymchuk, C. (2025). Late-orogenic retrograde zircon growth. *Contributions to Mineralogy and Petrology*, 180(5):31.

Eiler, J. M. (2001). Oxygen Isotope Variations of Basaltic Lavas and Upper Mantle Rocks. *Reviews in Mineralogy and Geochemistry*, 43(1):319–364.

Ellis, D. J. (1987). Origin and evolution of granulites in normal and thickened crusts. *Geology*, 15(2):167.

Errázuriz-Henao, C., Parolari, M., Gómez-Tuena, A., Gutiérrez-Aguilar, F., and García-RodrÍguez, H. (2024). Geochemical Evidence of Water-Fluxed Crustal Melting in the Northern Colombian Andes. *Journal of Petrology*, 65(7):egae073.

Ewing, T. A., Hermann, J., and Rubatto, D. (2013). The robustness of the Zr-in-rutile and Ti-in-zircon thermometers during high-temperature metamorphism (Ivrea-Verbano Zone, northern Italy). *Contributions to Mineralogy and Petrology*, 165(4):757–779.

Farina, F. and Stevens, G. (2011). Source controlled 87Sr/86Sr isotope variability in granitic magmas: The inevitable consequence of mineral-scale isotopic disequilibrium in the protolith. *Lithos*, 122(3-4):189–200.

Farina, F., Stevens, G., Gerdes, A., and Frei, D. (2014). Small-scale Hf isotopic variability in the Peninsula pluton (South Africa): The processes that control inheritance of source 176Hf/177Hf diversity in S-type granites. *Contributions to Mineralogy and Petrology*, 168(4):1065.

Finch, M., Hasalova, P., Weinberg, R. F., and Fanning, C. M. (2014). Switch from thrusting to normal shearing in the Zanskar shear zone, NW Himalaya: Implications for channel flow. *Geological Society of America Bulletin*, 126(7-8):892–924.

Finch, M., Weinberg, R., Barrote, V., and Cawood, P. (2021). Hf isotopic ratios in zircon reveal processes of anatexis and pluton construction. *Earth and Planetary Science Letters*, 576:117215.

Fraser, G., Ellis, D., and Eggins, S. (1997). Zirconium abundance in granulite-facies minerals, with implications for zircon geochronology in high-grade rocks. *Geology*, 25(7):607.

Gaidies, F. and George, F. R. (2021). The interfacial energy penalty to crystal growth close to equilibrium. *Geology*, 49(8):988–992.

Gardien, V., Thompson, A. B., Grujic, D., and Ulmer, P. (1995). Experimental melting of biotite + plagioclase + quartz ± muscovite assemblages and implications for crustal melting. *Journal of Geophysical Research: Solid Earth*, 100(B8):15581–15591.

Gardien, V., Thompson, A. B., and Ulmer, P. (2000). Melting of Biotite + Plagioclase + Quartz Gneisses: The Role of H2O in the Stability of Amphibole. *Journal of Petrology*, 41(5):651–666.

Genier, F., Bussy, F., Epard, J.-L., and Baumgartner, L. (2008). Water-assisted migmatization of metagraywackes in a Variscan shear zone, Aiguilles-Rouges massif, western Alps. *Lithos*, 102(3-4):575–597.

George, F. R. and Gaidies, F. (2017). Characterisation of a garnet population from the Sikkim Himalaya: Insights into the rates and mechanisms of porphyroblast crystallisation. *Contributions to Mineralogy and Petrology*, 172(7):57.

Gervais, F., Beaudry, A., Kavanagh-Lepage, C., Moukhsil, A., Larson, K. P., and Guilmette, C. (2023). Far from boring: A new Grenvillian perspective on Mesoproterozoic tectonics. *Earth and Planetary Science Letters*, 610:118129.

Glazner, A. F. (2019). The ascent of water-rich magma and decompression heating: A thermodynamic analysis. *American Mineralogist*, 104(6):890–896.

Green, E. C. R., White, R. W., Diener, J. F. A., Powell, R., Holland, T. J. B., and Palin, R. M. (2016). Activity-composition relations for the calculation of partial melting equilibria in metabasic rocks. *Journal of Metamorphic Geology*, 34(9):845–869.

Guernina, S. and Sawyer, E. W. (2003). Large-scale melt-depletion in granulite terranes: An example from the Archean Ashuanipi Subprovince of Quebec. *Journal of Metamorphic Geology*, 21(2):181–201.

Hacker, B. R., Kelemen, P. B., and Behn, M. D. (2011). Differentiation of the continental crust by relamination. *Earth and Planetary Science Letters*, 307(3-4):501–516.

Hammouda, T., Pichavant, M., and Chaussidon, M. (1996). Isotopic equilibration during partial melting: An experimental test of the behaviour of Sr. *Earth and Planetary Science Letters*, 144(1-2):109–121.

Hanson, G. N. (1980). Rare Earth Elements in Petrogenetic Studies of Igneous Systems. *Annual Review of Earth and Planetary Sciences*, 8(1):371–406.

Harley, S. and Kelly, N. (2007). The impact of zircon–garnet REE distribution data on the interpretation of zircon U–Pb ages in complex high-grade terrains: An example from the Rauer Islands, East Antarctica. *Chemical Geology*, 241(1-2):62–87.

Harley, S. L. (1989). The origins of granulites: A metamorphic perspective. *Geological Magazine*, 126(3):215–247.

Hawthorne, F. C., Oberti, R., Harlow, G. E., Maresch, W. V., Martin, R. F., Schumacher, J. C., and Welch, M. D. (2012). Nomenclature of the amphibole supergroup. *American Mineralogist*, 97(11-12):2031–2048.

Hermann, J. and Rubatto, D. (2003). Relating zircon and monazite domains to garnet growth zones: Age and duration of granulite facies metamorphism in the Val Malenco lower crust. *Journal of Metamorphic Geology*, 21(9):833–852.

Holk, G. J. and Taylor, H. P. (2000). Water as a Petrologic Catalyst Driving 18O/16O Homogenization and Anatexis of the Middle Crust in the Metamorphic Core Complexes of British Columbia. *International Geology Review*, 42(2):97–130.

Holland, T. and Powell, R. (2003). Activity–composition relations for phases in petrological calculations: An asymmetric multicomponent formulation. *Contributions to Mineralogy and Petrology*, 145(4):492–501.

Holland, T. J. B. and Powell, R. (1998). An internally consistent thermodynamic data set for phases of petrological interest: An internally consistent thermodynamic data set. *Journal of Metamorphic Geology*, 16(3):309–343.

Holland, T. J. B. and Powell, R. (2011). An improved and extended internally consistent thermodynamic dataset for phases of petrological interest, involving a new equation of state for solids: Thermodynamic dataset for phases of petrological interest. *Journal of Metamorphic Geology*, 29(3):333–383.

Horstwood, M. S. A., Košler, J., Gehrels, G., Jackson, S. E., McLean, N. M., Paton, C., Pearson, N. J., Sircombe, K., Sylvester, P., Vermeesch, P., Bowring, J. F., Condon, D. J., and Schoene, B. (2016). Community-Derived Standards for LA - ICP - MS U-(Th-)Pb Geochronology – Uncertainty Propagation, Age Interpretation and Data Reporting. *Geostandards and Geoanalytical Research*, 40(3):311–332.

Hoskin, P. W. O. and Schaltegger, U. (2003). The Composition of Zircon and Igneous and Metamorphic Petrogenesis. *Reviews in Mineralogy and Geochemistry*, 53(1):27–62.

Hynes, A. and Rivers, T. (2010). Protracted continental collision — evidence from the Grenville OrogenThis article is one of a series of papers published in this Special Issue on the theme *Lithoprobe — parameters, processes, and the evolution of a continent* . *Canadian Journal of Earth Sciences*, 47(5):591–620.

Indares, A. (2020). Deciphering the metamorphic architecture and magmatic patterns of large hot orogens: Insights from the central Grenville Province. *Gondwana Research*, 80:385–409.

Jackson, J., Austrheim, H., McKenzie, D., and Priestley, K. (2004). Metastability, mechanical strength, and the support of mountain belts. *Geology*, 32(7):625.

Jamieson, R. A. and Beaumont, C. (2011). Coeval thrusting and extension during lower crustal ductile flow - implications for exhumation of high-grade metamorphic rocks. *Journal of Metamorphic Geology*, 29(1):33–51.

Jamieson, R. A. and Beaumont, C. (2013). On the origin of orogens. *Geological Society of America Bulletin*, 125(11-12):1671–1702.

Jamieson, R. A., Beaumont, C., Nguyen, M. H., and Culshaw, N. G. (2007). Synconvergent ductile flow in variable-strength continental crust: Numerical models with application to the western Grenville orogen. *Tectonics*, 26(5):2006TC002036.

Jamieson, R. A., Beaumont, C., Warren, C. J., and Nguyen, M. H. (2010). The Grenville Orogen explained? Applications and limitations of integrating numerical models with geological and geophysical data. *Canadian Journal of Earth Sciences*, 47(4):517–539.

Jochum, K. P. and Stoll, B. (2008). Reference materials for elemental and isotopic analyses by LA-(MC)-ICP-MS: Successes and outstanding needs. *Laser ablation ICP-MS in the Earth sciences: Current practices and outstanding issues*, 40:147–168.

Jochum, K. P., Willbold, M., Raczek, I., Stoll, B., and Herwig, K. (2005). Chemical Characterisation of the USGS Reference Glasses GSA-1G, GSC-1G, GSD-1G, GSE-1G, BCR-2G, BHVO-2G and BIR-1G Using EPMA, ID-TIMS, ID-ICP-MS and LA-ICP-MS. *Geostandards and Geoanalytical Research*, 29(3):285–302.

Johannes, W. and Holtz, F. (1996). *The Haplogranite System Qz-Ab-Or*, volume 22, pages 18–57. Springer Berlin Heidelberg, Berlin, Heidelberg.

Johnson, T. E., Brown, M., Gardiner, N. J., Kirkland, C. L., and Smithies, R. H. (2017). Earth's first stable continents did not form by subduction. *Nature*, 543(7644):239–242.

Johnson, T. E., Fischer, S., White, R. W., Brown, M., and Rollinson, H. R. (2012). Archaean Intracrustal Differentiation from Partial Melting of Metagabbro–Field and Geochemical Evidence from the Central Region of the Lewisian Complex, NW Scotland. *Journal of Petrology*, 53(10):2115–2138.

Kelly, N. M. and Harley, S. L. (2005). An integrated microtextural and chemical approach to zircon geochronology: Refining the Archaean history of the Napier Complex, east Antarctica. *Contributions to Mineralogy and Petrology*, 149(1):57–84.

Kelsey, D. E., Clark, C., and Hand, M. (2008). Thermobarometric modelling of zircon and monazite growth in melt-bearing systems: Examples using model metapelitic and metapsammitic granulites. *Journal of Metamorphic Geology*, 26(2):199–212.

Kelsey, D. E. and Powell, R. (2011). Progress in linking accessory mineral growth and breakdown to major mineral evolution in metamorphic rocks: A thermodynamic approach in the $Na_2O$-CaO-$K_2O$-FeO-MgO-$Al_2O_3$-$SiO_2$ -$H_2O$-$TiO_2$-$ZrO_2$ system. *Journal of Metamorphic Geology*, 29(1):151–166.

Kendrick, J., Duguet, M., and Yakymchuk, C. (2022). Diversification of Archean tonalite-trondhjemite-granodiorite suites in a mushy middle crust. *Geology*, 50(1):76–80.

Ketchum, J. W. F. and Davidson, A. (2000). Crustal architecture and tectonic assembly of the Central Gneiss Belt, southwestern Grenville Province, Canada: A new interpretation. *Canadian Journal of Earth Sciences*, 37:18.

King, J., Harris, N., Argles, T., Parrish, R., and Zhang, H. (2011). Contribution of crustal anatexis to the tectonic evolution of Indian crust beneath southern Tibet. *Geological Society of America Bulletin*, 123(1-2):218–239.

Kinney, C., Kendrick, J., Duguet, M., and Yakymchuk, C. (2024). Redistribution of heat-producing elements during melting of Archean crust. *Journal of Metamorphic Geology*, 42(2):197–224.

Kirkland, C., Johnson, T., Kinny, P., and Kapitany, T. (2020a). Modelling U-Pb discordance in the Acasta Gneiss: Implications for fluid–rock interaction in Earth's oldest dated crust. *Gondwana Research*, 77:223–237.

Kirkland, C., Yakymchuk, C., Gardiner, N., Szilas, K., Hollis, J., Olierook, H., and Steenfelt, A. (2020b). Titanite petrochronology linked to phase equilibrium modelling constrains tectono-thermal events in the Akia Terrane, West Greenland. *Chemical Geology*, 536:119467.

Kirkland, C., Yakymchuk, C., Szilas, K., Evans, N., Hollis, J., McDonald, B., and Gardiner, N. (2018). Apatite: A U-Pb thermochronometer or geochronometer? *Lithos*, 318–319:143–157.

Klein, B. Z. and Eddy, M. P. (2023). What's in an age? Calculation and interpretation of ages and durations from U-Pb zircon geochronology of igneous rocks. *Geological Society of America Bulletin*.

Kohn, M. J., Corrie, S. L., and Markley, C. (2015). The fall and rise of metamorphic zircon. *American Mineralogist*, 100(4):897–908.

Kohn, M. J., Spear, F. S., and Valley, J. W. (1997). Dehydration-Melting and Fluid Recycling during Metamorphism: Rangeley Formation, New Hampshire, USA. *Journal of Petrology*, 38(9):1255–1277.

Krneta, S., Ciobanu, C., Cook, N., and Ehrig, K. (2018). Numerical Modeling of REE Fractionation Patterns in Fluorapatite from the Olympic Dam Deposit (South Australia). *Minerals*, 8(8):342.

Kunz, B. E., Regis, D., and Engi, M. (2018). Zircon ages in granulite facies rocks: Decoupling from geochemistry above 850 °C? *Contributions to Mineralogy and Petrology*, 173(3):26.

Lanari, P. and Duesterhoeft, E. (2019). Modeling Metamorphic Rocks Using Equilibrium Thermodynamics and Internally Consistent Databases: Past Achievements, Problems and Perspectives. *Journal of Petrology*, 60(1):19–56.

Lanari, P. and Engi, M. (2017). Local Bulk Composition Effects on Metamorphic Mineral Assemblages. *Reviews in Mineralogy and Geochemistry*, 83(1):55–102.

Lanari, P. and Hermann, J. (2021). Iterative thermodynamic modelling—Part 2: Tracing equilibrium relationships between minerals in metamorphic rocks. *Journal of Metamorphic Geology*, 39(6):651–674.

Laurent, O., Björnsen, J., Wotzlaw, J.-F., Bretscher, S., Pimenta Silva, M., Moyen, J.-F., Ulmer, P., and Bachmann, O. (2020). Earth's earliest granitoids are crystal-rich magma reservoirs tapped by silicic eruptions. *Nature Geoscience*, 13(2):163–169.

Le Fort, P., Cuney, M., Deniel, C., France-Lanord, C., Sheppard, S., Upreti, B., and Vidal, P. (1987). Crustal generation of the Himalayan leucogranites. *Tectonophysics*, 134(1-3):39–57.

Lei, K., Wang, X.-C., and Wilde, S. A. (2024). Role and origin of water-fluxed melting in the generation of High Himalayan leucogranites. *Journal of Asian Earth Sciences*, 266:106118.

Liang, Y. and Parmentier, E. M. (2010). A Two-Porosity Double Lithology Model for Partial Melting, Melt Transport and Melt-rock Reaction in the Mantle: Mass Conservation Equations and Trace Element Transport. *Journal of Petrology*, 51(1-2):125–152.

Lumbers, S. B. and Vertolli, V. M. (2003). Precambrian Geology, Kawagama Lake area; Ontario Geological Survey, Preliminary Map P. 3525.

Manning, C. E. (2018). Fluids of the Lower Crust: Deep Is Different. *Annual Review of Earth and Planetary Sciences*, 46(1):67–97.

Marsh, J. H. and Culshaw, N. G. (2014). Timing and conditions of high-pressure metamorphism in the western Grenville Province: Constraints from accessory mineral composition and phase equilibrium modeling. *Lithos*, 200–201:402–417.

McCulloch, M. and Gamble, J. (1991). Geochemical and geodynamical constraints on subduction zone magmatism. *Earth and Planetary Science Letters*, 102(3-4):358–374.

McDonough, W. and Sun, S.-s. (1995). The composition of the Earth. *Chemical Geology*, 120(3-4):223–253.

McLeod, C. L., Davidson, J. P., Nowell, G. M., and De Silva, S. L. (2012). Disequilibrium melting during crustal anatexis and implications for modeling open magmatic systems. *Geology*, 40(5):435–438.

McMullen, S. M. (1999). *Tectonic Evolution of the Bark Lake Area, Eastern Central Gneiss Belt, Ontario Grenville: Constraints from Geology, Geochemistry and U-Pb Geochronology*. BSc Thesis, Carleton University.

Miyazaki, K., Mori, Y., Nishiyama, T., Suga, K., and Shigeno, M. (2018). Determination of reaction kinetics using grain size: An application for metamorphic zircon growth. *Terra Nova*, 30(2):162–168.

Miyazaki, K., Suga, K., Mori, Y., Iwano, H., Yagi, K., Shigeno, M., Nishiyama, T., Danhara, T., and Hirata, T. (2019). Kinetics and duration of metamorphic mineral growth in a subduction complex: Zircon and phengite in the Nagasaki metamorphic complex, western Kyushu, Japan. *Contributions to Mineralogy and Petrology*, 174(11):91.

Möller, A., O'Brien, P. J., Kennedy, A., and Kröner, A. (2003). Linking growth episodes of zircon and metamorphic textures to zircon chemistry: An example from the ultrahigh-temperature granulites of Rogaland (SW Norway). *Geological Society, London, Special Publications*, 220(1):65–81.

Morisset, C.-E. and Scoates, J. S. (2008). Origin of zircon rims around ilmenite in mafic plutonic rocks of proterozoic anorthosite suites. *The Canadian Mineralogist*, 46(2):289–304.

Moyen, J.-F. (2011). The composite Archaean grey gneisses: Petrological significance, and evidence for a non-unique tectonic setting for Archaean crustal growth. *Lithos*, 123(1-4):21–36.

Moyen, J.-F. and Stevens, G. (2006). Experimental constraints on TTG petrogenesis: Implications for Archean geodynamics. In Benn, K., Mareschal, J.-C., and Condie, K. C., editors, *Geophysical Monograph Series*, volume 164, pages 149–175. American Geophysical Union, Washington, D. C.

Mulder, J. A., Nebel, O., Gardiner, N. J., Cawood, P. A., Wainwright, A. N., and Ivanic, T. J. (2021). Crustal rejuvenation stabilised Earth's first cratons. *Nature Communications*, 12(1):3535.

Mungall, J. E. (2002). Empirical models relating viscosity and tracer diffusion in magmatic silicate melts. *Geochimica et Cosmochimica Acta*, 66(1):125–143.

Nielsen, R. L. and Beard, J. S. (2000). Magnetite–melt HFSE partitioning. *Chemical Geology*, 164(1-2):21–34.

Palin, R. M., Weller, O. M., Waters, D. J., and Dyck, B. (2016). Quantifying geological uncertainty in metamorphic phase equilibria modelling; a Monte Carlo assessment and implications for tectonic interpretations. *Geoscience Frontiers*, 7(4):591–607.

Pape, J., Mezger, K., and Robyr, M. (2016). A systematic evaluation of the Zr-in-rutile thermometer in ultra-high temperature (UHT) rocks. *Contributions to Mineralogy and Petrology*, 171(5):44.

Paton, C., Hellstrom, J., Paul, B., Woodhead, J., and Hergt, J. (2011). Iolite: Freeware for the visualisation and processing of mass spectrometric data. *Journal of Analytical Atomic Spectrometry*, 26(12):2508.

Paton, C., Woodhead, J. D., Hellstrom, J. C., Hergt, J. M., Greig, A., and Maas, R. (2010). Improved laser ablation U-Pb zircon geochronology through robust downhole fractionation correction. *Geochemistry, Geophysics, Geosystems*, 11(3):2009GC002618.

Pichavant, M., Villaros, A., Michaud, J. A.-S., and Scaillet, B. (2024). Granite magmatism and mantle filiation. *European Journal of Mineralogy*, 36(1):225–246.

Plunder, A., Le Pourhiet, L., Räss, L., Gloaguen, E., Pichavant, M., and Gumiaux, C. (2022). Pegmatites as geological expressions of spontaneous crustal flow localisation. *Lithos*, 416–417:106652.

Powell, R., Guiraud, M., and White, R. W. (2005). Truth and beauty in metamorphic phase-equilibria: Conjugate variables and phase diagrams. *The Canadian Mineralogist*, 43(1):21–33.

Powell, R. and Holland, T. J. B. (2008). On thermobarometry. *Journal of Metamorphic Geology*, 26(2):155–179.

Qi, H., Zhao, J.-H., and Johnson, T. E. (2023). The Fundamental Role of H2O in the Generation of Coeval Sodic and Potassic Granitoids at Continental Arcs: An Example from the Yangtze Block, South China. *Journal of Petrology*, 64(5):egad024.

Rey, P., Teyssier, C., and Whitney, D. (2009). The role of partial melting and extensional strain rates in the development of metamorphic core complexes. *Tectonophysics*, 477(3-4):135–144.

Rivers, T. (2008). Assembly and preservation of lower, mid, and upper orogenic crust in the Grenville Province—Implications for the evolution of large hot long-duration orogens. *Precambrian Research*, 167(3-4):237–259.

Rivers, T. (2012). Upper-crustal orogenic lid and mid-crustal core complexes: Signature of a collapsed orogenic plateau in the hinterland of the Grenville Province. *Canadian Journal of Earth Sciences*, 49(1):1–42.

Rivers, T., Culshaw, N. G., Hynes, A., Indares, A., Jamieson, R. A., and Martignole, J. (2012). The Grenville Orogen–A post-LITHOPROBE perspective. In *Tectonic Styles in Canada: The LITHOPROBE Perspective*, number 49 in Geological Association of Canada Special Paper, pages 97–236. Geological Association of Canada.

Rivers, T. and Schwerdtner, W. (2015). Post-peak Evolution of the Muskoka Domain, Western Grenville Province: Ductile Detachment Zone in a Crustal-scale Metamorphic Core Complex. *Geoscience Canada*, 42(4):403.

Roberts, N. M. W., Yakymchuk, C., Spencer, C. J., Keller, C. B., and Tapster, S. R. (2024). Revisiting the discrimination and distribution of S-type granites from zircon trace element composition. *Earth and Planetary Science Letters*, 633:118638.

Rubatto, D. (2002). Zircon trace element geochemistry: Partitioning with garnet and the link between U–Pb ages and metamorphism. *Chemical Geology*, 184(1-2):123–138.

Rubatto, D. (2017). Zircon: The Metamorphic Mineral. *Reviews in Mineralogy and Geochemistry*, 83(1):261–295.

Rubatto, D., Burger, M., Lanari, P., Hattendorf, B., Schwarz, G., Neff, C., Keresztes Schmidt, P., Hermann, J., Vho, A., and Günther, D. (2020). Identification of growth mechanisms in metamorphic garnet by high-resolution trace element mapping with LA-ICP-TOFMS. *Contributions to Mineralogy and Petrology*, 175(7):61.

Rubatto, D. and Hermann, J. (2007). Experimental zircon/melt and zircon/garnet trace element partitioning and implications for the geochronology of crustal rocks. *Chemical Geology*, 241(1-2):38–61.

Rudnick, R. L. and Fountain, D. M. (1995). Nature and composition of the continental crust: A lower crustal perspective. *Reviews of Geophysics*, 33(3):267.

Sauerzapf, U., Lattard, D., Burchard, M., and Engelmann, R. (2008). The Titanomagnetite–Ilmenite Equilibrium: New Experimental Data and Thermo-oxybarometric Application to the Crystallization of Basic to Intermediate Rocks. *Journal of Petrology*, 49(6):1161–1185.

Sawyer, E. (2010). Migmatites formed by water-fluxed partial melting of a leucogranodiorite protolith: Microstructures in the residual rocks and source of the fluid. *Lithos*, 116(3-4):273–286.

Sawyer, E. W. (2008). *Atlas of Migmatites*. Number 9 in The Canadian Mineralogist. Special Publication. NRC research press, Ottawa.

Schneider, D., Cope, N., and Holm, D. (2013). Thermochronology of the Mont Laurier terrane, southern Canadian Grenville Province, and its bearing on defining orogenic architecture. *Precambrian Research*, 226:43–58.

Schwerdtner, W., Rivers, T., Zeeman, B., Wang, C., Tsolas, J., Yang, J., and Ahmed, M. (2014). Post-convergent structures in lower parts of the 1090–1050 Ma (early-Ottawan) thrust-sheet stack, Grenville Province of Ontario, southern Canadian Shield. *Canadian Journal of Earth Sciences*, 51(3):243–265.

Sievwright, R. H., O'Neill, H. St. C., Tolley, J., Wilkinson, J. J., and Berry, A. J. (2020). Diffusion and partition coefficients of minor and trace elements in magnetite as a function of oxygen fugacity at 1150 ºC. *Contributions to Mineralogy and Petrology*, 175(5):40.

Simpson, A., Glorie, S., Hand, M., Spandler, C., and Gilbert, S. (2023). Garnet Lu-Hf speed dating: A novel method to rapidly resolve polymetamorphic histories. *Gondwana Research*, 121:215–234.

Singh, S. (2019). Protracted zircon growth in migmatites and In situ melt of Higher Himalayan Crystallines: U–Pb ages from Bhagirathi valley, NW Himalaya, India. *Geoscience Frontiers*, 10(3):793–809.

Slagstad, T. (2003). *Muskoka and Shawanaga Domains, Central Gneiss Belt, Grenville Province, Ontario: Geochemical and Geochronological Constraints on Pre-Grenvillian and Grenvillian Geological Evolution*. PhD thesis, Dalhousie University, Halifax, Nova Scotia.

Slagstad, T., Easton, R. M., Huyskens, M., and Culshaw, N. (2025). Complementarity of Hf isotopes from detrital and igneous zircon: An example from the Central Gneiss Belt, Grenville Province, Ontario. *Canadian Journal of Earth Sciences*, 62(2):192–210.

Slagstad, T., Hamilton, M. A., Jamieson, R. A., and Culshaw, N. G. (2004). Timing and duration of melting in the mid orogenic crust: Constraints from U–Pb (SHRIMP) data, Muskoka and Shawanaga domains, Grenville Province, Ontario. *Canadian Journal of Earth Sciences*, 41:27.

Slagstad, T., Jamieson, R. A., and Culshaw, N. G. (2005). Formation, Crystallization, and Migration of Melt in the Mid-orogenic Crust: Muskoka Domain Migmatites, Grenville Province, Ontario. *Journal of Petrology*, 46(5):893–919.

Sláma, J., Košler, J., Condon, D. J., Crowley, J. L., Gerdes, A., Hanchar, J. M., Horstwood, M. S., Morris, G. A., Nasdala, L., Norberg, N., Schaltegger, U., Schoene, B., Tubrett, M. N., and Whitehouse, M. J. (2008). Plešovice zircon — A new natural reference material for U–Pb and Hf isotopic microanalysis. *Chemical Geology*, 249(1-2):1–35.

Sláma, J., Košler, J., and Pedersen, R. B. (2007). Behaviour of zircon in high-grade metamorphic rocks: Evidence from Hf isotopes, trace elements and textural studies. *Contributions to Mineralogy and Petrology*, 154(3):335–356.

Smit, M. A. and Kooijman, E. (2024). A common precursor for global hotspot lavas. *Nature Geoscience*, 17(10):1053–1058.

Solar, G. S. and Brown, M. (2001). Petrogenesis of Migmatites in Maine, USA: Possible Source of Peraluminous Leucogranite in Plutons? *Journal of Petrology*, 42(4):789–823.

Spear, F. S. (1995). *Metamorphic Phase Equilibria and Pressure-Temperature-Time Paths*. Mineralogical Society of America, Troy, New York, 2 edition.

Spear, F. S. (2010). Monazite–allanite phase relations in metapelites. *Chemical Geology*, 279(1-2):55–62.

Stuart, C. A., Daczko, N. R., and Piazolo, S. (2017). Local partial melting of the lower crust triggered by hydration through melt–rock interaction: An example from Fiordland, New Zealand. *Journal of Metamorphic Geology*, 35(2):213–230.

Tafur, L. A. and Diener, J. F. A. (2020). Mineral equilibrium constraints on the feasibility of diffusive H2O-fluxed melting in the continental crust. *Journal of Metamorphic Geology*, 38(7):719–742.

Tan, W., Liu, P., He, H., Wang, C. Y., and Liang, X. (2016). Mineralogy and Origin of Exsolution In Ti-Rich Magnetite From Different Magmatic Fe-Ti Oxide-Bearing Intrusions. *The Canadian Mineralogist*, 54(3):539–553.

Tang, M., Chu, X., Hao, J., and Shen, B. (2021). Orogenic quiescence in Earth's middle age. *Science*, 371(6530):728–731.

Tang, M., Wang, X.-L., Shu, X.-J., Wang, D., Yang, T., and Gopon, P. (2014). Hafnium isotopic heterogeneity in zircons from granitic rocks: Geochemical evaluation and modeling of "zircon effect" in crustal anatexis. *Earth and Planetary Science Letters*, 389:188–199.

Taylor, R. J. M., Clark, C., Harley, S. L., Kylander-Clark, A. R. C., Hacker, B. R., and Kinny, P. D. (2017). Interpreting granulite facies events through rare earth element partitioning arrays. *Journal of Metamorphic Geology*, 35(7):759–775.

Timmerman, H., Jamieson, R. A., Parrish, R. R., and Culshaw, N. G. (2002). Coeval migmatites and granulites, Muskoka domain, southwestern Grenville Province, Ontario. *Canadian Journal of Earth Sciences*, 39:239–258.

Timmermann, H., Jamieson, R. A., Culshaw, N. G., and Parrish, R. R. (1997). Time of metamorphism beneath the Central Metasedimentary Belt boundary thrust zone, Grenville Orogen, Ontario: Accretion at 1080 Ma? *Canadian Journal of Earth Sciences*, 34(7):1023–1029.

Tomkins, H. S., Williams, I. S., and Ellis, D. J. (2005). *In Situ* U–Pb dating of zircon formed from retrograde garnet breakdown during decompression in Rogaland, SW Norway. *Journal of Metamorphic Geology*, 23(4):201–215.

Tual, L., Smit, M., Cutts, J., Musiyachenko, K., Kooijman, E., Majka, J., Foulds, I., and Ielpi, A. (2025). Garnet growth in a geological blink of an eye. *Geology*, 53(3):248–252.

Tuttle, O. F. and Bowen, N. L. (1958). Origin of granite in the light of experimental studies in the system NaAlSi3O8–KAlSi3O8–SiO2–H2O. In *Geological Society of America Memoirs*, volume 74, pages 1–146. Geological Society of America.

Vanardois, J., Trap, P., and Marquer, D. (2024). Crucial role of water-present melting in metagranite: Implications for the instigation of crustal-scale shear zones. *Geology*, 52(3):199–204.

Vermeesch, P. (2018). IsoplotR: A free and open toolbox for geochronology. *Geoscience Frontiers*, 9(5):1479–1493.

Vermeesch, P. (2021). On the treatment of discordant detrital zircon U–Pb data. *Geochronology*, 3(1):247–257.

Volante, S., Blereau, E., Guitreau, M., Tedeschi, M., Van Schijndel, V., and Cutts, K. (2024). Current applications using key mineral phases in igneous and metamorphic geology: Perspectives for the future. *Geological Society, London, Special Publications*, 537(1):57–121.

Volante, S., Pourteau, A., Li, Z.-X., Collins, W. J., Doucet, L. S., Olierook, H. K. H., Martin, L., and Smit, M. A. (2025). Oxygen isotope shifts reveal fluid-fluxed melting in continental anatexis. *Communications Earth & Environment*, 6(1):282.

Wang, D., Wang, X.-L., Cai, Y., Goldstein, S. L., and Yang, T. (2018). Do Hf isotopes in magmatic zircons represent those of their host rocks? *Journal of Asian Earth Sciences*, 154:202–212.

Watson, E. B. (1981). Diffusion in magmas at depth in the Earth: The effects of pressure and dissolved H2O. *Earth and Planetary Science Letters*, 52(2):291–301.

Watson, E. B. (1991). Diffusion in fluid-bearing and slightly-melted rocks: Experimental and numerical approaches illustrated by iron transport in dunite. *Contributions to Mineralogy and Petrology*, 107(4):417–434.

Watson, E. B. and Harrison, T. M. (1983). Zircon saturation revisited: Temperature and composition effects in a variety of crustal magma types. *Earth and Planetary Science Letters*, 64(2):295–304.

Weinberg, R. F. and Hasalová, P. (2015). Water-fluxed melting of the continental crust: A review. *Lithos*, 212–215:158–188.

White, D. J., Forsyth, D. A., Asudeh, I., Carr, S. D., Wu, H., Easton, R. M., and Mereu, R. F. (2000). A seismic-based cross-section of the Grenville Orogen in southern Ontario and western Quebec. *Canadian Journal of Earth Sciences*, 37.

White, R. W., Pomroy, N. E., and Powell, R. (2005). An *in situ* metatexite–diatexite transition in upper amphibolite facies rocks from Broken Hill, Australia. *Journal of Metamorphic Geology*, 23(7):579–602.

White, R. W. and Powell, R. (2002). Melt loss and the preservation of granulite facies mineral assemblages. *Journal of Metamorphic Geology*, 20(7):621–632.

White, R. W., Powell, R., and Clarke, G. L. (2002). The interpretation of reaction textures in Fe-rich metapelitic granulites of the Musgrave Block, central Australia: Constraints from mineral equilibria calculations in the system $K_2O$–FeO–MgO–$Al_2O_3$–$SiO_2$–$H_2O$–$TiO_2$–$Fe_2O_3$. *Journal of Metamorphic Geology*, 20(1):41–55.

White, R. W., Powell, R., and Holland, T. J. B. (2007). Progress relating to calculation of partial melting equilibria for metapelites. *Journal of Metamorphic Geology*, 25(5):511–527.

White, R. W., Powell, R., Holland, T. J. B., Johnson, T. E., and Green, E. C. R. (2014a). New mineral activity–composition relations for thermodynamic calculations in metapelitic systems. *Journal of Metamorphic Geology*, 32(3):261–286.

White, R. W., Powell, R., and Johnson, T. E. (2014b). The effect of Mn on mineral stability in metapelites revisited: New a–x relations for manganese-bearing minerals. *Journal of Metamorphic Geology*, 32(8):809–828.

Whitney, D. L. and Evans, B. W. (2010). Abbreviations for names of rock-forming minerals. *American Mineralogist*, 95(1):185–187.

Whitney, D. L., Teyssier, C., Rey, P., and Buck, W. R. (2013). Continental and oceanic core complexes. *Geological Society of America Bulletin*, 125(3-4):273–298.

Wiedenbeck, M., Hanchar, J. M., Peck, W. H., Sylvester, P., Valley, J., Whitehouse, M., Kronz, A., Morishita, Y., Nasdala, L., Fiebig, J., Franchi, I., Girard, J.-P., Greenwood, R., Hinton, R., Kita, N., Mason, P., Norman, M., Ogasawara, M., Piccoli, P., Rhede, D., Satoh, H., Schulz-Dobrick, B., Skår, O., Spicuzza, Mj., Terada, K., Tindle, A., Togashi, S., Vennemann, T., Xie, Q., and Zheng, Y.-F. (2004). Further Characterisation of the 91500 Zircon Crystal. *Geostandards and Geoanalytical Research*, 28(1):9–39.

Wodicka, N. (1994). *Middle Proterozoic Evolution of the Parry Sound Domain, Southwestern Grenville Orogen, Ontario: Structural, Metamorphic, U/Pb, and 40Ar/39 Ar Constraints*. PhD thesis, Dalhousie University.

Wodicka, N., Jamieson, R. A., and Parrish, R. R. (1996). The Parry Sound domain: A far-travelled allochthon? New evidence from U–Pb zicon geochronology. *Canadian Journal of Earth Sciences*, 33(7):1087–1104.

Wodicka, N., Ketchum, J. W., and Jamieson, R. A. (2000). Grenvillian metamorphism of monocyclic rocks, georgian bay, ontario, canada: Implications for convergence history. *The Canadian Mineralogist*, 38(2):471–510.

Xia, Y.-S., Gao, P., Sun, G.-C., Zhao, Z.-F., Qin, L., Wen, G., Li, Z.-X., and Dai, L.-Q. (2025). Fluid-fluxed melting of juvenile lower crust traced by molybdenum isotopes. *Geology*, 53(2):125–129.

Yakymchuk, C. (2017). Behaviour of apatite during partial melting of metapelites and consequences for prograde suprasolidus monazite growth. *Lithos*, 274–275:412–426.

Yakymchuk, C. (2023). Prograde zircon growth in migmatites. *Journal of Metamorphic Geology*, 41(5):719–743.

Yakymchuk, C. and Brown, M. (2014a). Behaviour of zircon and monazite during crustal melting. *Journal of the Geological Society*, 171(4):465–479.

Yakymchuk, C. and Brown, M. (2014b). Consequences of open-system melting in tectonics. *Journal of the Geological Society*, 171(1):21–40.

Yakymchuk, C., Kirkland, C., Hollis, J., Kendrick, J., Gardiner, N., and Szilas, K. (2020). Mesoarchean partial melting of mafic crust and tonalite production during high-T–low-P stagnant tectonism, Akia Terrane, West Greenland. *Precambrian Research*, 339:105615.

Yakymchuk, C., Kirkland, C. L., and Clark, C. (2018). Th/U ratios in metamorphic zircon. *Journal of Metamorphic Geology*, 36(6):715–737.

Yardley, B. W. D. and Barber, J. P. (1991). Melting reactions in the Connemara Schists: The role of water infiltration in the formation of amphibolite facies migmatites. *American Mineralogist*, 76:848–856.

Yardley, B. W. D. and Valley, J. W. (1997). The petrologic case for a dry lower crust. *Journal of Geophysical Research: Solid Earth*, 102(B6):12173–12185.

Yogi, M. T. A. G., Gaidies, F., Heldwein, O. K. A., and Rice, A. H. N. (2025). The Distribution of Major and Trace Elements Across a Garnet Population From the Kalak Nappe Complex (Finnmark, Scandinavian Caledonides): Evidence for Size-Dependent Growth and Compositional Equilibration in the Garnet Zone. *Journal of Metamorphic Geology*, page jmg.12820.

Zhang, C., Chen, T.-W., and Vervoort, J. D. (2023). An optimized chromatography method and MC-ICP-MS technique for apatite Lu–Hf geochronology. *Journal of Analytical Atomic Spectrometry*, 38(12):2636–2647.

Zhang, C., Liu, D., Zhang, X., Spencer, C., Tang, M., Zeng, J., Jiang, S., Jolivet, M., and Kong, X. (2020). Hafnium isotopic disequilibrium during sediment melting and assimilations. *Geochemical Perspectives Letters*, pages 34–39.

Zhang, J.-B., Liu, Y.-S., Foley, S. F., Moynier, F., Zhao, L., Xu, R., and Wang, C.-Y. (2024a). Widespread two-layered melt structure in the asthenosphere. *Nature Geoscience*, 17(5):472–477.

Zhang, Y. and Gan, T. (2022). Diffusion in Melts and Magmas. *Reviews in Mineralogy and Geochemistry*, 87(1):283–337.

Zhang, Y., Guo, L., Zhang, W., Zhang, H., and Luo, T. (2024b). Zircon Zr Hf isotope disequilibrium during crustal anatexis: A record from the Mesozoic migmatite in the eastern Gangdese arc, South Tibet. *Chemical Geology*, 659:122144.

Zhang, Y., Ni, H., and Chen, Y. (2010). Diffusion Data in Silicate Melts. *Reviews in Mineralogy and Geochemistry*, 72(1):311–408.

Zhong, S., Li, S., Seltmann, R., Lai, Z., and Zhou, J. (2021). The influence of fractionation of REE-enriched minerals on the zircon partition coefficients. *Geoscience Frontiers*, 12(3):101094.

Zhu, D.-C., Wang, Q., Li, S.-M., Zhan, Q.-Y., Liu, Z., Xie, J.-C., Liu, L., Zhang, L.-L., Zhong, X.-Y., and Zhao, Y.-X. (2025). Magma genesis and crustal evolution in continental collision zones. *Science China Earth Sciences*, 68(5):1346–1370.

# APPENDICES

# Appendix A

# Supplementary Material for Chapter 2

Supplementary data tables are available in an online data repository accessible at https://doi.org/10.5683/SP3/TYCCSR. The following is a description of the supplementary tables.

**Table A.1:** On peak and background collection times for each element analyzed by electron microprobe

**Table A.2:** Experimental conditions for trace element analyses of various minerals

**Table A.3:** Experimental run conditions for U-Pb geochronology of zircon

**Table A.4:** QAQC results for LA-MC-ICP-MS U-Pb analyses. Ples = Plesovice. RV = Reference Values, Concordia plots and ages shown in Fig. A.1

**Table A.5:** Partition coefficients used in mineral-melt Zr partition models

**Table A.6:** Bulk rock trace element composition of each sample in ppm

**Table A.7:** Average electron microprobe major element analyses of each major mineral in weight percent (wt%) and atoms per formula unit (apfu)

**Table A.8:** Individual electron microprobe major element analyses of each major mineral in weight percent (wt%) and atoms per formula unit (apfu). Empty cells are unanalyzed elements.

**Table A.9:** Individual LA-ICP-MS trace element analyses of silicate minerals and apatite

**Table A.10:** Individual LA-ICP-MS trace element analyses of oxides

**Table A.11:** Individual LA-MC-ICP-MS U-Pb analyses of zircon

**Table A.12:** QAQC results for LA-ICP-MS trace element analyses

**Table A.13:** UTM coordinates of each sample

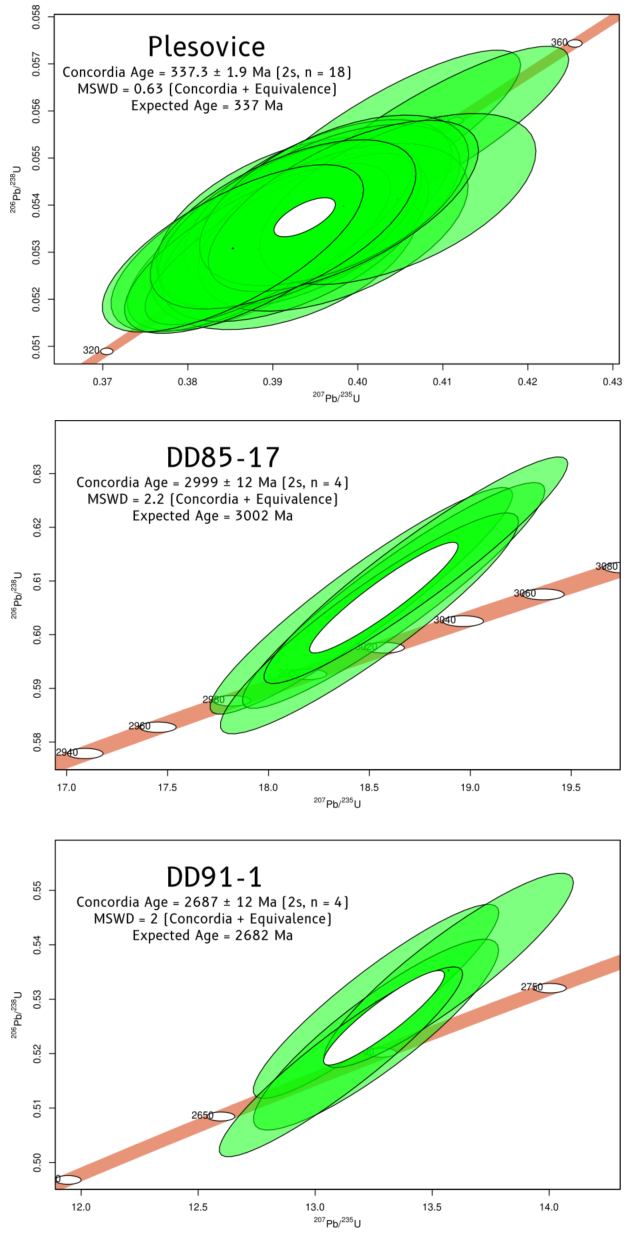


**Figure A.1:** Concordia diagrams of the secondary standards, individual analyses shown in table S4

# Appendix B

# Supplementary Material for Chapter 3

Supplementary data tables are available in an online data repository accessible at https://doi.org/10.5683/SP3/TYCCSR. The following is a description of the supplementary tables.

**Table B.1:** Experimental run conditions for trace elements in zircon

**Table B.2:** Experimental run conditions for U, Th, and Pb isotopes in zircon

**Table B.3:** On peak and background collection times for each element analyzed by electron microprobe

**Table B.4:** QAQC results of 91500 for LA-ICP-MS trace element analyses on zircon

**Table B.5:** QAQC results for LA-MC-ICP-MS U-Pb analyses. Ples = Plesovice. RV = Reference Values

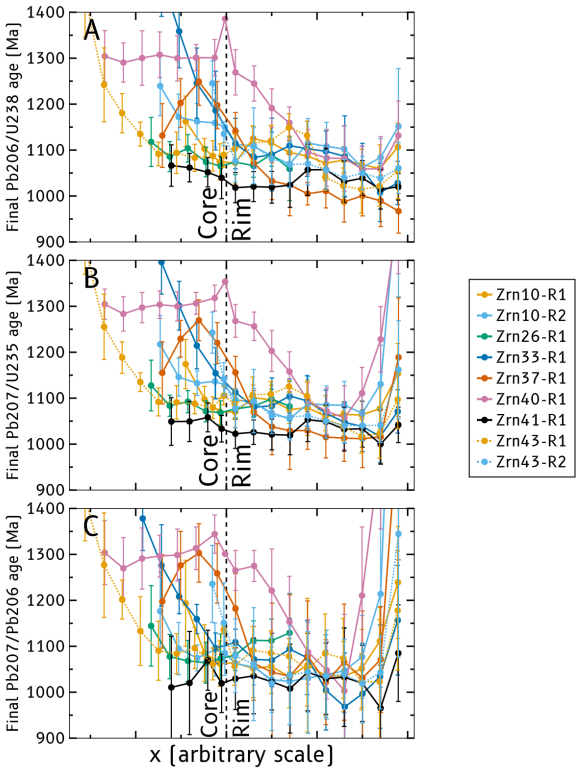


**Figure B.1:** 206Pb/235U **(A)**, 207Pb/235U **(B)**, and 207Pb/296Pb **(C)** age profiles of select zircons. Dashed lines indicate core/rim interface. Profiles are average ages and $1\sigma$ of multiple measurements in an interval. Intervals have 10% of the measurements between the core-rim interface and rim edge.

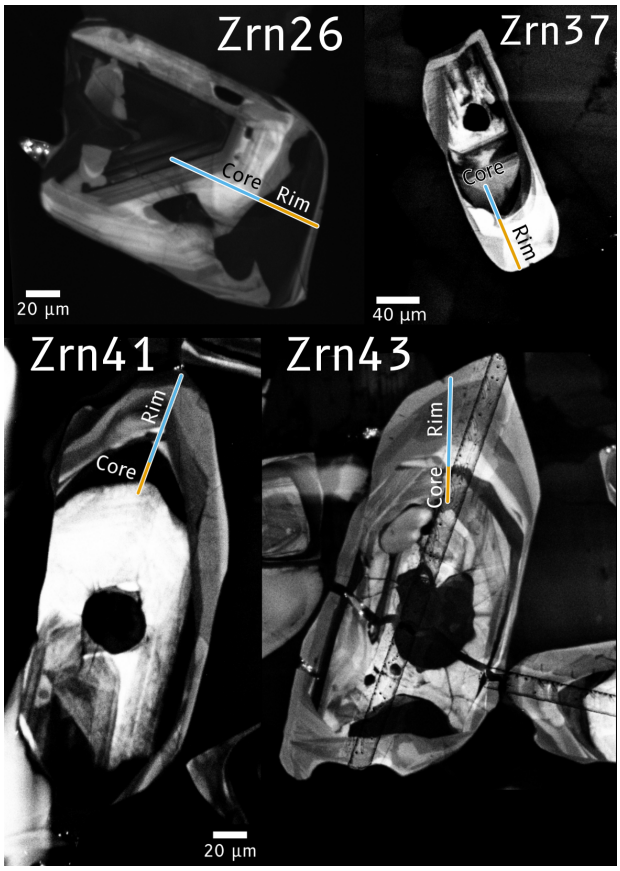


**Figure B.2:** Cathodoluminescence images of zircons analyzed with EPMA with the extent of transects shown on Fig. 3.4 F.

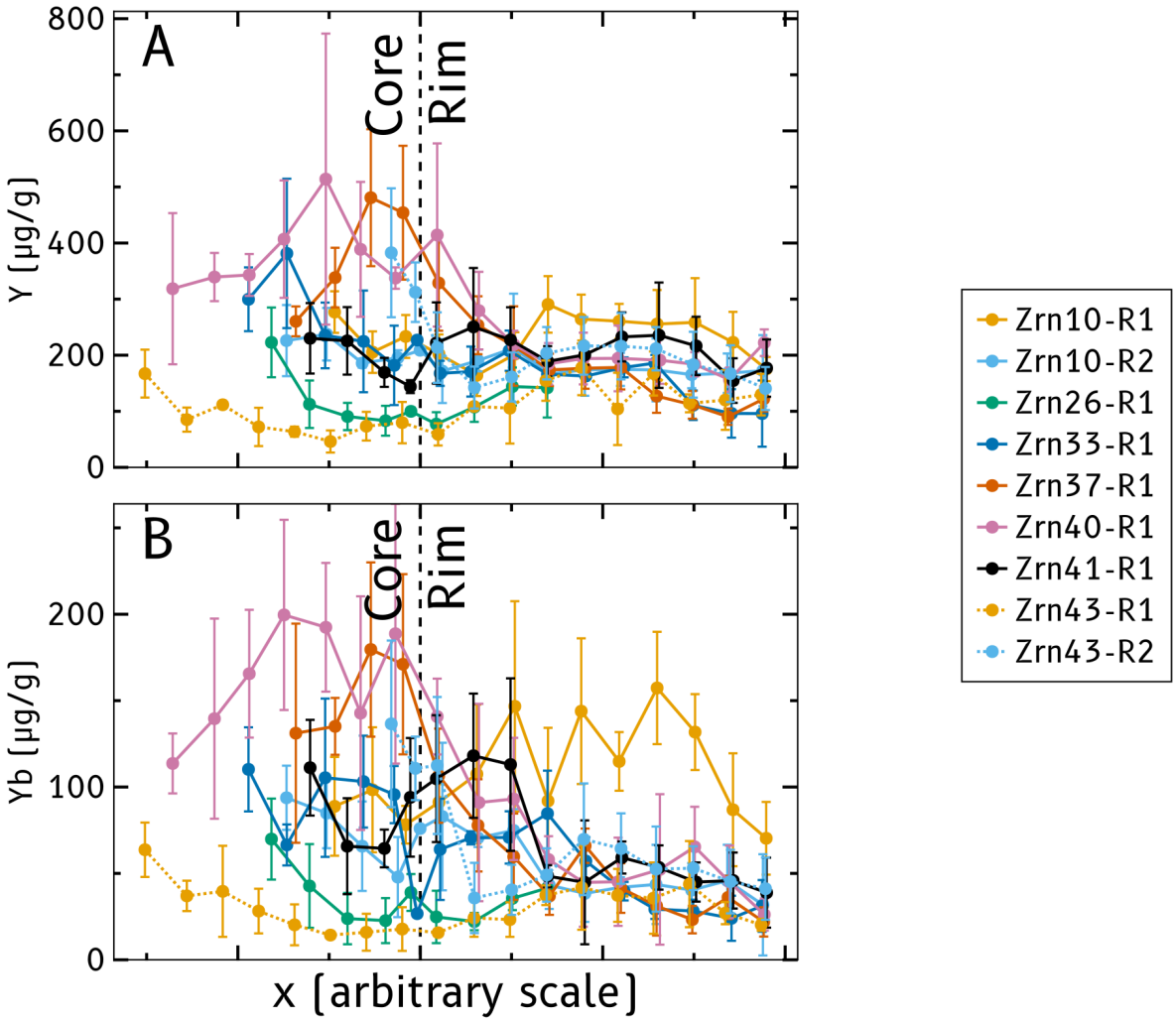


**Figure B.3:** Full set of Y **(A)** and Yb **(B)** LA-ICP-MS profiles. Dashed lines indicate core/rim interface. Profiles are average ages and 1$\sigma$ of multiple measurements in an interval. Intervals have 10% of the measurements between the core-rim interface and rim edge.

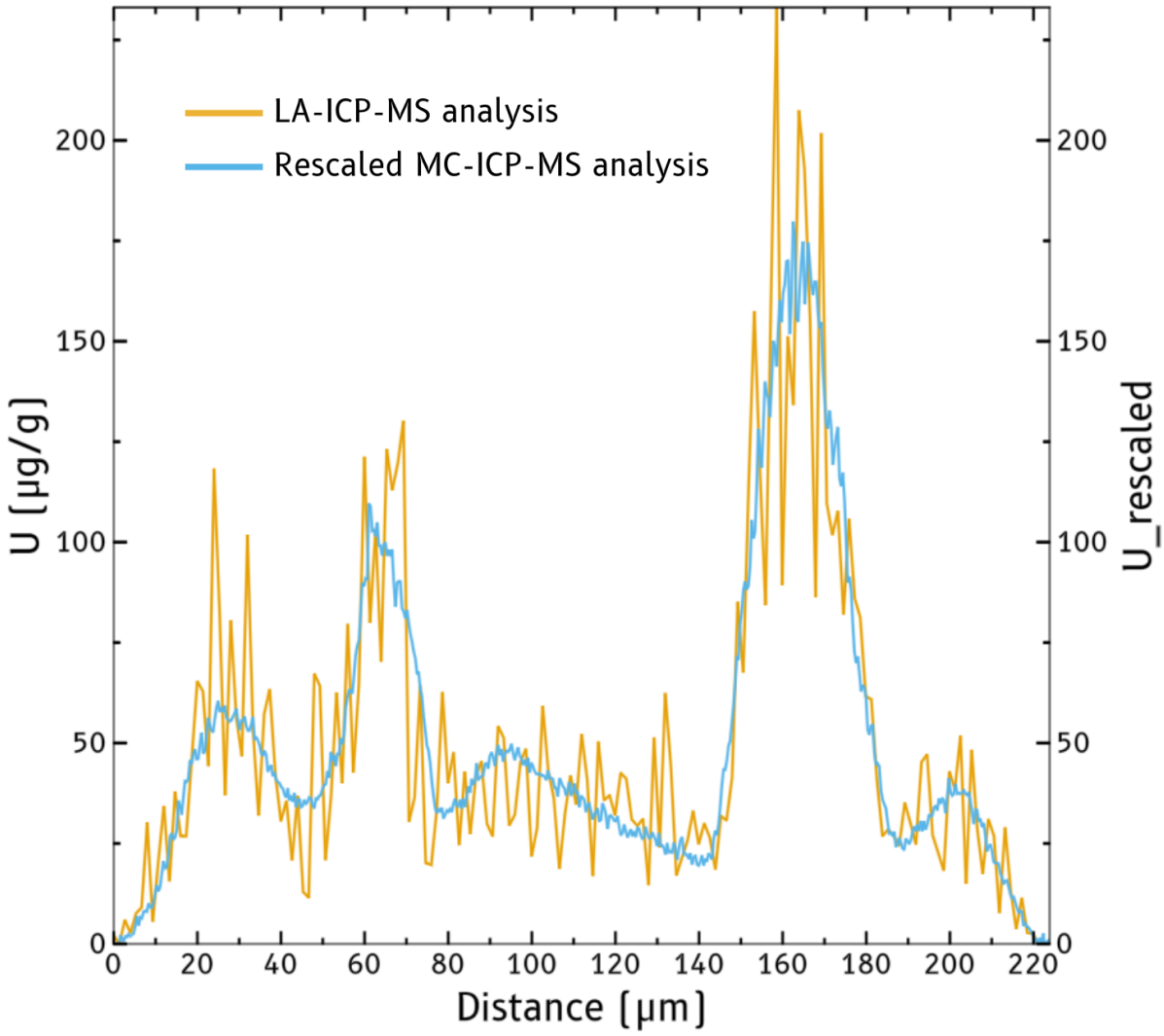


**Figure B.4:** Example of U measurements from LA-ICP-MS and LA-MC-ICP-MS analyses of Zrn10 after rescaling LA-MC-ICP-MS data.

# Appendix C

# Supplementary Material for Chapter 4

Supplementary data tables are available in an online data repository accessible at https://doi.org/10.5683/SP3/TYCCSR. The following is a description of the supplementary tables.

**Table C.1:** On peak and background collection times for each element analyzed by electron microprobe

**Table C.2:** Experimental run conditions for trace elements in amphibole

**Table C.3:** Experimental run conditions for U-Pb geochronology in zircon

**Table C.4:** QAQC results for LA-ICP-MS trace element analyses on amphibole

**Table C.5:** QAQC results for LA-MC-ICP-MS U-Pb analyses. Ples = Plesovice. RV = Reference Values, Concordia plots and ages shown in Fig. C.1

**Table C.6:** Bulk rock major element (wt%) and trace element composition (ppm) of each sample

**Table C.7:** UTM coordinates of sample locations

**Table C.8:** Individual electron microprobe major element analyses of amphibole in weight percent (wt%) and atoms per formula unit (apfu)

**Table C.9:** Individual LA-ICP-MS trace element analyses of amphibole in ppm

**Table C.10:** Individual LA-ICP-MS U-Pb analyses of zircon

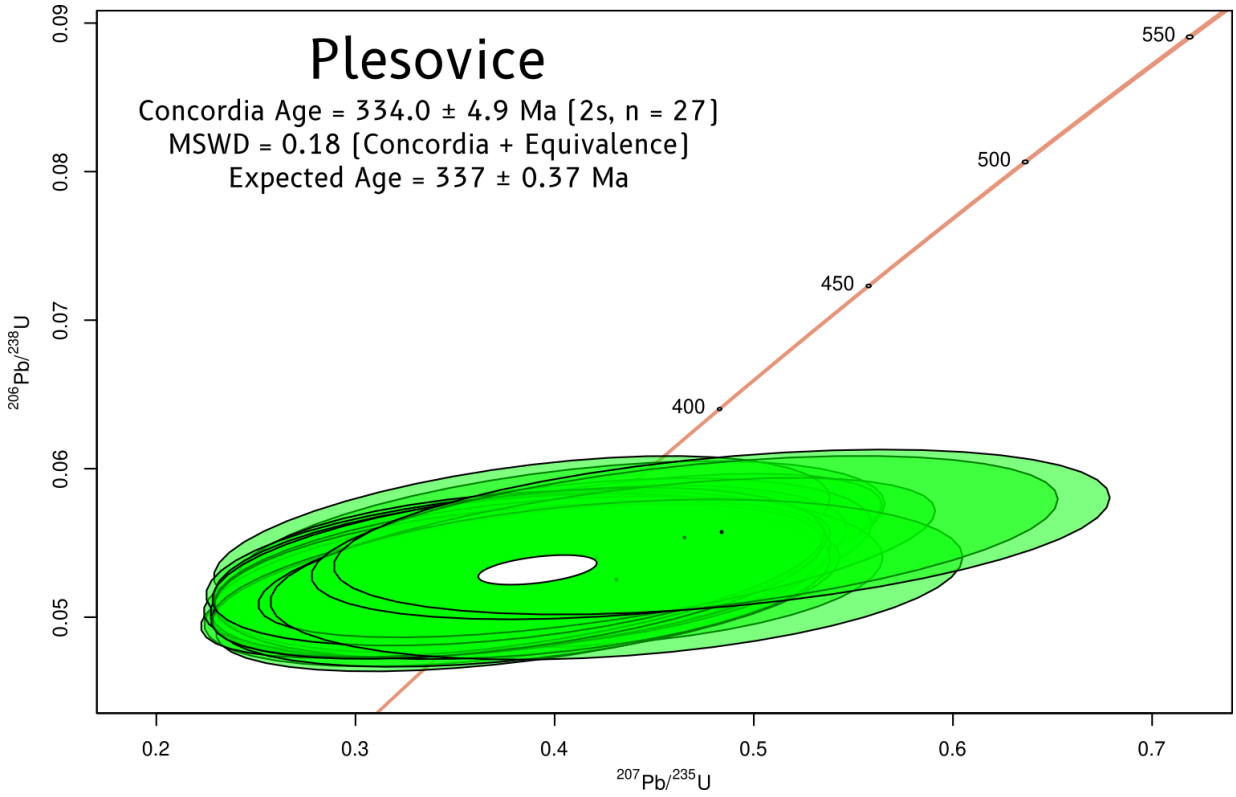


**Figure C.1:** Concordia diagrams of the secondary standard, Plesovice, individual analyses shown in table S4